Investigation into Noise and Stability Effects on CCD and Readout Electronics with Reference to the PLATO Mission

Robert Wacholc

Thesis submitted for the degree of

Doctor of Philosophy (PhD)

of

University College London

Mullard Space Science Laboratory

Department of Space and Climate Physics

University College London

January 2019

I, Robert Wacholc, confirm that work presented in this thesis is my own. Where information has been derived from other sources, I confirm that this has been indicated in the thesis.

Abstract

This thesis addresses various noise and stability effects with respect to Charge-Coupled Devices (CCDs), CCD camera readout electronics and Light-Emitting Diodes (LEDs).

In Chapter 1 a general overview of CCD technology and description of the various detector types and their parameters is given, followed by a brief review of the planet finding missions that use instruments containing CCD cameras.

A more detailed description of the PLATO mission is provided in Chapter 2. This includes mission objectives and a short characterisation of the CCD detector and the readout electronics intended for the PLATO normal cameras.

The initial study presented in Chapter 3 focuses on investigation of the photometric stability of LEDs and their applicability to the study of highly stable CCD cameras. Two key issues are explored, the ageing effect and temperature sensitivity.

Chapter 4 discusses various aspects of ElectroMagnetic Compatibility (EMC) testing of space equipment with emphasis on the PLATO mission EMC requirements.

Chapter 5 describes the conducted susceptibility study of the PLATO Normal-Front-End Electronics (N-FEE) board. A technique for performing conducted susceptibility measurements in practice is demonstrated in both Common Mode (CM) and Differential Mode (DM) configurations. In addition, a simulation of the Correlated Double Sampling (CDS) circuit is presented and compared against the output of a real measurement.

In the final study described in Chapter 6, the temperature sensitivities of

the CCD output stage and PLATO N-FEE board are investigated. Two key effects are studied, offset and gain temperature sensitivities.

Chapter 7 presents the final interpretation of the findings in the form of implications for the PLATO mission. Requirements for the filter board are discussed, as well as the temperature stability requirements for both the CCD and the N-FEE.

Acknowledgements

- Thanks to my supervisors Alan Smith and Dave Walton for all the guidance along the way, for their technical support and tons of useful comments on drafts of this thesis.
- Thanks to Patricia Tomkins for giving me the opportunity to do this PhD.
- Thanks to Mark Hailey for providing me with his expertise and help with organising test equipment (countless times).
- Thanks to Jason Gow and Richard Darnley for all the interesting chats and good advice.
- Thanks to Magdalena Szafraniec for sharing her professional experience.
- Thanks to Daisuke Kawata for the great chats and moral support.
- Thanks to Andy Fenney, Paul Prior and Damron McLeod for solving my computer and networking problems.
- Last, but not least, thanks to my family and in particular to my partner Anna for her understanding, patience and enormous support.

"Per aspera ad astra"

Contents

Abbreviations

AC	Alternating Current
ADC	Analogue-to-Digital Converter
ADU	Analogue-to-Digital-Unit
AIMO	Advanced Inverted Mode Operation
BCCD	Buried-channel Charge-Coupled Device
BSI	Back-Side Illuminated
CCD	Charge-Coupled Device
CDS	Correlated Double Sampling
CE	Conducted Emissions
CIC	Clock Induced Charge
CM	Common Mode
CMOS	Complementary Metal-Oxide-Semiconductor
CNES	Centre National d'Études Spatiales
CoRoT	COnvection, ROtation and planetary Transits
CS	Conducted Susceptibility
CTE	Charge Transfer Efficiency
CTI	Charge Transfer Inefficiency
DAC	Digital-to-Analogue Converter
DC	Direct Current

DM	Differential Mode
DMM	Digital Multimeter
DN	Digital Number
DR	Dynamic Range
ECSS	European Cooperation for Space Standardisation
EGSE	Electrical Ground Support Equipment
EM	Electron Multiplying
EMC	ElectroMagnetic Compatibility
EMI	ElectroMagnetic Interference
ESA	European Space Agency
EUT	Equipment Under Test
FET	Field-Effect Transistor
FF	Full-Frame
FGS	Fine Guidance Sensor
FPGA	Field-Programmable Gate Array
FPN	Fixed Pattern Noise
FSI	Front-Side Illuminated
FT	Frame Transfer
GaAsP	Gallium Arsenide Phosphide
GaP	Gallium Phosphide
IC	Integrated Circuit
ICP	Injection Current Probe
IMO	Inverted Mode Operation

IT	Interline Transfer
LDO	Low-DropOut
LED	Light-Emitting Diode
LISN	Line Impedance Stabilisation Network
LPF	Low-Pass Filter
MIS	Metal-Insulator-Semiconductor
MIT	Massachusetts Institute of Technology
MPP	Multi-Pinned Phase
MSSL	Mullard Space Science Laboratory
MTF	Modulation Transfer Function
N-DPU	Normal-Data Processing Unit
N-FEE	Normal-Front-End Electronics
NASA	National Aeronautics and Space Administration
NIMO	Non-Inverted Mode Operation
NIR	Near Infrared
NTC	Negative Temperature Coefficient
OD	Open Drain
OT	Orthogonal Transfer
PC	Personal Computer
PCB	Printed Circuit Board
PLATO	PLAnetary Transits and Oscillations of stars
PSF	Point Spread Function

PSU	Power Supply Unit
QE	Quantum Efficiency
QY	Quantum Yield
RE	Radiated Emissions
RF	Radio Frequency
rms	root mean square
ROI	Region Of Interest
RS	Radiated Susceptibility
SAC	Semi-Anechoic Chamber
SCCD	Surface-channel Charge-Coupled Device
SMC	Space and Missile systems Center
SNR	Signal-to-Noise Ratio
SRAM	Static Random-Access Memory
SuperWASP	Super Wide Angle Search for Planets
TCR	Temperature Coefficient of Resistance
TDI	Time Delay and Integration
TESS	Transiting Exoplanet Survey Satellite
TIFF	Tagged Image File Format
TTi	Thurlby Thandar instruments
USB	Universal Serial Bus
VI	Virtual Instrument

List of Figures

List of Tables

Chapter 1

Charge Coupled Devices

Charge-Coupled Devices (CCDs) are popular semiconductor detectors invented in 1969 at AT&T Bell Labs (Boyle and Smith, 1970). This innovation earned its authors, Willard S. Boyle and George S. Smith, the 2009 Nobel Prize in Physics. The CCD was originally invented as a memory storage device to be a semiconductor equivalent of a magnetic bubble memory (concept described in Bobeck (1972)). Nevertheless, they were soon considered as imaging devices and gradually replaced the less efficient vidicon tubes, which had been in use up to that time. Nowadays, despite the fast growing popularity of Complementary Metal-Oxide-Semiconductor (CMOS) detectors, CCDs still remain the technology of choice for many scientific applications, especially in the space sector, due to their high photometric performance and mature technology with significant flight heritage.

1.1 Photon Detection Processes in CCDs

CCDs detect light through a physical process known as the photoelectric effect (see Einstein (1905)), where the incident photons generate electron-hole pairs in the semiconductor material (discovering the law of the photoelectric effect earned Einstein the Nobel Prize in 1921; there was another Nobel Prize awarded for work on the photoelectric effect to Robert Millikan in 1923). Only photons above a certain energy are accepted. The lower energy limit is de-

fined by a semiconductor's band-gap energy that can be approximated from the following equation (Varshni, 1967):

$$E_g = E_g(0) - \frac{\alpha T^2}{T + \beta}, \tag{1.1}$$

where $E_g(0)$, α and β are fitting parameters, and T is the temperature in Kelvins. Table 1.1 contains fitting parameter values for silicon, germanium and gallium arsenide. These were fitted into Equation 1.1 and plotted in Figure 1.1 to show band-gap energy variation with temperature for these three popular semiconductor materials.

Material	$E_g(0)$ [eV]	α [eV/K]	β [K]
Si	1.166	4.73×10^{-4}	636
Ge	0.7437	4.77×10^{-4}	235
GaAs	1.519	5.41×10^{-4}	204

Table 1.1: Fitting parameters for different semiconductor materials (data taken from Van Zeghbroeck (2011)).

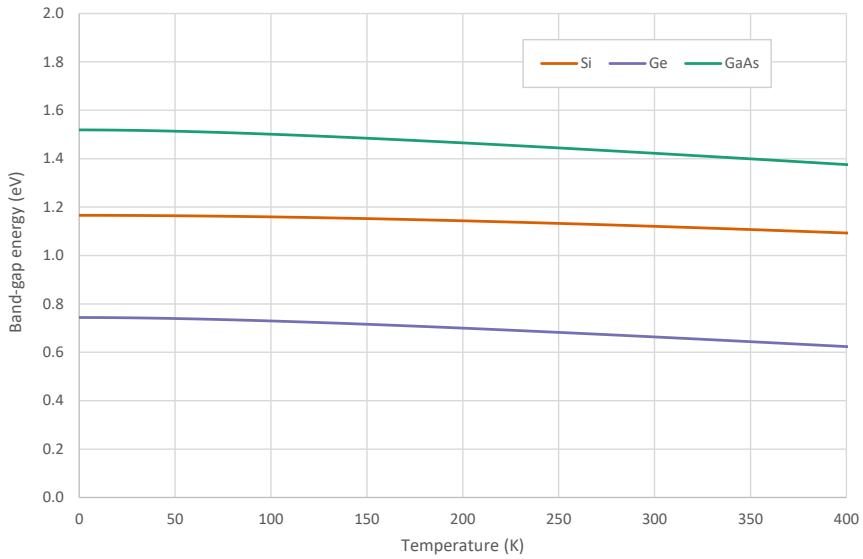

Figure 1.1: Temperature dependence of band-gap energy in various semiconductors.

At 293 K, silicon is able to detect photons with energies above 1.12 eV (or shorter than 1100 nm in terms of wavelength), which is its band-gap energy at this temperature. Silicon, like any other semiconductor material, is not sensitive to photons with energies below the band-gap; moreover, it gradually loses its sensitivity to photons with energies greater than ∼10 keV. This is due to silicon's absorption and reflection characteristics, as well as the effect of charge diffusion. Figure 1.2 shows the absorption length of silicon plotted as a function of wavelength and energy of the interacting photon. It is characteris-

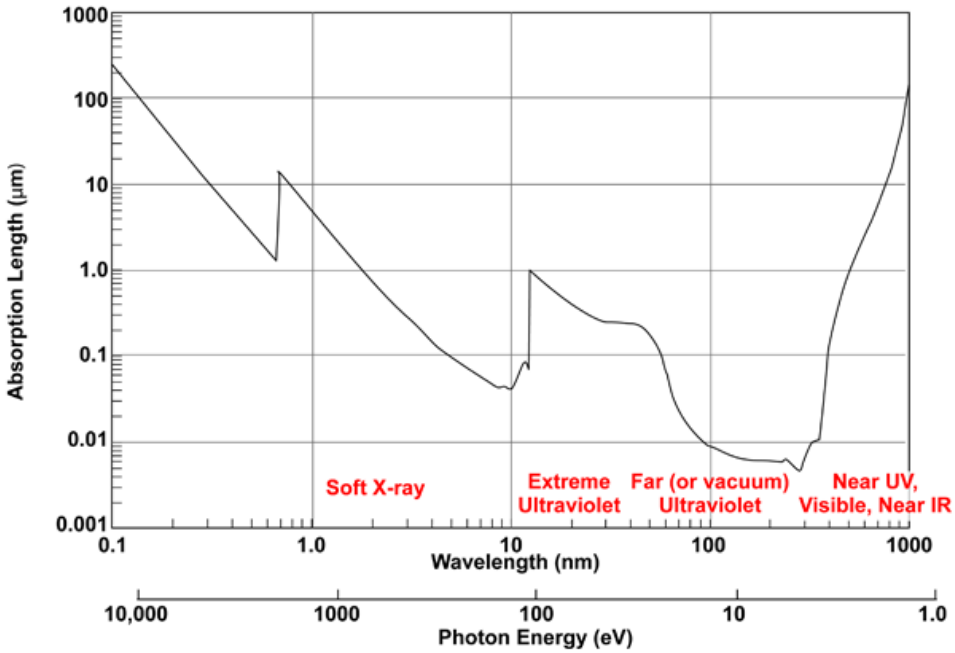

Figure 1.2: Wavelength dependence of absorption length in silicon (from Lincoln Laboratory (MIT) (2015)).

tic, that starting from the band-gap energy (right edge of the plot), absorption length is decreasing to reach its minimum at about 300 nm (∼4.1 eV), where photons only penetrate 5 nm of the silicon material. Beyond this point the parameter increases, with the exception of energies at the so-called edges, where absorption length drops rapidly (this due to the fact that the energy levels within the atoms are quantized).

The silicon reflection characteristics are shown in Figure 1.3. At the long wavelength end of the plotted range, reflectivity stays at roughly 30% level

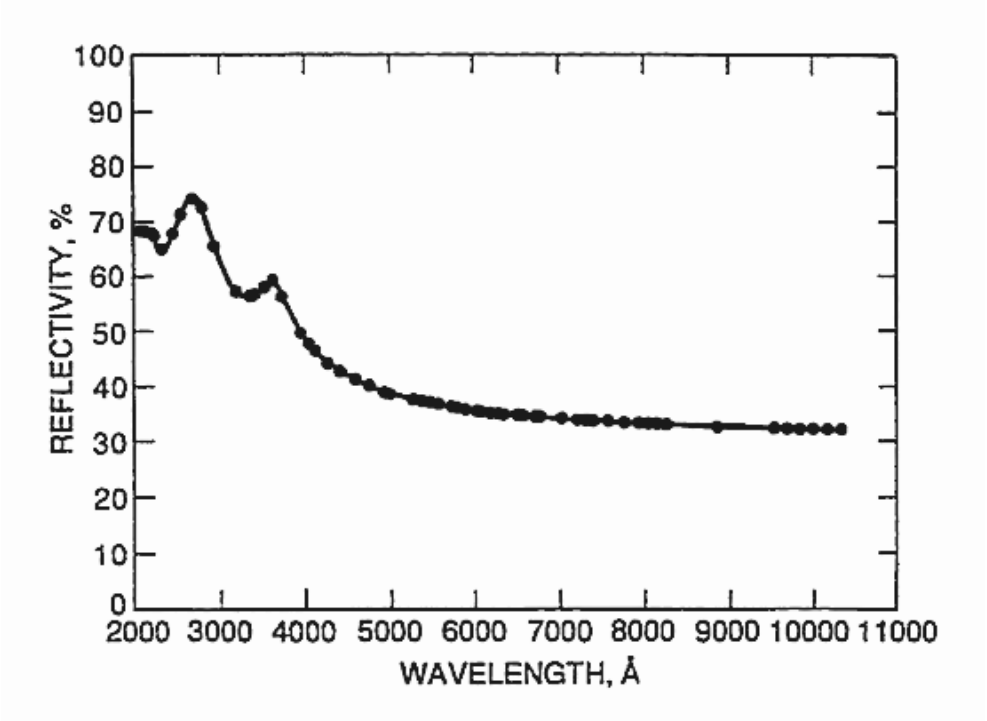

Figure 1.3: Silicon reflection characteristics (from Janesick (2001)).

(i.e. 30% of incident photons are reflected from the silicon surface), and it peaks at about 2600 Å (10 Å = 1 nm), where over 70% of photons are reflected.

Generally, photons with energy from 1.12 eV to 3.1 eV will generate a single electron (often called a 'photoelectron'), and from above 3.1 eV they will generate multiple electrons. The average number of free electron-hole pairs generated per absorbed photon is called the Quantum Yield (QY), and for photons with energies greater than 10 eV it can be estimated from the following formula (Janesick, 2007):

$$QY = \frac{E_{ph}}{E_{e-h}}, \tag{1.2}$$

where E_{ph} is the energy of the incident photon and E_{e-h} is the energy required to generate an electron-hole pair. For silicon at 293 K, E_{e-h} is approximately 3.65 eV per electron.

1.2 CCD Construction

The fundamental element of a CCD detector is known as a gate. Structurally it is a Metal-Insulator-Semiconductor (MIS) capacitor, however the metal electrodes have been substituted with transparent poly-silicon structures in order to improve the electrode transparency (Beynon and Lamb, 1980). A positive voltage applied to the gate electrode creates a depletion region formed at the reverse biased p-n junction, as shown in Figure 1.4. Assumed is the use of

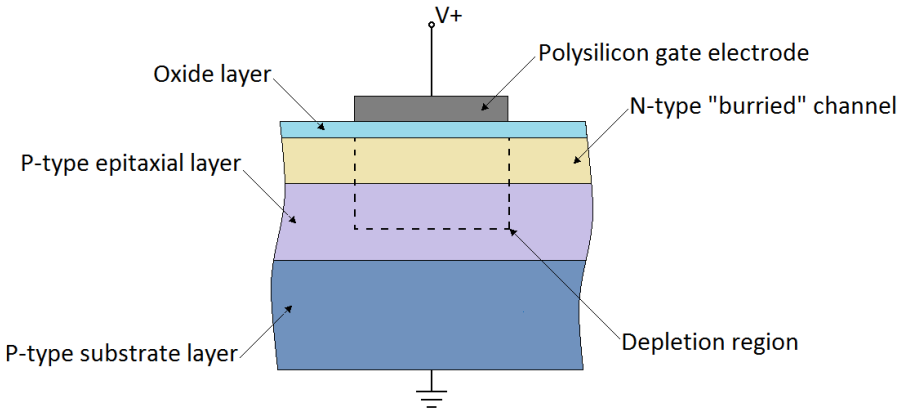

Figure 1.4: MIS gate structure for p-type silicon.

a p-type silicon substrate; for an n-type substrate the applied voltage would have to be negative. A group of a few overlapping gates (usually two, three or four) forms a single pixel structure (see Figure 1.5). This overlapping technique helps to improve performance of the sensor and obtain higher packing density, through minimising the gaps between adjacent electrodes (Bertram et al., 1974). An image area of the CCD consists of an array of pixels grouped in a series of vertical shift registers. Below the vertical structure, there is an additional row of pixels known as the horizontal shift register (see Figure 1.6).

Collected photoelectrons are stored in so-called potential wells, where they are kept in place by electrode voltages and channel stops (barriers isolating columns of pixels). Figure 1.7 shows that the peak of the electrostatic potential occurs at about 1 µm below the oxide layer. This is exactly where the potential well is formed. The maximum number of electrons that can be

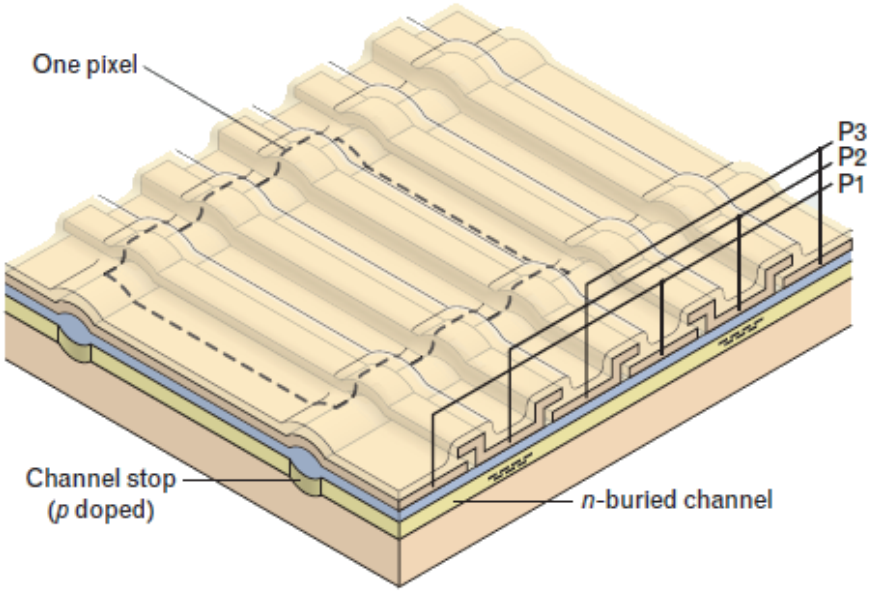

Figure 1.5: Cross-sectional view of a three-phase CCD structure (from Burke et al. (2007)).

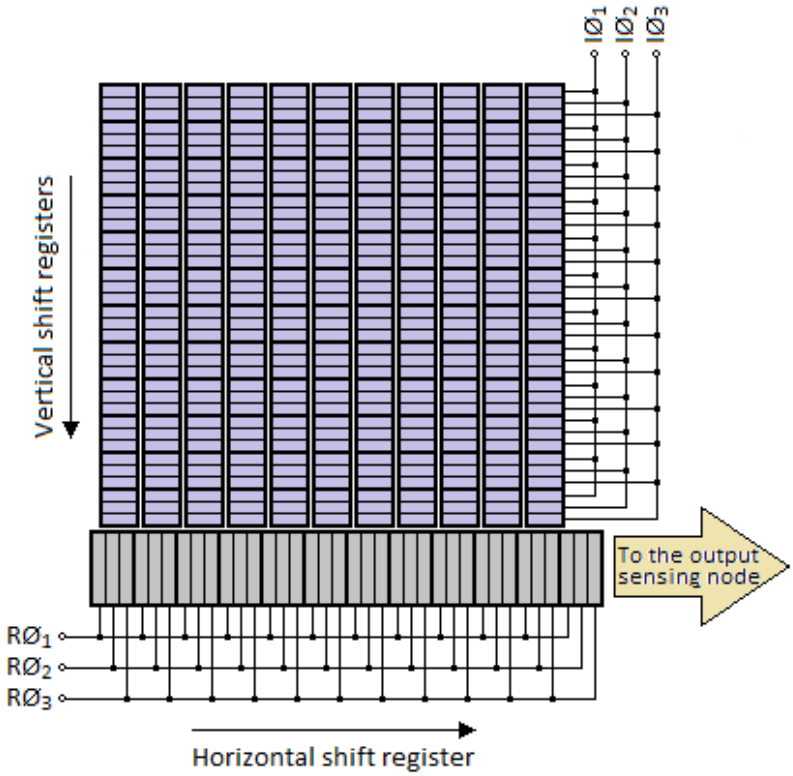

Figure 1.6: CCD shift registers in a three-phase device. $I\phi_1$, $I\phi_2$ and $I\phi_3$ act as image area clocks, while $R\phi_1$, $R\phi_2$ and $R\phi_3$ represent output register clocks.

held is called 'full well capacity'. The size of the well depends on the voltage applied to the gate, thickness of the oxide layer and gate's electrode area.

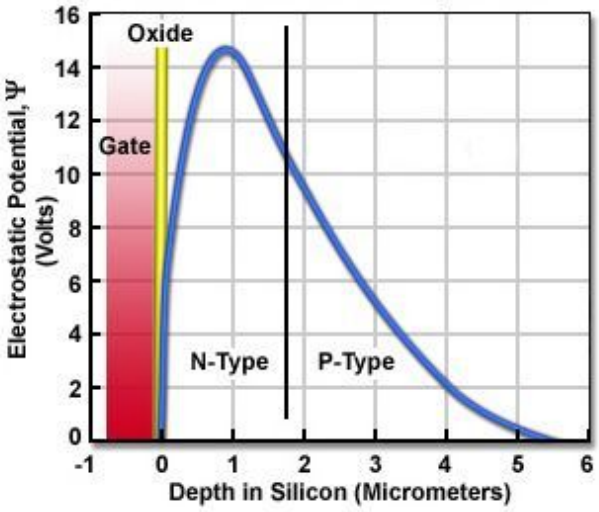

Figure 1.7: Potential distribution in buried channel MIS capacitor (from Hamamatsu (2017)).

The accumulated charge can be transferred from one well to its neighbour by the appropriate manipulation of the gate potentials. Depending on the number of phases, i.e. clock signals required to shift the charge from one pixel to the other, typically single-, two-, three-, and four-phase devices exist. Figure 1.8 illustrates the process of charge transfer in the case of a three-phase CCD. As can be seen, six steps are required in such a device to move charge by one pixel. A suitable clocking scheme is shown in Figure 1.9. Although all three waveforms are identical in terms of frequency, pulse width and amplitude, they are phase shifted relative to each other.

During the readout, rows of pixels are fed into the output register one after the other. From there, pixels are clocked out through a sensing node and an output amplifier, where the individual charge packets are converted to a voltage level.

Ideally, a photoelectron(s) generated by a photon within a certain pixel should stay in this pixel. Unfortunately, this is not always true, due to the adverse effect known as 'charge diffusion'. In front illuminated CCDs (see

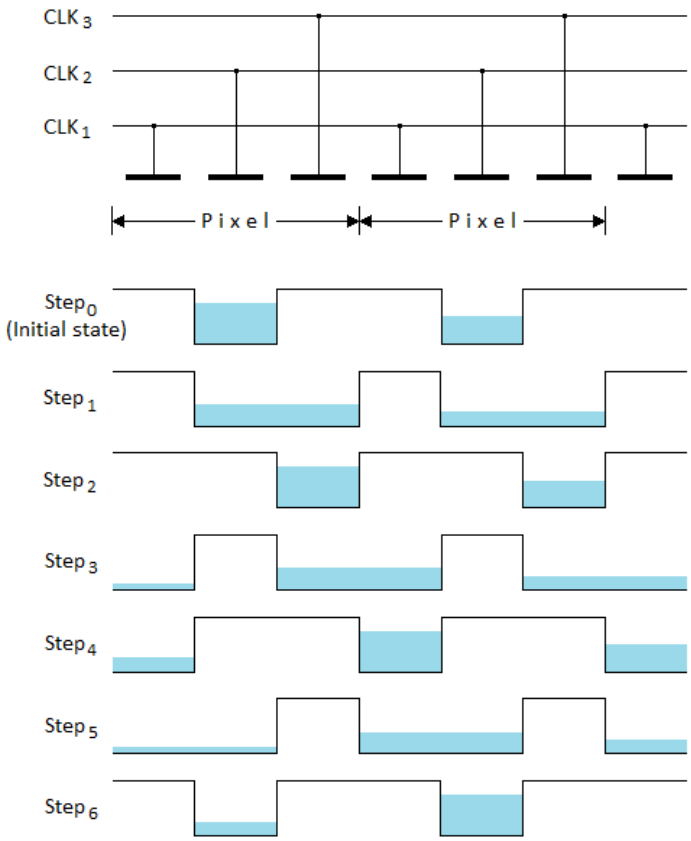

Figure 1.8: Illustration of charge transfer in a three-phase device (charge packets are shown in blue).

Section 1.3.2), photons with longer wavelengths penetrate the silicon material beyond the depletion layer, generating photoelectrons in the field-free region. In the absence of the electric field charge may easily wander to one of the neighbouring pixels. Equally, the interacting short wavelength photons may cause charge diffusion in back illuminated devices (see Section 1.3.2).

Charge diffusion directly affects the Point Spread Function (PSF) and spatial resolution of an imaging device (Karcher et al., 2004). The lateral diameter of diffusion for back-illuminated CCDs (in cm) can be estimated from the following formula (Janesick, 2001):

$$C_{ff} = 2x_{ff}\left(1 - \frac{L_A}{x_{ff}}\right), \tag{1.3}$$

where x_{ff} (in cm) is the amount of field-free material and L_A (in cm) is the

distance from the back surface at which the photon interacts.

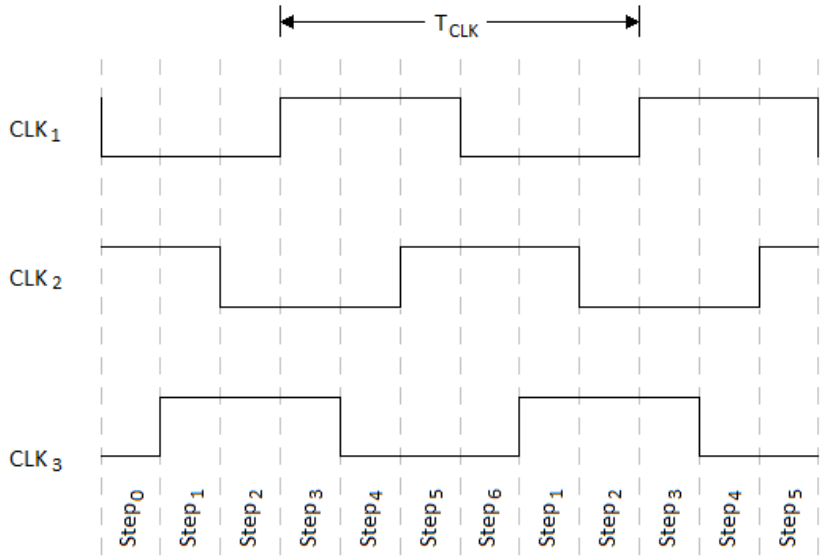

Figure 1.9: Three-phase system clocking scheme.

1.3 CCD Array Architectures

1.3.1 Surface- and Buried-channel CCDs

The earliest CCDs used to transfer the charge from one potential well to the other in channels located at the silicon-insulator interface. They are known as Surface-channel Charge-Coupled Devices (SCCDs). Such an approach may lead to the loss of photoelectrons, due to the presence of trapping states at the boundaries of the overlapping gates. These are the imperfections of the gate structures and the silicon lattice. As a result, the Charge Transfer Efficiency (CTE) (see Section 1.4.2) is poor, but can be slightly improved by implementing a pre-flash (a technique that is based on illuminating the CCD with a uniform light flux just prior to the actual object exposure). Such an approach helps to avoid non-linearity issues resulting from traps by filling them with charge from the pre-flash, for the price of some minor image quality degradation, as the resulting image is slightly noisier (Djorgovsky, 1984).

Most of the modern sensors are Buried-channel Charge-Coupled Devices (BCCDs). In this type of device the charge is transferred in the channel created in bulk silicon below the surface (see Figure 1.4). This approach has certain advantages, like improved CTE ($> 99.995\%$) and higher dynamic range, due to improved very low signal level operation. Their main disadvantage is the reduced charge capacity of the pixels. In comparison to SCCDs, their volume is three- to four-times smaller (Howell, 2006).

1.3.2 Front-side and Back-side Illuminated CCDs

CCDs can be manufactured as Front-Side Illuminated (FSI) or Back-Side Illuminated (BSI) devices. The difference between these two configurations arises from the direction the sensor is exposed to incoming light (see Figure 1.10). As already explained in Section 1.1, the front of the CCD is occupied by the gate structures, while its back side consists of just a pure layer of silicon. In FSI sensors, the incoming photons have to pass through the gate structures before they can be absorbed in the depleted region. This results in lower Quantum Efficiency (QE) in comparison to BSI sensors, where photons enter directly into the light sensitive volume of silicon. The BSI detectors have almost twice the QE per given wavelength, as well as extending to shorter wavelengths (as shown in Figure 1.22). BSI devices require extra manufacturing steps to thin the device from the back side, so that the photons are absorbed sufficiently close to the potential wells. One disadvantage is that they suffer from flat-field non-uniformities, being a consequence of a non-uniform thinning. They also have shallower pixels (reduced full-well capacity) and higher manufacturing costs, due to the required thinning and mounting processes (Howell, 2006).

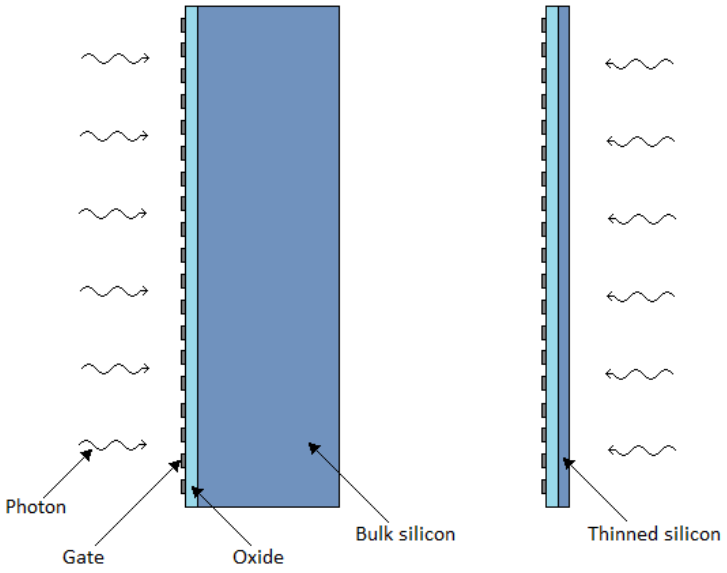

Figure 1.10: Front-side (left) and back-side (right) illuminated arrays.

1.3.3 Full-Frame, Frame Transfer and Interline Transfer CCDs

Depending on the way the charge is manipulated after the exposure, there are three main types of devices available: Frame Transfer (FT), Full-Frame (FF) and Interline Transfer (IT) CCDs.

IT arrays consist of alternating unmasked and masked columns of pixels (see Figure 1.11). The latter are light-protected by an opaque metal shield. After integration, charge is quickly transferred ($\sim$1 µs, no sampling is required at this point) from the light sensitive (unmasked) columns into the contiguous masked columns. This helps to minimise a smear effect in the image, eliminating the need for a shutter. The main disadvantage of IT CCDs is that their QE is reduced by half, as only every second column of pixels is active Holst and Lomheim (2011). Also, their spatial resolution is reduced (aliasing in one axis).

FT CCDs are comprised of two almost identical arrays, one called the active array, and other called the storage array (see Figure 1.12). The latter is covered with an opaque shield in order to protect the pixels from the incoming

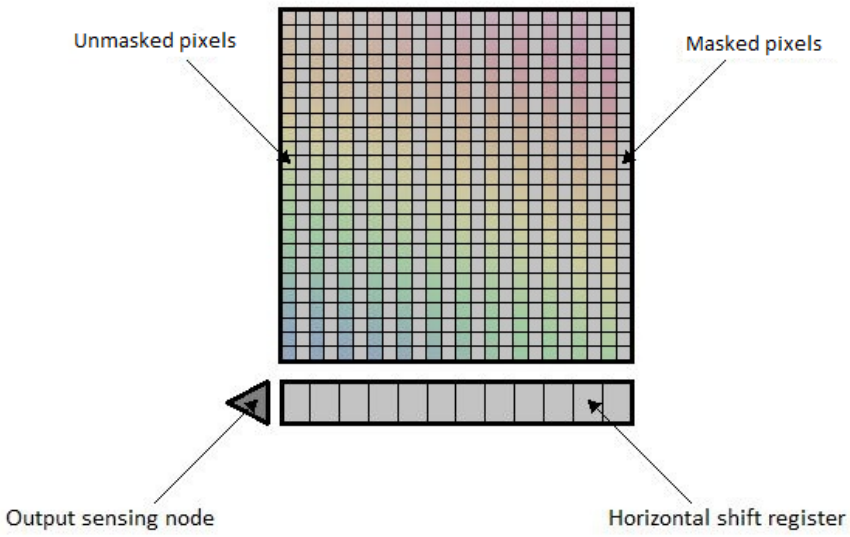

Figure 1.11: Interline Transfer CCD array.

light. After integration, collected charge is quickly transferred from the active to the storage area. From there, line after line is fed to the serial register and clocked out at much slower rate. At this time the active area is ready to start a new integration. The main disadvantage of FT CCDs is the image smear, resulting from the fact that integration and charge shifting from the active to the storage area occur simultaneously. On the positive side they have 100% fill factor (improved spatial resolution) and higher QE when compared to IT CCDs.

FF sensors are simply FT CCDs without a storage area, i.e. the whole array is unmasked and used during the integration (see Figure 1.13). FF CCDs are less expensive (for the same active image area they are half the size of FT CCDs), or alternatively, larger field of view (same resolution, but more active pixels) is possible for the same sensor dimensions. The main drawback of FF devices is their long readout time (no storage area), resulting in much worse image smear compared to IT CCDs or even FT arrays. For this reason such sensors are mainly used in applications requiring long exposure times and are usually equipped with a mechanical shutter.

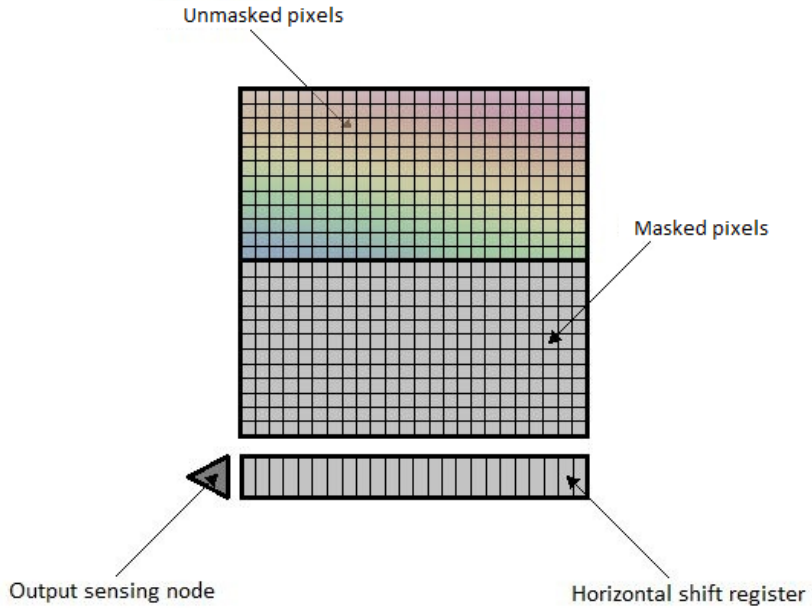

Figure 1.12: Frame Transfer CCD array.

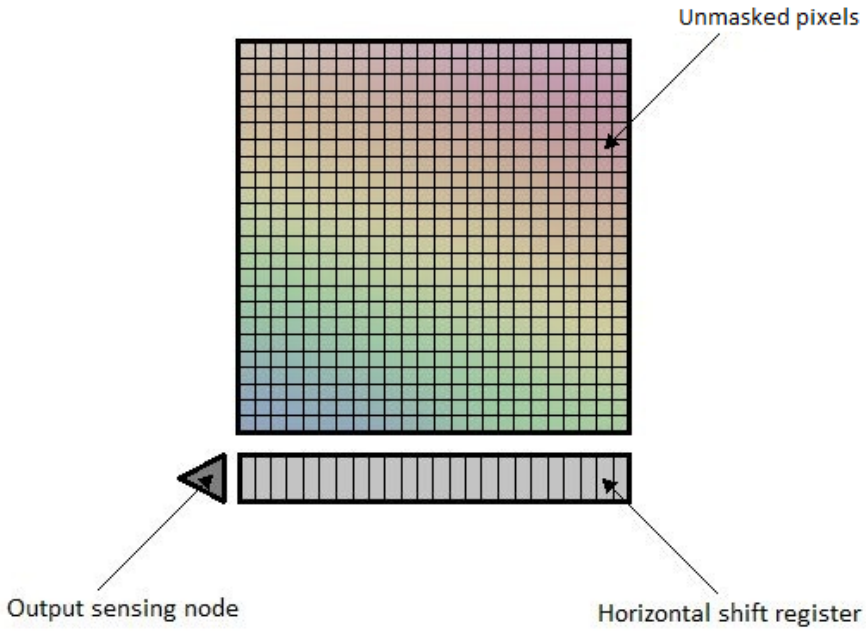

Figure 1.13: Full-Frame CCD array.

1.3.4 Orthogonal Transfer CCDs

In a typical CCD charge within each pixel can only be shifted in the vertical direction. A different type of detector, called Orthogonal Transfer (OT) CCD,

was developed to allow charge shifting in either horizontal or vertical direction during the exposure time. The two-directional operation, as shown in Figure 1.14, is possible due to a complex four-phase mode of operation. Each pixel consists of four gates; two central ones are triangular, while the other two are rectangular (of which one is positioned horizontally and the other one vertically). During the operation, depending on the required direction of the charge shift, either the rectangular-horizontal or rectangular-vertical gates are set low, forming the channel stops.

The typical application of OT CCDs is in astronomy, where they can compensate for image motion caused by e.g. atmospheric turbulence.

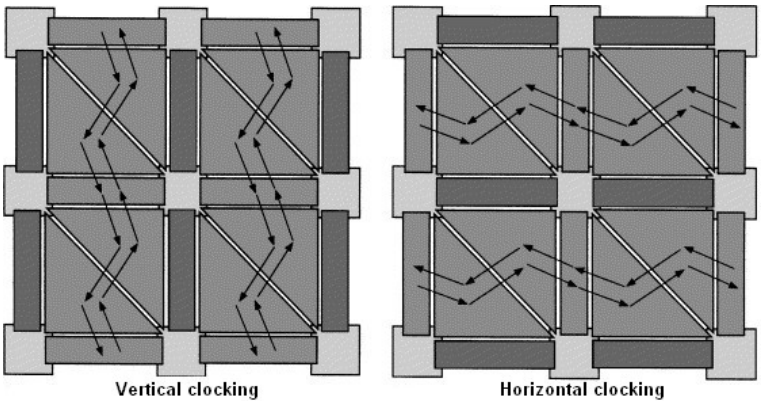

Figure 1.14: Vertical and horizontal operation of OT CCD (from Gregory et al. (1999)).

1.3.5 Multi-Pinned Phase CCDs

Multi-Pinned Phase (MPP) CCDs are a type of detector that can operate in a multi-pinned phase mode. They are also known as Inverted Mode Operation (IMO), in contrast to the 'standard' Non-Inverted Mode Operation (NIMO) devices. In the latter, the largest contribution to dark signal (noise sources are discussed in Section 1.4.3) comes from thermal generation due to surface states (Holst and Lomheim, 2011). MPP detectors, due to the unique design (boron or phosphorus doping of the last phase gate in conjunction with the inversion of all the CCD array clock biases) minimise this effect and provide

the output signal containing ultra-low dark current. For this reason they can be operated at higher temperatures than conventional devices. The main disadvantage of IMO detectors is reduced full well capacity and hence the dynamic range. However, currently there are newer, improved MPP structures available, called Advanced Inverted Mode Operation (AIMO), that are offering higher peak signal levels, e.g. Teledyne e2v's CCD42-10 (E2V Technologies, 2016a).

1.3.6 Time Delay and Integration CCDs

The principle of operation of Time Delay and Integration (TDI) CCD is based on synchronisation of the sensor's vertical charge transfer timing with the relative movement between the image and the target. As the image is swept across the CCD surface, the charge packets are clocked at the same rate. This helps to remove the smearing effect and eliminates the need for a mechanical shutter. At the same time it allows for longer integration times without introducing smear. The number of TDI stages (effectively the number of lines of the detector) determines the sensor's sensitivity. The TDI concept is illustrated in Figure 1.15.

TDI CCDs have application in document flatbed scanners, airborne reconnaissance, digital radiography and satellite mapping.

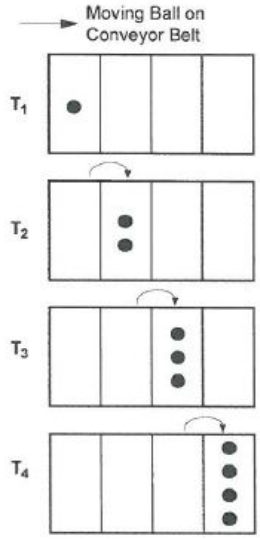

Figure 1.15: TDI sensor concept (from Holst and Lomheim (2011)). At T_1 the image is focused onto the first detector element. At T_2, the same image is focused onto the second detector element and the created charge packet is added to the one that has simultaneously moved from the first detector. At T_4 the original signal is increased 4×.

1.3.7 Electron Multiplying CCDs

Electron Multiplying (EM) CCDs are designed for low light level conditions. They contain an extension to the standard serial output register (see Figure 1.16), called the gain register, typically with several hundreds of elements (multiplying cells).

By applying higher than normal clock voltage to one of the phases, the gain register creates secondary electrons through the process of impact ionization (see Figure 1.17), where in a large electric field, an electron with higher kinetic energy can create an electron-hole pair through colliding with another electron in the valence band, moving it to the conducting band. Electrons created this way are also accelerated by the electric field and can create further carriers via impact ionization (Hu, 2010).

EM gain (typically in the region of 1000× over the full length of the multiplication register) occurs before the readout process, so it effectively reduces the CCD read noise and can be controlled by varying the potential of the high voltage phase. In addition, EM gain is temperature dependent

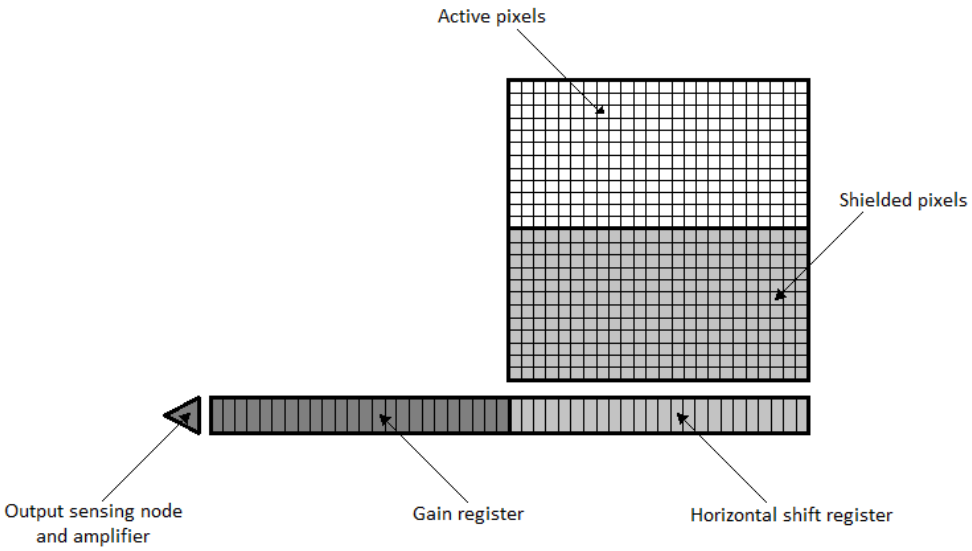

Figure 1.16: Electron Multiplying CCD array.

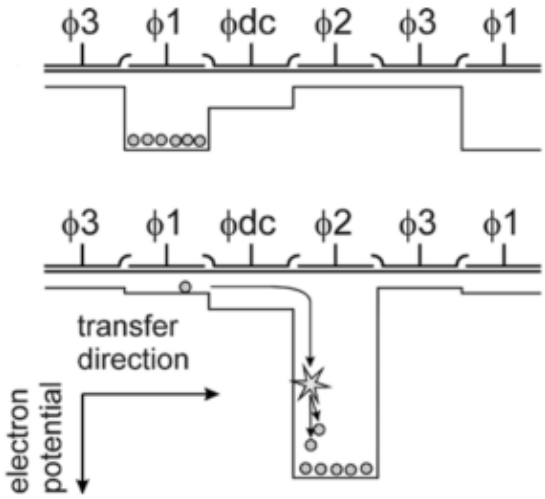

Figure 1.17: Process of impact ionization in EM CCDs (from Robbins and Hadwen (2003)).

(higher gain can be achieved by cooling the sensor, which in turn also reduces the dark current). The relationship between EM gain, EM clock voltage and operating temperature is shown in Figure 1.18.

On the negative side, the signal amplification process introduces an additional noise source called multiplicative noise, which increases the overall signal shot noise by $\sqrt{2}$. The other issue is a presence of spurious noise, also referred to as Clock Induced Charge (CIC), which appears in the form of sin-

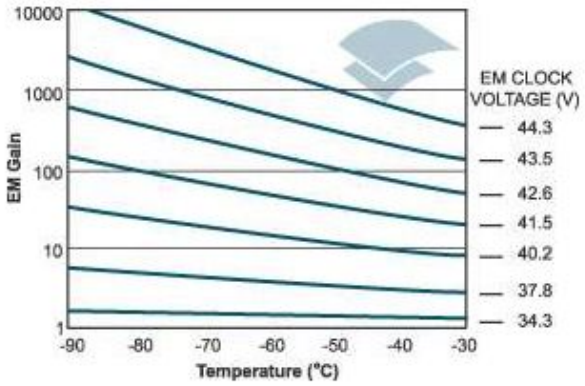

Figure 1.18: EM gain as a function of temperature (from Andor Technology (2012b)).

gle electrons generated during the charge shift. An EM CCD set to a high gain may create hundreds of such unwanted carriers, limiting the detection level (Andor Technology, 2012c).

1.3.8 Anti-blooming Drains

When potential well capacity is exceeded, the excess charge bleeds into the neighbouring pixels. This causes the adverse effect called blooming. To prevent this from happening, sensor manufacturers incorporate special anti-blooming/overflow structures (drains) into some of their devices, which help to get rid of the unwanted portion of charge. Although the individual pixels may still get saturated, the overflow drains stop the charge from flowing into the neighbouring pixels.

The two most common types of anti-blooming structures are called lateral overflow drain and vertical overflow drain (shown in Figures 1.19 and 1.20 respectively).

In the case of lateral drains, the structure is implemented on the surface of the detector, adjacent to the pixel's charge collection area. Such drains are more effective and can be fabricated at lower cost than the vertical anti-blooming structures. Their main disadvantage is the reduced active area of the pixels and hence lower overall QE of the detector.

The vertical overflow drain structure is buried beneath the charge col-

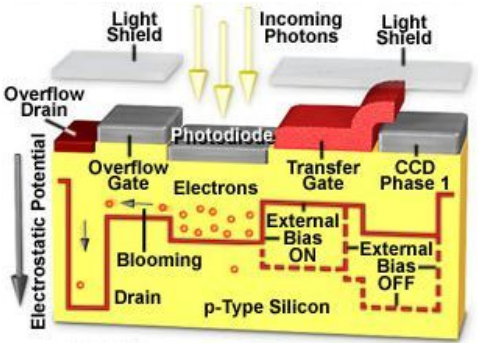

Figure 1.19: Lateral anti-blooming drain structure (from Hamamatsu (2012)).

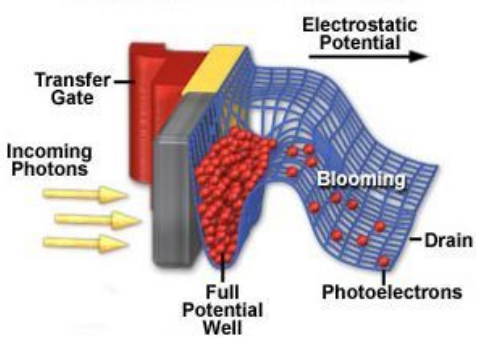

Figure 1.20: Vertical anti-blooming drain structure (from Hamamatsu (2012)).

lection well and the excess charge overflows directly into the substrate. The primary disadvantage of vertical drains is the reduced well capacity of the pixels that is limiting absorption of longer wavelengths (which in turn reduces QE).

1.4 CCD Performance Parameters

This section provides information on typical parameters characterising the properties of CCD detectors, including a brief description of measurement methods for some of these quantities.

1.4.1 Quantum Efficiency

Quantum Efficiency (QE) is the ratio of photons detected by the sensor to all incoming photons (detected and undetected):

$$QE(\%) = \frac{P_I}{P} * 100\%, \tag{1.4}$$

where P_I is the average number of interacting photons per pixel, and P is the average number of incident photons per pixel (Janesick, 2007).

The ability of the sensor to detect the incoming photons is limited by the absorption coefficient of the detector's material, i.e. reciprocal of the absorption length (see Section 1.1). The absorption coefficient of photons in silicon (as used in CCDs), plotted as a function of wavelength, is shown in Figure 1.21.

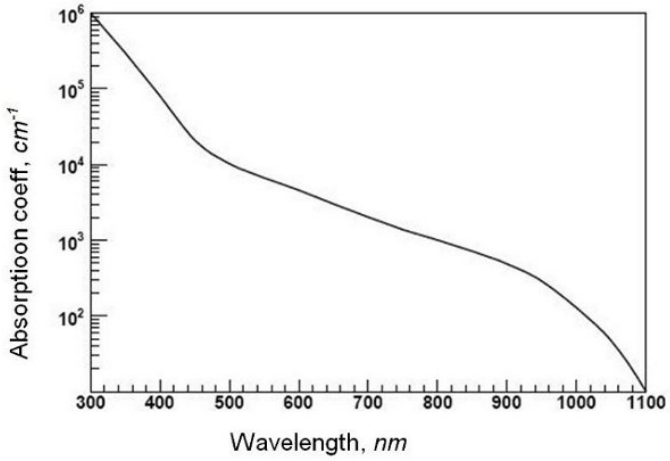

Figure 1.21: Absorption coefficient as a function of wavelength in silicon (from Saveliev (2010)).

QE is temperature dependent; at longer wavelengths (red, NIR), QE increases with increasing temperature, being a result of silicon's band-gap energy decreasing as temperature increases. At shorter wavelengths (blue), for a back-illuminated device, QE decreases as temperature increases, which is typically due to backside surface physics and is manufacturer process dependent (Lesser, 2014).

The thickness of the silicon is another parameter that can change the overall QE response of the detector. Generally thicker devices are more red-sensitive than their thinner counterparts, as for the longer wavelengths the absorption coefficient is lower (as shown in Figure 1.21). In addition, the thinned BSI CCDs have better blue-response and much higher overall QE than FSI devices, due to the absence of the gate structures on the illuminated side of the sensor. Figure 1.22 shows a response comparison of the typical BSI and FSI CCDs.

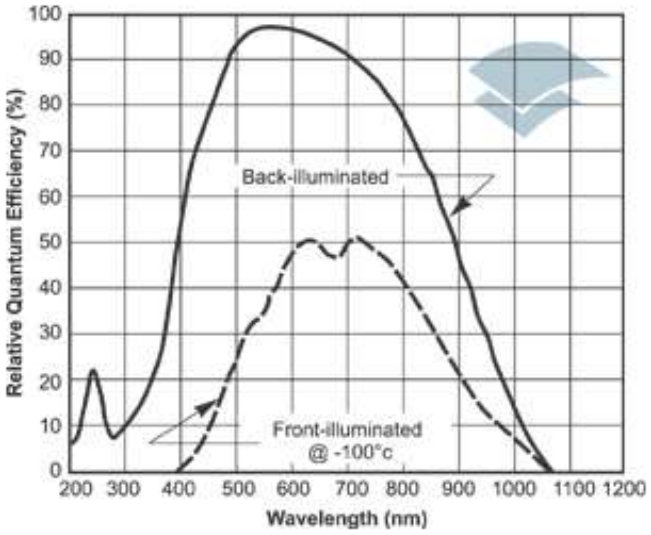

Figure 1.22: QE of the front and backside illuminated CCDs (from Andor Technology (2012a)).

One of the most popular methods used for estimating QE of the CCDs makes use of a calibrated photodiode. Both CCD and the photodiode are illuminated by the light source providing different wavelengths, selectable through using interference filters. QE is then determined by comparing their responses through the following equation Janesick (2007):

$$QE = \frac{A_D \times S \times K_{ADC} \times QE_D}{P_A \times S_D \times t_I}, \tag{1.5}$$

where A_D is the active area of the standard photodiode (in cm^2), S is the signal (in ADU), K_{ADC} is a constant converting the ADU to electrons, QE_D

is the QE of the diode (value supplied by the manufacturer), P_A is the area of the pixel (in cm^2), S_D is the photo signal generated by the diode (in e$^-$/s) and t_I is the sensor's exposure time (in s).

1.4.2 Charge Transfer Efficiency/Inefficiency

Charge Transfer Efficiency (CTE) specifies the fraction of electrons (fractional signal) that is successfully moved from one pixel to the other. Figure 1.23 shows the fractional signal plotted as a function of number of transfers for four different CTE values.

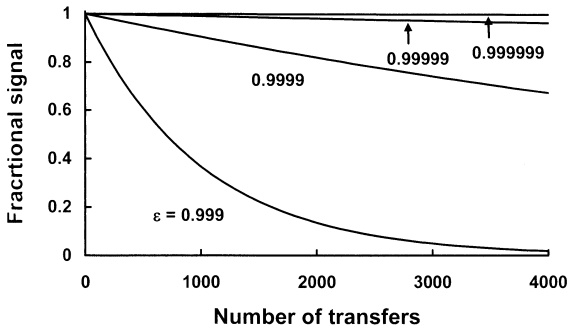

Figure 1.23: Fractional signal as a function of number of transfers (from Holst and Lomheim (2011)). CTE is labelled as ε.

Scientific devices often have their CTE values exceeding 0.999 999. Also, it is not uncommon for sensor manufacturers to use Charge Transfer Inefficiency (CTI) instead of CTE, where:

$$CTI = 1 - CTE. \tag{1.6}$$

The loss in charge from a CCD pixel, when CTI value is different in both horizontal and vertical directions, can be found from the following equation Howell (2006) (only true where CTI is very small):

$$L(e^-) = N_e(N_{SH} \times CTI_H + N_{SV} \times CTI_V), \tag{1.7}$$

where N_e is a number of electrons in the pixel, N_{SH} is a number of horizontal

shifts, N_{SV} is a number of vertical shifts, CTI_H is CTI in the horizontal direction, and CTI_V is CTI in the vertical direction. In a particular case when CTI is identical in both horizontal and vertical directions, the above formula can be simplified to:

$$L(e^-) = N_e \times N_S \times CTI, \tag{1.8}$$

where $N_S = N_{SH} + N_{SV}$ is the total number of charge shifts.

The standard approach for estimating CTE is through the stimulation of a CCD with Fe^{55}, which is a radioactive X-ray source. Silicon is known as a good X-ray detector and each collected X-ray photon generates about 1620 photoelectrons. After exposing the sensor to the Fe^{55} for a certain time, the signal is plotted versus the number of pixel transfers. If this X-ray transfer plot is horizontal, the tested CCD has good CTE. However, if the line starts at 1620 and then drops, the CTE is poor (Janesick, 2001).

1.4.3 Noise

There are various noise sources that can affect the CCD output signal. Some are introduced by the detector itself and its surrounding electronics, e.g. dark and readout noise. Other sources, like photon and background noise, result from the nature of the detected signal. The noise components introduced by the CCD can be controlled to some extent, minimised or even effectively eliminated (e.g. dark noise). This is not possible with those introduced by the signal source. A brief overview of the various noise components is presented in the following paragraphs.

Signal shot noise, also referred to as 'photon noise', is resulting from the discrete nature of light. Since the rate of the photon's arrival cannot be precisely predicted, noise is described by the Poisson distribution. However, for a large number of interacting photons per pixel, it can be approximated by the Gaussian distribution Janesick (2007). Photon noise (in e^-/pixel) is

equal to the square root of the total detected signal (also in e^-/pixel):

$$\sigma_{photon} = \sqrt{S_{tot}}, \tag{1.9}$$

and it can be reduced by either using multiple exposures (which also helps to eliminate the effect of cosmic rays) or through defocusing the observed object, which allows a longer integration time to obtain a larger signal.

Background shot noise in astronomical observations originates from photons generated by the background sky sources. Mathematically it can be described by Poisson statistics (as for the signal shot noise):

$$\sigma_{sky} = \sqrt{S_{sky}}, \tag{1.10}$$

where S_{sky} is the total number of interacting photons from the background sources. The effect of background noise can be reduced by using multiple exposures at the expense of reduced time resolution.

Dark noise. CCD applications requiring long integration times (e.g. low-light level operation) suffer from thermally generated electrons, called dark current. There are three main sources of these additional, undesirable carriers (Widenhorn et al., 2002):

- thermally generated electrons at the silicon – silicon oxide interface;
- thermally generated electrons in the depleted region;
- thermally generated and diffused electrons in the field-free bulk silicon.

Dark current is usually specified as the number of electrons generated per pixel per second and it is present even if the sensor is not exposed to light. Its fundamental feature is high dependence of its generation rate on the sensor's temperature. Typical CCD dark current curves are shown in Figure 1.24.

CCDs used in scientific applications are often cooled down to temperatures between $-30\,^{\circ}\mathrm{C}$ and $-130\,^{\circ}\mathrm{C}$, where dark current becomes negligible.

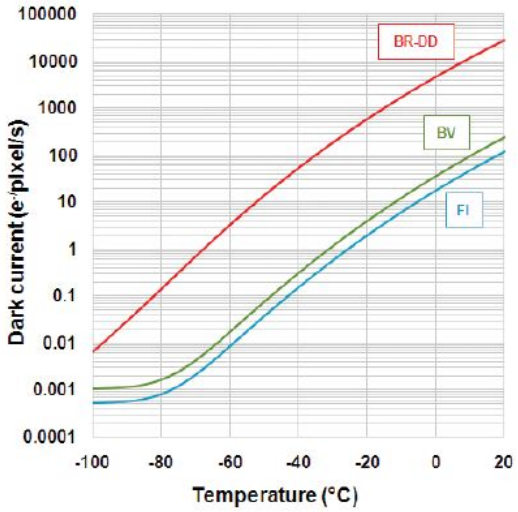

Figure 1.24: Dark current as a function of CCD temperature for front-illuminated (FI), back-illuminated visible-optimised (BV) and back-illuminated deep-depletion CCDs (BR-DD) (from Andor Technology (2012b)).

This can be achieved by the use of liquid nitrogen (LN_2), thermoelectric coolers (Peltiers) or mechanical coolers. In the case of the thermoelectric coolers, they are often built-in to the CCD package. Such a cooling method, combined with the application of passive radiators, allows for the operation at temperatures as low as 50 °C below the ambient temperature.

There are two types of noise associated with dark current: dark current shot noise and dark current non-uniformity (for CCDs, dark current non-uniformity is a type of Fixed Pattern Noise (FPN)). The first one arises from statistical variations in the number of thermally generated electrons and similarly to photon and background noise it can be described by Poisson statistics (Howell, 2006):

$$\sigma_{dark} = \sqrt{S_{dark}}, \tag{1.11}$$

where S_{dark} is dark current (in e^-/pixel/s). This component of dark noise can only be reduced by cooling the sensor. The other element (dark current non-uniformity) is associated with the pixel-to-pixel variation in dark signal generation rate. It may not only be reduced by cooling the CCD, but also by using image processing techniques, in which a dark reference frame is subtracted from the output image (dark frames are images taken with closed

shutter under the same conditions as the object frame, so with the same integration time and temperature). The errors associated with subtraction can be reduced by making multiple exposures and averaging.

Readout noise. The readout process introduces additional noise that originates from three different sources:

- the on-chip amplifier circuit, responsible for charge conversion from electrons to an adequate voltage level;
- the off-chip amplifier circuit, allowing for the signal gain adjustments;
- the Analogue-to-Digital Converter (ADC) circuit, responsible for the transformation of analogue signal into the corresponding digital number (such noise is referred to as 'quantisation noise').

Only the top source of noise in the above list is introduced by the CCD itself; the other two originate from the external electronics.

The on-chip amplifier's noise is Johnson noise, so proportional to bandwidth and temperature.

1.4.4 Signal-to-Noise Ratio

Signal-to-Noise Ratio (SNR) of a given detector characterises a quality of its measurement. Large SNR can be achieved by sensors with high QE and low overall noise contribution. In addition, increasing exposure time (if it is possible) may also improve it. SNR of a given CCD detector can be estimated from the following formula (Merline and Howell, 1995):

$$\frac{S}{N} = \frac{S_{tot}}{\sqrt{\sigma^2_{photon} + n_{pix}\left(\sigma^2_{sky} + \sigma^2_{dark} + \sigma^2_{read}\right)}}, \tag{1.12}$$

where S_{tot} is the total number of photons collected from the object of interest (that may cover one or more pixels), σ_{photon} represents the shot noise on the collected source signal, n_{pix} is the number of pixels occupied by the observed

object, σ_{sky} represents the shot noise on the background signal per pixel, σ_{dark} is the shot noise on dark current per pixel per second, and σ_{read} is the readout noise per pixel.

Equation 1.12 can be also written as:

$$\frac{S}{N} = \frac{S_{tot}}{\sqrt{S_{tot} + n_{pix}\left(S_{sky} + S_{dark} + \sigma_{read}^2\right)}}, \tag{1.13}$$

where S_{sky} is the total number of photons collected from the background signal per pixel and S_{dark} is dark current per pixel per second. It is worth noting that the readout noise factor has been left unchanged. This is due to the fact that Poisson statistics does not apply to this noise term, as there is no signal associated with it. The above equation can be enhanced by adding the integration time variable t to it:

$$\frac{S}{N} = \frac{S_{tot} \times t}{\sqrt{S_{tot} \times t + n_{pix}\left(S_{sky} \times t + S_{dark} \times t + \sigma_{read}^2\right)}}. \tag{1.14}$$

For bright sources and/or long exposures photon noise often becomes a dominant source of uncertainty. In such a case, the formula from Equation 1.13 can be simplified:

$$\frac{S}{N} = \frac{S_{tot}}{\sqrt{S_{tot}}} = \sqrt{S_{tot}}. \tag{1.15}$$

For faint sources and/or short exposures errors are dominated by the read noise. Again, Equation 1.13 can be presented in a simpler form:

$$\frac{S}{N} = \frac{S_{tot}}{\sqrt{n_{pix} \times \sigma_{read}^2}} = \frac{S_{tot}}{\sigma_{read}\sqrt{n_{pix}}}. \tag{1.16}$$

Figure 1.25 shows SNR per pixel plotted as a function of integration time. The SNR values were calculated with the aid of Equation 1.14, using the following parameters: $S_{tot} = 1000$ photons, $n_{pix} = 1$, $S_{sky} = 0$ e^-, $S_{dark} = 0.1$ e^-/s and $\sigma_{read} = 10$ e^-.

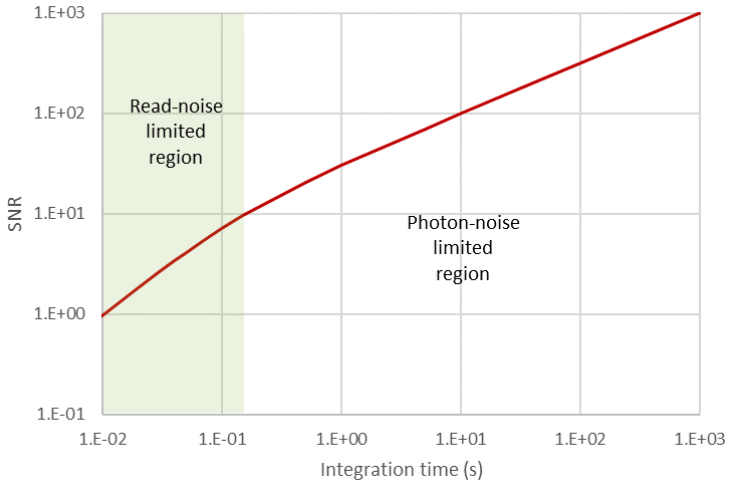

Figure 1.25: SNR as a function of integration time.

1.4.5 Dynamic Range and CCD Gain

Dynamic Range (DR) of an imaging sensor can be interpreted as its ability to measure both low and high intensities on the same image. Mathematically this is represented by the ratio of the device's full well capacity (in e^-) to its noise floor (also in e^-):

$$DR = \frac{Full\ well\ capacity}{Noise\ floor}. \tag{1.17}$$

The noise floor is defined as a sum in quadrature of all the noise sources introduced by the detector. In most cases it is the sum of sensor's dark and readout noise. By using the appropriate CCD cooling method, the dark current can be practically eliminated, leaving the readout noise as the detector's noise floor. In practical use, DR is often expressed in dB or left as a unit-less number.

The CCD gain specifies how many electrons are assigned per single Analogue-to-Digital-Unit (ADU) during the process of analogue to digital conversion and is found as the ratio of full well capacity (in e^-) to the total number of binary steps provided by the ADC (in ADUs), assuming that the ADC zero and full scale values correspond to the CCD zero and full-well

signals:

$$G_{CCD} = \frac{Full\ well\ capacity}{Total\ number\ of\ ADUs}. \tag{1.18}$$

The minimum number of bits required for an ADC in order to achieve a sufficient number of binary steps can be found from the following equation:

$$n = \frac{log(DR)}{log2}. \tag{1.19}$$

Note that the resulting number should be rounded up to the nearest integer. Due to the noise introduced by the ADC circuit itself (called the quantization noise), it is good practice to use devices with one or two extra bits above the required minimum (e.g. for a sensor with 12-bit DR it is sensible to use a 14-bit ADC chip).

1.4.6 Spatial Resolution

Resolution is a parameter specifying the finest detail possible to resolve by a given imaging system. Quantities such as Modulation Transfer Function (MTF) and PSF are often used to characterise spatial quality of the camera (sensor). MTF in general is the ratio of output to input modulation and it is normalised to one at zero frequency. A total MTF of a given CCD detector is associated with two components:

- integration (sometimes called 'geometric') MTF (MTF_I);
- diffusion MTF (MTF_D).

MTF_I is given by (Janesick, 2001):

$$MTF_I = \frac{sin\left(\frac{\pi f \Delta_p}{2 f_N p}\right)}{\frac{\pi f \Delta_p}{2 f_N p}}, \tag{1.20}$$

where f is the spatial frequency of the sinusoidal input (in cycles/cm), Δ_p is the length of pixel's open aperture (in cm), p is pixel pitch (in cm) and f_N is

the Nyquist spatial frequency (in cm^{-1}).

Since f_N is defined as $1/2p$, Equation 1.20 can be rewritten as:

$$MTF_I = \frac{sin\,(\pi f \Delta_p)}{\pi f \Delta_p} = sinc\,(\pi f \Delta_p)\,. \tag{1.21}$$

Figure 1.26 shows MTF_I plotted as a function of spatial frequency f for either front or back-side illuminated CCD.

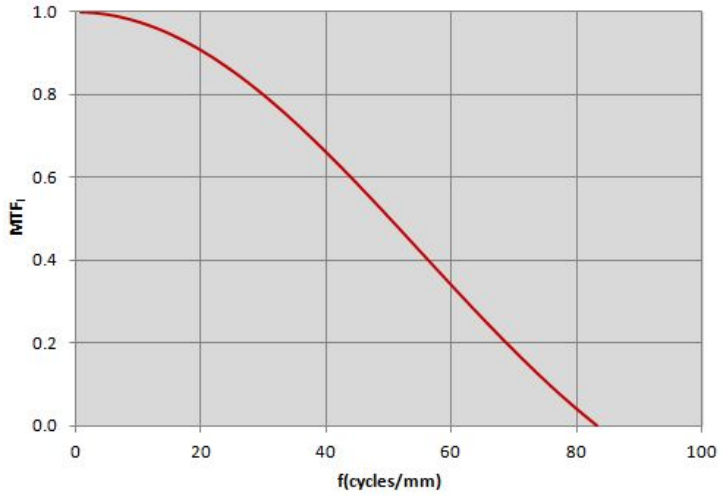

Figure 1.26: Integration MTF as a function of spatial frequency.

MTF_D for a back-side illuminated CCD can be expressed as (Janesick, 2001):

$$MTF_D = \frac{N_K}{N_O}. \tag{1.22}$$

N_O can be found from (Janesick, 2001):

$$N_O = \frac{\alpha L_n}{\alpha^2 L_n^2 - 1}\left[\frac{2\left(\alpha L_n + \dfrac{V_S L_n}{D_n}\right) - (\beta_+ - \beta_-)\, e^{-\alpha x_{ff}}}{\beta_+ - \beta_-} - \frac{e^{-\alpha x_{ff}}}{\alpha L_n}\right] - e^{[-\alpha(x_{ff}+x_p)]}, \tag{1.23}$$

where

$$\beta_+ = \left(1 + \frac{V_S L_n}{D_n}\right) e^{\dfrac{x_{ff}}{L_n}}, \tag{1.24}$$

and

$$\beta_+ = \left(1 - \frac{V_S L_n}{D_n}\right) e^{-\frac{x_{ff}}{L_n}}. \tag{1.25}$$

In the above equations α is the optical absorption coefficient (in cm^{-1}), V_S is the surface recombination velocity (in cm/s), L_n is the diffusion length in the epitaxial silicon (in cm), D_n is the diffusion coefficient (39 cm^2/s), x_{ff} is the field-free thickness (in cm) and x_p is the depletion length of the p-region. N_K can be found by substituting L_n for L in equations 1.23, 1.24 and 1.25, where (Janesick, 2001):

$$L = \frac{1}{\sqrt{\frac{1}{L_n^2} + K^2}}, \tag{1.26}$$

and

$$K = \frac{\pi f}{p f_N}, \tag{1.27}$$

where p is the pixel pitch (in cm) and f_N is the Nyquist spatial frequency (in cm^{-1}).

Figure 1.27 shows MTF_D plotted as a function of spatial frequency f for a back-side illuminated CCD.

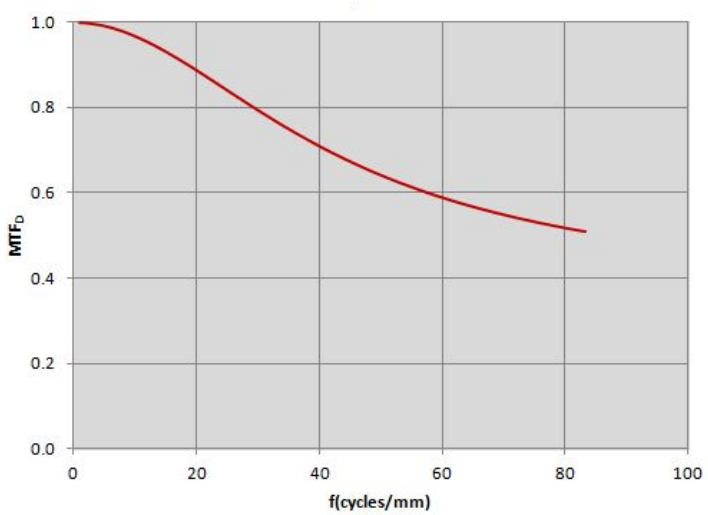

Figure 1.27: Diffusion MTF as a function of spatial frequency.

The total MTF is defined as the product of integration and diffusion MTFs:

$$MTF = MTF_I \times MTF_D. \tag{1.28}$$

Figure 1.28 shows the total MTF plotted as a function of spatial frequency for a back-side illuminated CCD.

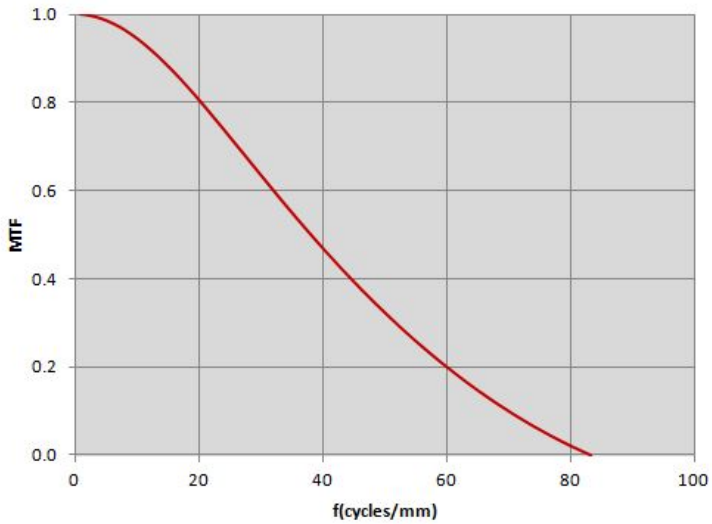

Figure 1.28: Total MTF as a function of spatial frequency.

Just as MTF characterises detector's resolution capabilities in the spatial frequency domain, PSF expresses it in the spatial domain. PSF can be defined as the imaging system's response to a point input (impulse response), while MTF is the system's frequency response. These two parameters are correlated and can be converted from one to the other using a Fourier transform:

$$MTF = \mathcal{F}(PSF), \tag{1.29}$$

and

$$PSF = \mathcal{F}(MTF). \tag{1.30}$$

1.5 CCD Space Cameras in Planet Finding Missions

1.5.1 CoRoT

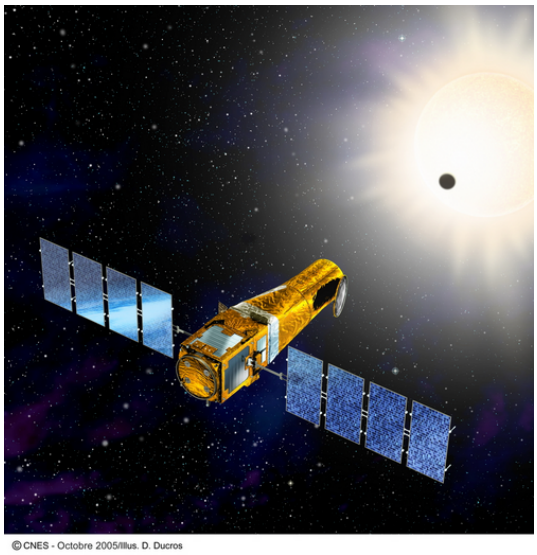

Figure 1.29: Artist's view of CoRoT telescope (from ESA (2006b)).

COnvection, ROtation and planetary Transits (CoRoT) was the first space mission dedicated to detection of new extrasolar planets. It operated between 2006 and 2012 (de-orbited in 2014) and was led by Centre National d'Études Spatiales (CNES) in collaboration with Austria, Belgium, Brazil, European Space Agency (ESA), Germany and Spain (Moutou et al., 2013). The main mission objectives were to search for exoplanets and observe star oscillations. At the time of writing there were 35 confirmed CoRoT planetary systems (Exoplanet.eu, 2017). Figure 1.29 shows the artist's impression of the CoRoT satellite.

The CoRoT telescope's focal plane was composed of four 42-80 CCDs manufactured by Teledyne e2v. Two of them were dedicated to the asteroseismology program and the other two to the exoplanet search (Lapeyrere et al., 2006). Each detector was a back-illuminated, AIMO, frame transfer device, with 2048 × 2048 pixels image area and 2048 × 2052 pixels storage area

(pixel size was 13.5×13.5 µm^2). The CoRoT focal unit is shown in Figure 1.30.

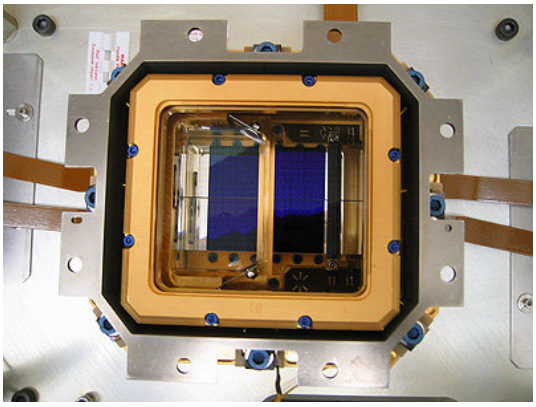

Figure 1.30: CoRoT camera's focal unit (from ESA (2006a)).

1.5.2 Kepler and K2

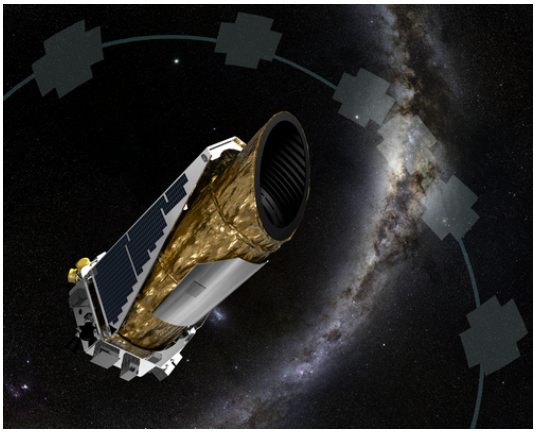

Figure 1.31: The artistic concept of the Kepler spacecraft operating in a new mission profile called K2 (from NASA (2015)).

Kepler, a planet finding mission that was named after the famous German astronomer Johannes Kepler (1571–1630), was launched in 2009 by National Aeronautics and Space Administration (NASA). Initially, the mission was planned to be operated over a period of 3.5 years, however, due to the problems with a higher than expected noise level in acquired data, it was necessary to extend it by another 3–4 years. This extra time was supposed to allow for

recording more transits, that were now necessary to confirm the potential detections. Unexpectedly, one of the four reaction wheels used for pointing of the spacecraft failed in July 2012, followed by the defect of another one in May 2013. This ended the Kepler mission in its initial form and led to the development of a new concept for spacecraft operation, known as K2 'Second Light' (see Figure 1.31). The new mission was approved in 2014 and since then it has been monitoring different fields distributed around the ecliptic plane, which simplified control of spacecraft attitude (Cleve et al., 2016).

Kepler's focal plane (see Figure 1.32) consists of 21 Science CCD modules designated for planetary transit detection and 4 Fine Guidance Sensor (FGS) CCD modules, placed one in each corner of the focal plane and used for improving spacecraft pointing accuracy. Each Science module contains two back

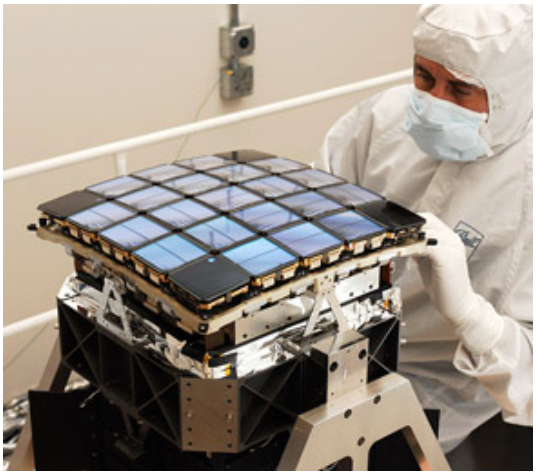

Figure 1.32: Kepler's detector array assembly (from Fanson et al. (2011)).

illuminated, full frame, 2200 × 1024 CCD arrays with 27 × 27 µm^2 pixels. In contrast, each FGS module contains just a single 550 × 535, back illuminated, frame transfer detector with 13 × 13 µm^2 pixels (Argabright et al. (2008)). Both types of sensors were manufactured by Teledyne e2v.

So far, Kepler and its extension K2 have helped to detect nearly 2500 exoplanets (confirmed transits), of which 2330 were discovered by Kepler and 140 by K2 (NASA, 2017b).

1.5.3 TESS

Even though the Kepler mission is still operational, NASA in collaboration with Massachusetts Institute of Technology (MIT) has already launched (in April 2018) its successor, named as Transiting Exoplanet Survey Satellite (TESS) (see Figure 1.33). The main goal of the mission is to discover exo-

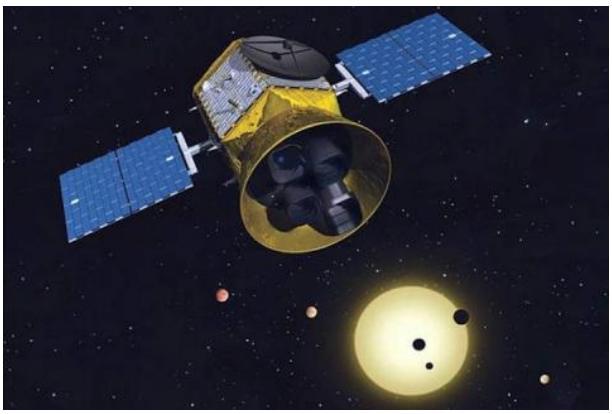

Figure 1.33: Artist's conception of the TESS spacecraft and payload (from MIT (2015)).

planets orbiting the brightest stars in an all-sky survey. TESS is equipped with four identical cameras, each of them containing four CCDs. These are frame transfer, back illuminated CCID-80 devices manufactured by MIT/Lincoln Laboratory. Each array has 4096×2048 pixels (15×15 µm^2 each), of which 2048×2048 form the imaging area and the remaining 2048×2048 - the storage region (Ricker et al., 2014). Figure 1.34 shows the single camera's focal plane with CCDs' storage areas covered by the metal plate.

The TESS mission is planned to have a duration of two years and is expected to catalogue more than 3000 transiting exoplanet candidates.

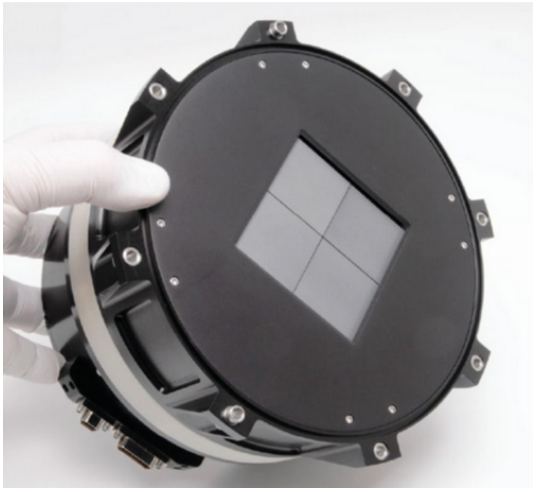

Figure 1.34: One of the four identical TESS CCD cameras' focal plane (from NASA (2017a)).

1.5.4 PLATO

PLAnetary Transits and Oscillations of stars (PLATO) is ESA's medium class mission adopted in 2017 and due for launch in 2026. Its main goal will be to search and characterise extrasolar planets through photometric transit detection, in particular Earth-like planets orbiting in the habitable zone around Sun-like stars (Rauer et al. (2014); Ragazzoni et al. (2016)). In addition, it will be possible to estimate various stellar parameters through asteroseismic analysis of the recorded light curves.

The spacecraft design provided by OHB System AG (shown in Figure 1.35) incorporates 26 imagers, of which 24 are normal cameras for observing stars with magnitudes greater than 8 and 2 are fast cameras for monitoring stars in magnitude range 4-8 (Gow et al., 2017). Each camera consists of four 4510×4510 CCD270 devices with 18 µm square pixels, made by Teledyne e2v (Endicott et al., 2012). Normal cameras will incorporate the FF variant of this CCD detector, while fast cameras will be equipped with the FT alternative (shown in Figures 1.36 and 1.37 respectively).

The mission is described in greater detail in Chapter 2.

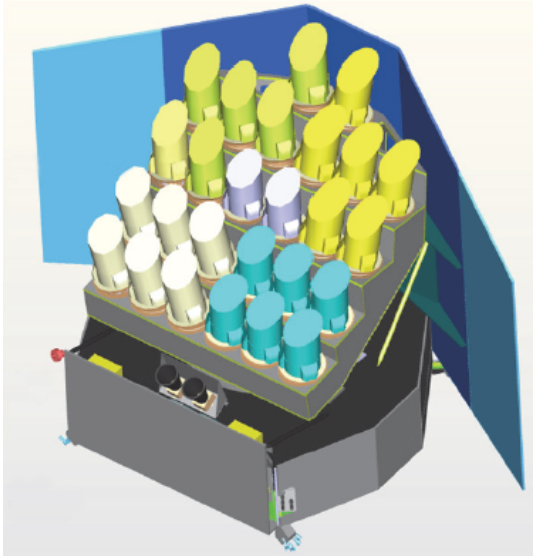

Figure 1.35: Design concept of PLATO spacecraft by OHB System AG (from ESA (2017)).

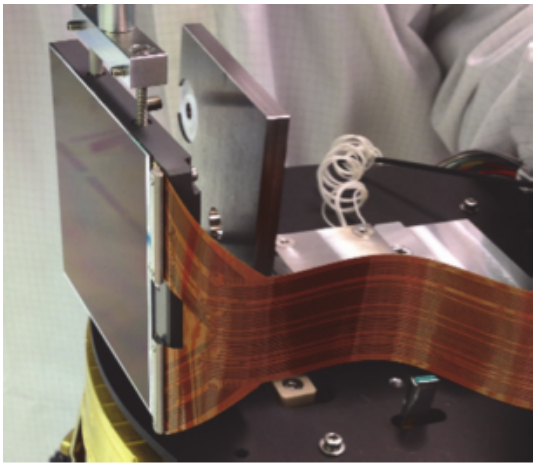

Figure 1.36: PLATO CCD270 detector in FF variant (from ESA (2017)).

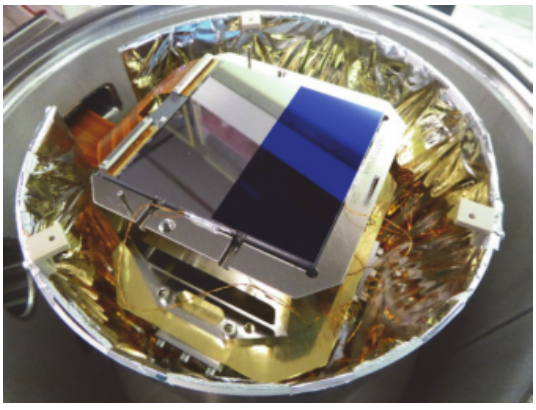

Figure 1.37: PLATO CCD270 detector in FT version (from ESA (2017)).

1.5.5 SuperWASP

Super Wide Angle Search for Planets (SuperWASP) is a ground-based planet detection program first operational in November 2003, currently led and funded by Warwick and Keele Universities. It consists of two robotic observatories: SuperWASP-North situated on the Spanish island of La Palma, surveying the Northern Hemisphere and SuperWASP-South, shown in Figure 1.38, located near Sutherland in the Republic of South Africa and covering the Southern Hemisphere of the sky. Both installations contain essentially very similar hardware. Each observatory is equipped with eight Canon 200 mm, f/1.8 telephoto lenses backed with 2048 × 2048 CCDs made by Teledyne e2v, all secured on an equatorial fork mount (Christian et al. (2005); Pollacco et al. (2006)). Such an arrangement allows for covering a large area of sky with high photometric precision, typically a dozen fields per night along a strip of constant declination (Smith and The WASP consortium, 2014).

As of December 2017, SuperWASP has so far helped to discover 146 extrasolar planets (Exoplanet.eu, 2017).

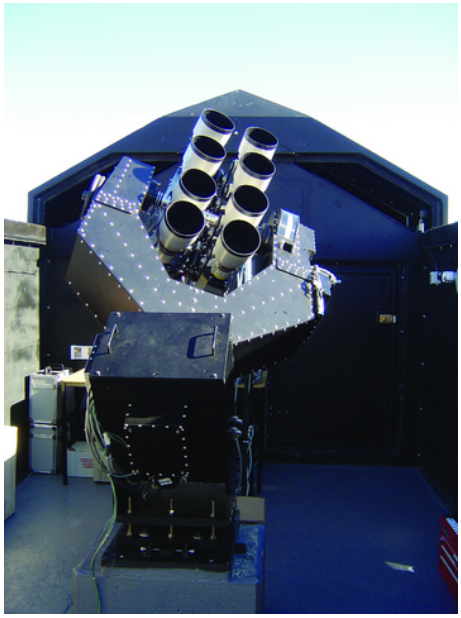

Figure 1.38: SuperWASP-South instrument installed on the robotic mount and housed under a two-room fibreglass enclosure incorporating a custom roll-off roof structure (from Pollacco et al. (2006)).

Chapter 2

PLATO

2.1 Mission

The main objective of the PLATO mission (Rauer et al., 2014) is to detect and characterise terrestrial exoplanets orbiting bright, solar-type stars (terrestrial planets are those with a radius in the range ∼0.8 to 2.2 times Earth's radius and surface temperatures allowing for the presence of liquid water (Borucki et al., 1997)). Besides that, PLATO will detect and characterise other varieties of planets, including rocky, ice and gas giant types in order to improve our understanding of planet formation and evolution processes. In addition, it will help to accurately estimate various stellar parameters. All these will be achieved through a combination of photometric transits detection, ground-based radial velocity measurement and asteroseismology. The photometric transit method will be used for detecting the planets and will help to determine their radius with 3 % precision. The ground-based radial velocity measurements will allow for determining the planetary masses with around 10 % precision. Finally, asteroseismology will help to determine stellar masses, radii and age with 10 % precision (ESA, 2017).

2.1.1 Detection of Exoplanets

The transit detection method has already proved its effectiveness through numerous planet discoveries made by both space- and ground-based observatory missions, such as CoRoT, Kepler and SuperWASP (see Section 1.5 for their brief description). In principle, this technique relies on identification of U-shaped dips in the collected stellar light-curves, indicating the possibility of a planet transit, as illustrated in Figure 2.1. This can only happen when the observer/imager, the star and the planet are in-line. At least three detected transits are required to confirm the presence of a planet, its radius and orbital period.

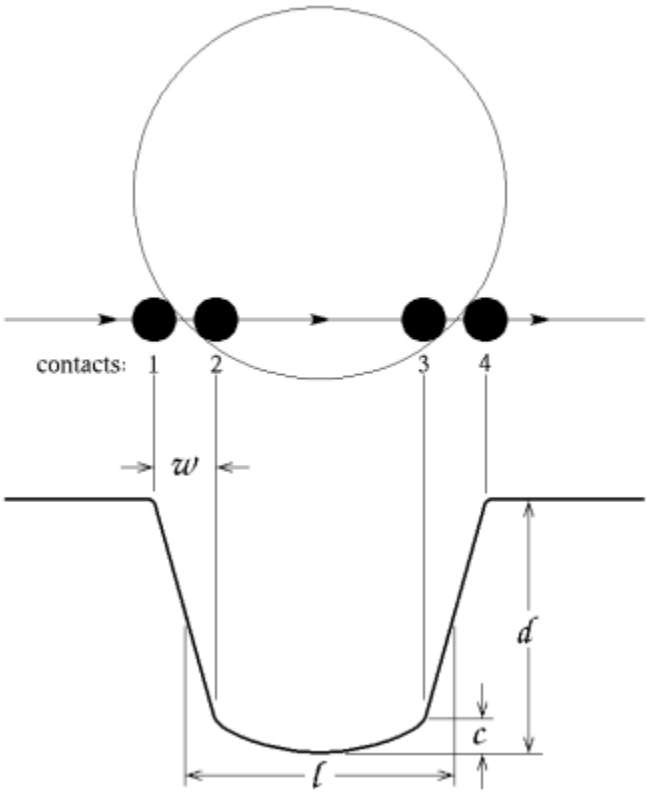

Figure 2.1: Schematic illustration of the planetary transit method (from Brown et al. (2001)). l represents the duration of the transit, d is the transit depth, w is the ingress/egress duration and c is the central curvature of the light-curve.

The first exoplanet confirmed by the transit method was HD 209458b

(Charbonneau et al. (2000); Henry et al. (2000)) orbiting its parent star HD 209458 in constellation Pegasus. The planet was first identified using radial velocity measurements and then confirmed by the transit detection method. Figure 2.2 shows the photometric time series acquired for the star HD 209458 on 09 September 1999 and 16 September 1999. The same data after binning and additional processing is shown in Figure 2.3.

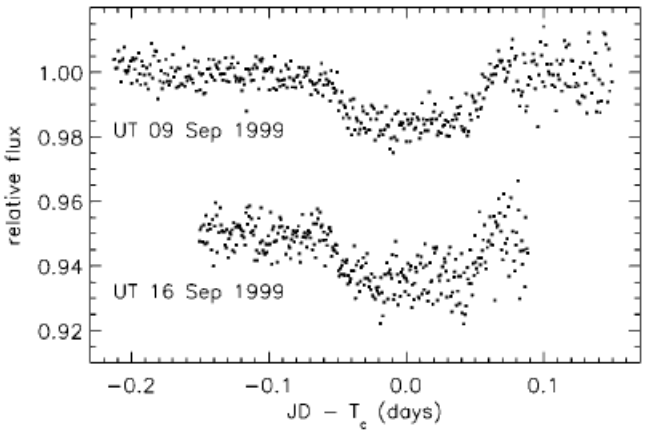

Figure 2.2: Photometric time series showing the first observed exoplanet transit (from Charbonneau et al. (2000)). Data acquired on 16 September are offset relative to data from 09 September. T_c is the time at the center of the transit.

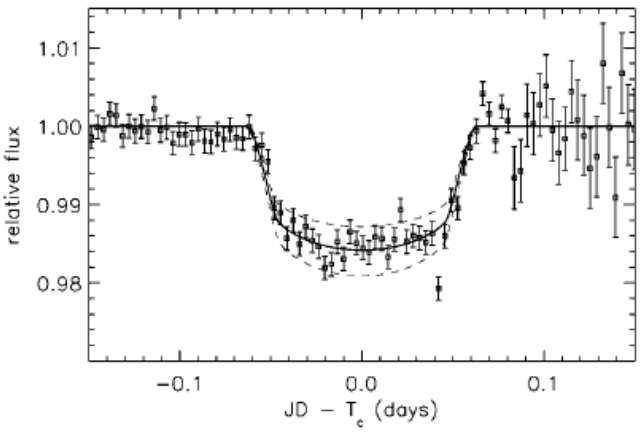

Figure 2.3: Data from Figure 2.2 after processing (Charbonneau et al., 2000).

In the case of star HD 209458 the orbiting body (HD 209458b) is a gas

giant. A dip in the light curve caused by a terrestrial planet would be much shallower, in the range 0.5 to 13×10^{-4} (Favata et al., 2000).

In certain circumstances the transit method may lead to misleading false alarms. The most common source of them is eclipsing binaries, or in general, multiple-star systems (Brown, 2003). False alarms may also be caused by transiting very low mass stars (such as brown dwarves) or stellar spots.

PLATO will specialise in detecting and characterising Earth-like planets in Earth-like orbits around Sun-like stars. In order to achieve this, an instrument photometric noise level (random noise in the light curves) of less than or equal to 3.4×10^{-5} (34 ppm) in one hour is required. Such high sensitivity will also allow for detection of planetary rings and moons, as well as large comets (ESA, 2017).

2.1.2 Asteroseismology

Asteroseismology determines the internal structure and evolution of stars by the interpretation of their pulsation periods (see Chaplin and Miglio (2013)). Different oscillation modes penetrate to different depths inside the star and can be detected through long term photometric monitoring. As an example, Figure 2.4 shows the brightness fluctuations of the star KIC 4726268 and the corresponding oscillation frequencies.

The characteristics of the oscillation modes depend on the type of the star. For instance, stars like white dwarfs have been found to have the gravity modes (g-modes), which result from internal gravity waves. In the case of the Sun and solar-like stars, the observed pulsations are essentially pressure modes, designated as p-modes (Brown and Gilliland, 1994). Such oscillations are due to trapped acoustic waves. Furthermore, there are stars manifesting oscillations derived from the mixture of p- and g-modes.

PLATO will measure the oscillations of more than 300 000 stars with $V \leqslant 13$, with the goal to achieve precisions of about 0.1 µHz (ESA, 2017).

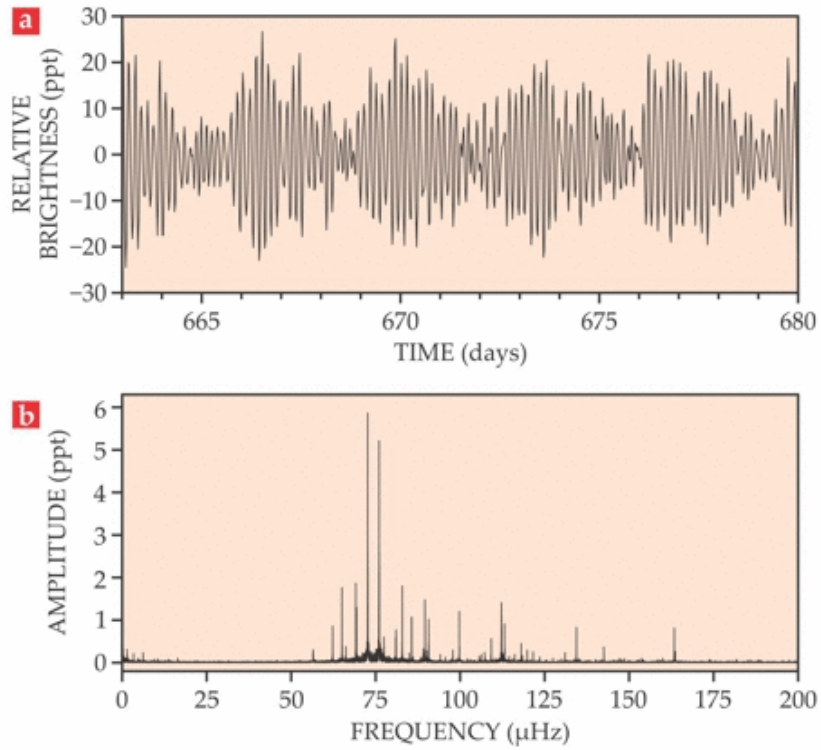

Figure 2.4: Kepler satellite's observation of the star KIC 4726268. (a) Collected light curve time series. (b) The Fourier transform of the light curve showing oscillations of the star in the frequency domain (from Aerts (2015)).

2.2 PLATO Charge-Coupled Devices

As already mentioned in Section 1.5.4, PLATO cameras will incorporate CCD270 detectors designed specially for the mission by Teledyne e2v. These are four-phase BSI devices intended for NIMO in either FT or FF configuration (as used in the two fast and twenty-four normal cameras respectively). Figure 2.5 shows the schematic layout of the CCD270 detector in the FT variant. The FF counterpart (which is of interest in this thesis) is essentially the same, except that it has a double-sized image section in the absence of a store-shield (see Section 1.3 for description of BSI, NIMO, FT and FF CCDs).

Rows of data are read out consecutively by the output register, which is split into two halves (left and right), each having its own output circuit. For this particular model of CCD, each of the two outputs, OSF and OSE, has an associated optional 'dummy' output ($DOSF$ and $DOSE$ respectively) not connected to the output register, so not receiving any signal charge. By

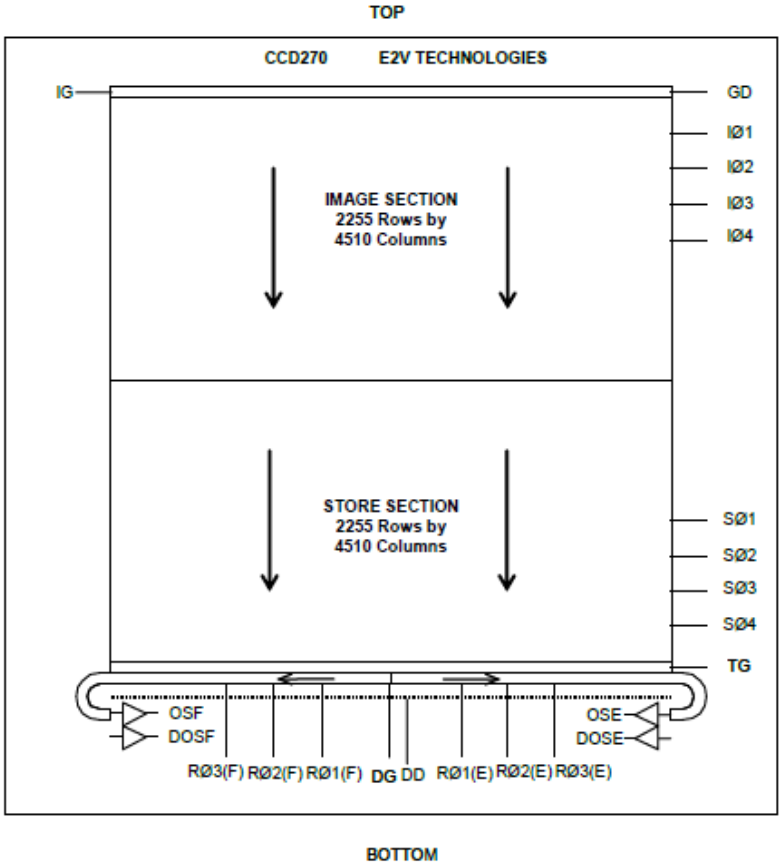

Figure 2.5: Schematic of the CCD270 FT layout (E2V Technologies, 2016b). $I\phi1$, $I\phi2$, $I\phi3$ and $I\phi4$ represent image area clocks, $S\phi1$, $S\phi2$, $S\phi3$ and $S\phi4$ are storage area clocks, and $R\phi1$, $R\phi2$ and $R\phi3$ are left and right output register clocks (F and E respectively). OSF and OSE represent left and right CCD output pins.

application of a differential-pair readout, it is possible to remove the Common Mode (CM) noise in the CCD. However, it comes at a cost of increased power consumption and also the resulting readout noise is increased by a factor of $\sqrt{2}$ (the uncorrelated noise adds in quadrature).

All four CCD270 outputs (two 'normal' and two 'dummy') contain two-stage amplifiers. Each stage is a single voltage follower with a load resistor on its output. As shown in Figure 2.6, the stages are coupled with a capacitor. The reset transistor restores the base voltage of the capacitance node after each pixel is sampled. Another transistor's gate (TG) is pulsed before each line read-out to reset the interstage DC level. Each output is connected to an external 3.4 kΩ load resistance in the form of a parallel configuration of two

6.8 kΩ resistors located on the Normal-Front-End Electronics (N-FEE).

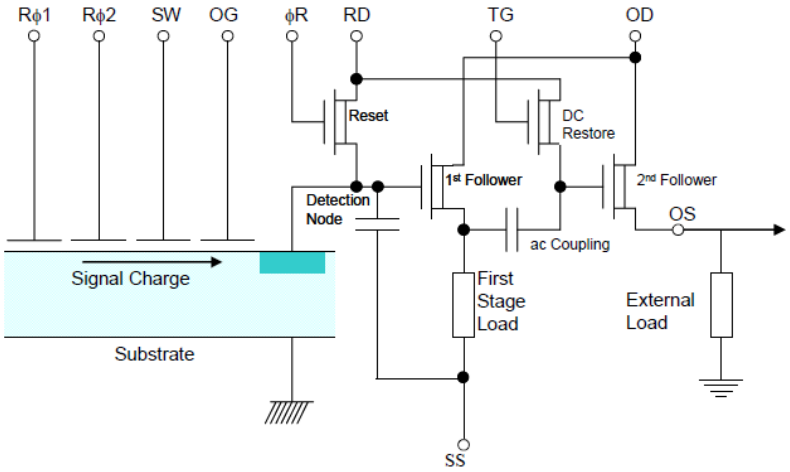

Figure 2.6: CCD270 output circuit (E2V Technologies, 2010).

2.2.1 CCD Related Challenges for PLATO

PLATO CCDs are required to provide extremely stable performance over long observation sequences. Apparent brightness variations due to small pointing changes of the spacecraft can lead to uncertainty in a detection of exoplanets. There are a number of processes specific to CCDs that can have impact in this area, mostly related to the transfer of electrical charge during readout. These include radiation induced trapping and flat band voltage shifts. Also the full well capacity of the CCD may be affected which in turn affects the measurement of bright stars. However, these phenomena are outside of the scope of this work, because they are CCD properties controlled by the device physics and the manufacturing process, while this thesis is related to aspects which can be addressed using the readout electronics.

Relevant here is the effect of temperature change both on the CCD itself (the output stage) and the N-FEE (see Section 2.3.1), this is an important effect which has not been investigated by practical measurements for a CCD connected to a set of PLATO readout electronics. Chapter 6 shows how the CCD gain and offset change with temperature. This is particularly important

since thermal control of the CCD is limited although the temperature of the CCD is continuously monitored and some post-facto correction may be possible. The implementation of such corrections will depend critically on the magnitude and repeatability of these thermal effects.

2.3 Normal-Front-End Electronics (N-FEE)

The N-FEEs are being developed at Mullard Space Science Laboratory (MSSL) (design of this electronics is not part of the thesis). The version used for the measurements in this work is BreadBoard_Version1 (BB_V1). Each of the twenty-four units (one per normal camera, as explained in Section 1.5.4) controls the readout of four CCDs, digitises the acquired image data and sends them to the Normal-Data Processing Unit (N-DPU). In addition, it controls acquisition of the housekeeping information and data from the temperature sensors located at the N-FEE Printed Circuit Board (PCB) and integrated into each CCD.

The N-FEE block diagram is shown in Figure 2.7. The central component is the Field-Programmable Gate Array (FPGA) (clocked from the 50 MHz oscillator), which generates all the CCD clock waveforms and controls the Digital-to-Analogue Converters (DACs) that set the bias voltages. The four detectors connected to each N-FEE are biased by linear low-noise Low-DropOut (LDO) voltage regulators, that are also used for generating the digital supplies.

Each acquired CCD image is split into two halves and routed through detector's left and right output channels. These are connected to two identical video chains (see Figure 2.8). The multiplexers (one for each image-half) are controlled by the FPGA and enable the output from four CCDs in a rotating sequence, one at a time every 6.25 s. The video signal chains' bandwidth is limited to 20 MHz (this is required for the 4 MHz operation as per requirement PLT-N-FEE-242 in PLATO document PLATO-OHB-PL-RS-005 (2017)) by the second order Low-Pass Filters (LPFs) located after the multiplexers and

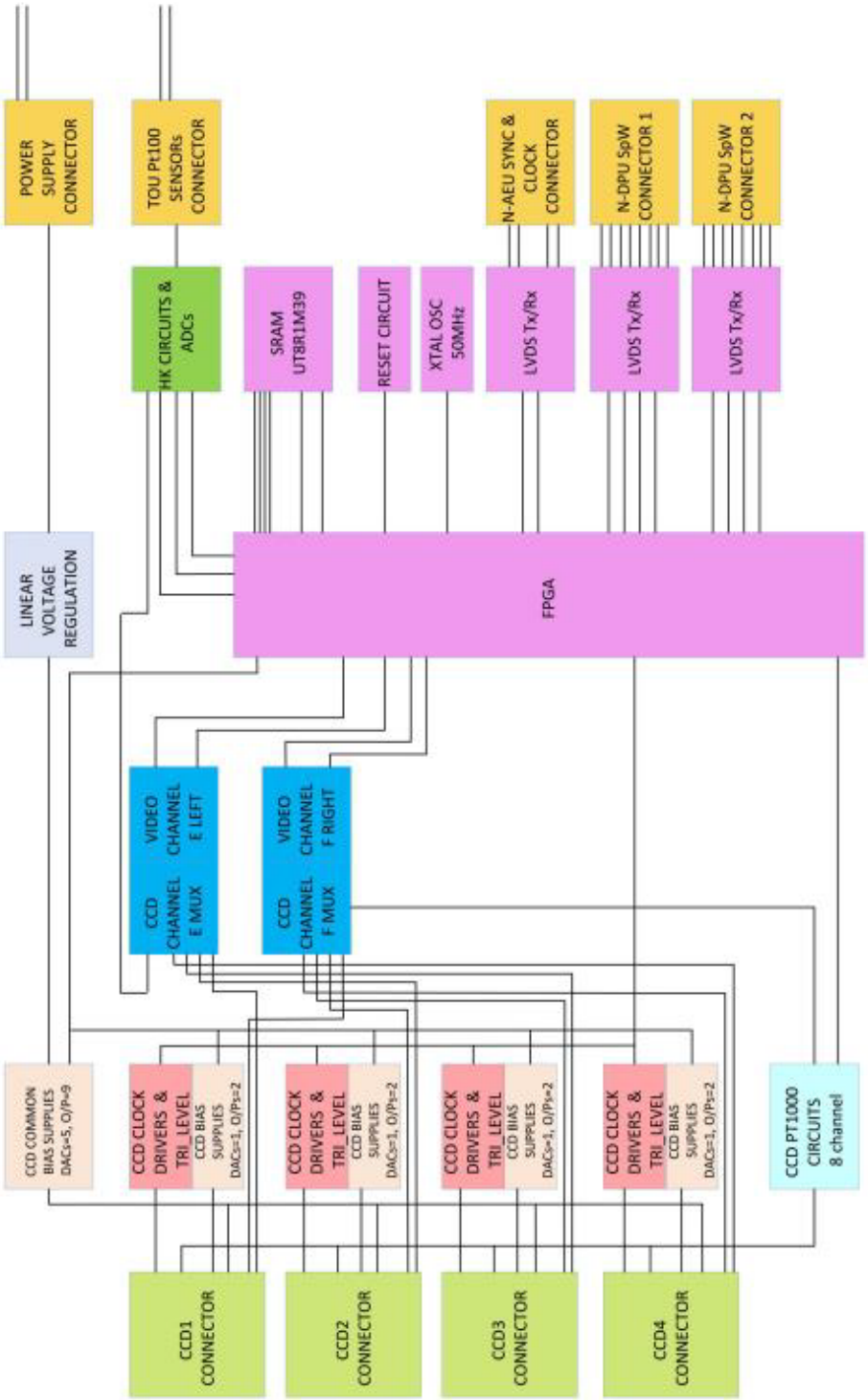

Figure 2.7: Block diagram of the PLATO EMv1 N-FEE (Gow et al., 2017).

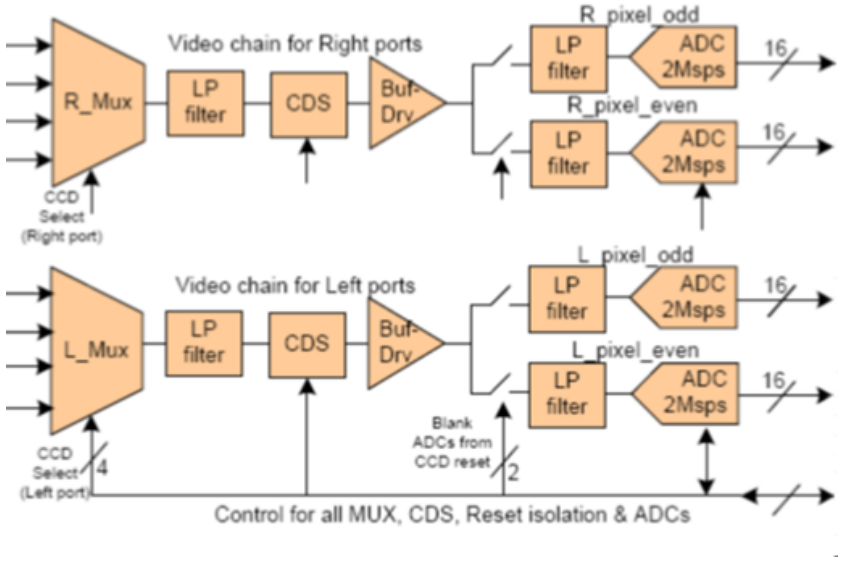

Figure 2.8: PLATO N-FEE video signal chains (extracted from ESA (2016)).

before the ADCs. Each video chain has its own two 16-bit ADCs, one converting the odd pixels and the other one processing the even pixels. Such an arrangement allows for the use of 2 MS/s devices, while still providing the overall digitization at 4 MS/s.

The N-FEEs are equipped with Static Random-Access Memory (SRAM) chips to reduce the required bandwidth for transfer of the digitised data to the N-DPU and provide sufficient storage for certain on-board image processing tasks. The communication between N-FEE and N-DPU is provided through two SpaceWire links.

2.3.1 N-FEE Related Challenges for PLATO

The N-FEE is required to provide a stable and low-noise digitised output, with very low power consumption. Processes that can affect this are conducted and radiated ElectroMagnetic Compatibility (EMC) issues and thermal variations. Only conducted EMC susceptibility (Chapter 5) and thermal sensitivity (Chapter 6) was investigated as part of this research. Radiated EMC was outside of the scope due to the very specialised equipment needed. Chapter 4 gives an overview of the subject of EMC.

Chapter 3

Photometric Stability of LED Light Source

To simulate in the laboratory the response to a transit of a terrestrial planet, a light source whose brightness can be controlled to $< 0.01\,\%$ is required. This is a demanding situation and warrants consideration in its own right. This chapter looks at stability of Light-Emitting Diode (LED) sources (a likely method).

A process of CCD characterisation involves illumination of its photosensitive side with a light source of precisely known emission. The problem with any type of light source is that, over a period of time, its output optical power will exhibit changes. Such an output variability can have both a short- and a long-term character. The short-term changes are related to stabilisation of the light source itself (e.g. its warm up time). The long-term variations result from light source ageing effects. Popular tungsten-halogen light sources are known for their short life expectancy when compared to LED light sources (up to 10 000 hours versus over 50 000 hours). Furthermore, they require a relatively long time to stabilise in contrast to their LED counterparts and cannot be used in vacuum conditions. The above reasons plus the fact that LED light sources are cheaper, more compact and easier to control, result in their ever-growing popularity.

The LED, a fundamental component of every LED light source, lights up

when current flows through it in the forward direction. For this to happen, a sufficient voltage with correct polarity has to be applied across the LED terminals. It is possible to maintain an LED's optical power by controlling its forward current, due to the almost linear relationship between these two parameters (see Figure 3.1). Moreover, it is known that an LED's luminous in-

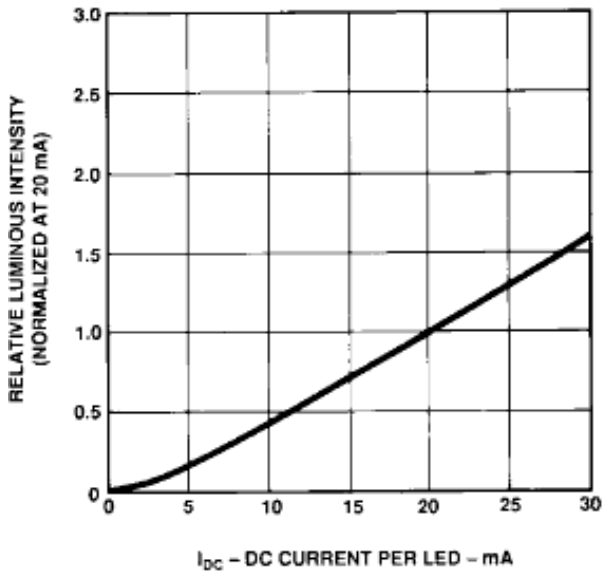

Figure 3.1: Relative luminous intensity vs forward current for HLMP-3750 LED (Avago Technologies, 2013).

tensity and peak emission wavelength are functions of temperature. Luminous intensity has temperature dependence of $e^{k(T-T_A)}$ (Avago Technologies, 2010), where T is the diode's junction temperature, T_A is the ambient temperature, and k is an empirical constant on the order of $-0.01/°\mathrm{C}$. This means that linear temperature changes cause exponential changes of the LED intensity.

Figure 3.2 shows a block diagram of the setup used for measuring the LED's spectral response. The device tested was an HLMP-3750 Gallium Arsenide Phosphide (GaAsP) on Gallium Phosphide (GaP) red LED, manufactured by Avago Technologies. The diode was driven from a TTi PL330 bench Power Supply Unit (PSU) set to deliver a fixed 2 Vdc signal. The current limit on the supply was set to 25 mA, eliminating the need for a current-limiting resistor. The emitted spectrum was measured with StellarNET's EPP2000 High

Resolution Spectrometer coupled to the LED with a fibre optic cable. The readings were acquired and visualised with SpectraWiz Personal Computer (PC) software supplied with the spectrometer.

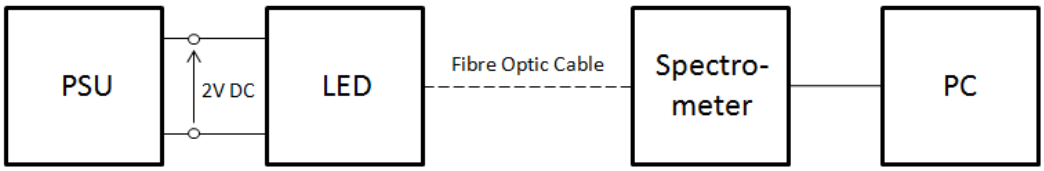

Figure 3.2: Block diagram of the setup used for measuring LED spectrum.

According to the LED manufacturer's datasheet (Avago Technologies, 2013), the typical peak wavelength λ_{pk} for this device is 635 nm and the typical spectral line half-width $\Delta\lambda$ is 40 nm. The results of the spectral response measurements conducted at ambient temperature of +23 °C are plotted in Figure 3.3. As shown, the actual peak wavelength is 642 nm and the spectral line half-width is 43 nm.

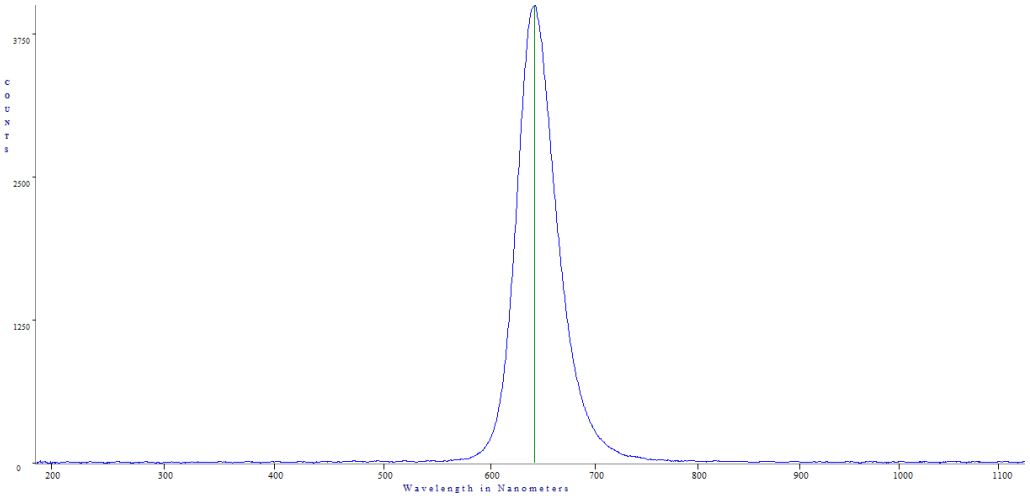

Figure 3.3: Spectral response of the tested LED.

The two sets of experiments described in the upcoming sections were conducted in order to estimate the photometric stability of the HLMP-3750 LED's output. The first experiment concentrates on estimating the LED ageing effect. The second one looks more closely at the relationships between

LED output optical power, LED forward current and LED temperature.

3.1 LED Ageing

3.1.1 Experimental Setup

The experimental setup used for monitoring temperature and optical power of the LED is shown in Figure 3.4. The HLMP-3750 LED was powered from the

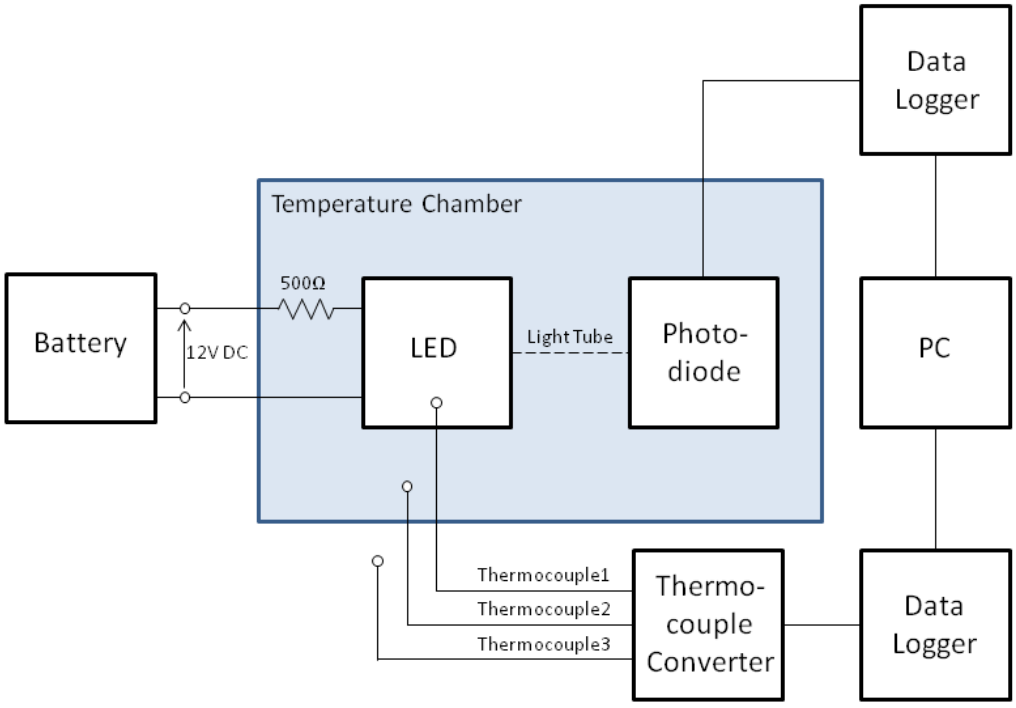

Figure 3.4: Block diagram of the setup used for monitoring optical power and temperature of an LED.

caravan-type, rechargeable 12 V lead-acid battery. The diode was protected with Vishay's Z201 Series 500 Ω high precision resistor featuring a Temperature Coefficient of Resistance (TCR) of just ±0.05 ppm/°C. An additional role of the resistor was to linearise the *I-V* curve of the system, making the current less sensitive to voltage changes. The required resistance value was

calculated from the following equation:

$$R = \frac{V_{bat} - V_F}{I_F}, \tag{3.1}$$

where $V_{bat} = 12.3\,\mathrm{V}$ is the battery voltage, $V_F = 2\,\mathrm{V}$ represents the diode's forward voltage, and $I_F = 20\,\mathrm{mA}$ is the diode's forward current.

The LED's output optical power was measured with Thorlab's S120VC Photodiode Power Sensor coupled to Thorlab's PM100USB 16-bit power meter interface, pre-configured to sample data at 1 S/s (sample per second) rate. The PM100USB output was interfaced to the data logging PC running PM100 utility software. The S120VC can detect photons with wavelengths from 200 to 1100 nm and measures the optical power with 1 nW resolution.

Both the photodiode and the LED (including the protective resistor) were operated inside the temperature chamber to minimise the temperature fluctuations. This was necessary, as the LED's output optical power depends strongly on its operating temperature. Figure 3.5 shows the LED output power and corresponding temperature over an eight day period. This data

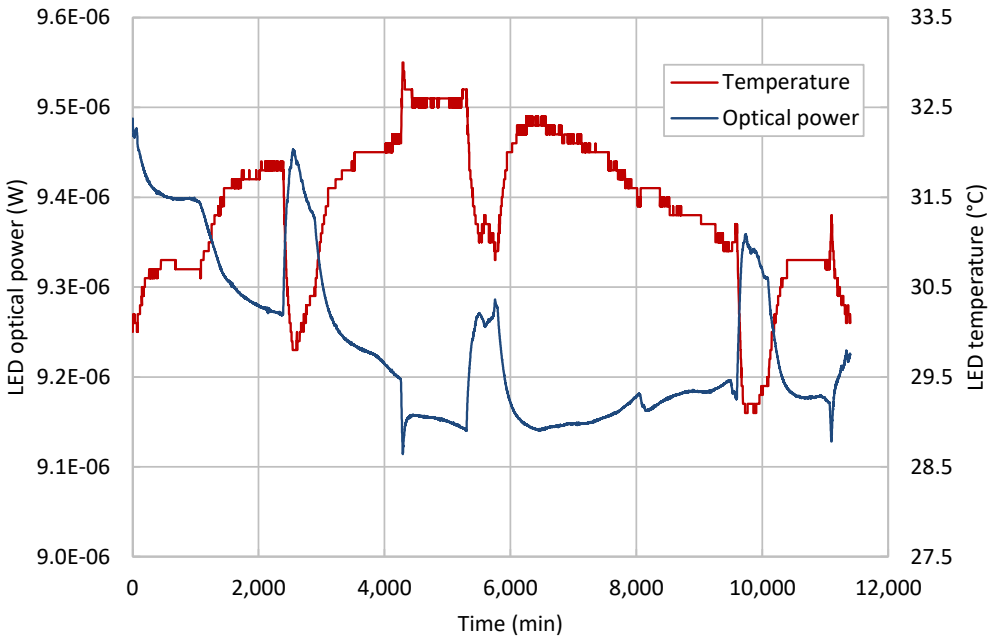

Figure 3.5: Anticorrelation between LED temperature and its output optical power. Data was acquired over a period of eight days.

shows the anticorrelation between LED output power and temperature and gives a variation of power with temperature of $\sim 0.05 \times 10^{-6}\,\mathrm{W/^{\circ}C}$. Temperature was measured with 0.1 °C resolution, with the aid of the three J-type thermocouples attached to the Pico EnviroMon EL041 4-channel thermocouple converter (as previously shown in Figure 3.4). Thermocouple1 was monitoring the temperature of the LED (it was attached to the cathode pin using a thermal epoxy), thermocouple2 was measuring the temperature inside the chamber, and thermocouple3 was monitoring the room temperature. The thermocouple converter was connected to a Pico EnviroMon EL005 data logger, which was pre-configured to sample data at 1 S/s in order to match the PM100USB photodiode interface sampling rate. The data logger was coupled to the PC running EnviroMon software, where the data was visualised with an option of exporting it into an MS Excel spreadsheet.

3.1.2 Setup Limitations

The environmental test chamber is operated in a dedicated control loop that maintains its internal temperature set by the user. Two identical thermocouples were used in order to assess the thermal stability of the chamber; one measuring the temperature inside and another one monitoring the temperature outside the chamber (in the laboratory room). The result of the test is shown in Figure 3.6. The blue trace shows that the chamber's temperature control loop had to make larger adjustments from about 2300 minutes onwards, when the room temperature varied more rapidly. Although the room temperature fluctuated between 28 and 37 °C throughout the test, the temperature inside the chamber was maintained at the average level of 22 °C, with a standard deviation of 0.14 °C. Figure 3.7 shows the LED's optical power plotted as a function of the LED's temperature for the experimental run shown in Figures 3.5 and 3.6. The visible quantisation noise results from an inherently low resolution of the thermocouple (just 0.1 °C). Moreover, there are often a few different optical power values corresponding to a single LED temperature. Note that these effects do not correlate with the small temperature variabil-

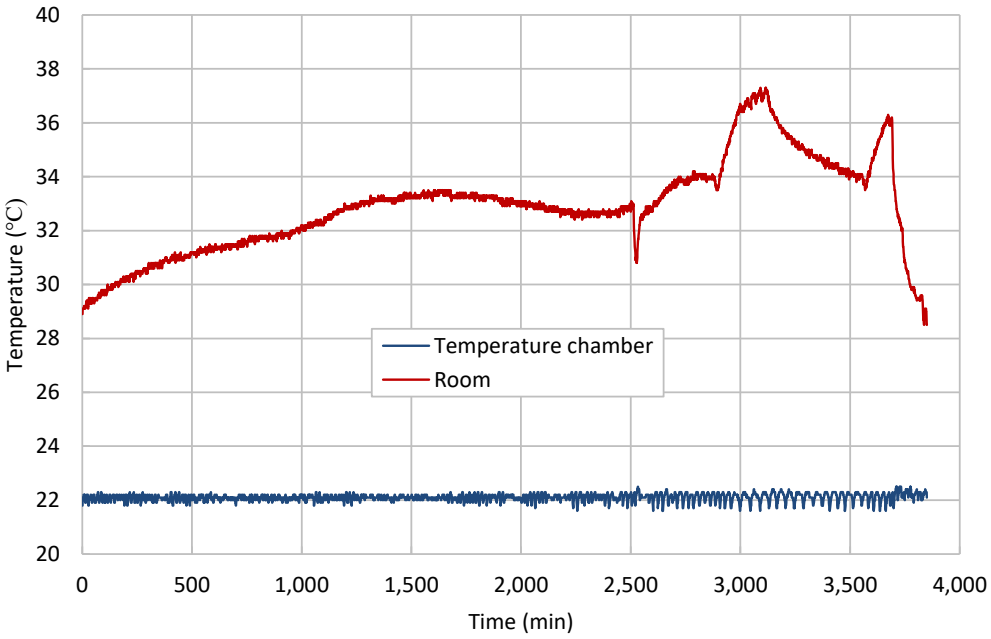

Figure 3.6: Thermal stability of the temperature chamber.

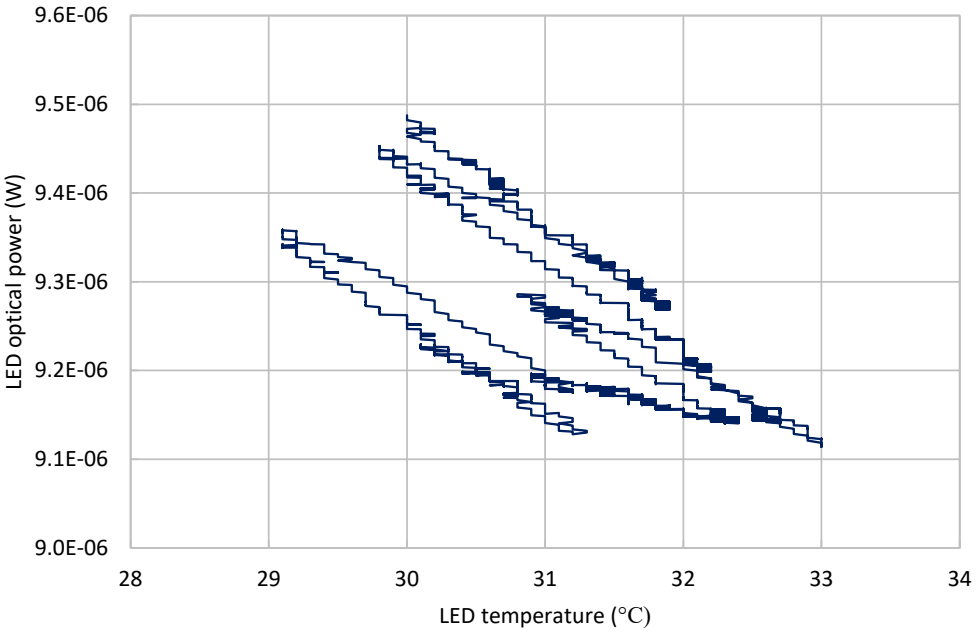

Figure 3.7: LED's optical power vs temperature.

ity of the chamber and so are not thermal in origin. This suggests that the diode's brightness was also affected by some additional variable(s) other than its temperature (e.g. we can not rule out an instability in the LED or photo-

diode circuit). The fact that in Figure 3.7 the slope changes when the sense of temperature versus time changes, suggests a hysteresis effect. Section 3.2 shows results from a significantly improved setup.

Table 3.1 shows values for LED optical power to temperature ratios for the straight segments extracted from Figure 3.7 (eight in total).

Segment no.	Ratio [W/°C]	Fractional change/°C
1	-1×10^{-7}	-0.0109
2	-6×10^{-8}	-0.0065
3	-4×10^{-8}	-0.0043
4	-9×10^{-8}	-0.0098
5	-8×10^{-8}	-0.0087
6	-1×10^{-7}	-0.0109
7	-8×10^{-8}	-0.0087
8	-1×10^{-7}	-0.0109

Table 3.1: LED optical power temperature coefficient expressed as measured optical power change (W/°C, column 2) and fractional change (/°C, column 3) for the segments in Figure 3.7. The segments are numbered in the order they appear on the plot (from left to right).

In order to estimate the noise introduced by both the photodiode and the power meter interface, the setup was tested in darkness (with the LED in the off-state). The two primary noise components intrinsic to the photodiode itself are shot noise and Johnson noise. As shown in Figure 3.8, a measured signal with optical power lower than 1 nW would be lost in noise.

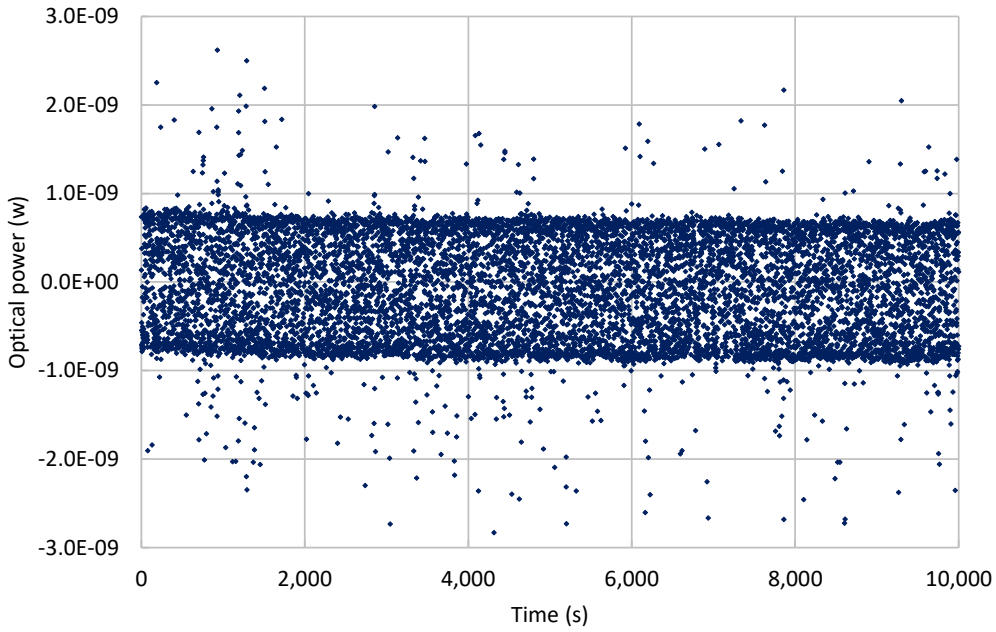

Figure 3.8: Photodiode response in darkness.

3.1.3 Results

In the first of the stability tests the LED's optical power was monitored over a period of seven days, with two 5-hour long intervals when the diode was inactive (i.e. in its off-state). The on/off cycles were operated as follows:

- Test cycle 1: LED left 'on' for ∼2 days, then 'off' for ∼5 hours;
- Test cycle 2: LED turned back 'on' for ∼2 days, then 'off' again for ∼5 hours;
- Test cycle 3: LED turned back 'on' for ∼3 days.

The resulting plot is shown in Figure 3.9. During these cycles the battery voltage fell from 12.22 to 12.20 V, a change of 0.2 %. The three test cycles are colour-coded. For the clarity of the plot the LED's off-state intervals are not shown. There is a visible initial transient, appearing each time the LED was turned on (the left edge of the plot). This suggests the need for an initial ∼30-minute wait time before the diode can be used for stable work. Furthermore, all three curves have almost identical slopes (the LED's brightness is dropping

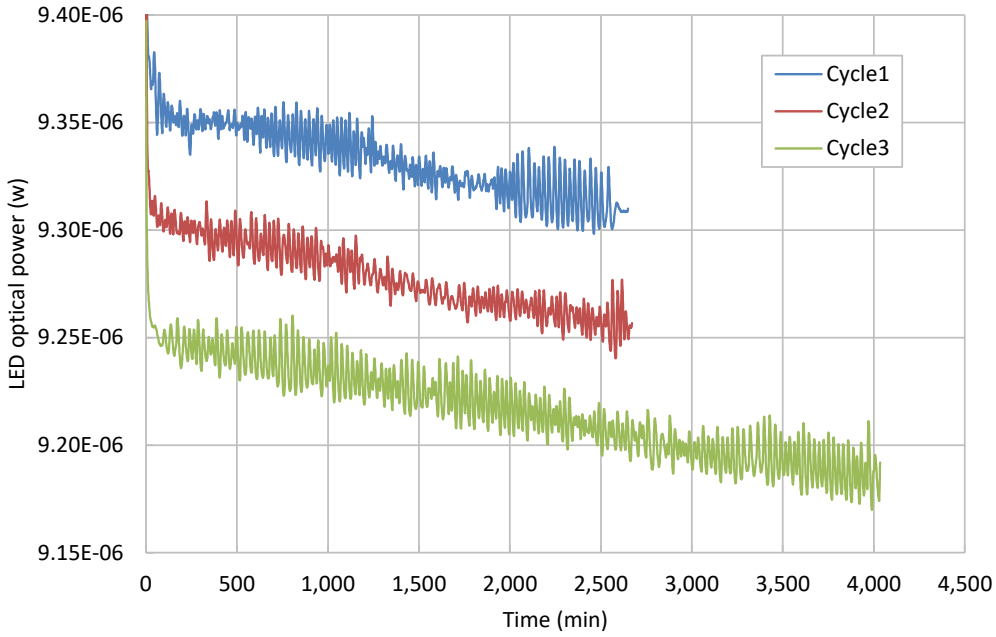

Figure 3.9: LED optical power measured in three test cycles over period of seven days.

at the rate of ∼0.01 % per hour) and it appears that for each following test cycle the resulting curve starts roughly at the same optical power level as its predecessor's final level. This is even more visible in Figure 3.10, where the three test cycles are plotted one after the other (again omitting the periods of LED inactivity). Potentially there are two possible explanations of such observed LED output power decay: the diode's ageing effect (see Trevisanello et al. (2007)) or the battery discharge. By substituting a 620 Ω resistor for the LED with its 500 Ω series resistor, it was possible to simulate the presence of the diode as if it was in its active state, but eliminating the possibility of an occurrence of the ageing effect. The battery was loaded for a period of ∼2.5 days before the LED was reconnected and turned back on for a period of ∼2 days. The resulting LED output optical power is shown in Figure 3.11 and it is designated as 'Cycle4' (the other three traces are copied from Figure 3.10 for comparison purposes). If the slopes were caused by the battery discharge, the fourth test cycle trace would start at a significantly lower optical power level. Instead, it continued roughly from where the third cycle has left off.

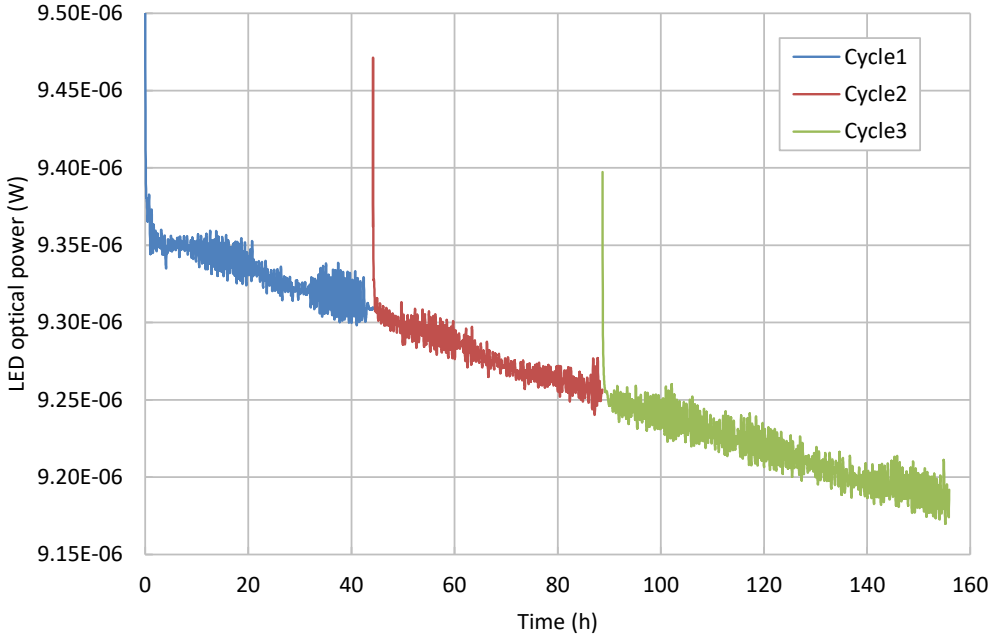

Figure 3.10: Three concatenated LED optical power test cycles.

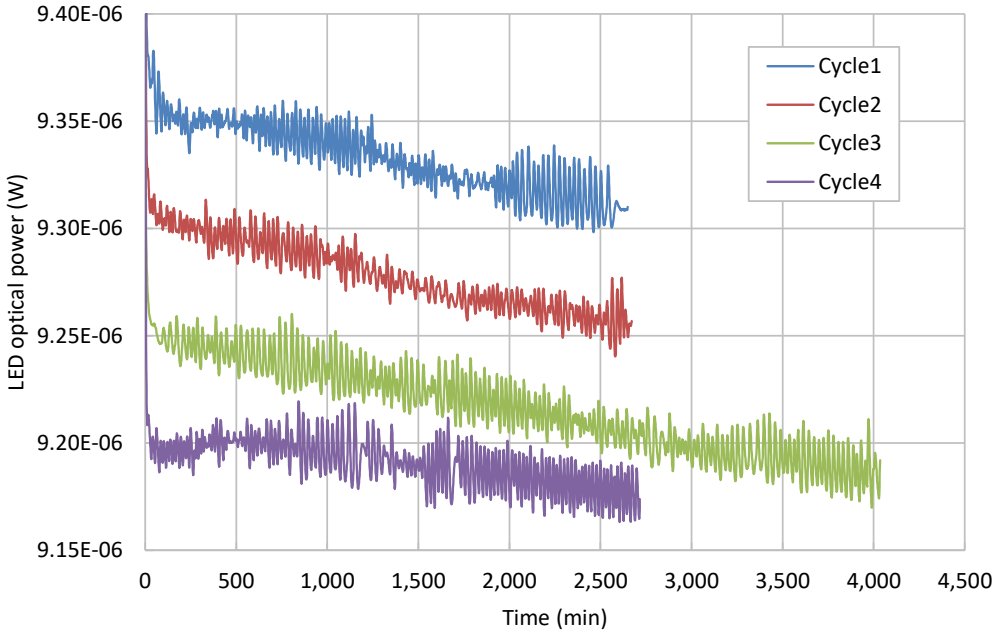

Figure 3.11: LED's optical power recorded during four test cycles.

This indicates that the observed decay was a result of the LED's intrinsic ageing effect rather than the battery drainage. The slightly different slope at the very beginning of the fourth cycle was caused by higher than average

temperature of the LED for the first 300 minutes (see Figure 3.12 for details). The reason for this unusual behaviour remains unknown (the thermocouple that measured temperature inside the chamber did not record any sudden change during that time).

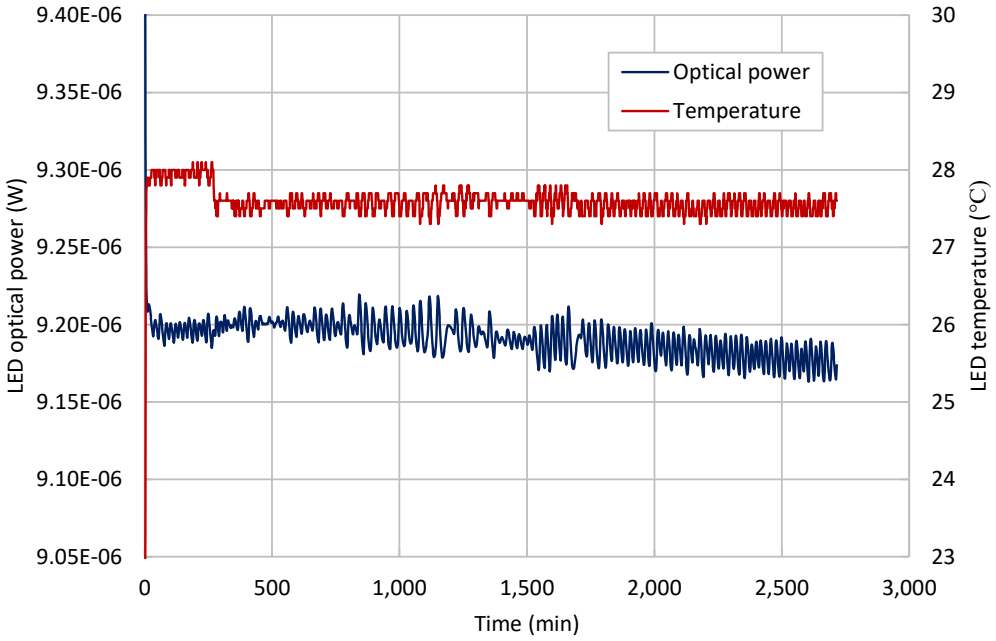

Figure 3.12: LED's optical power and temperature during the fourth test cycle.

3.2 Further Investigation of LED Stability

3.2.1 Experimental Setup

The setup shown in Figure 3.13 adds the ability to monitor the LED current and improves the precision of the temperature measurements when compared to the setup from Figure 3.4. The LED is powered from the 12 V caravan-type battery (the same as the one used in Section 3.1) with added voltage regulator that stabilises the supply at 9 V. The LED's temperature is measured with the 10 kΩ Negative Temperature Coefficient (NTC) thermistor manufactured by GE Thermometrics, whose resistance is monitored by the Keysight

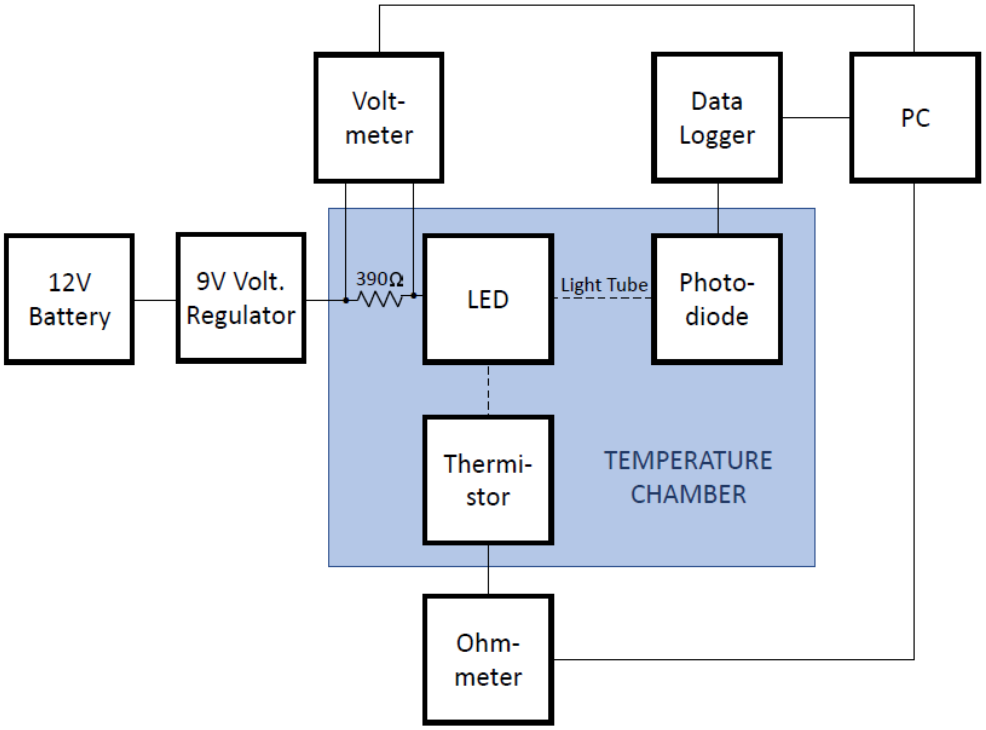

Figure 3.13: Block diagram of the setup used for monitoring optical power, forward current and temperature of an LED.

Technologies' (formerly part of Agilent Technologies) 34461A programmable digital multimeter. By replacing the thermocouple with the thermistor, the measured temperature resolution is increased from 0.1 °C to 0.001 °C. The current flowing through the LED is monitored by measuring the potential difference across the diode's ultra-stable 390 Ω series resistor using an additional Keysight Technologies' 34461A digital multimeter. Finally, the LED's output optical power is measured with a Thorlabs S120VC photodiode connected to the PC through the PM100USB power meter interface (this part of the setup has not changed). The LED, resistor, thermistor and photodiode are all enclosed in the temperature chamber for an improved thermal stability of the setup.

A LabVIEW hardware control and user interface was developed for controlling the two 34461A multimeters and the photodiode. This was necessary to synchronise the readouts and save all the acquired data into a file for further analysis.

3.2.2 Results

The experiment was carried out over a period of five days and divided into the following four LED on/off test cycles:

- Test cycle 1: LED powered up and left operating for 20.5 hours, then turned off for 3.5 hours;
- Test cycle 2: LED turned back 'on' for 14 hours, then switched 'off' for 10 hours;
- Test cycle 3: LED turned 'on' for 21.5 hours, then turned 'off' for 2 hours;
- Test cycle 4: LED turned back 'on' for 46 hours, then finally switched 'off' (end-of-experiment).

Figures 3.14, 3.15 and 3.16 show, respectively, measured LED optical power, LED forward current and LED temperature. The plots show only part of each cycle, when the LED was in its on-state.

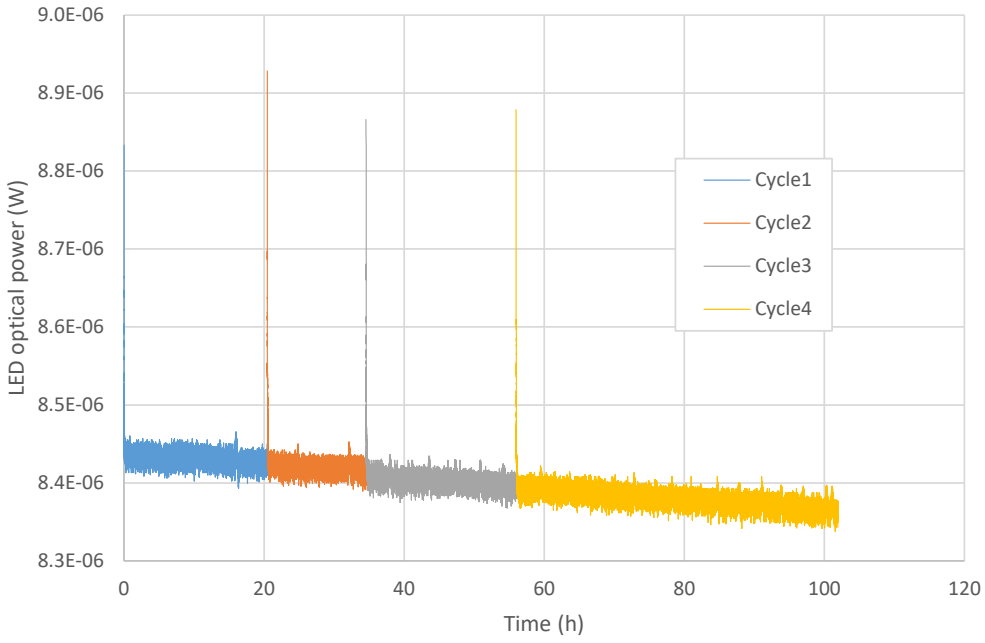

Figure 3.14: LED optical power measured in four separate test cycles.

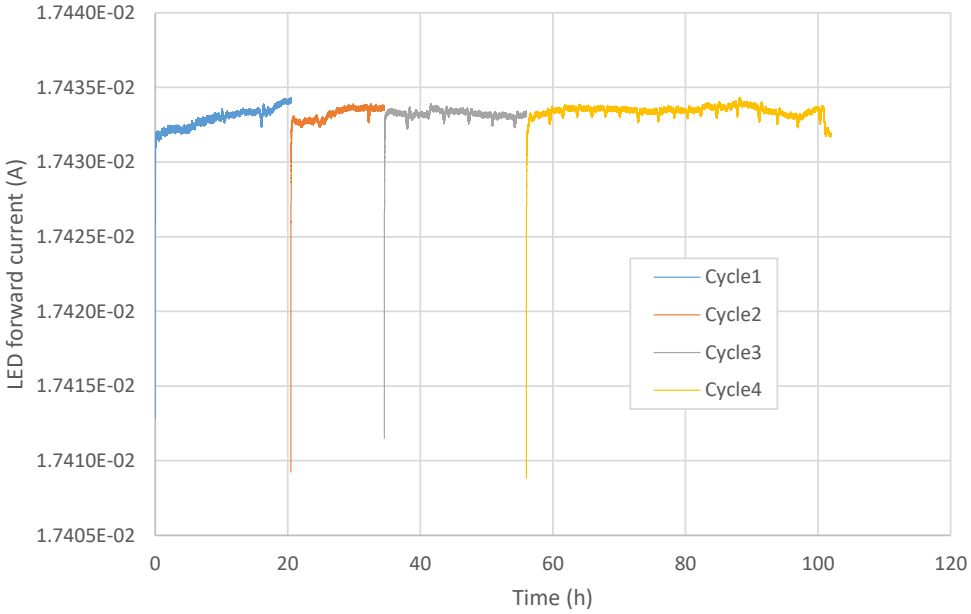

Figure 3.15: LED forward current acquired during four separate test cycles.

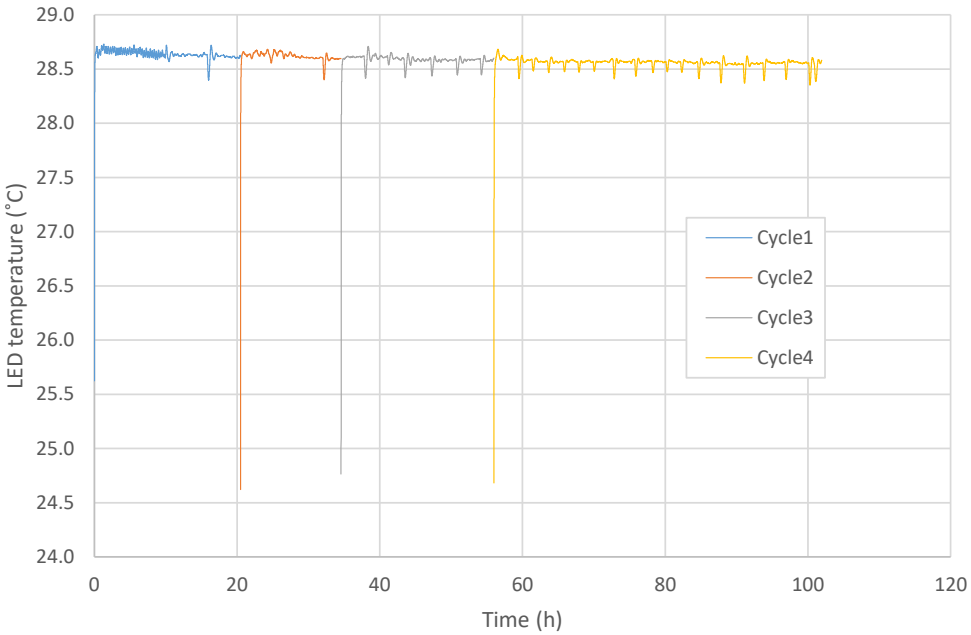

Figure 3.16: LED temperature measured in four separate test cycles.

Data acquired in the fourth cycle was selected for additional analysis as the most extensive data set from the all four test cycles. In order to smooth the time-series, the moving average technique was used, where each successive

data point was calculated as the average of the previous two hundred and the following two hundred data points. The value of two hundred was chosen by inspection, ensuring that faster effects were not being hidden. Furthermore, the positive and negative peaks were removed, leaving gaps in the data sets. The LED optical power, LED forward current and LED temperature plots before and after processing are shown, respectively, in Figures 3.17, 3.18 and 3.19.

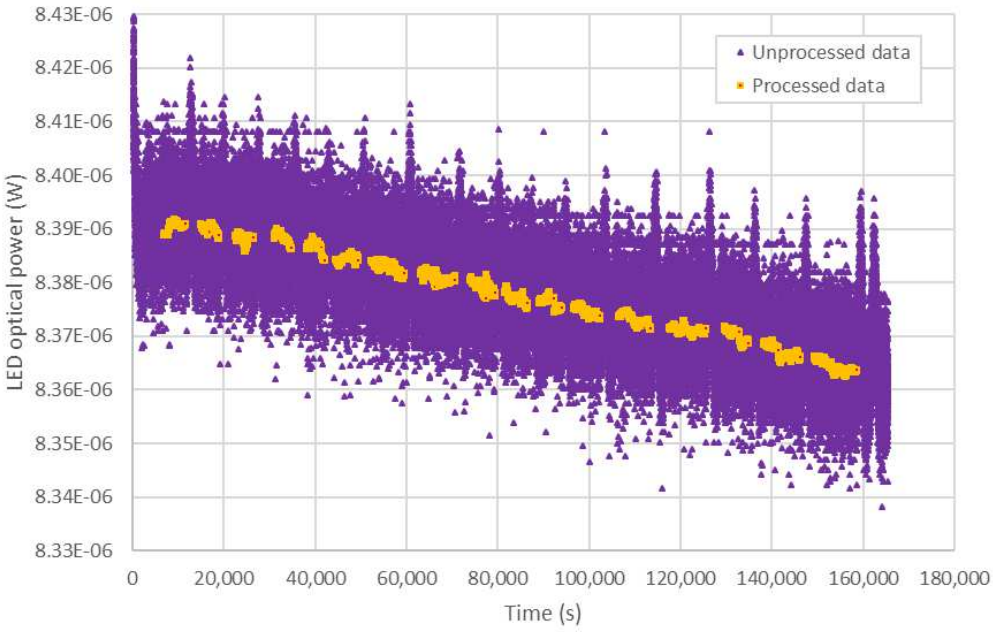

Figure 3.17: LED optical power measured in the fourth test cycle, before and after data processing.

The previously processed LED optical power, LED forward current and LED temperature time-series were normalised and plotted on a single graph, as shown in Figure 3.20. There is no visible and obvious correlation or anti-correlation between LED output optical power and LED forward current or temperature. In order to further investigate these relationships, the variables were plotted against each other.

Figure 3.21 shows the LED optical power plotted as a function of the LED temperature. As already mentioned, both data sets were initially smoothed and had their peaks removed. In addition, the time variable was also elim-

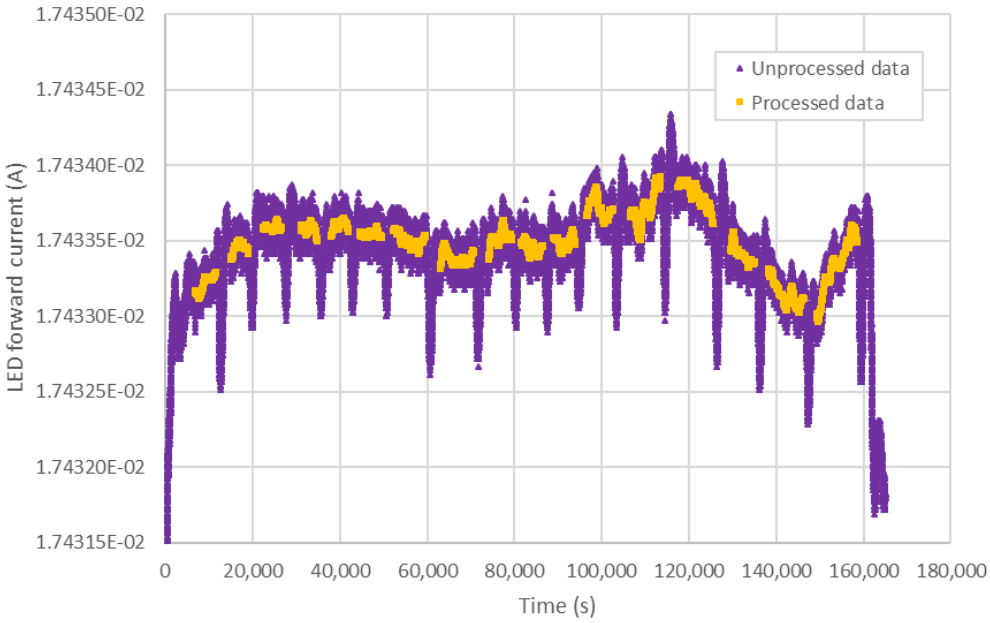

Figure 3.18: LED forward current measured in the fourth test cycle, before and after data processing.

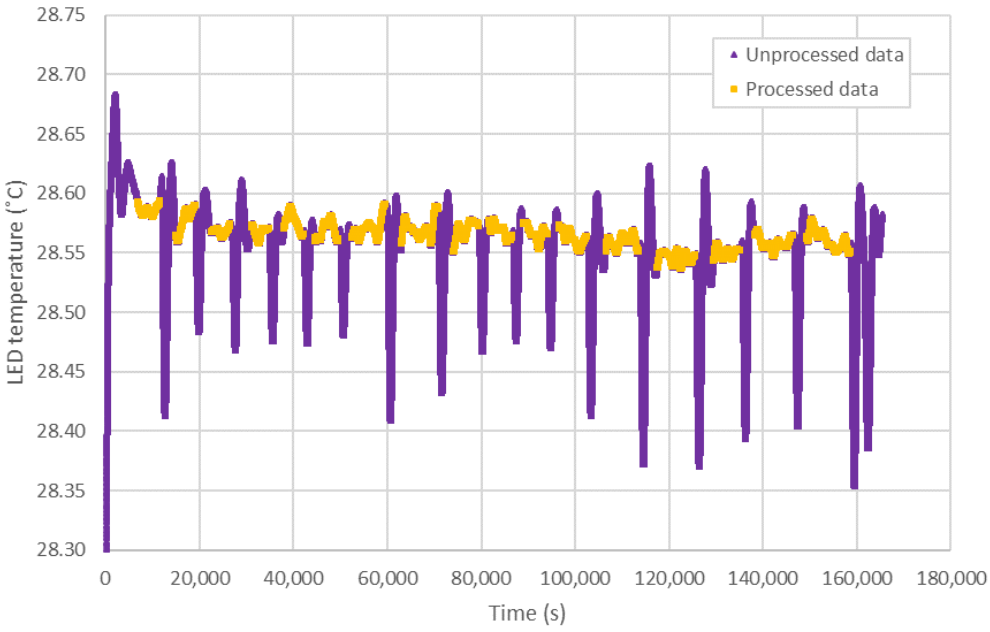

Figure 3.19: LED temperature measured in the fourth test cycle, before and after data processing.

inated from both time-series prior to plotting. The temperature stability is greatly improved when compared to Figure 3.7 (a temperature range of 0.04 °C

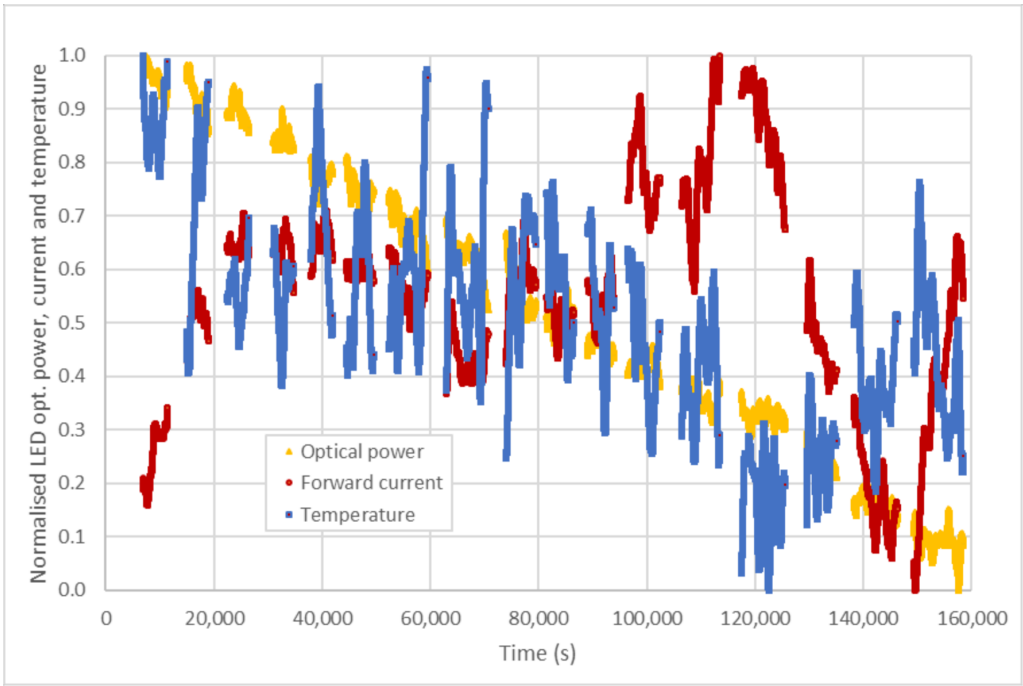

Figure 3.20: Normalised LED optical power, LED forward current and LED temperature. The time-series were initially smoothed and the peaks were removed.

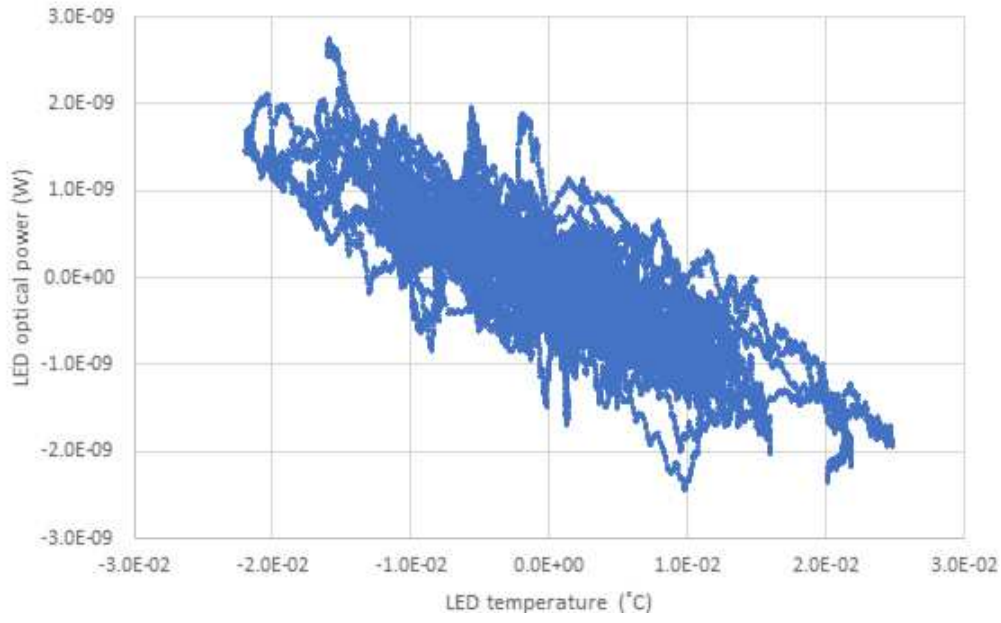

Figure 3.21: LED optical power as a function of LED temperature. The time variable was removed from both data sets before plotting.

compared with 4 °C). The improvements in the temperature and LED drive circuit resulted in an optical power stability of $\sim 3 \times 10^{-4}$. The slope is ap-

proximately -8×10^{-8} W/°C (-0.0087/°C as a fractional change), similar to the one shown previously in Figure 3.7.

The LED output optical power is plotted in Figure 3.22 as a function of LED forward current. The smoothed time-series with peaks removed were used. Furthermore, the optical power data set had its time and temperature variables removed.

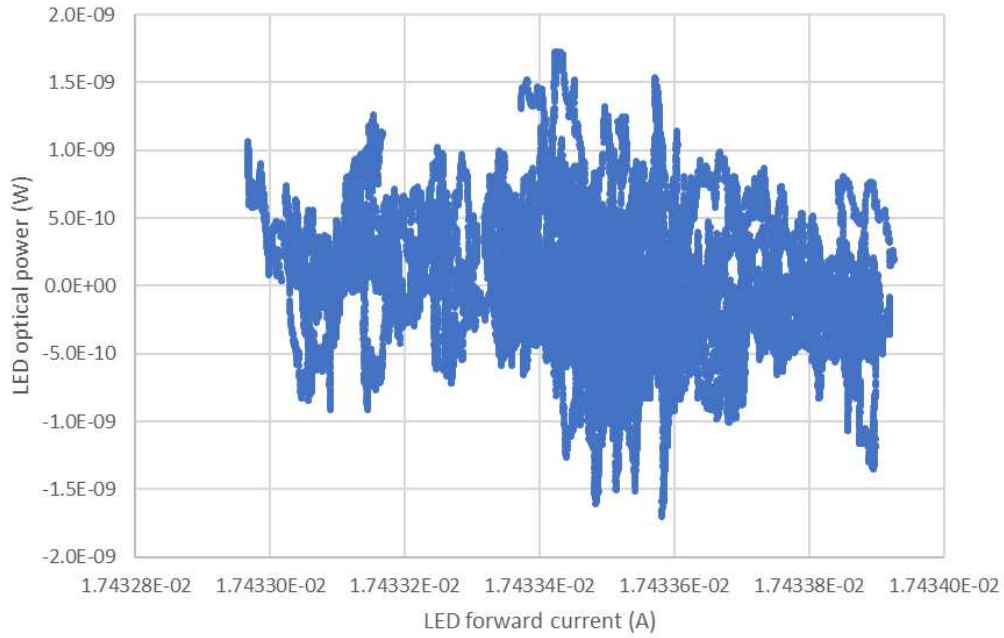

Figure 3.22: LED optical power as a function of LED forward current. The optical power data set had the time and temperature variables removed prior to plotting.

3.3 Conclusions

The chapter presents a study of LED illumination stability and their applicability to the study of highly stable CCD cameras. The main conclusions of the study are given below. Two key effects were investigated, ageing and temperature sensitivity.

- Ageing: a reduction in LED output of ∼0.01 %/h was observed when the LED was powered. While unpowered no ageing was observed (see

Figure 3.10).

- Temperature sensitivity: the LED output as a function of temperature showed a complex behaviour. At times a simple relationship can be seen in which the optical power decreased with increasing temperature by approximately $-0.0087/^{\circ}\mathrm{C}$ (see Table 3.1 and Figure 3.21). However, it was observed that there is present another effect that can be seen in Figure 3.7. This indicates times when the optical power switches between discrete levels. Moreover, these times seem to occur when the temperature change reverses sense, which suggests hysteresis (the points in Figure 3.7 are connected in time sequence). However the results in Figure 3.21 show much improved optical flux stability requiring a further factor of three improvement to reach the stability needed to simulate an Earth-like transit.

- A weak correlation was found between LED output and LED forward current: $\sim 0.07/\mathrm{mA}$ (see Figure 3.22).

The features described above mean that the improved setup from Figure 3.13 cannot yet reliably achieve a stability of $\sim 0.01\,\%$ to simulate an Earth-like transit, but requires a relatively small further improvement. The next section describes future work that would address these issues.

3.4 Future Work

A future planetary transit simulator will require a highly stable optical system. Stability of alignment and source brightness are necessary. For the source brightness a stabilised LED is an option, however the apparent step changes seen in this work would need to be better understood and the contribution from the photodiode, if present, removed in order to achieve a stability of $\sim 0.01\,\%$ required to simulate an Earth-like transit. The following steps are recommended:

- Construct a test apparatus that can separate the effects of the LED and photodiode, e.g. by using two LEDs, individual shutters, and a beam combiner using a half silvered mirror.

- Examine alternative means of achieving $\sim$0.01 % brightness reduction, such as two separate LEDs or the use of a movable neutral density filter.

- Consider alternatives to a photodiode, e.g. a photomultiplier tube.

Chapter 4

Electromagnetic Compatibility Testing of Space Equipment

An area of interest for PLATO, from the point of view of stability, is the effects of ElectroMagnetic Interference (EMI). The theory/principles of EMI performance and testing are outlined in this chapter, while results of conducted EMC tests are given in Chapter 5.

4.1 Electromagnetic Interference

EMI can be described as an unwanted electromagnetic disturbance (noise) that interferes with susceptible electronic equipment. To exist, it requires a source of energy, a coupling path for transferring the noise and a victim circuit (receiver). Depending on whether the interference is caused by another device within the same system or is generated externally, it can be categorised as either intra-system or inter-system EMI. The noise can be coupled from the source to the receiver in various ways, as shown in Figure 4.1.

Inductive (magnetic field) coupling occurs when a time-varying current in one conductor (source) induces a voltage change across the other adjacent conductor (receiver). Analogically, capacitive (electric field) coupling takes place when a time-varying voltage in one conductor (source) induces a voltage change on the other nearby conductor (receiver). These two coupling

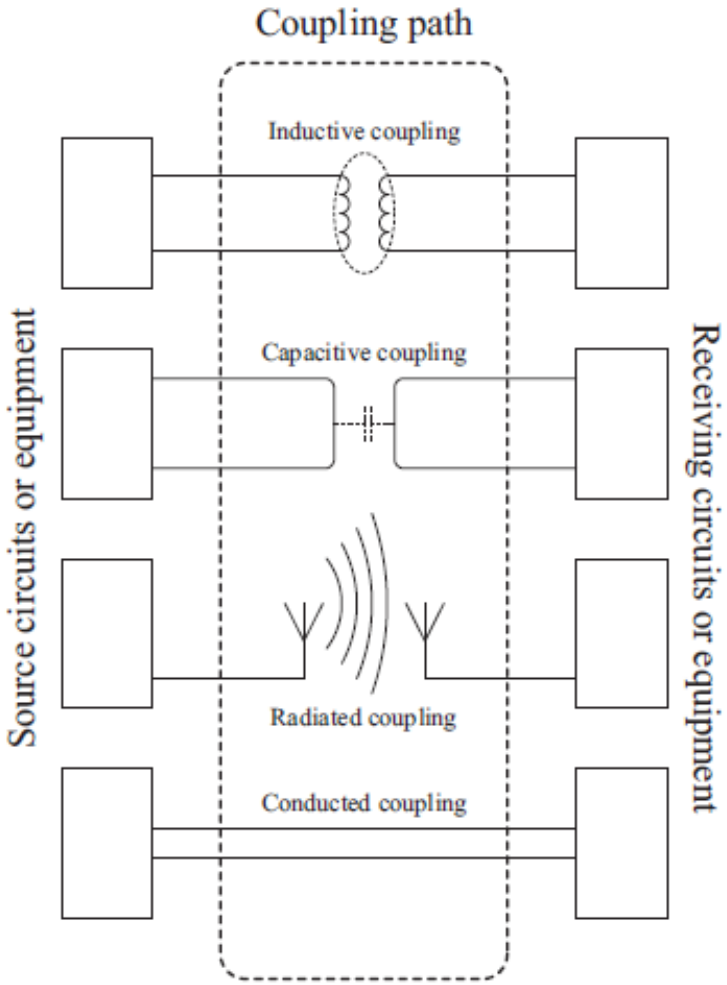

Figure 4.1: EMI coupling mechanisms (from André and Wyatt (2014)).

mechanisms typically occur within the same system (device) and can be reduced by increasing a physical distance between the two coupled structures (André and Wyatt, 2014).

Radiated (electromagnetic) coupling takes place when the transmitter (source) emits an interference waveform which then propagates through space and is picked up by the receiver. The source is often external to the system and can be situated many wavelengths away from the receptor. Such a coupling mechanism can be diminished through filtering out the interference currents (usually in the Radio Frequency (RF) band), before they reach the victim circuit (system), by shielding the receiver and through reducing its geometrical dimensions (i.e. limiting the antenna effect).

Conducted coupling may occur when there is a common current path between the source and the receiving circuit. It can be classified by the way it appears on both conductors, as either Common Mode (CM) coupling or Differential Mode (DM) coupling. In the first instance (CM), current of equal

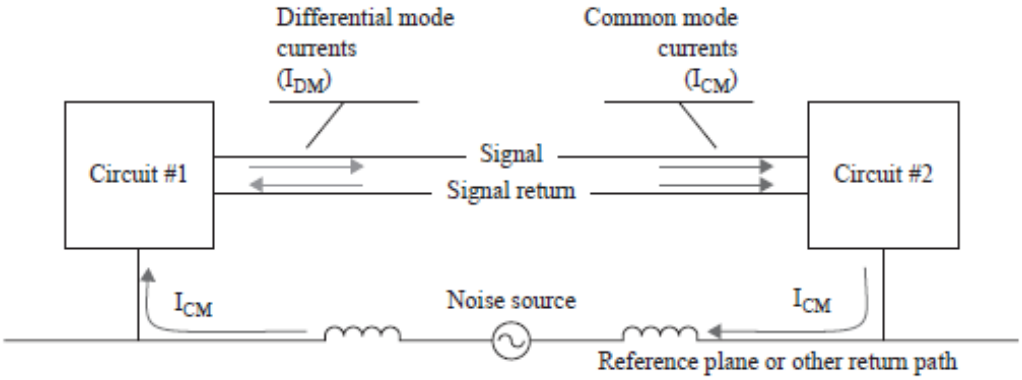

Figure 4.2: Conceptual view of CM and DM currents (from André and Wyatt (2014)).

phase and magnitude flows in the same direction on both conductors (e.g. signal and signal return wires) and returns through an additional ground conductor, such as e.g. an earth plane (see Figure 4.2). In the second case (DM), an equal phase and magnitude interference signal is conducted on both lines in the opposite direction to each other (Paul, 1989). Generally, the conductive coupling can be limited by using appropriate filters and decoupling capacitors.

4.2 Electromagnetic Compatibility

EMC is a discipline concerned with analysing, fixing and preventing EMI issues. For a system to be electromagnetically compatible, it must not cause interference with other systems and/or itself, and at the same time it must not be susceptible to emissions from other systems (Paul, 2006). Figure 4.3 illustrates four aspects of EMC problems, which lead directly to the four common EMC tests:

- Conducted Emissions (CE),
- Conducted Susceptibility (CS),
- Radiated Emissions (RE),
- Radiated Susceptibility (RS).

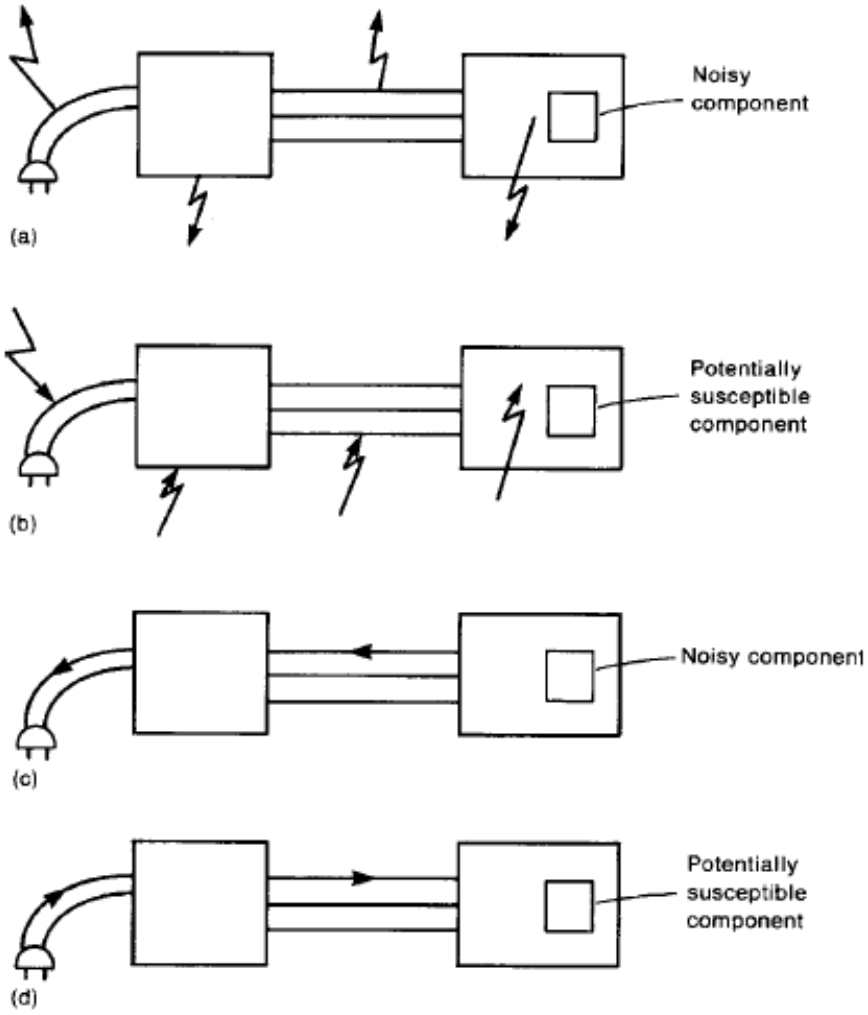

Figure 4.3: Fundamental EMC issues: (a) radiated emissions; (b) radiated susceptibility; (c) conducted emissions; (d) conducted susceptibility (from Paul (2006)).

Procedures for EMC testing are defined by a number of standards that depend primarily on the field of application. In the case of the space environment, the applicable standards are very similar to the military ones, such as

e.g. MIL-STD-461G (2015) or MIL-STD-462D (1993). The test methods are generally the same, the differences are mainly in the test limits, specific test parameters' values (e.g. frequency range) or in instrumentation (Tsatalas, 2018). The most popular standards for space applications are: ECSS-E-ST-20-07C Rev.1 (2012), SMC-S-008 (2008), AIAA (2017) and MIL-STD-464C (2010).

4.2.1 Conducted Emissions Test

The purpose of the CE test is to measure the level of noise that is unintentionally generated by the Equipment Under Test (EUT) and coupled to its input power or signal lines. Figures 4.4 and 4.5 show block diagrams of the typical setups used for CE tests (in DM and CM configuration respectively). The noise is measured with a current probe connected to either an individ-

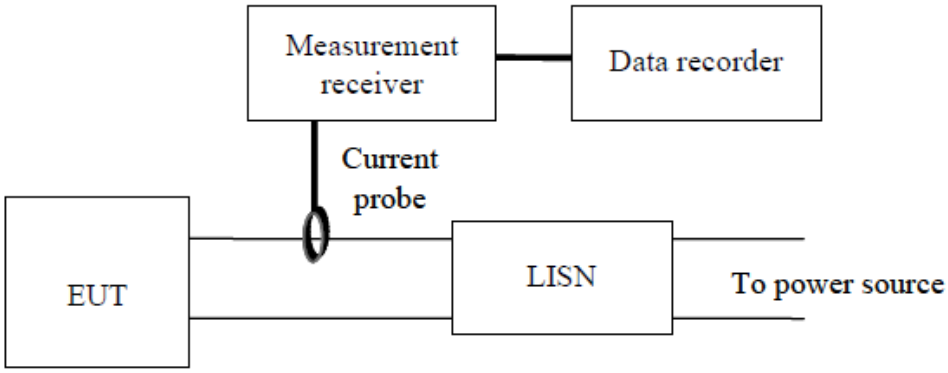

Figure 4.4: Test setup for measuring CE differential mode interference currents (from ECSS-E-ST-20-07C Rev.1 (2012)).

ual signal/power line or both signal and signal return lines at the same time, depending on the measured current mode. The Line Impedance Stabilisation Network (LISN) (shown in Figure 4.6) should be used in all conducted tests (both CE and CS). Its role is to make the impedance seen by the EUT independent of the facility/Electrical Ground Support Equipment (EGSE) power supply impedance, to reproduce the power line impedance of the actual installation, to maintain constant conditions between the tests (e.g. when testing

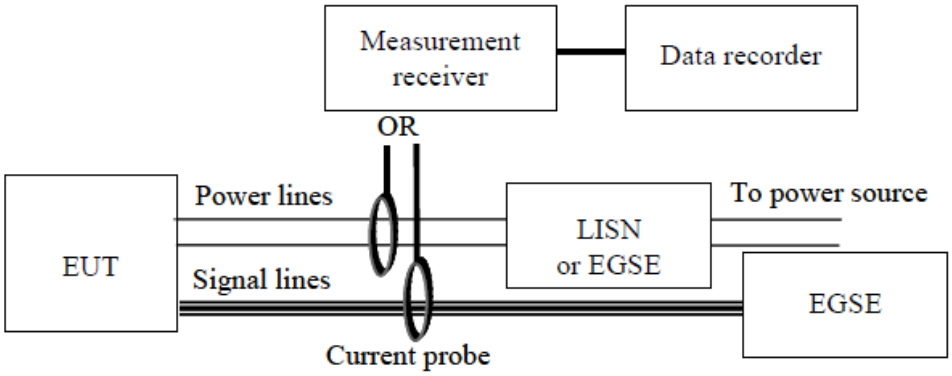

Figure 4.5: Test setup for measuring CE common mode interference currents (from ECSS-E-ST-20-07C Rev.1 (2012)).

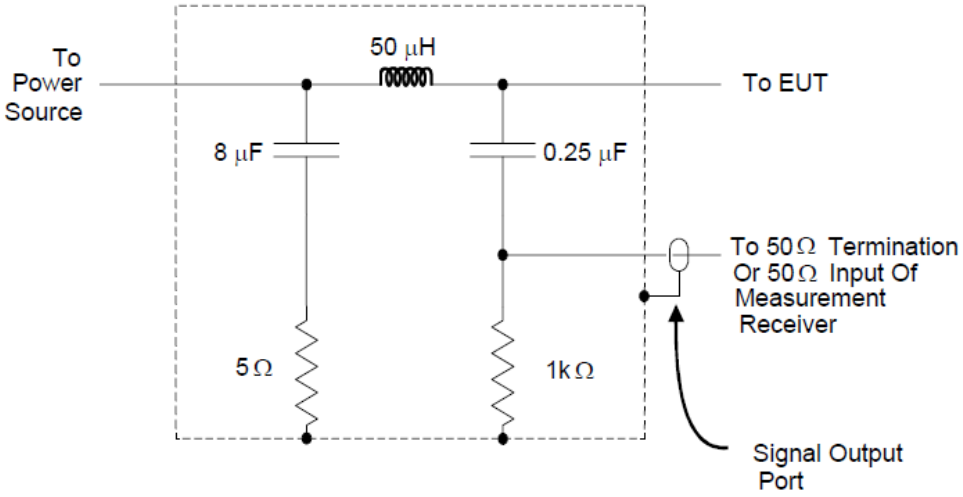

Figure 4.6: LISN block diagram (from MIL-STD-461G (2015)).

various equipment belonging to the same spacecraft) and to decouple the CE and CS signals from the facility/EGSE power supply (Trougnou, 2012). Typical CE levels are shown in Figure 4.7.

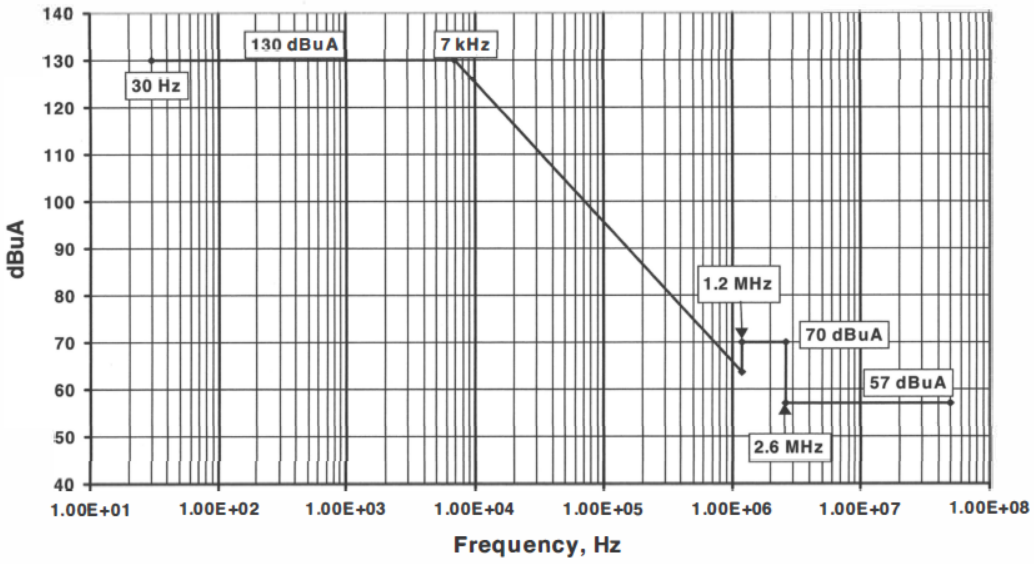

Figure 4.7: Typical CE levels (from Mallette and Adams (2011)).

4.2.2 Conducted Susceptibility Test

The purpose of the CS test is to evaluate susceptibility of the EUT to the interference signal injected onto its input power/data lines. The measurement setup block diagram is shown in Figure 4.8. The calibrated high frequency sine

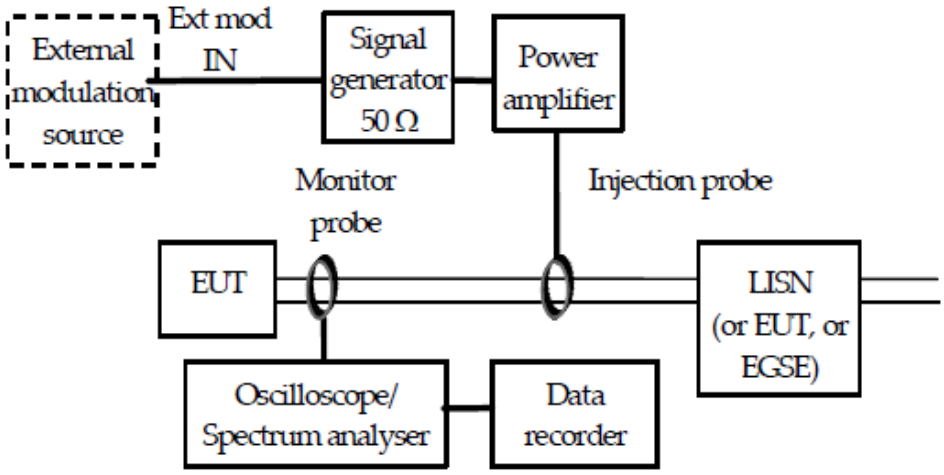

Figure 4.8: Block diagram of the CS test setup (from ECSS-E-ST-20-07C Rev.1 (2012)).

wave is injected with the aid of the Injection Current Probe (ICP), while the performance of the EUT is monitored. In the case of improper operation of the

tested system, the injected noise amplitude is reduced until an acceptable level is found (through trial and error). The whole process is repeated for different noise frequencies, over the range specified by the adopted EMC standard.

A typical outcome of a CS measurement is shown in Figure 4.9.

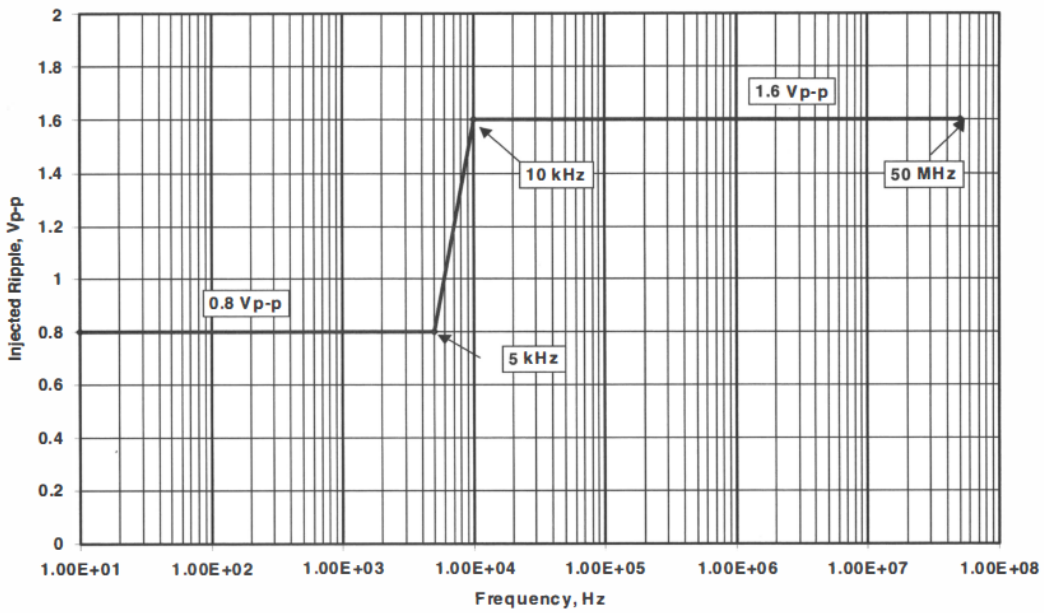

Figure 4.9: Typical CS levels (from Mallette and Adams (2011)).

4.2.3 Radiated Emissions Test

The RE test is a measure of interference signals (in the form of electromagnetic waveforms) generated and radiated by the EUT. Such noise may arise from various digital signals (e.g. system clocks, timing signals etc.), or even from the combination of their harmonics. The main purpose of the RE test is to make sure that the emitted interference does not exceed the allowed limits, in order to protect all the devices sensitive to radiated fields. This can be achieved through measurements using special calibrated antennas (electric field RE) or receiving loops (magnetic field RE), as shown in the block diagrams in Figures 4.10 and 4.11.

RE tests are often conducted inside a Semi-Anechoic Chamber (SAC) (see Figure 4.12). The SAC is a room, in which the ceiling and walls are lined

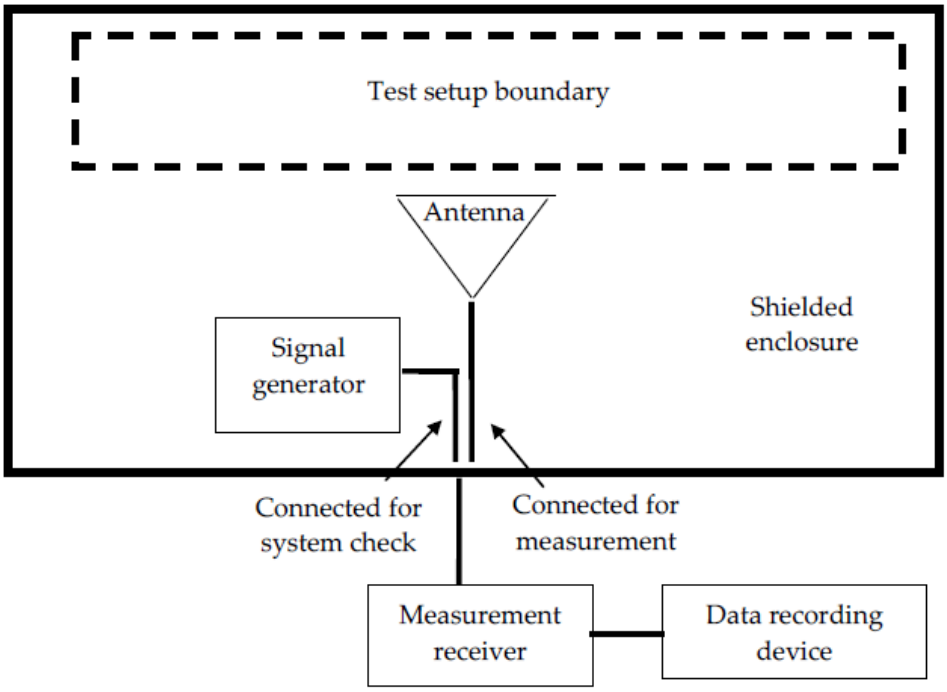

Figure 4.10: Block diagram of the setup for electric field RE measurements (from ECSS-E-ST-20-07C Rev.1 (2012)).

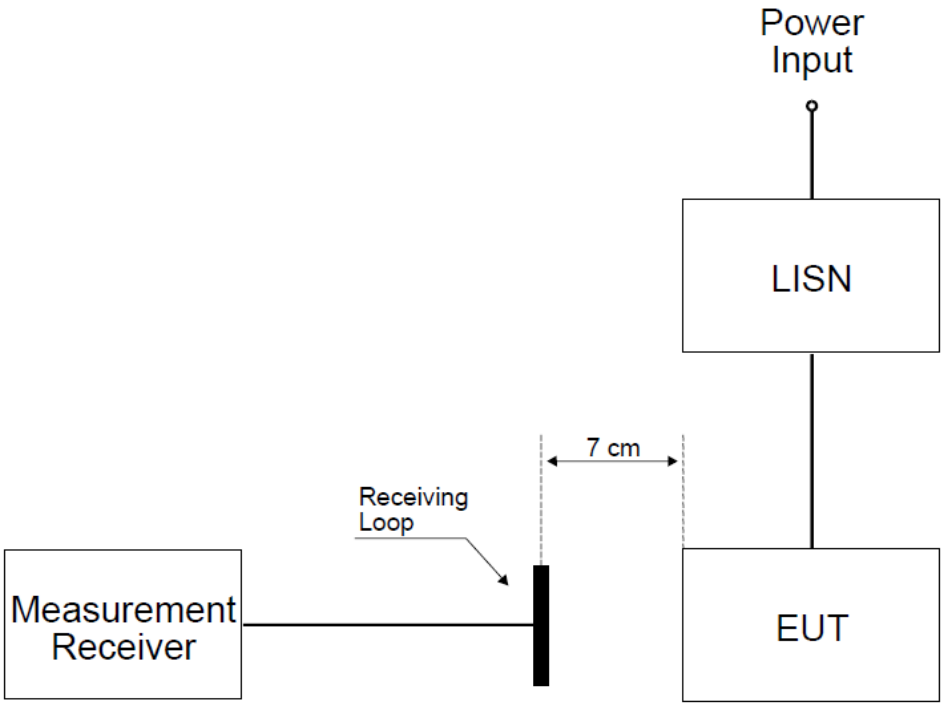

Figure 4.11: Block diagram of the setup for magnetic field RE measurements (from MIL-STD-461G (2015)).

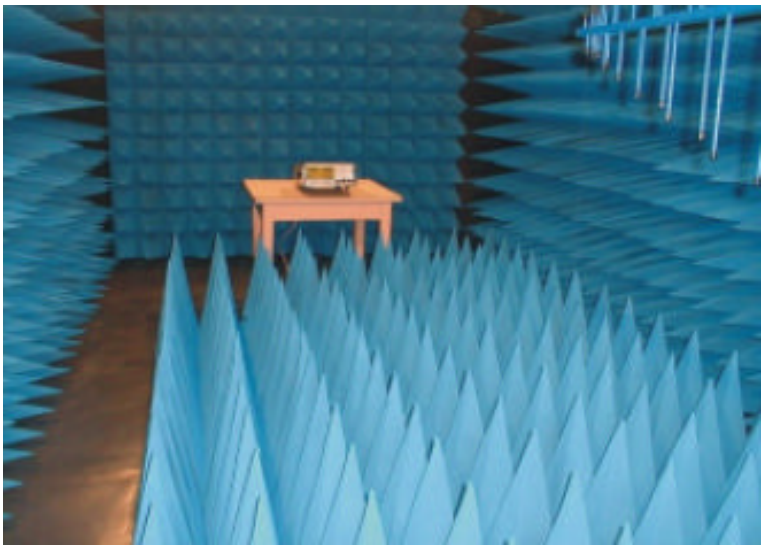

Figure 4.12: View in the semi-anechoic chamber (from Marinescu et al. (2006)).

with a special RF absorber material. The purpose of such a test environment is to simulate free space, prevent reflections and isolate its interior from a potential external interference. The typical RE levels are shown in Figure 4.13.

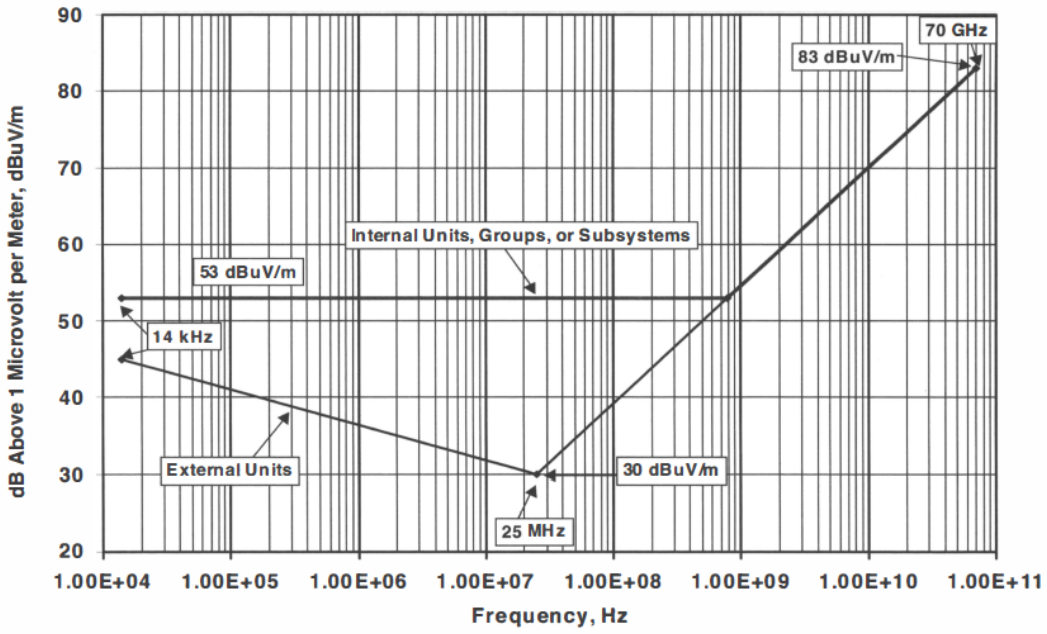

Figure 4.13: Typical RE levels (from Mallette and Adams (2011)).

4.2.4 Radiated Susceptibility Test

The purpose of the RS test is to evaluate the effect of the radiated electric and magnetic fields on the EUT, which shall not exhibit any malfunction or degradation of performance when exposed to interference not exceeding tolerances indicated in the test specification. Figures 4.14 and 4.15 show the basic test setups used for the magnetic and electric field RS measurements.

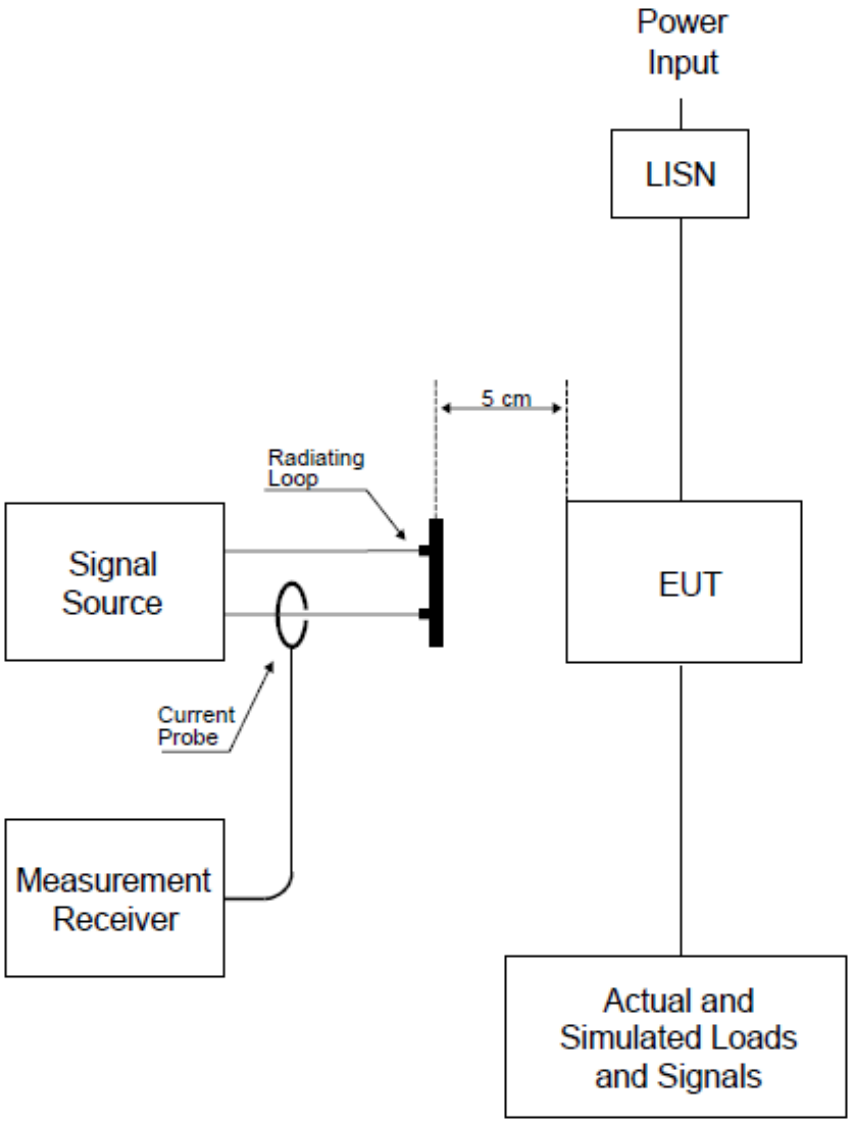

Figure 4.14: Block diagram of the setup used for magnetic field RS measurements (from MIL-STD-461G (2015)).

As in the case of RE tests, the RS measurements are often conducted

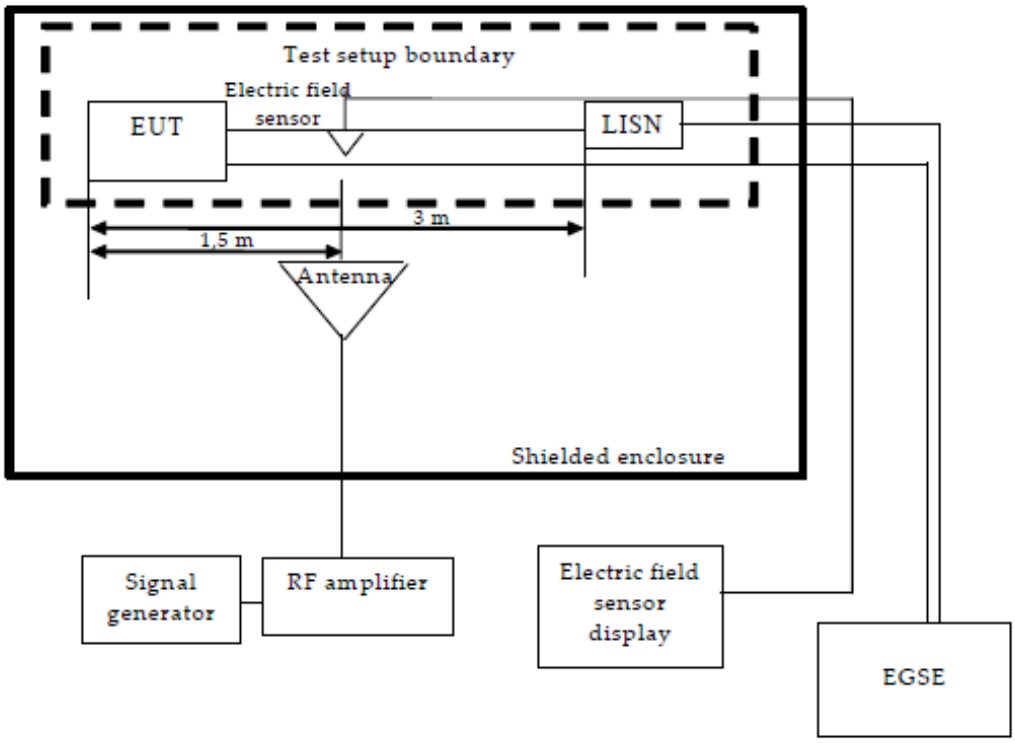

Figure 4.15: Block diagram of the setup used for electric field RS measurements (from ECSS-E-ST-20-07C Rev.1 (2012)).

inside the SAC, to isolate the setup from any external interference and prevent reflections. Typical electric field RS levels and frequency ranges are shown in Table 4.1.

Frequency range	E-field intensity at EUT
20 kHz to 50 MHz	10 V/m
50 MHz to 10 GHz	5 V/m
10 GHz to 70 GHz	5 V/m

Table 4.1: Typical electric field RS levels and frequency ranges (adopted from Mallette and Adams, 2011).

4.3 PLATO Electromagnetic Compatibility Requirements

EMC performance requirements for the PLATO payload are specified in ESA-PLATO-ESTEC-MIS-SP-002 (2014). Selected requirements are cited in the sections below.

4.3.1 Conducted Emissions on Primary Power Leads

CE should be measured over the range 30 Hz to 50 MHz for the DM and 100 kHz to 50 MHz for CM measurements. CE limits are shown in Figures 4.16 and 4.17 (for DM and CM respectively).

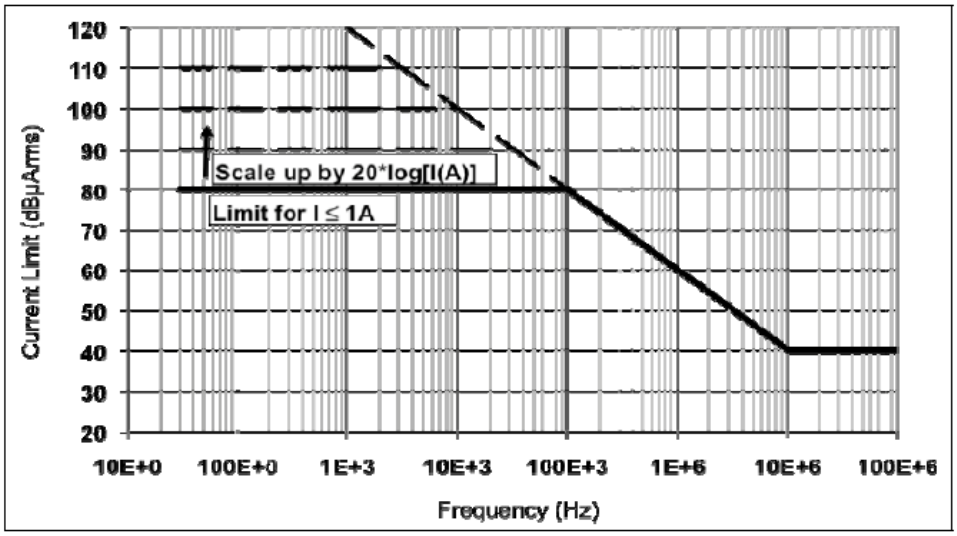

Figure 4.16: CE limits for DM measurements (ESA-PLATO-ESTEC-MIS-SP-002 (2014)).

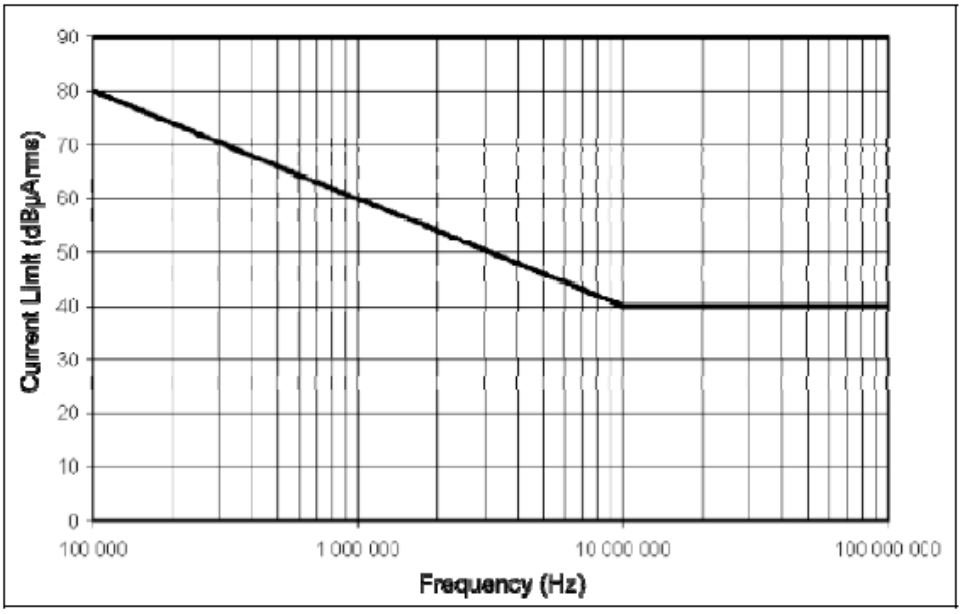

Figure 4.17: CE limits for CM measurements (ESA-PLATO-ESTEC-MIS-SP-002 (2014)).

4.3.2 Conducted Susceptibility on Power Leads

The unit equipment shall not exhibit any performance degradation when subjected to 1 Vrms DM or CM injection (1 kHz 50 % square wave modulated) over the frequency range 50 kHz to 50 MHz.

The N-FEE has got its own set of CS requirements specified in PLATO-OHB-PL-RS-005 (2017). According to requirement PLT-N-FEE-1015, the design of the N-FEE shall ensure its specified performance when exposed to DM noise and ripple with peak-to-peak amplitudes as shown in Table 4.2 over the range 10 Hz to 50 MHz.

Supply line	DM noise and ripple (pk-pk)
VCCD	20 mV
VCLK	20 mV
VAN1	20 mV
VAN2	20 mV
VAN3	20 mV
VDIG	20 mV

Table 4.2: CS differential mode noise and ripple.

Requirement PLT-N-FEE-1040 in the same document states that the N-FEE shall preserve its specified performance when subjected to CM sinusoidal interference with the following parameters:

- Injected current: 20 mArms,
- Frequency range: 50 kHz to 50 MHz,
- Modulation: 1 kHz pulse repetition rate, 50 % duty cycle.

4.3.3 Electric Field Radiated Emissions

The equipment units shall fulfil requirement limits for the electric field RE as shown in Figure 4.18, for the frequency range 30 MHz to 18 GHz.

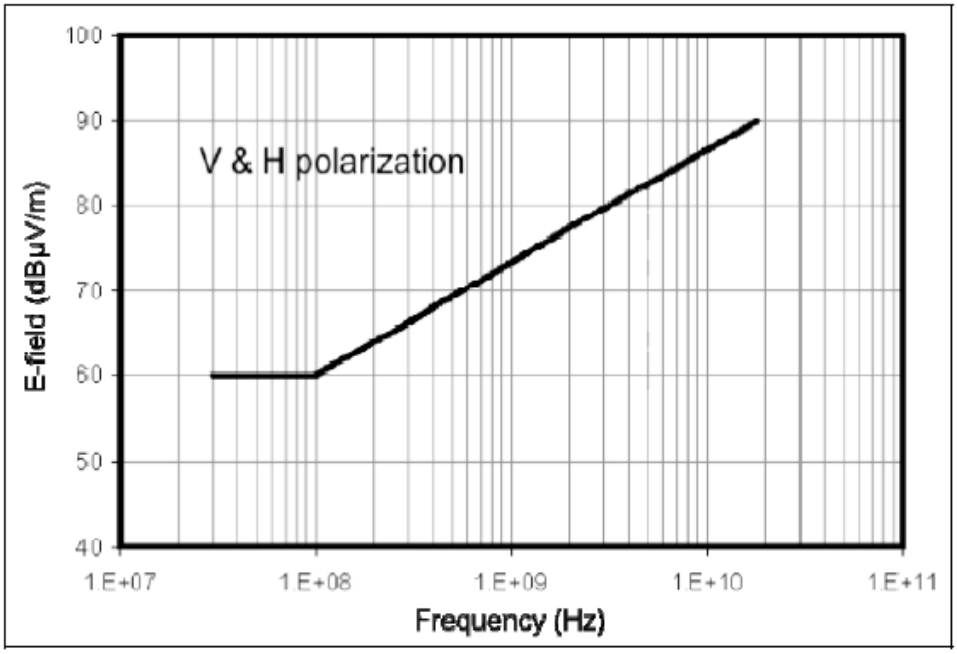

Figure 4.18: Electric field RE requirements (from ESA-PLATO-ESTEC-MIS-SP-002 (2014)).

4.3.4 Electric Field Radiated Susceptibility

The equipment units shall not exhibit any performance degradation when exposed to electromagnetic radiation in the frequency range 30 MHz to 18 GHz

in both vertical and horizontal polarizations, 1 kHz square wave modulated with 50 % duty cycle and with the following intensity:

- 2 V/m inside the spacecraft body,
- 10 V/m outside the spacecraft body.

4.4 Summary

This chapter has covered the principles of EMI performance and testing. In the next chapter these principles are put into practice in the form of EMC testing of the PLATO breadboard N-FEE.

Chapter 5

Conducted Susceptibility of PLATO Normal-Front-End Electronics

The aim of the following study was to test the susceptibility of the PLATO N-FEE to CM and DM interference signals superimposed on its power lines, over the specified frequency range. For this purpose, a series of tests was conducted for both CM and DM modes, each investigating the camera's output image sensitivity to a different frequency interference signal superimposed, respectively, on each of the individual supply lines. Results were checked against the output of a simulation that modelled the behaviour of the Correlated Double Sampling (CDS) circuit and attached low-pass filters, as well as against the outcomes of an additional test, in which a sinusoidal interference signal was injected directly into the CDS circuit's input. A full simulation of the N-FEE which took into consideration the EMC coupling between individual printed circuit board lands and components is a very considerable task and beyond the scope of this work. Rather, the simulation focusses on the CDS circuit, the heart of the measurement approach and where EMC related image artefacts will be generated.

5.1 Correlated Double Sampling Circuit and Filters Simulation

5.1.1 Correlated Double Sampling Principles

CDS is a noise reduction technique used, inter alia, in imaging cameras to eliminate kTC reset noise from the charge-sensing capacitor node (traditionally the term 'kTC noise' is associated with thermal noise on capacitors) and to restrain 1/f and white noises from the CCD output amplifier. In principle, the CDS circuit samples the CCD output waveform at reset (reference) and signal (data) levels and outputs the difference between them on a per-pixel basis. This means that any noise source that is correlated to the two samples within a single pixel period gets cancelled out. In addition, the amplitude of any uncorrelated low frequency noise will get reduced (Barnes, 1998).
The concept of CDS is illustrated in Figure 5.1.

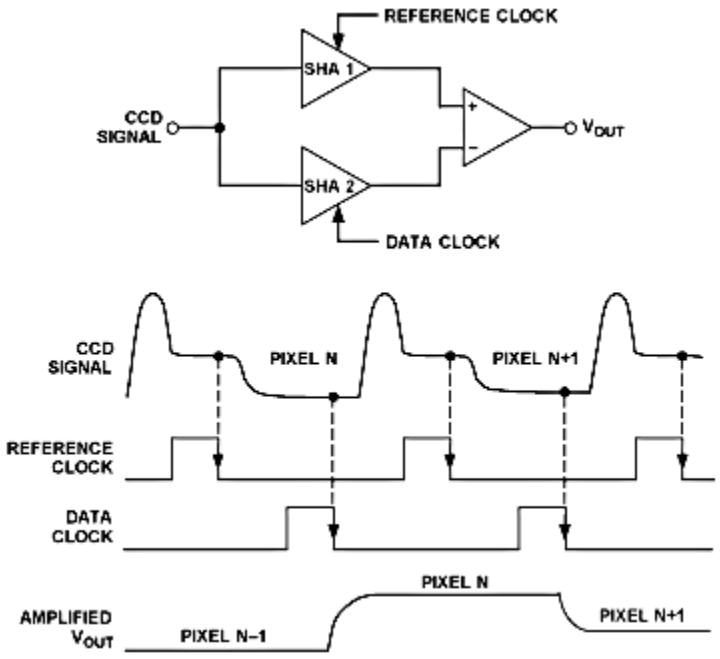

Figure 5.1: Correlated Double Sampling. $SHA1$ and $SHA2$ represent the sample-and-hold amplifiers. The reset voltage level is sampled on the falling edge of the reference clock, while the video voltage level is probed during the falling edge of the data clock (illustration taken from Barnes (1998)).

5.1.2 Low-Pass Filters

Figure 5.2 shows a simple second order low-pass filter.

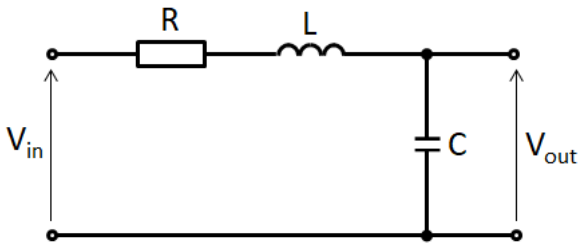

Figure 5.2: Second order low-pass filter.

From the voltage divider rule:

$$V_{out} = V_{in} \times \frac{X_C}{Z}, \tag{5.1}$$

where V_{out} (in V) is the output voltage, V_{in} (in V) is the input voltage, X_C (in Ω) is the capacitive reactance, Z (in Ω) is the circuit's impedance.
The attenuation A of such a filter varies with frequency and is defined as follows:

$$A = \frac{V_{out}}{V_{in}} = \frac{X_C}{\sqrt{R^2 + (X_L - X_C)^2}} = \frac{\frac{1}{2\pi f C}}{\sqrt{R^2 + \left(2\pi f L - \frac{1}{2\pi f C}\right)^2}}, \tag{5.2}$$

where V_{out} (in V) is the output voltage, V_{in} (in V) is the input voltage, X_C (in Ω) is the capacitive reactance, Z (in Ω) is the circuit's impedance, R (in Ω) is the resistance, X_L (in Ω) is the inductive reactance, C (in F) is the capacitance, L (in H) is the inductance, and f (in Hz) is the frequency.

Figure 5.3 illustrates a simplified fragment of the PLATO N-FEE video conditioning circuit, containing three cascaded low-pass filters. Components R_1, L_1 and C_1 form the first, R_2, L_2 and C_2 the second, and R_3, L_3 and C_3 the third low-pass filter. U_1 and U_2 represent CDS driver and CDS buffer ICs respectively. The total attenuation A_{tot} of such a configuration is defined as

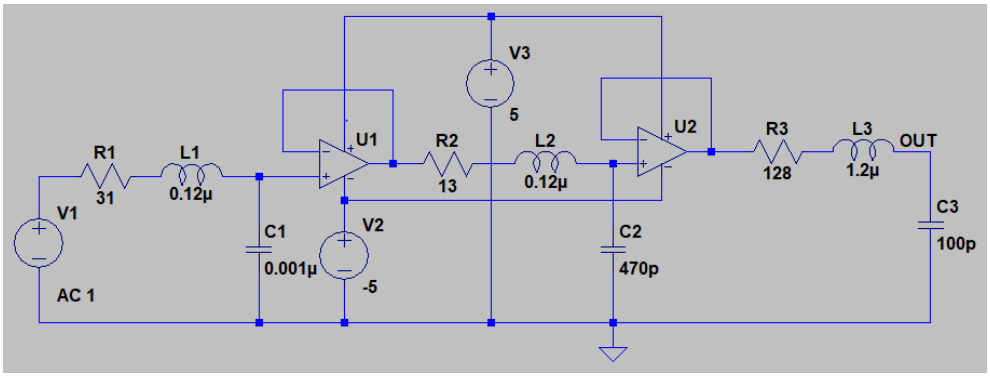

Figure 5.3: Schematic showing three PLATO N-FEE's low-pass filters.

the product of the individual filters' attenuations:

$$A_{tot} = A_1 \times A_2 \times A_3. \tag{5.3}$$

where A_1, A_2 and A_3 are attenuations of filters 1, 2 and 3 respectively.

5.1.3 Simulation Method

The purpose of the simulation was to observe how the sinusoidal interference signal fed into the input of the CDS circuit affects the output image (see Appendix A for the complete Python code). In order to achieve this, it was necessary to find the difference of the interference sinusoidal function values calculated at video and reset sampling times for each consecutive pixel, with an assumed image size of 512 × 512 pixels. The interference frequencies used in the simulation covered the range 50 kHz to 50 MHz in order to comply with the PLATO N-FEE User Requirements Document (see Section 4.3.2) and they were spaced at 50 kHz to deliver a sufficient level of detail. A few additional frequencies were also included in order to better resolve certain specific features (these are the frequencies at predicted minima and maxima).

Figure 5.4 shows the base values for the PLATO normal camera pixel period and the CDS circuit sampling times for both reset and signal levels, that were used in calculations.

Another required parameter, the row transfer time t_{tr} (in ns), was calcu-

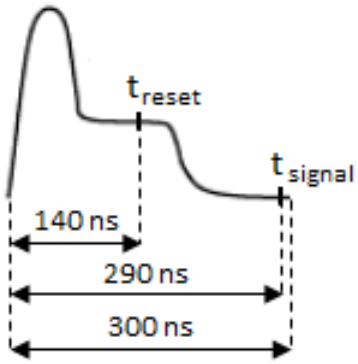

Figure 5.4: Pixel period and CDS timing of the PLATO normal camera.

lated as follows:

$$t_{tr} = t_{int} - N_{pix} \times t_{pix} = 250\,000 - 512 \times 300 = 96\,400, \tag{5.4}$$

where t_{int} (in ns) was the time interval separating two consecutive row starts (measured with oscilloscope), N_{pix} was the number of pixels in a single row, and t_{pix} (in ns) was the single pixel period.

The CDS reset sampling time t_{rst} (in ns) of each consecutive pixel was defined as:

$$t_{rst} = t_{row} + c_n \times t_{pix} + t_{grst}, \tag{5.5}$$

where c_n was the column number, t_{pix} (in ns) was the single pixel period, and t_{grst} (in ns) was the generic CDS reset sampling time (140 ns, as shown in Figure 5.4). The row start time t_{row} (in ns) was calculated as:

$$t_{row} = r_n \times (N_{pix} \times t_{pix} + t_{tr}), \tag{5.6}$$

where r_n was the row number, N_{pix} was the number of pixels in a single row, t_{pix} (in ns) was the single pixel period, and t_{tr} (in ns) was the row transfer time (calculated as per Equation 5.4).

Similarly, the CDS signal sampling time of each successive pixel was specified as:

$$t_{sig} = t_{row} + c_n \times t_{pix} + t_{gsig}, \tag{5.7}$$

where t_{row} was the row start time (in ns), c_n was the column number, t_{pix} (in ns) was the single pixel period, and t_{gsig} (in ns) was the generic CDS signal sampling time (290 ns, as illustrated in Figure 5.4).

Once the reset and signal sampling times of every pixel in the image were accessible, the next step was to work out the state of the interference signal function at those time stamps. To achieve this, it was necessary to calculate the number of whole interference signal periods completed up to respectively the reset and signal sampling times of a given pixel, multiply them by the interference waveform period and subtract the results from the CDS reset and signal sampling times. Subsequently, the difference of the interference function values at the signal and reset sampling times was calculated for each of the 262 141 pixels forming a single 512×512 image array.

In the final step, after the whole image was complete for a given interference frequency, the image standard deviation was calculated.

All the above steps were repeated for each of the pre-selected interference frequencies.

5.1.4 Simulation Results

Results of the CDS simulation are shown in Figure 5.5, where the image standard deviation was plotted as a function of the interference signal frequency. It is symptomatic, that the minima appear at the multiples of $6666.\dot{6}$ kHz. The shape results from the time-domain filtering effect of the CDS circuit.

Figure 5.6 shows the outcome of another simulation, where the CDS output was coupled to the low-pass filters. The characteristic shape of the trace is a form of rectified and attenuated sine-wave, arising from a combination of the three low-pass filters response and the time-domain filtering effect of the CDS circuit. The filters effectively attenuated interference signals with frequencies greater than 20 000 kHz.

It should be noted that the image standard deviation values shown in both Figure 5.5 and 5.6 are for an arbitrary simulated input signal level and can be normalised to match the experimental data. The odd single-point fea-

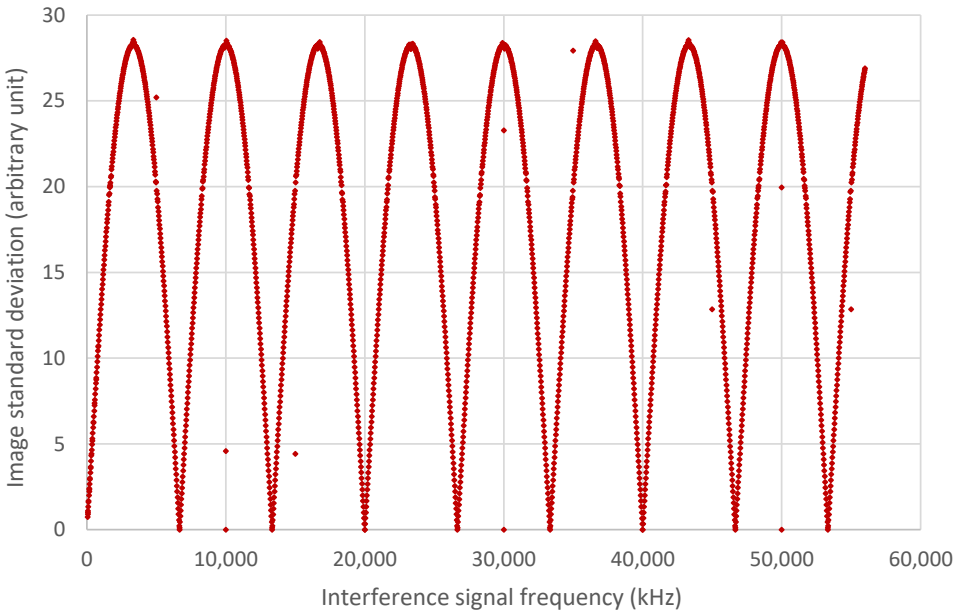

Figure 5.5: CDS circuit simulation output.

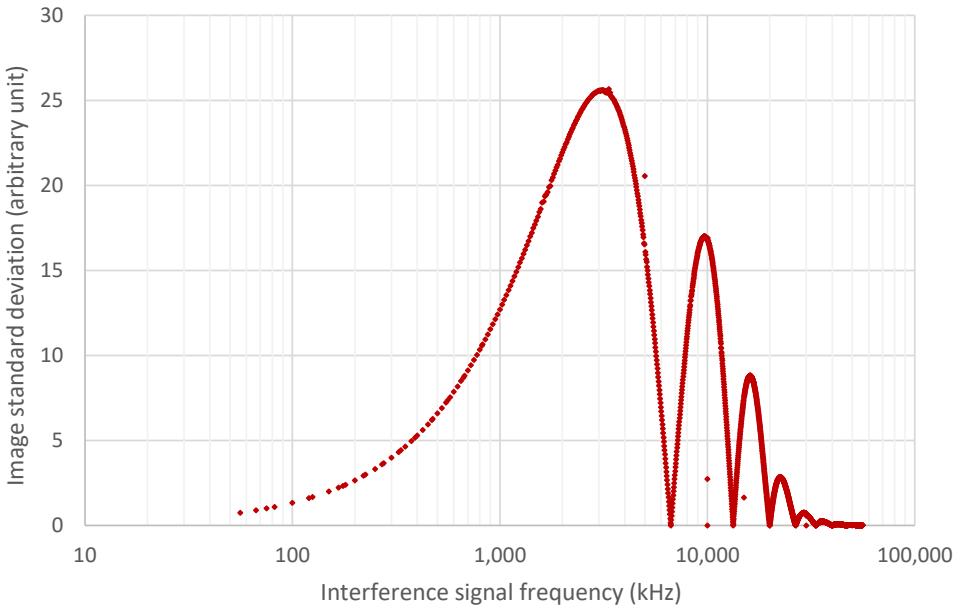

Figure 5.6: CDS circuit simulation outcome after including filters response.

tures/outliers (10 of them) present on both plots are computational artefacts believed to be due to divide-by-zero type effects arising from the combination of time domain and frequency domain calculations and should be ignored.

5.2 Correlated Double Sampling Circuit Direct Injection

The most effective way to compare the results of the CDS circuit simulation with its real-life performance was to inject the interference waveform directly into the CDS circuit's input. Figure 5.7 shows a diagram of the setup used for such a measurement. The signal generator was set to output a 1 Vpk-pk

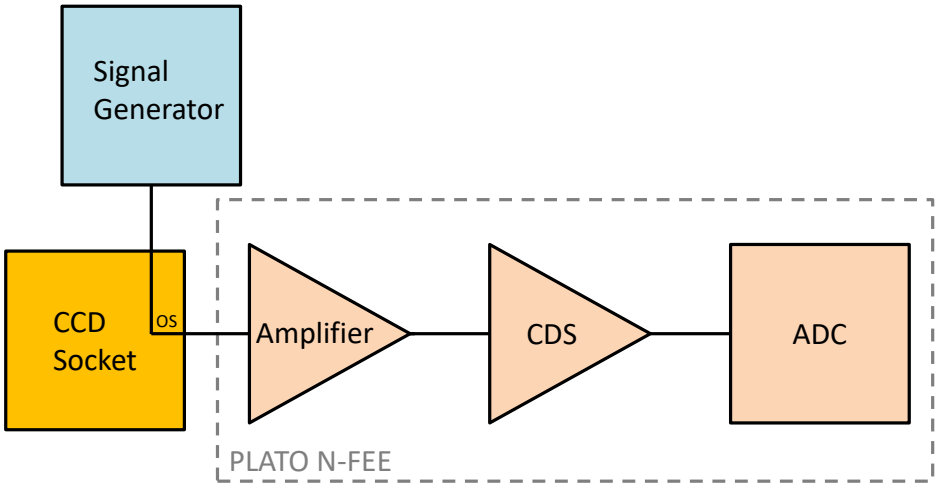

Figure 5.7: Block digram of the setup used for the direct CDS injection test.

sinusoidal waveform (with 1 V offset, to prevent the signal from going negative) that was injected directly into the *OS* pin of the CCD socket (the detector was removed for this test). Just as in the case of the simulation, the injected interference frequencies ranged from 50 kHz to 50 MHz. The resulting plot is shown in Figure 5.8.

A direct comparison between the CDS circuit simulation (including filters) and direct CDS injection test results is shown in Figure 5.9. The rise at higher frequencies is not predicted in the simulation. The predicted fall-off at high frequencies comes about from a low-pass filter. In practice it is likely that EMC routes exist within the N-FEE that bypass this filtering, leading to this slight excess. Similar complicated inductive and capacitive effects in the

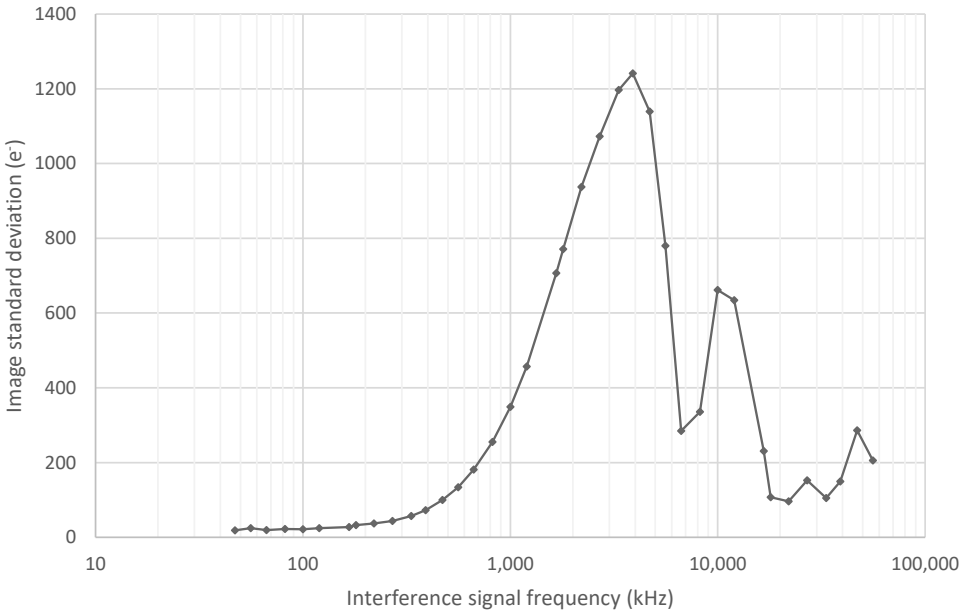

Figure 5.8: The effect of direct interference injection into the CDS circuit.

real electronics compared with the simple model could explain the difference between the model and the measurements at low frequencies. However the overall shape of the response is reasonably well-matched given the necessary simplicity of the model.

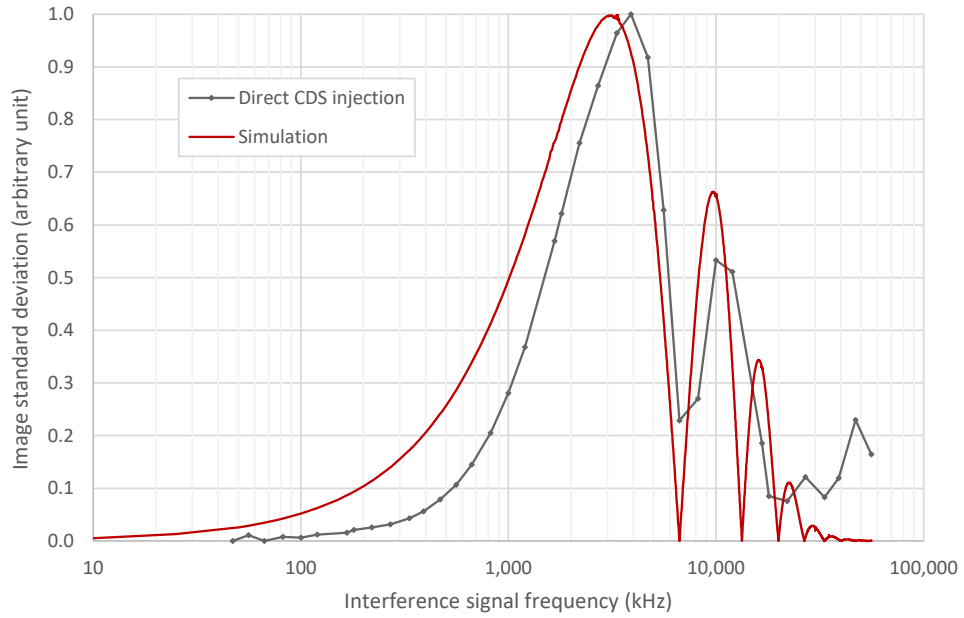

Figure 5.9: Comparison of direct CDS injection and simulation results.

5.3 Conducted Susceptibility Common Mode Measurements

5.3.1 Experimental Setup

The experimental setup block diagram for the CS CM measurements is shown in Figure 5.10. The tested power line is drawn in red and the corresponding power return line is coloured blue.

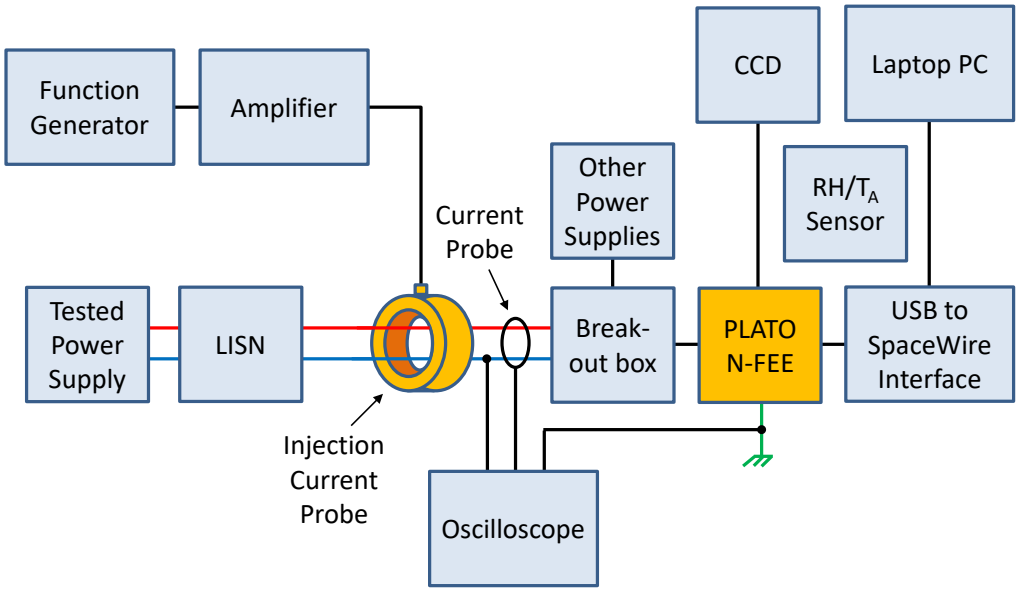

Figure 5.10: Setup block diagram for the CS CM test. The 'Other Power Supplies' block represents six other power supplies.

The setup consists of the following hardware:

- PLATO N-FEE: BB_V1 (MSSL),
- CCD: CCD47-20 (Teledyne e2v),
- Bench DC Power Supplies: QL355TP and PL303QMD-P (TTi),
- LISN: from the Solar Orbiter EGSE (MSSL),
- Breakout Box (MSSL),

- Function Generator: AFG3102 (Tektronix),
- Amplifier: Model 15A250 (Amplifier Research),
- ICP: ICP-621 (A.H. Systems),
- Laptop PC: XPS 15 9530 (Dell),
- USB to SpaceWire Interface: SpaceWire Brick Mk2 (STAR-Dundee),
- Oscilloscope: MDO3024 Mixed Domain Oscilloscope (Tektronix),
- Oscilloscope Current Probe: TCP0020 (Tektronix),
- Relative Humidity/Ambient Temperature Sensor: RH-USB (Omega).

The photograph of setup is shown in Figure 5.11. The test room temperature

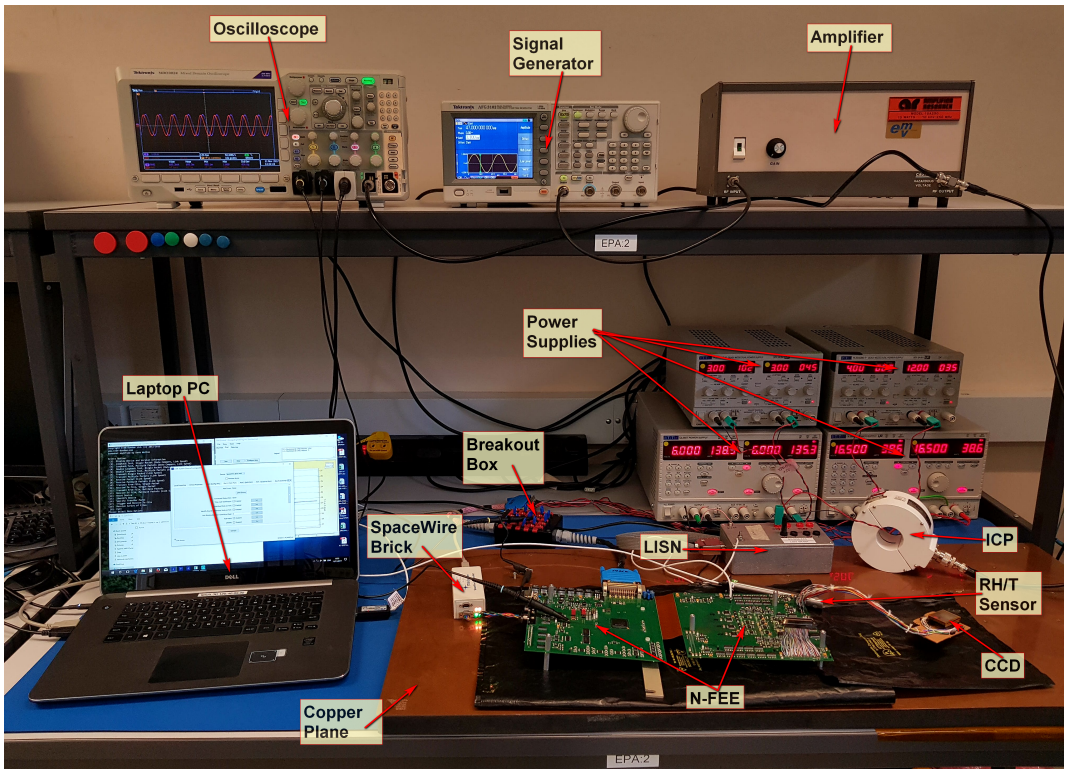

Figure 5.11: A photograph of the CS test setup.

was stabilised by the air-conditioning unit and monitored with the temperature and humidity sensor. There was a single star point common ground connection on the copper plane, joining the N-FEE's analog ground, the LISN's

chassis ground and the earth ground (through one of the bench PSUs). The setup allowed for the injection of sinusoidal interference signals with frequencies ranging from 50 kHz to 50 MHz. For each tested frequency the injected waveform was created by the function generator, amplified by the power amplifier and fed into the supply line under test using the ICP. The interference amplitude was measured with the oscilloscope and adjusted, when needed, from the front panel of the signal generator in order to provide the constant value of 250 mV peak–to–peak (pk–pk). Such an amplitude level was chosen by trial and error, to enable covering the whole required frequency range without experiencing any setup instability issues. Once the interference signal's frequency and amplitude were set, the CCD output data was read and saved into the corresponding binary file for further analysis.

As access to any of the PLATO's CCD270 detectors was not possible, a CCD47-20 device (E2V Technologies, 2011) was used instead. This FT CCD has a 1024×1024 pixel image area and 1024×1033 pixel storage area. Its horizontal shift register is split into separate left and right channels, each leading to its own output amplifier (the output circuits are analogues to the one inside the CCD270 detector, shown previously in Figure 2.6). The sensor was operated with the output registers clocked in a reversed direction, which is known as the reverse clocking mode. In such a configuration the charge is swept away from the output amplifier, allowing for measuring the noise contribution from the CCD array output stage. As the dark current component is eliminated, it is possible to conduct such a test at room temperature.

The readout and acquisition process was manually triggered from the PC that was communicating with the N-FEE through the SpaceWire protocol. Two oscilloscope channels were configured to operate in a subtraction mode, in which the value sampled on one probe connected to the N-FEE chassis ground was subtracted from the value sampled on the other probe attached to the tested power line return terminal on the breakout box. The resulting difference value represented the actual amplitude of the injected interference waveform. An additional oscilloscope probe was used for measuring current

flowing through the tested power line and its return path.

The CS CM measurements were carried out in a few stages, each focused on a single power line. Every supply (see Table 5.1 for the complete list) was tested in accordance with the following acquisition scheme:

- 20 reference frames (no noise injected) prior to the main test,
- 38 frames with injected noise (main test; one frame per injected interference frequency),
- 20 reference frames (no noise injected) post the main test.

The reference frames acquired before and after each main set of measurements (i.e. measurements with the interference signal superimposed on the power line under test) were used for assuring that the system's noise floor was stable throughout the test, as well as for calculating the actual readout noise figure.

Supply name	Input voltage (V)	Regulated output(s) (V)	Purpose
VCCD	+33	+32 and +5	Low-noise CCD biases, DACs and op-amps
VCLK	+12	+10.6 and +10	CCD horizontal and vertical clocks, analogue switches and op-amps
VDIG_SPW	+4	+3.3	SpaceWire driver chips, other general digital logic
VAN3	−6	−5	Analogue video and temperature sensor circuits, op-amps
VAN1	+6	+5 and +3.3	Analogue video and temperature sensor circuits, CCD-selection switches, op-amps and ADCs
VDIG_FPGA	+3	+2.5 and +1.5	FPGA
VAN2	+3	+2.5	Analogue video circuit and ADCs

Table 5.1: PLATO N-FEE power supply lines.

In order to provide a sufficient number of pixels per image for further statistical analysis and at the same time avoid a requirement for an extensive hard drive storage, it was chosen to acquire frames with the size of 512×512 pixels (only the left CCD output channel was used). Because of the 4 Mpix/s sensor's clocking rate and the 333 ns minimum conversion time for the ADCs used, each analogue video signal is fed into two ADCs in parallel, which are operated in a ping-pong fashion on successive pixels in the time domain. The ADCs have slightly different gain and offset, resulting in alternating brighter and darker pixel-wide sections visible on the image (see Figure 5.12). This

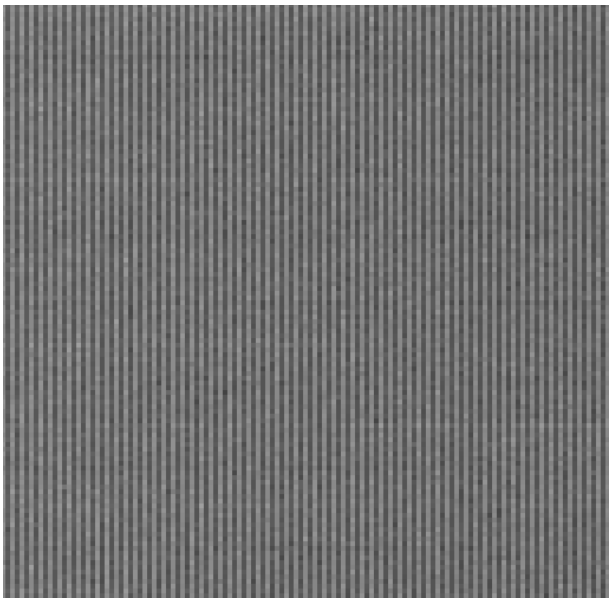

Figure 5.12: Alternating brighter and darker columns present on the CCD reverse clock image.

undesirable effect can be removed by subtracting the average reference frame from an affected image. A dedicated Python program was written (see Appendix B) to generate such a frame from the group of reference images. The other function of this code was to calculate the standard deviation of each individual reference image, to ensure (after comparison) that the system was stable.

A different Python program was used for processing images with injected noise (see Appendix C). The code iterates through the complete list of im-

ages obtained as a result of the measurements for each tested power supply line, subtracts the reference frame from every processed image, saves the resulting frames as Tagged Image File Format (TIFF) files and calculates their standard deviations. Furthermore, both programs (Appendix B and C) save the text files (one each) containing standard deviation values for all the processed images. In the next step, the above figures were copied into an Excel spreadsheet, where they were converted from ADUs to electrons (e^-), using the formula:

$$e^- = ADU \times G, \tag{5.8}$$

where $G = 20$ is the CCD gain conversion ratio, for which the requirement is specified in PLATO-DLR-PL-RP-006 (2016).
The read noise figure for each power supply test was found from:

$$\sigma_{read} = \sqrt{\frac{\sum_{m=1}^{n} \sigma_m^2}{n}}, \tag{5.9}$$

where σ (in e^-) is the standard deviation of each acquired reference image and n represents the total number of such images.

Once the value of read noise was known, it was subtracted in quadrature from the image standard deviations already established for all the frames with injected noise. Following this, it was necessary to scale the injected voltage amplitudes for each tested frequency, such that their corresponding current amplitudes were equal to 20 mA rms, in order to meet the requirements stated previously in Section 4.3.2. This was achieved by applying the following equation:

$$V_{new} = \frac{V_{old} \times I_{new}}{I_{old}}, \tag{5.10}$$

where $V_{old} = 88.4$ mV rms (i.e. 250 mVpk-pk) is the fixed voltage amplitude of the interference superimposed on the tested power supply lines, $I_{new} = 20$ mA rms and I_{old} (in mA rms) represents the previously measured injected current amplitudes.

In the final step, the image standard deviations were scaled accordingly

with the new interference voltage amplitude values found from Eq. (5.10). The following equation was used to complete this task:

$$\sigma_{new} = \frac{\sigma_{old} \times V_{new}}{V_{old}}, \tag{5.11}$$

where σ_{old} (in e^-) represents the original image standard deviation values with subtracted read noise, V_{new} (in mV rms) are the scaled injected voltage amplitudes found from Eq. (5.10) and $V_{old} = 88.4\,\text{mV}$ rms (or 250 mVpk-pk) is the fixed voltage amplitude of the interference that was superimposed on the tested power supply lines.

5.3.2 Results

This section presents the outcomes of CM CS measurements conducted for each of the seven N-FEE board power supplies. The results below are subsequently used in Chapter 7, where they are evaluated against the available PLATO noise budget.

5.3.2.1 Common Mode Conducted Susceptibility of the +33 V (VCCD) Supply Line

After subtracting in quadrature 36 e^- read noise (see Section 5.3.1) and plotting image standard deviations as a function of injected interference frequency, it was found that there was still an additional offset present in the data (of the order of approximately 45 e^-, varying slightly between the tested power supply lines). This baseline noise, as it is called from this point, must be related to the setup, as it was not present in the images without injected noise. Therefore, it was subtracted in quadrature, to allow for different interference sources that were not related to the particular injected frequency.

A susceptibility of the +33 V (VCCD) power supply line to the 250 mVpk-pk CM sinusoidal interference is shown in Figure 5.13, where the image standard deviation (after removing both the read and baseline noise) is plotted as a function of injected signal frequency. One of the dips (at $6666.\dot{6}$ kHz) seems

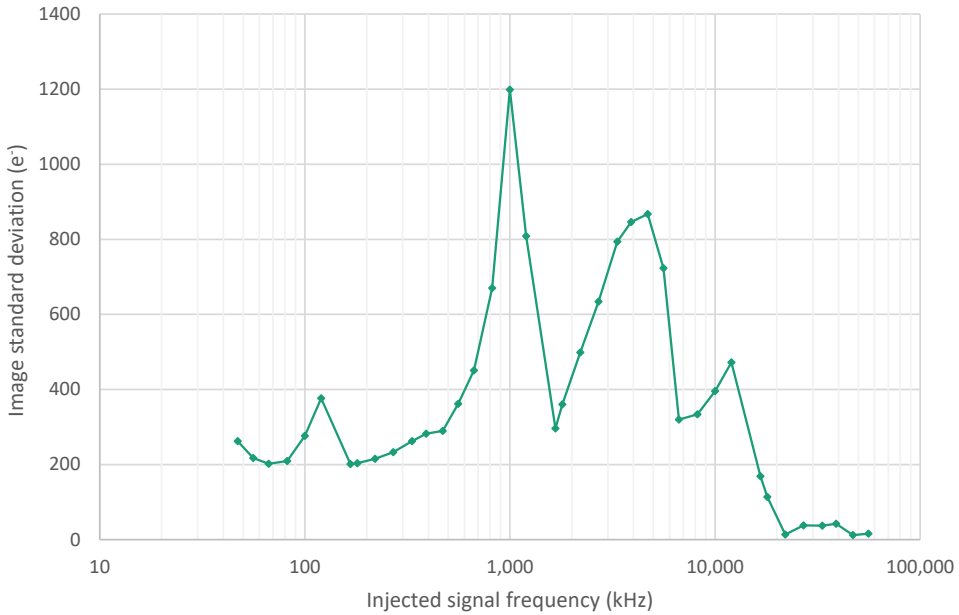

Figure 5.13: Image standard deviation as a function of injected CM interference frequency for the +33 V (VCCD) supply line.

to appear exactly where it was predicted by the simulation result (shown previously in Figure 5.6). Apart from this single feature, there are no other obvious similarities there.

Figure 5.14 illustrates the measured amplitude of the injected current plotted as a function of interference frequency. The curve flattens from about $6666.\dot{6}$ kHz onwards at the ∼31 mA rms level.

The standard deviations from Figure 5.13 after the scaling process (5.3.1) are shown in Figure 5.15. The modified values illustrate the standard deviation levels that would be measured if the injected CM current amplitude was kept fixed at 20 mA rms throughout the whole tested frequency range.

5.3.2.2 Common Mode Conducted Susceptibility of the +12 V (VCLK) Supply Line

The effects of superimposing the 250 mVpk-pk interference on top of the +12 V (VCLK) line's regular signal are shown in Figure 5.16, where the measured image standard deviation (after subtracting in quadrature 36 e^- read noise and the baseline noise) is plotted as a function of injected waveform frequency.

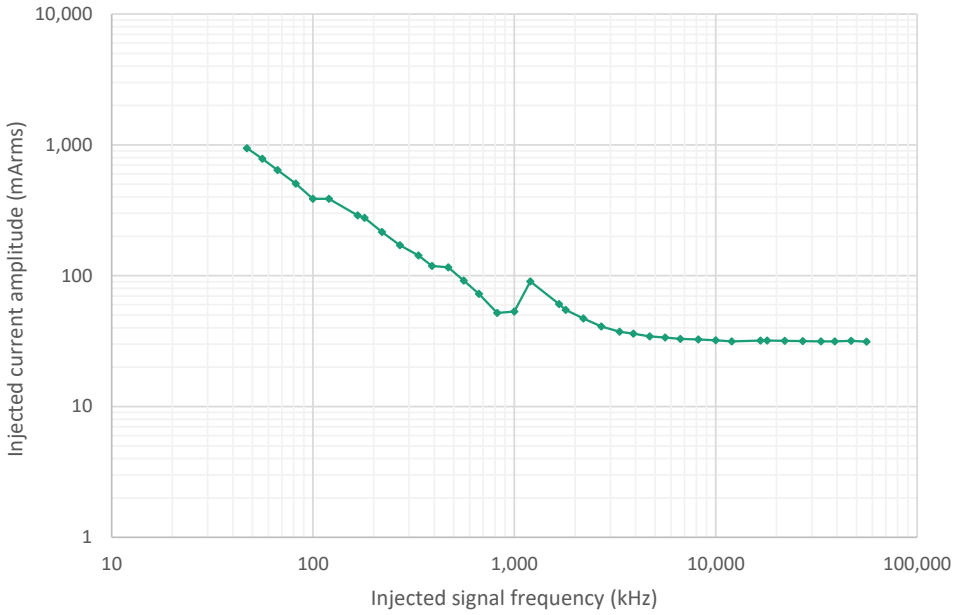

Figure 5.14: Injected CM current amplitude for the +33 V (VCCD) supply line.

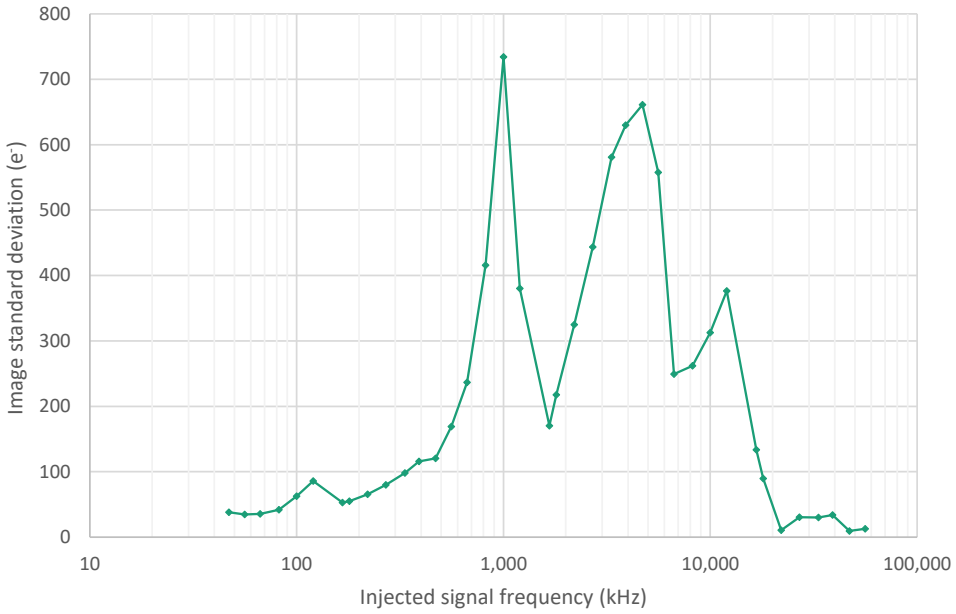

Figure 5.15: Scaled image standard deviation as a function of injected CM interference frequency for the +33 V (VCCD) supply line.

There is a peak present at 10 000 kHz and, just as in case of +33 V (VCCD) supply, a dip at 6666.$\dot{6}$ kHz that were predicted by the simulation.

Figure 5.17 shows the plot of measured injected current amplitude versus

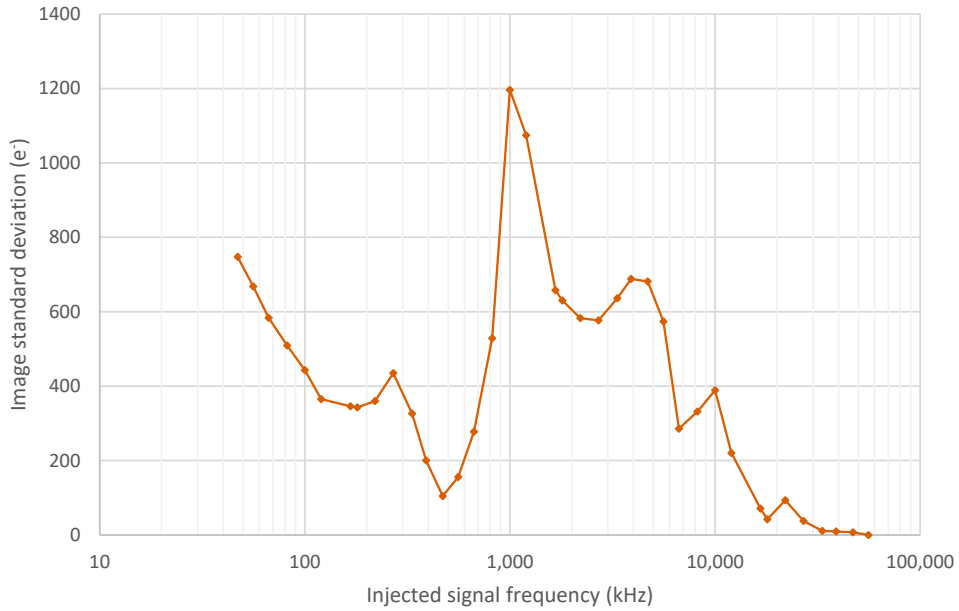

Figure 5.16: Image standard deviation as a function of injected CM interference frequency for the +12 V (VCLK) supply line.

injected signal frequency. The curve stabilises at ∼24 mA rms from above 12 MHz.

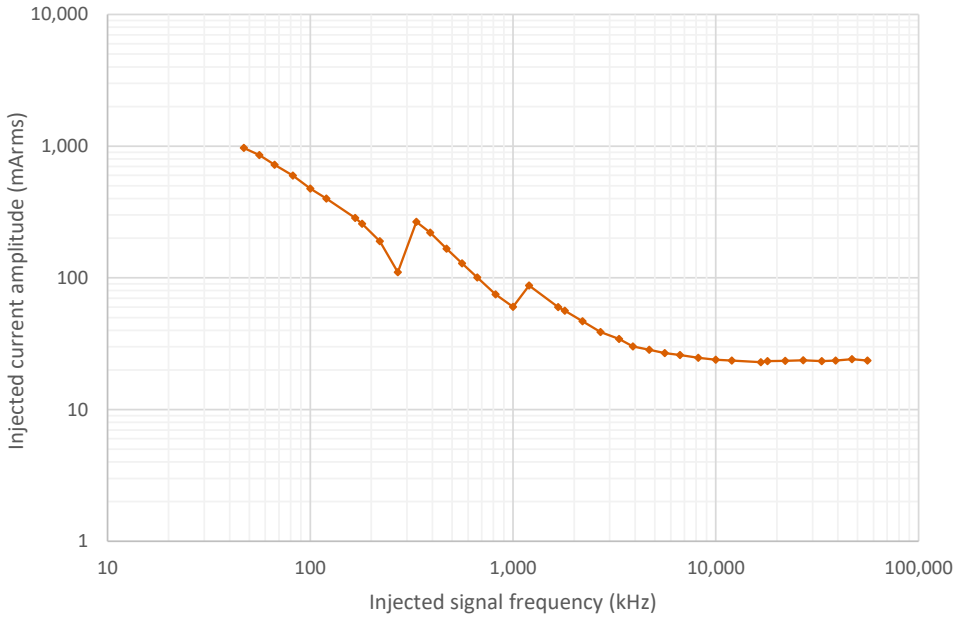

Figure 5.17: Injected CM current amplitude for the +12 V (VCLK) supply line.

The measured standard deviations scaled to the 20 mA rms injected current amplitude are presented in Figure 5.18.

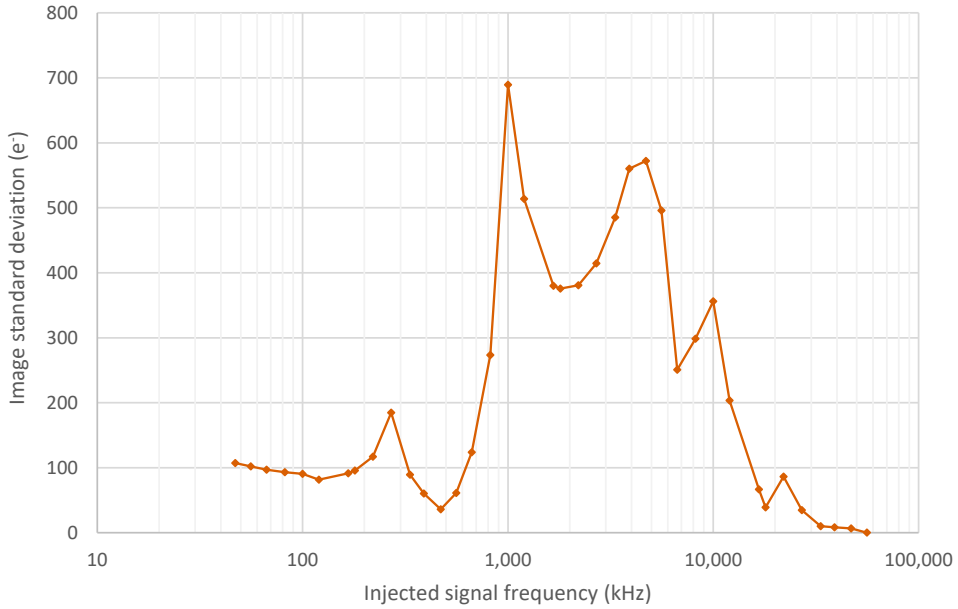

Figure 5.18: Scaled image standard deviation as a function of injected CM interference frequency for the +12 V (VCLK) supply line.

5.3.2.3 Common Mode Conducted Susceptibility of the +4 V (VDIG_SPW) Supply Line

Figure 5.19 illustrates susceptibility of the +4V (VDIG_SPW) power supply line to the 250 mVpk-pk sinusoidal interference signal. Prior to plotting, the 36 e^- read noise and the baseline noise were subtracted in quadrature from the image standard deviation values. There are no obvious similar features there when compared to the simulation outcomes. However, the highest peak occurs at 1 MHz and this is consistent with the test results for the +33 V and +12 V supplies.

The amplitude of the injected current is plotted in Figure 5.20 as a function of the injected signal frequency. The curve flattens to ~55 mA rms from about 3.9 MHz.

Data from Figure 5.19 after scaling is plotted in Figure 5.21. The new

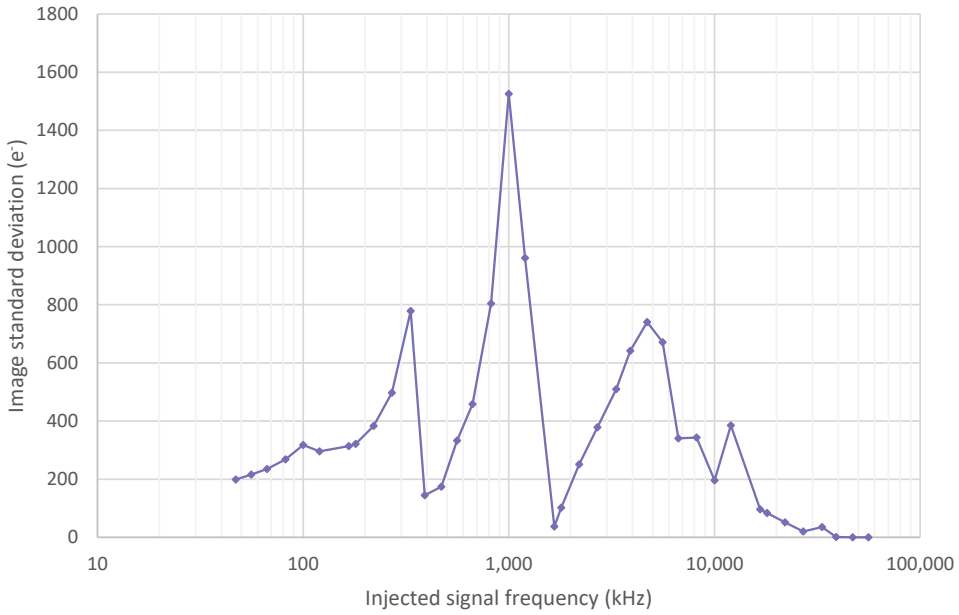

Figure 5.19: Image standard deviation as a function of injected CM interference frequency for the +4 V (VDIG_SPW) supply line.

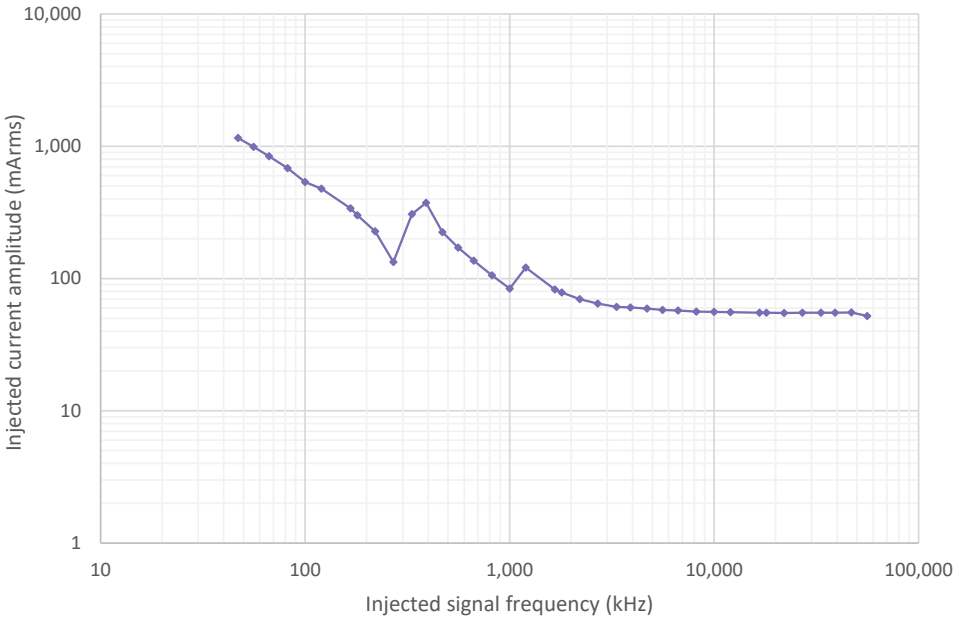

Figure 5.20: Injected CM current amplitude for the +4 V (VDIG_SPW) supply line.

standard deviation values represent susceptibility of the tested supply line to the 20 mA rms injected current amplitude.

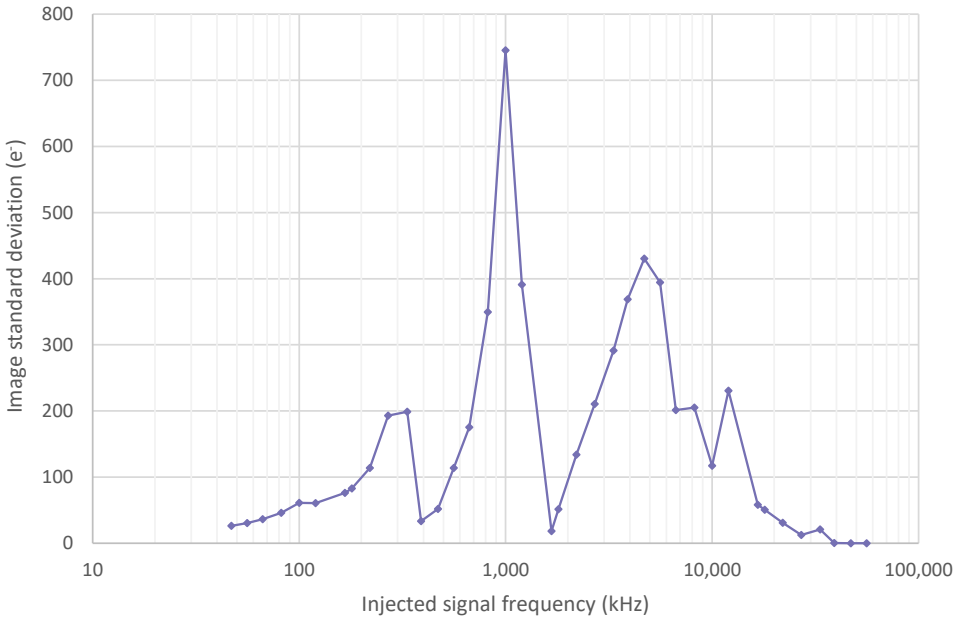

Figure 5.21: Scaled image standard deviation as a function of injected CM interference frequency for the +4 V (VDIG_SPW) supply line.

5.3.2.4 Common Mode Conducted Susceptibility of the −6 V (VAN3) Supply Line

Figure 5.22 shows image standard deviation levels after subtracting in quadrature 36 e^- read noise and the baseline noise, plotted as a function of injected waveform frequency for the −6 V (VAN3) supply line with superimposed 250 mVpk-pk interference signal. In this case, there are no apparent similarities to the simulation result.

The injected current amplitude is shown in Figure 5.23. The curve flattens to ∼103 mA rms from about 3333.$\dot{3}$ kHz.

Finally, Figure 5.24 shows the standard deviations from Figure 5.22 after scaling to an injected current amplitude of 20 mA rms for each tested frequency.

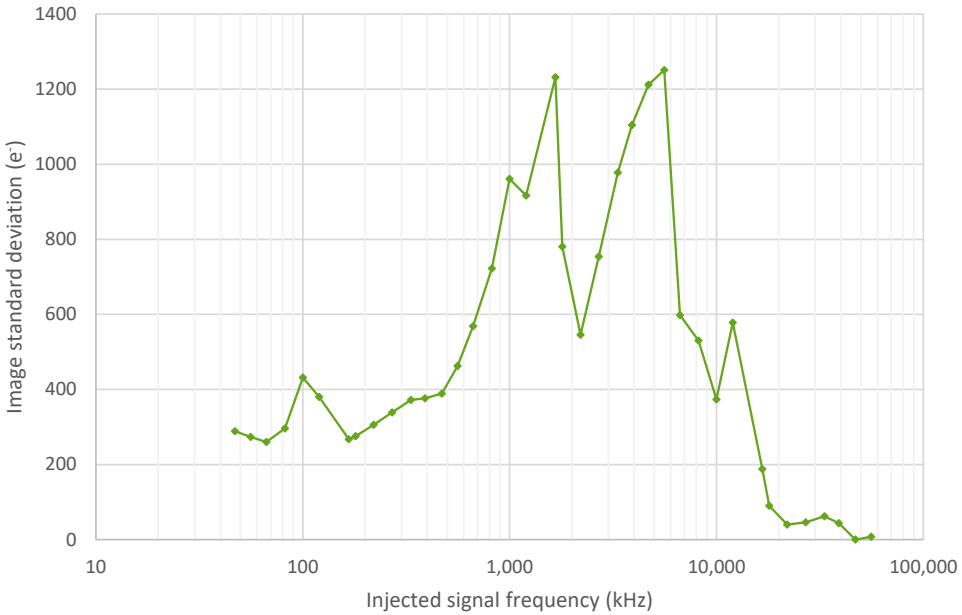

Figure 5.22: Image standard deviation as a function of injected CM interference frequency for the −6 V (VAN3) supply line.

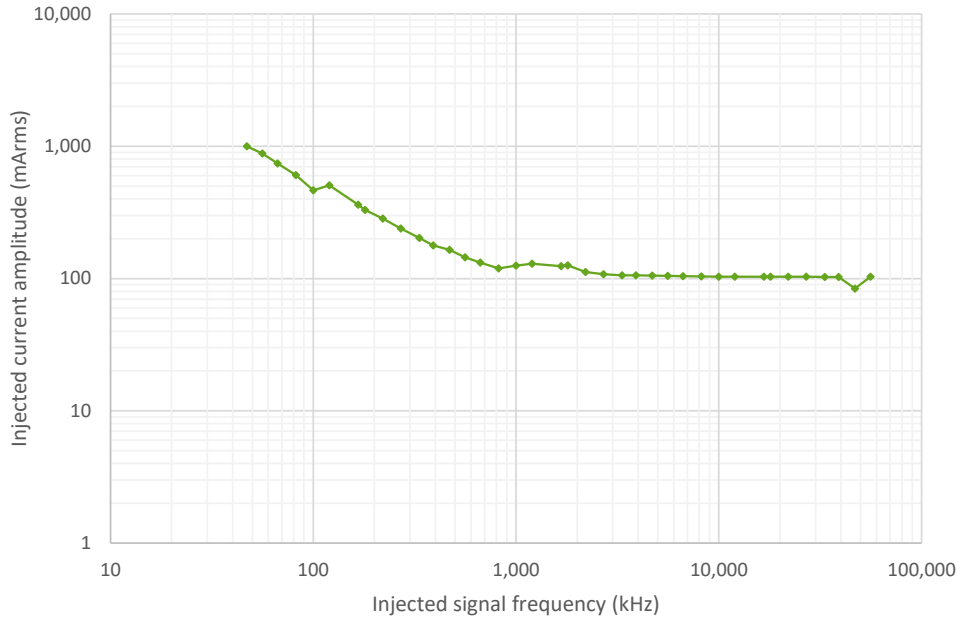

Figure 5.23: Injected CM current amplitude for the −6 V (VAN3) supply line.

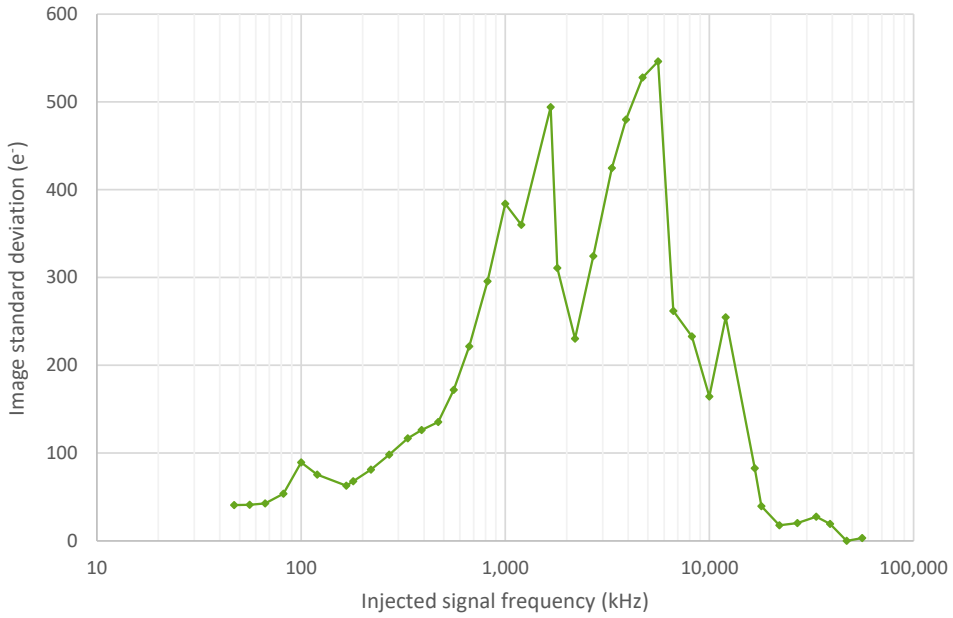

Figure 5.24: Scaled image standard deviation as a function of injected CM interference frequency for the −6 V (VAN3) supply line.

5.3.2.5 Common Mode Conducted Susceptibility of the +6 V (VAN1) Supply Line

The susceptibility of the +6 V (VAN1) power supply line to the 250 mVpk-pk CM interference signal is shown in Figure 5.25, where the image standard deviation (after subtracting in quadrature 36 e^- read noise and the baseline noise) is plotted as a function of injected waveform frequency. Just as in the case of the −6 V supply, there are no obvious similarities to the simulation result there, however both the +6 V and −6 V data sets have a lot in common between themselves, as their peaks and dips seem to appear at the same frequencies. This is due to the fact that both supplies have very similar electronic circuits.

As shown in Figure 5.26, the injected current amplitude curve flattens to ∼102 mA rms for the frequencies above 3333.$\dot{3}$ kHz.

The scaled image standard deviation plot, as shown in Figure 5.27, illustrates the +6 V supply line susceptibility to the injected 20 mA rms current amplitude for each tested interference frequency.

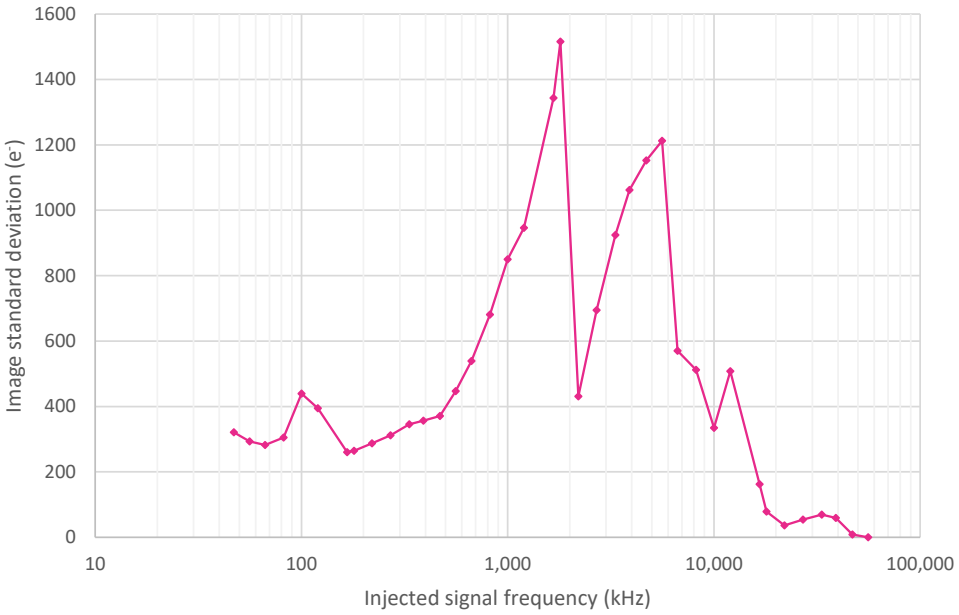

Figure 5.25: Image standard deviation as a function of injected CM interference frequency for the +6 V (VAN1) supply line.

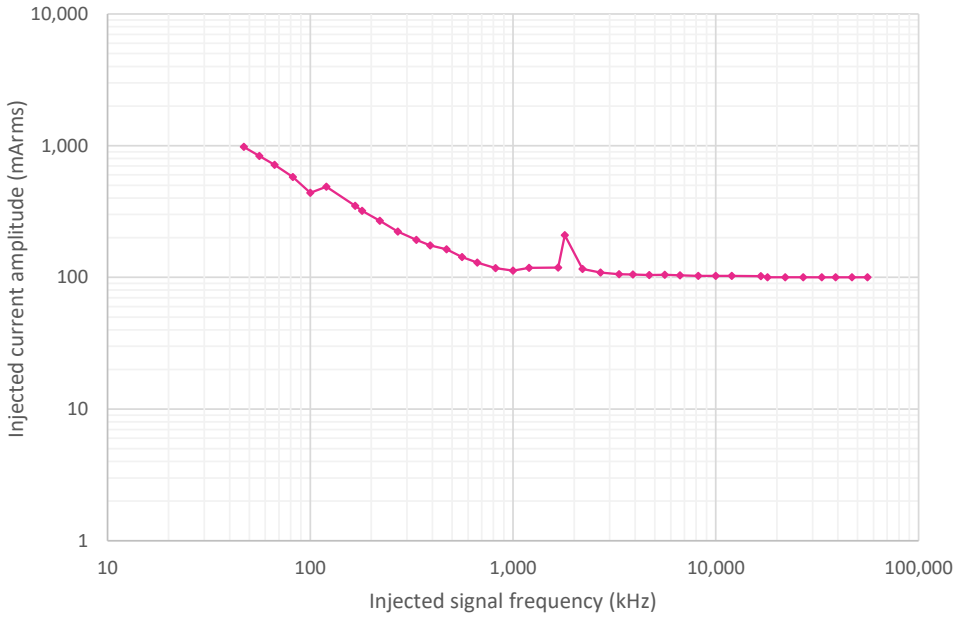

Figure 5.26: Injected CM current amplitude for the +6 V (VAN1) supply line.

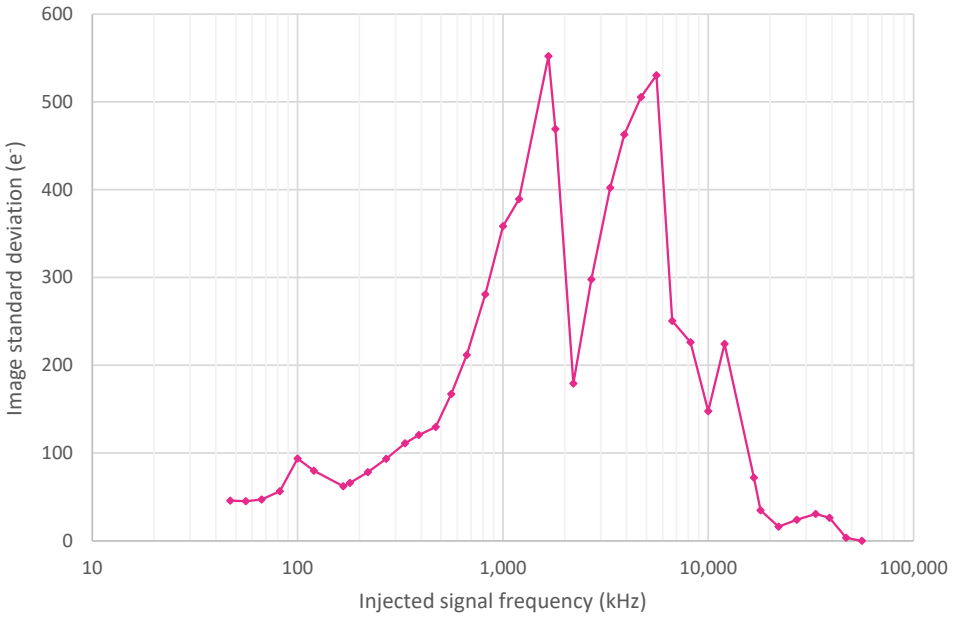

Figure 5.27: Scaled image standard deviation as a function of injected CM interference frequency for the +6 V (VAN1) supply line.

5.3.2.6 Common Mode Conducted Susceptibility of the +3 V (VDIG_FPGA) Supply Line

The plot in Figure 5.28 shows the impact of the injected 250 mVpk-pk CM interference signal on the output image standard deviation across the tested frequency range (the 36 e^- read noise and the baseline noise were subtracted in quadrature from all standard deviation values). The dip present at 6666.$\dot{6}$ kHz was predicted by the simulation result.

The curve in Figure 5.29 illustrates the injected current amplitude level that was measured at each tested frequency. It flattens to ∼36 mA rms from about 8 MHz onwards.

The image standard deviation plot from Figure 5.28 scaled to 20 mA rms of injected current is shown in Figure 5.30.

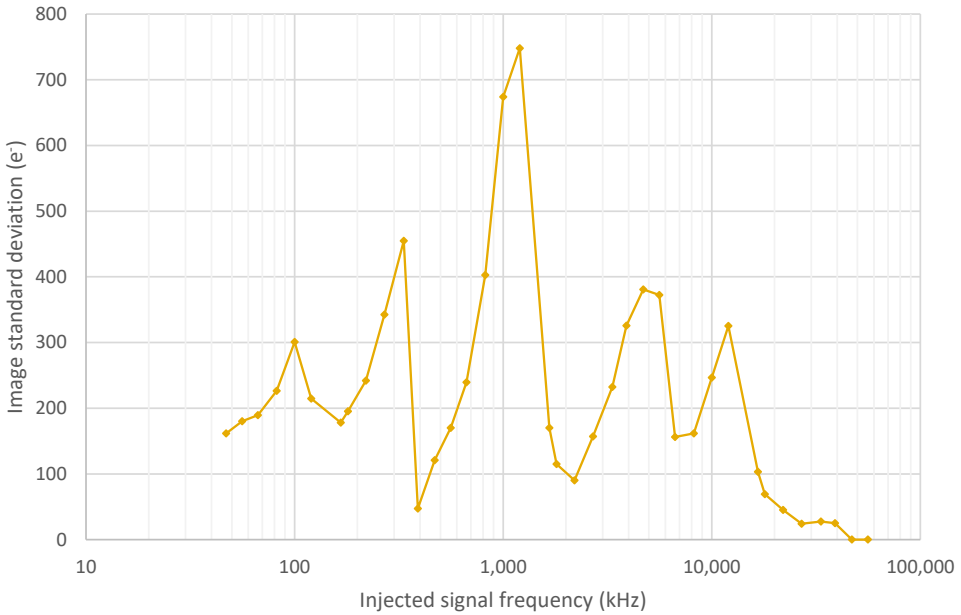

Figure 5.28: Image standard deviation as a function of injected CM interference frequency for the +3 V (VDIG_FPGA) supply line.

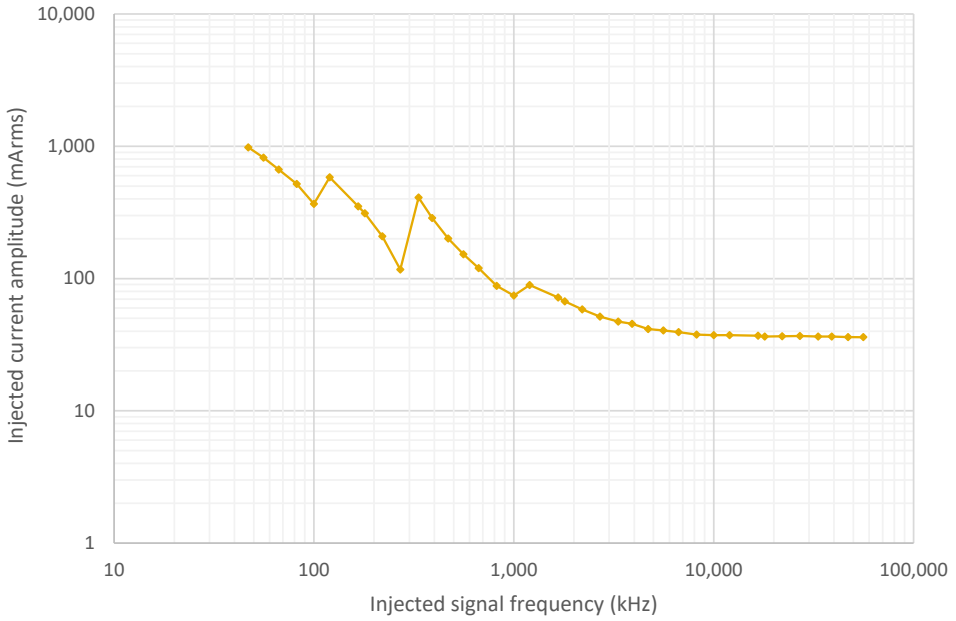

Figure 5.29: Injected CM current amplitude for the +3 V (VDIG_FPGA) supply line.

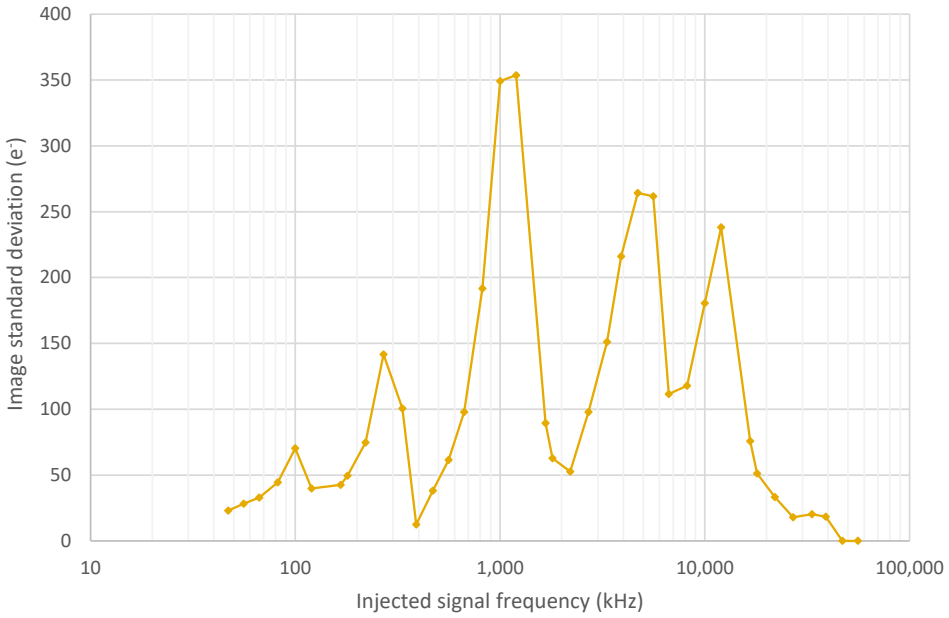

Figure 5.30: Scaled image standard deviation as a function of injected CM interference frequency for the +3 V (VDIG_FPGA) supply line.

5.3.2.7 Common Mode Conducted Susceptibility of the +3 V (VAN2) Supply Line

The susceptibility of the +3 V (VAN2) power supply line to the 250 mVpk-pk CM sinusoidal interference is shown in Figure 5.31, where the image standard deviation with subtracted in quadrature 36 e^- read noise and the baseline noise is plotted as a function of injected signal frequency. There are no apparent similarities between this curve and the simulation result.

The amplitude of the injected current is plotted in Figure 5.32 as a function of the injected signal frequency. The curve flattens to ~78 mA rms from about 8 MHz.

Finally, Figure 5.33 shows the standard deviations from Figure 5.31 after scaling to an injected current amplitude for each tested frequency of 20 mA rms.

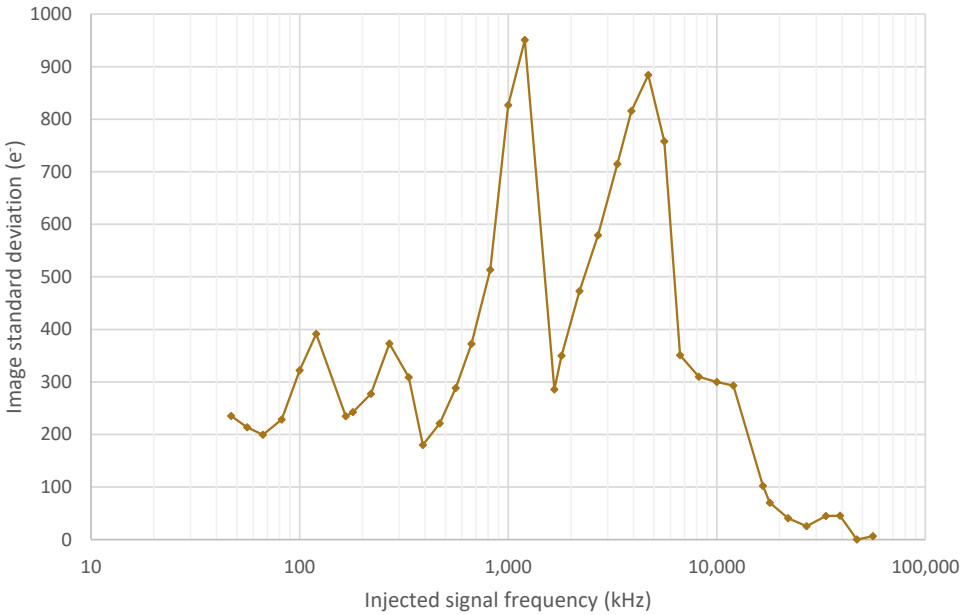

Figure 5.31: Image standard deviation as a function of injected CM interference frequency for the +3 V (VAN2) supply line.

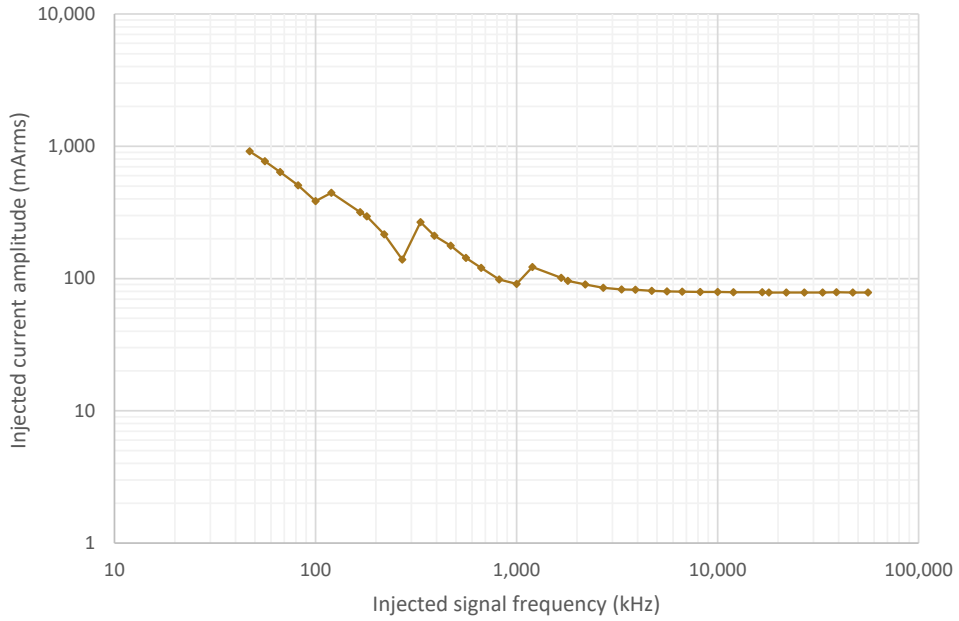

Figure 5.32: Injected CM current amplitude for the +3 V (VAN2) power supply line.

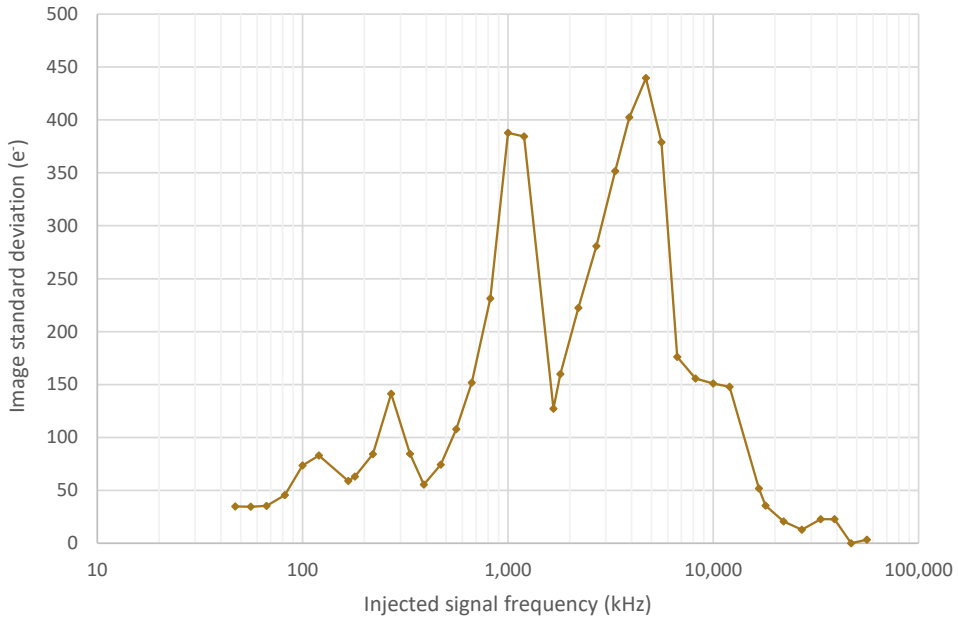

Figure 5.33: Scaled image standard deviation as a function of injected CM interference frequency for the +3 V (VAN2) supply line.

5.3.2.8 Combined Results from the Common Mode Conducted Susceptibility Measurements

In order to directly compare sensitivities of each of the individual N-FEE power lines to the CM interference, the combined image standard deviation plot is shown in Figure 5.34.

The combined plot of injected CM current amplitudes is shown in Figure 5.35. All the curves become flat for frequencies above 10 MHz.

Table 5.2 provides a list of all the tested frequencies and the corresponding standard deviations for each of the PLATO N-FEE power supply lines. The measured standard deviations were scaled to demonstrate the susceptibility of individual power lines that would be measured if the injected interference signal was 20 mA rms.

The results in this section are discussed in Section 5.5.

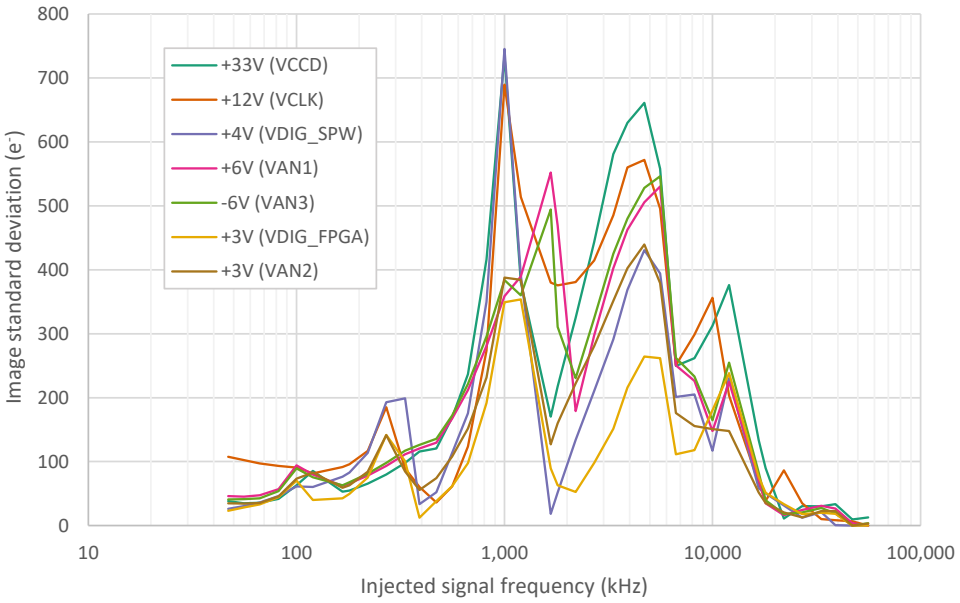

Figure 5.34: Image standard deviation as a function of injected CM interference frequency for all the tested N-FEE power lines. The image standard deviation values were scaled to the levels equivalent to 20 mA rms injection.

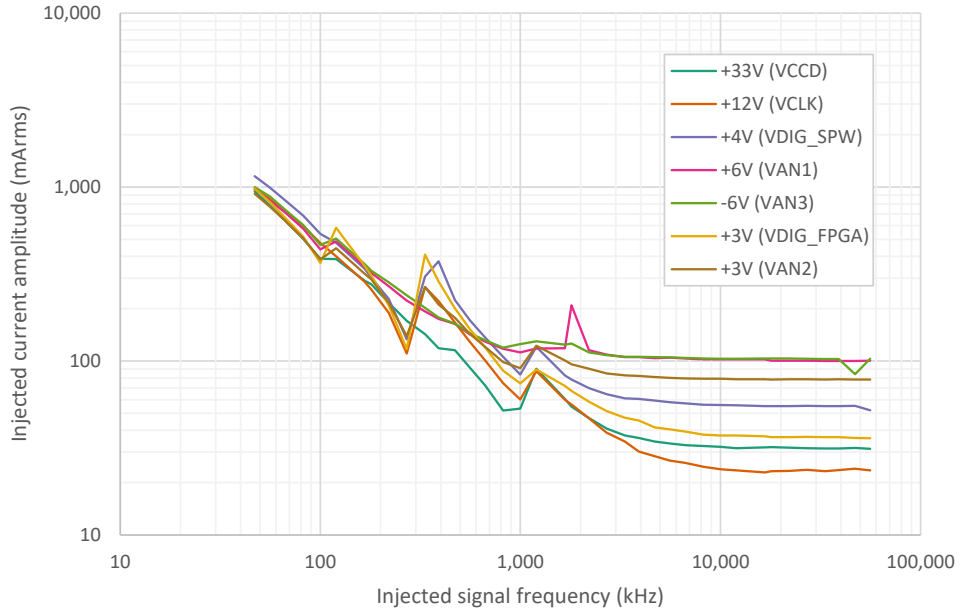

Figure 5.35: Injected CM current amplitudes.

Injected freq. [kHz]	Scaled image standard deviation [e$^-$]						
	+33V VCCD	+12V VCLK	+4V VDIG_ SPW	-6V VAN3	+6V VAN1	+3V VDIG_ FPGA	+3V VAN2
47	39	108	27	42	47	25	36
56	36	103	32	42	46	30	36
67	37	97	37	44	48	34	37
82	43	94	47	55	58	46	47
100	64	91	62	90	95	72	75
120	87	83	62	76	81	41	84
167	55	93	77	64	64	45	61
180	57	97	84	69	67	52	65
220	68	118	115	82	80	77	86
270	83	186	194	99	95	144	143
333	101	91	200	118	113	101	86
390	119	63	36	128	122	20	58
470	123	41	55	137	131	43	77
560	171	65	115	173	169	65	110
667	239	126	177	222	213	101	154
820	418	275	351	296	282	194	233
1000	735	690	746	385	359	351	389
1200	382	514	392	361	390	355	385
1667	174	381	34	495	553	95	130
1800	221	377	59	312	469	71	162
2200	327	383	138	232	181	63	224
2700	446	416	213	325	299	105	282
3333	583	487	293	426	403	156	353
3900	631	562	370	481	463	220	403
4700	663	574	432	528	506	268	441
5600	560	498	396	547	531	265	380
6667	254	255	204	263	252	119	179
8200	266	303	208	234	228	126	159
10 000	316	360	122	166	150	186	154
12 000	379	210	233	256	226	242	151
16 667	142	84	68	86	76	88	60
18 000	102	64	62	46	43	68	46
22 000	50	100	47	30	30	56	36
27 000	58	62	37	32	35	48	33
33 333	58	52	41	37	39	49	38
39 000	60	52	35	31	36	48	38
47 000	50	51	34	24	25	45	28
56 000	51	45	25	25	23	41	30

Table 5.2: Scaled image standard deviations obtained from the CM CS measurements for each individual power supply line. For clarity, standard deviations are rounded to the nearest electron and some frequencies are rounded to the nearest kHz.

5.4 Conducted Susceptibility Differential Mode Measurements

5.4.1 Experimental Setup

The experimental setup block diagram for the CS DM is presented in Figure 5.36 (the photograph of the setup was shown previously in Figure 5.11). The tested power line is drawn in red, while the corresponding power return line is coloured blue.

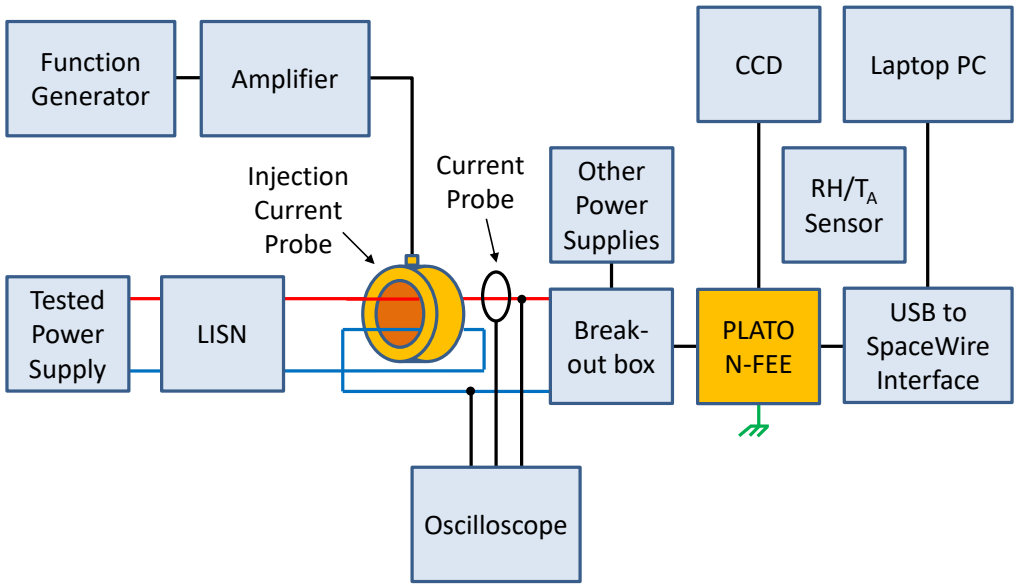

Figure 5.36: Setup for the CS DM measurements. The 'Other Power Supplies' block represents six other power supplies.

The functional blocks are specified as follows:

- PLATO N-FEE: BB_V1 (MSSL),
- CCD: CCD47-20 (Teledyne e2v),
- Bench DC Power Supplies: QL355TP and PL303QMD-P (TTi),
- LISN: from the Solar Orbiter EGSE (MSSL),
- Breakout Box (MSSL),

- Function Generator: AFG3102 (Tektronix),
- Amplifier: Model 15A250 (Amplifier Research),
- ICP: ICP-621 (A.H. Systems),
- Laptop PC: XPS 15 9530 (Dell),
- USB to SpaceWire Interface: SpaceWire Brick Mk2 (STAR-Dundee),
- Oscilloscope: MDO3024 Mixed Domain Oscilloscope (Tektronix),
- Oscilloscope Current Probe: TCP0020 (Tektronix),
- Relative Humidity/Ambient Temperature Sensor: RH-USB (Omega).

The setup allowed for injecting sinusoidal interference signals with frequencies covering the range from 50 kHz to 50 MHz. As for the CM measurements (described in Section 5.3), the required interference was created in the function generator, amplified by the power amplifier and superimposed on the tested supply's regular signal with the aid of the ICP. After setting the correct frequency level, the interference amplitude was measured with the oscilloscope (two channels configured to operate in subtraction mode, one probe connected to the tested power line, the other one to the corresponding power return line) and set to 250 mVpk-pk, as such a value allowed for covering the whole frequency range without experiencing setup instability. Once the adjustments were complete, the CCD output data was read and saved into a binary file. The imaging sensor was operated in the reverse clocking mode, to enable measuring the noise contribution from the CCD output stage. Each tested supply (the complete list was shown previously in Table 5.1) was tested in accordance with the following acquisition scheme:

- 20 reference frames (no noise injected) prior to the main test,
- 46 frames with injected noise (main test; one frame per injected interference frequency),

- 20 reference frames (no noise injected) post the main test,
- 5 frames with injected noise (repeatability check; one frame per injected interference frequency).

The reference frames were needed for establishing the mean readout noise figure and to confirm the system's noise floor stability throughout the test. The additional five images acquired at the very end, were used to confirm the measurements' repeatability (five frequencies were chosen, to cover different parts of the tested spectrum).

Once all the measurements were complete, The Python code from Appendix B was used to generate the mean reference frame. This frame was then subtracted from each saved image with injected noise using the Python code from Appendix C. Both programs calculated standard deviations of their processed images and saved them into the correct text files (two such files were created, one for each program).

An Excel spreadsheet was used to complete the following tasks:

- To convert the standard deviation units from ADUs to e^- with the aid of Equation 5.8 (see Section 5.3.1),
- To calculate the overall read noise figure for each tested power supply line,
- To subtract (in quadrature) the mean read noise from image standard deviation obtained for each frame with injected noise,
- To scale the standard deviations calculated for images with 250 mVpk-pk injected voltage amplitudes into the new levels that would be measured if the injected voltage amplitude for each tested frequency was set to 20 mVpk-pk (as specified in Section 4.3.2). The following equation was used to achieve this:

$$\sigma_{new} = \frac{\sigma_{old} \times V_{new}}{V_{old}}, \tag{5.12}$$

where σ_{old} (in e^-) represents the original image standard deviation value with subtracted read noise, $V_{new} = 20\,\text{mVpk-pk}$ is the new (scaled) injected voltage amplitude and $V_{old} = 250\,\text{mVpk-pk}$ is the original voltage amplitude of the interference that was superimposed on each tested power supply line.

5.4.2 Results

This section presents the outcomes of DM CS measurements conducted for each of the seven N-FEE board power supplies. The results below are subsequently used in Chapter 7, where they are evaluated against the available PLATO noise budget.

5.4.2.1 Differential Mode Conducted Susceptibility of the +33 V (VCCD) Supply Line

The susceptibility of the +33 V (VCCD) power supply line to the 250 mVpk-pk DM sinusoidal interference is shown in Figure 5.37, where the image standard deviation (after subtracting in quadrature $58\,e^-$ read noise and the baseline noise) is plotted as a function of injected signal frequency. There is a peak at $3333.\dot{3}\,\text{kHz}$ and dips at $13\,333.\dot{3}\,\text{kHz}$, $26\,666.\dot{6}\,\text{kHz}$ and $46\,666.\dot{6}\,\text{kHz}$ that were also present in the simulation output (Figures 5.5 and 5.6). The repeated measurements (plotted in red) appeared very close to the original ones, except the point located at 56 kHz. In early measurements whole scans were repeated to demonstrate stability of the setup. It was found that the data was repeatable except sometimes the low frequencies. The lack of repeatability of the 56 kHz point in Figure 5.37 may be caused by an electronics instability, because this frequency is close to the ICP's lower limit of 50 kHz and this may cause problems for the combination of oscillator, power amplifier and ICP. In addition, subtracting in quadrature the readout noise and the baseline noise leads to larger error bars for low noise values.

Figure 5.38 shows the measured injected current amplitude plotted as a function of the interference frequency. The curve peaks at 100 kHz, then

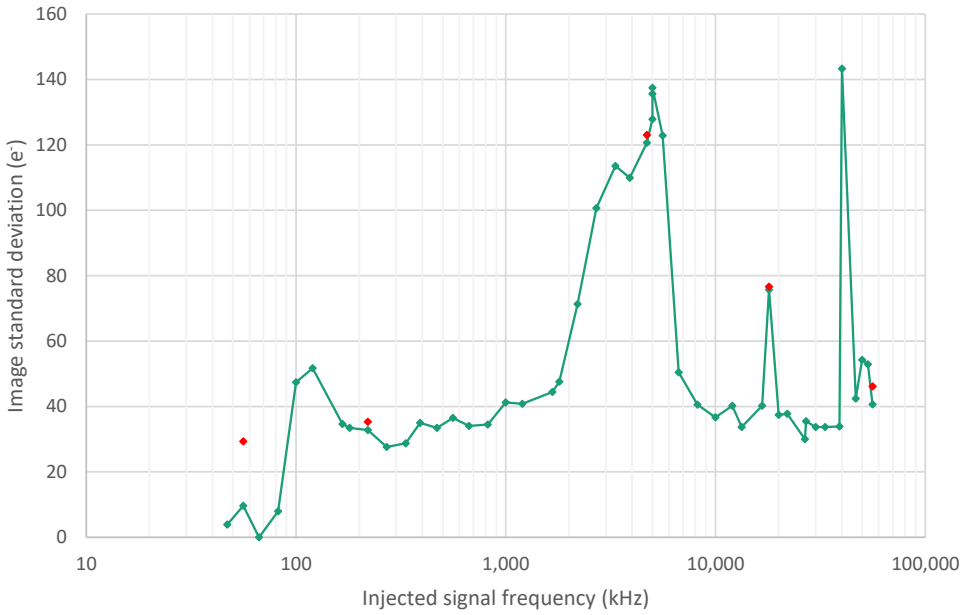

Figure 5.37: Image standard deviation as a function of injected DM interference frequency for the +33 V (VCCD) supply line. The five retested frequencies are plotted in red.

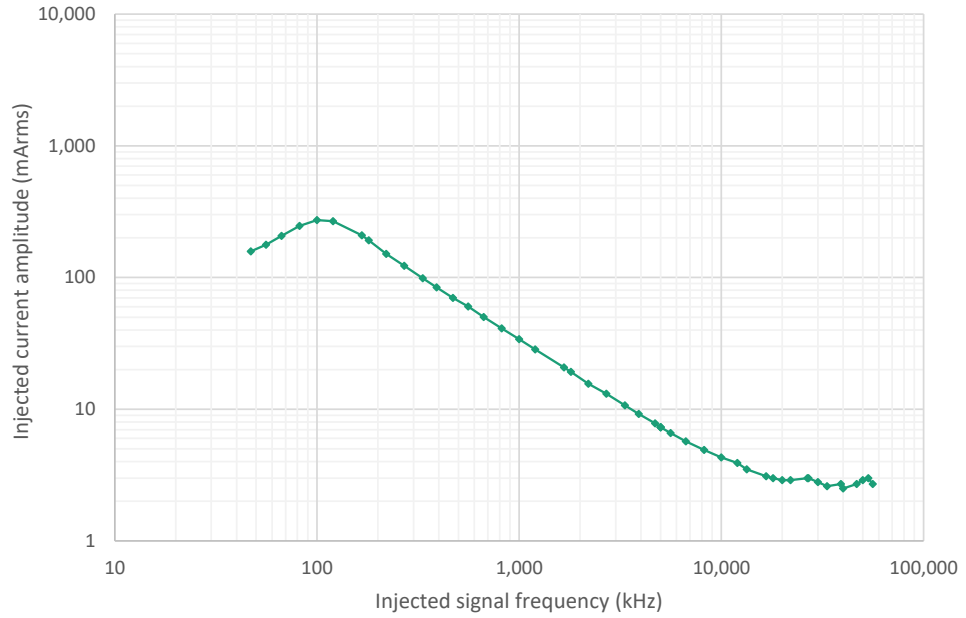

Figure 5.38: Injected DM current amplitude for the +33 V (VCCD) supply line.

decays exponentially and reaches the plateau current of ∼3 mA rms.

The standard deviation values from Figure 5.37 after scaling are shown

in Figure 5.39. The plot illustrates the standard deviation levels that would be measured if the injected DM voltage amplitude was held at 20 mVpk-pk across the tested frequency range.

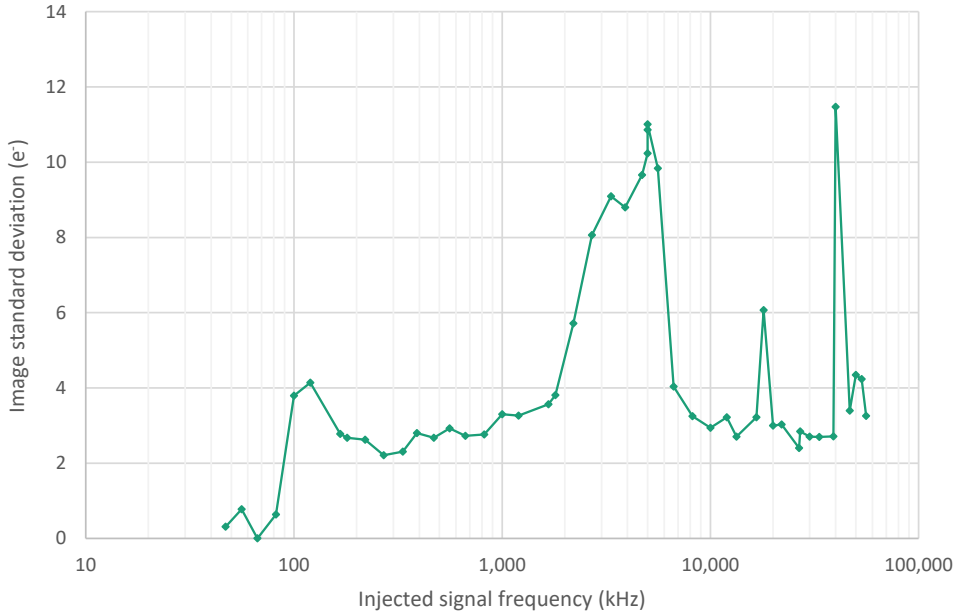

Figure 5.39: Scaled image standard deviation as a function of injected DM interference frequency for the +33 V (VCCD) supply line.

5.4.2.2 Differential Mode Conducted Susceptibility of the +12 V (VCLK) Supply Line

The impact of superimposing the 250 mVpk-pk DM interference on top of the +12 V line's regular signal is shown in Figure 5.40, where the measured image standard deviation (after subtracting in quadrature 57 e^- read noise and the baseline noise) is plotted as a function of injected waveform frequency. There are peaks at 3333.$\dot{3}$ kHz, 10 000 kHz and 50 000 kHz, and dips at 13 333.$\dot{3}$ kHz, 46 666.$\dot{6}$ kHz and 53 333.$\dot{3}$ kHz that were predicted by the simulation. The five additional points (plotted in red) confirm repeatability of the test.

Figure 5.41 shows a plot of the measured injected current amplitude versus interference signal frequency. The curve decays exponentially and finally levels out at ~3 mA rms.

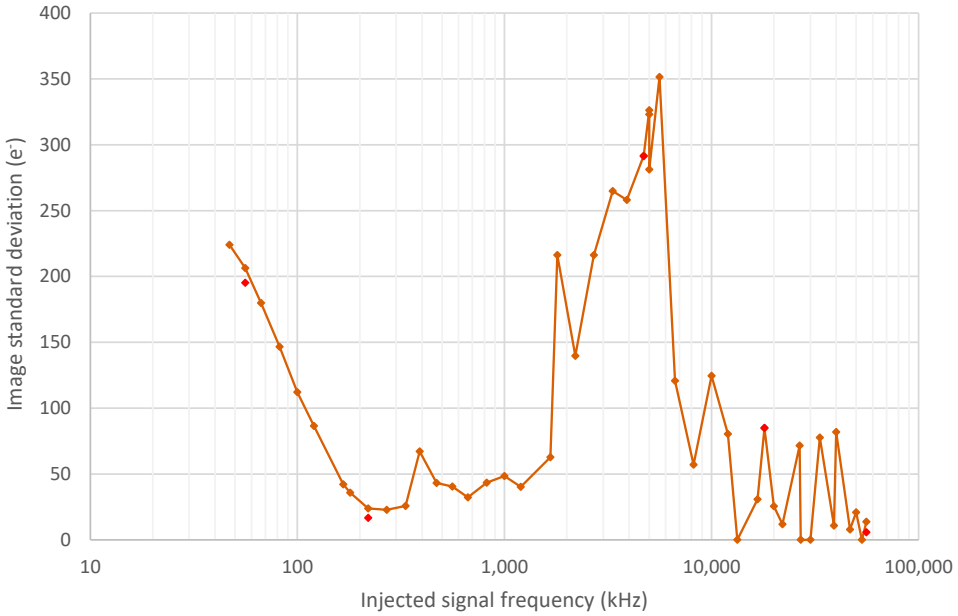

Figure 5.40: Image standard deviation as a function of injected DM interference frequency for the +12 V (VCLK) supply line. The five retested frequencies are plotted in red.

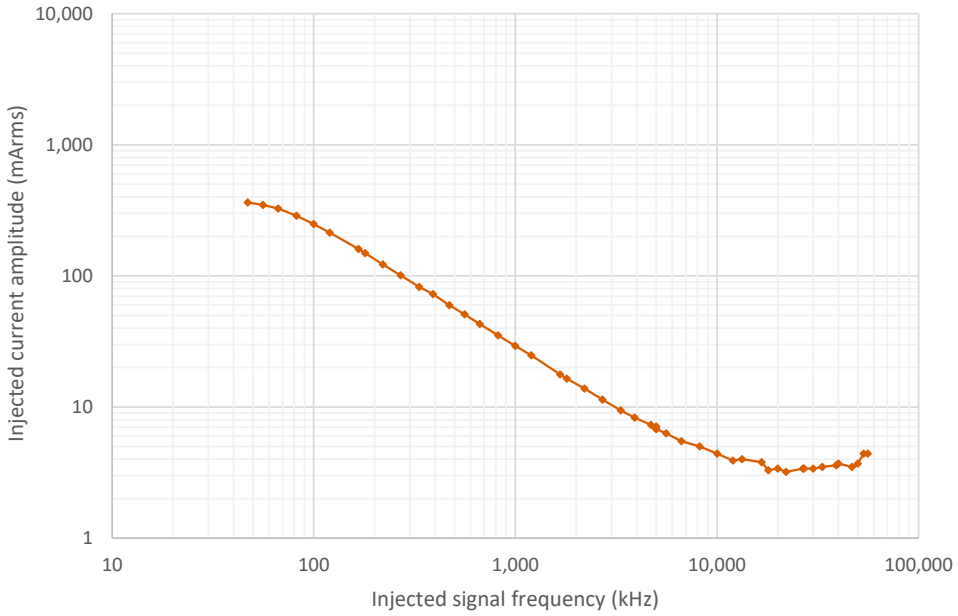

Figure 5.41: Injected DM current amplitude for the +12 V (VCLK) supply line.

The measured standard deviations scaled to the levels that would represent 20 mVpk-pk injection are presented in Figure 5.42.

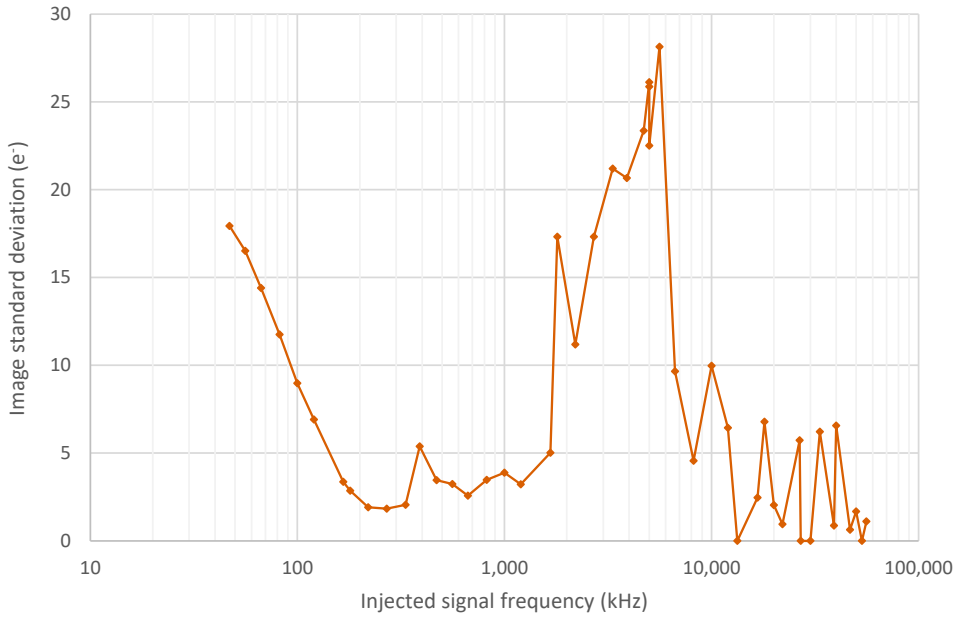

Figure 5.42: Scaled image standard deviation as a function of injected DM interference frequency for the +12 V (VCLK) supply line.

5.4.2.3 Differential Mode Conducted Susceptibility of the +4 V (VDIG_SPW) Supply Line

Figure 5.43 reflects susceptibility of the +4V (VDIG_SPW) power supply line to the 250 mVpk-pk sinusoidal interference signal (the standard deviations have subtracted in quadrature 58 e^- read noise and the baseline noise). The plotted curve has four common features with the simulation result: peaks at 10 000 kHz and 16 666.$\dot{6}$ kHz, and two dips: at 13 333.$\dot{3}$ kHz and 20 000 kHz. The repeated measurements (red data points) appear in close proximity to the original results.

The amplitude of the injected current is plotted in Figure 5.44 as a function of the injected signal frequency. The curve decays exponentially and reaches the plateau at ∼3 mA rms.

Data from Figure 5.43 after scaling is plotted in Figure 5.45. The scaled standard deviation values represent hypothetical susceptibility of the tested supply line to the injected 20 mVpk-pk voltage amplitude.

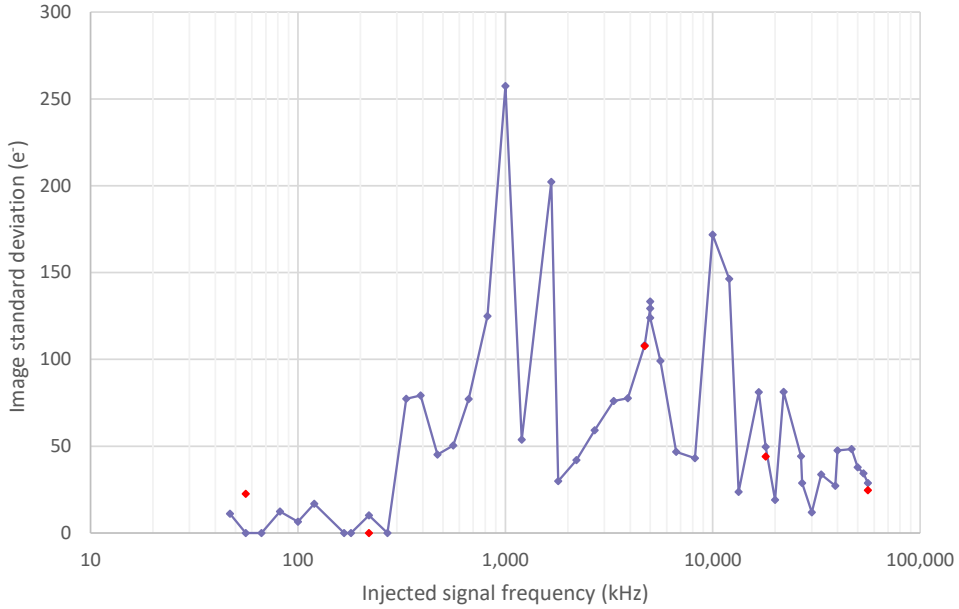

Figure 5.43: Image standard deviation as a function of injected DM interference frequency for the +4 V (VDIG_SPW) supply line. The five retested frequencies are plotted in red.

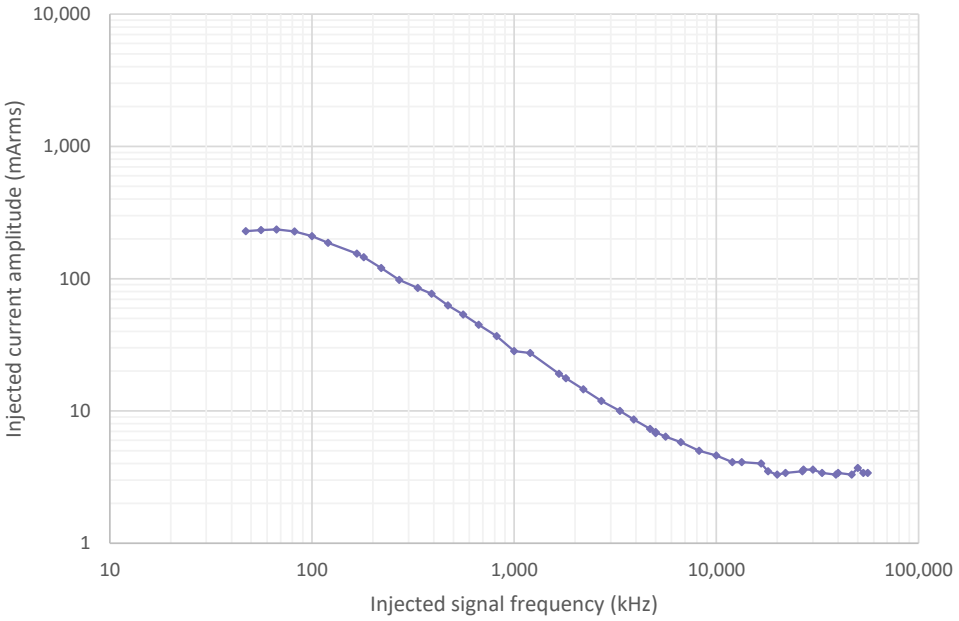

Figure 5.44: Injected DM current amplitude for the +4 V (VDIG_SPW) supply line.

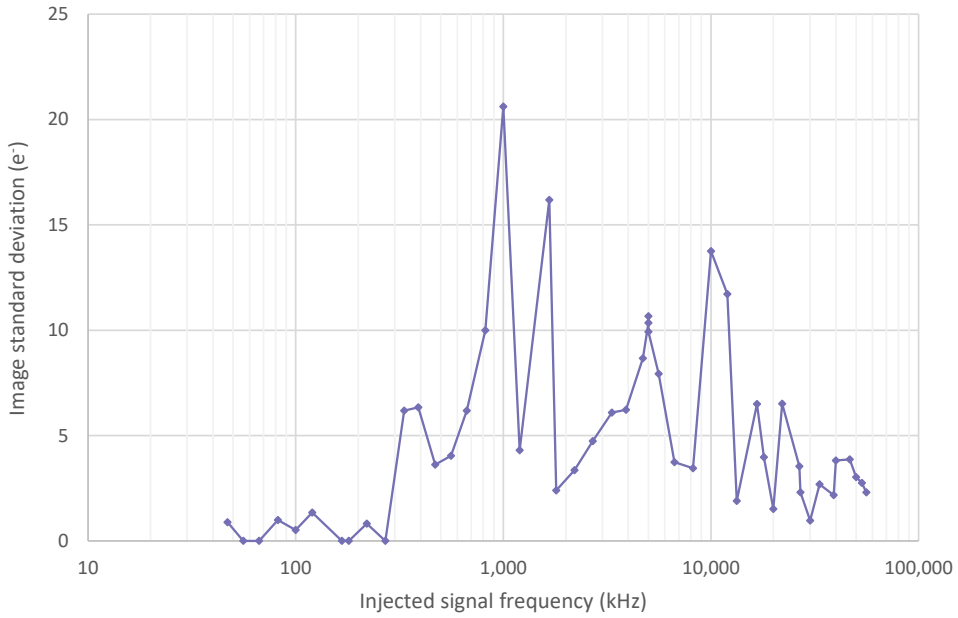

Figure 5.45: Scaled image standard deviation as a function of injected DM interference frequency for the +4 V (VDIG_SPW) supply line.

5.4.2.4 Differential Mode Conducted Susceptibility of the −6 V (VAN3) Supply Line

The result of injecting the DM 250 mVpk-pk interference signal into the −6 V supply line is shown in Figure 5.46, where the image standard deviations with subtracted in quadrature 57 e^- read noise and baseline noise are plotted as a function of injected waveform frequency. The curve features a peak and couple of dips that were also present in the simulation output. Theses are located at 10 000 kHz, 6666.$\dot{6}$ kHz and 13 333.$\dot{3}$ kHz. The five repeated measurements are shown in red. All but one (at 56 kHz) appear very close to the original results. The apparent value of zero from the repeated 56 kHz point is probably due to a combination of electronics instability and uncertainties in the subtraction in quadrature of the readout noise and the baseline noise, as previously described for the 33 V data.

The injected current amplitude is shown in Figure 5.47. After reaching a gentle peak at ∼70 kHz, the curve decays exponentially and stabilises at about 3 mA rms.

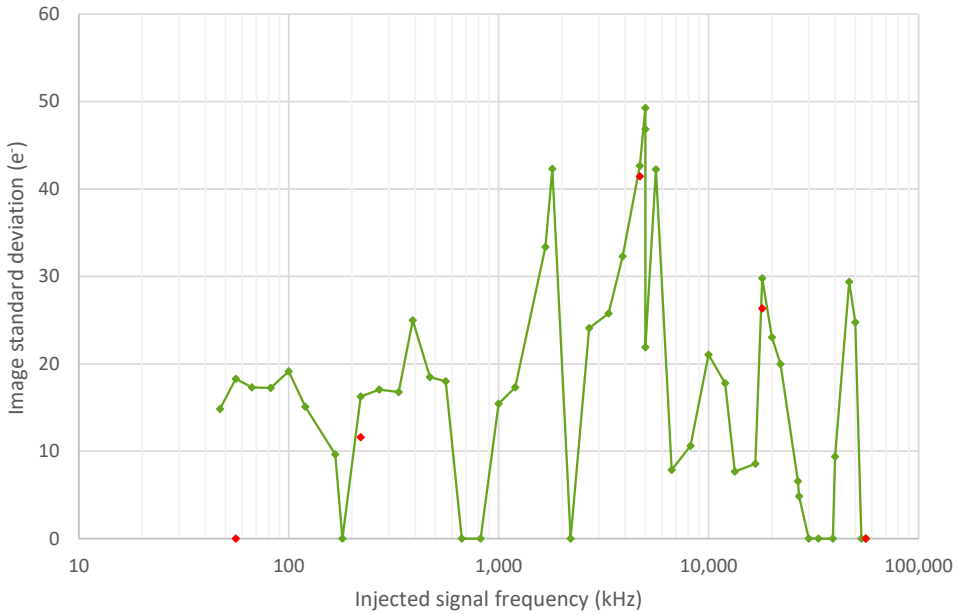

Figure 5.46: Image standard deviation as a function of injected DM interference frequency for the −6 V (VAN3) supply line. The five retested frequencies are plotted in red.

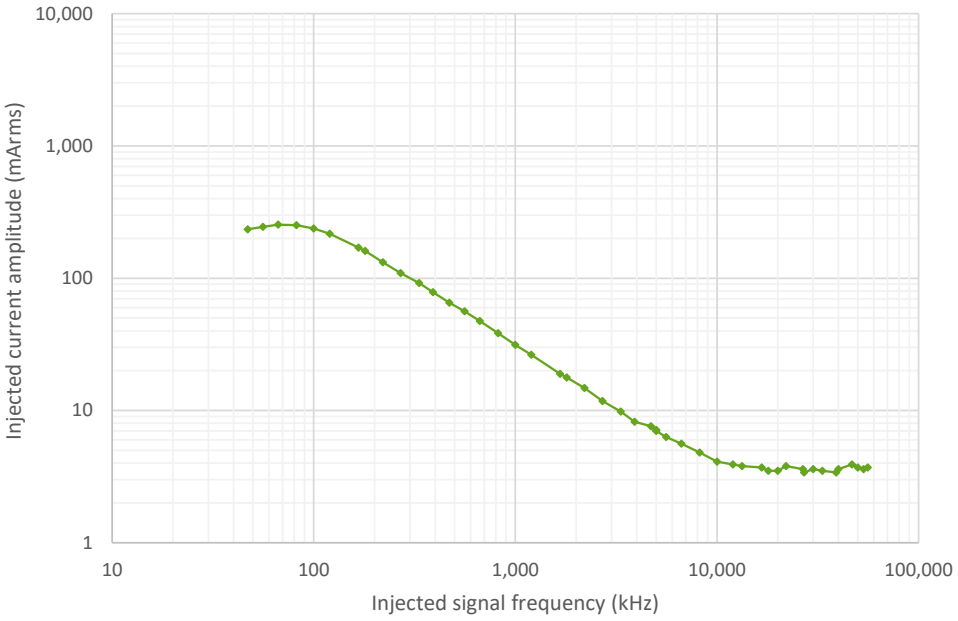

Figure 5.47: Injected DM current amplitude for the −6 V (VAN3) supply line.

Finally, Figure 5.48 shows the standard deviations from Figure 5.46 after scaling to an injected voltage amplitude for each tested frequency of

20 mVpk-pk.

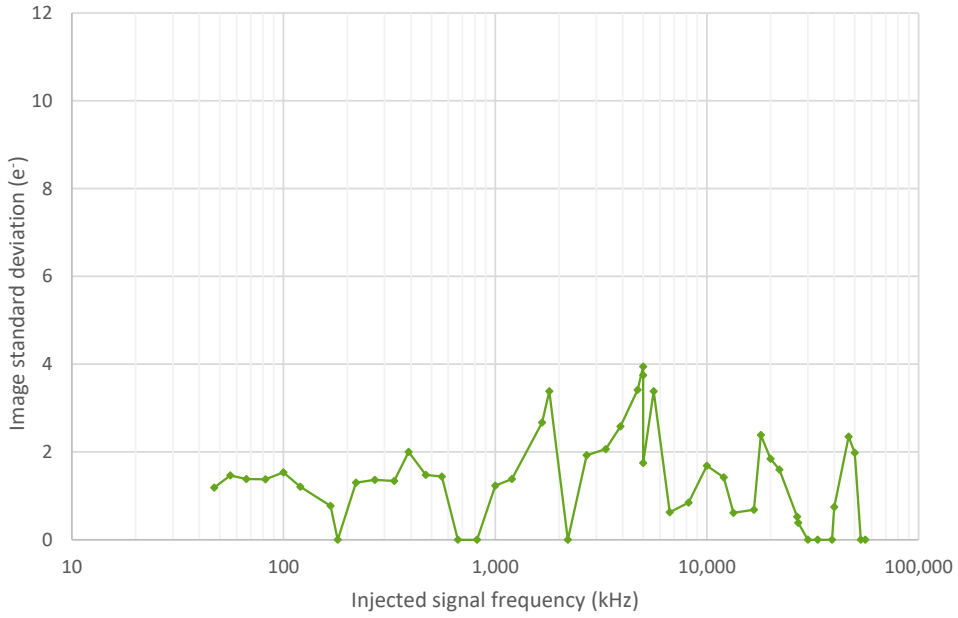

Figure 5.48: Scaled image standard deviation as a function of injected DM interference frequency for the −6 V (VAN3) supply line.

5.4.2.5 Differential Mode Conducted Susceptibility of the +6 V (VAN1) Supply Line

The susceptibility of the +6 V power supply line to the DM 250 mVpk-pk interference signal is shown in Figure 5.49, where the image standard deviation (after subtracting in quadrature 58 e^- read noise and the baseline noise) is plotted as a function of injected waveform frequency. The peaks at 3333.$\dot{3}$ kHz, 10 000 kHz and 30 000 kHz, and dips at 13 333.$\dot{3}$ kHz, 26 666.$\dot{6}$ kHz and 53 333.$\dot{3}$ kHz were also present in the simulation result. The data points for the five repeated frequencies (plotted in red) are located close to the original results.

As shown in Figure 5.50, the injected current amplitude curve peaks at ∼70 kHz and then decays exponentially to stabilise at the 3 mA rms level. This plot is almost an exact copy of the one obtained for the −6 V supply (Figure 5.47).

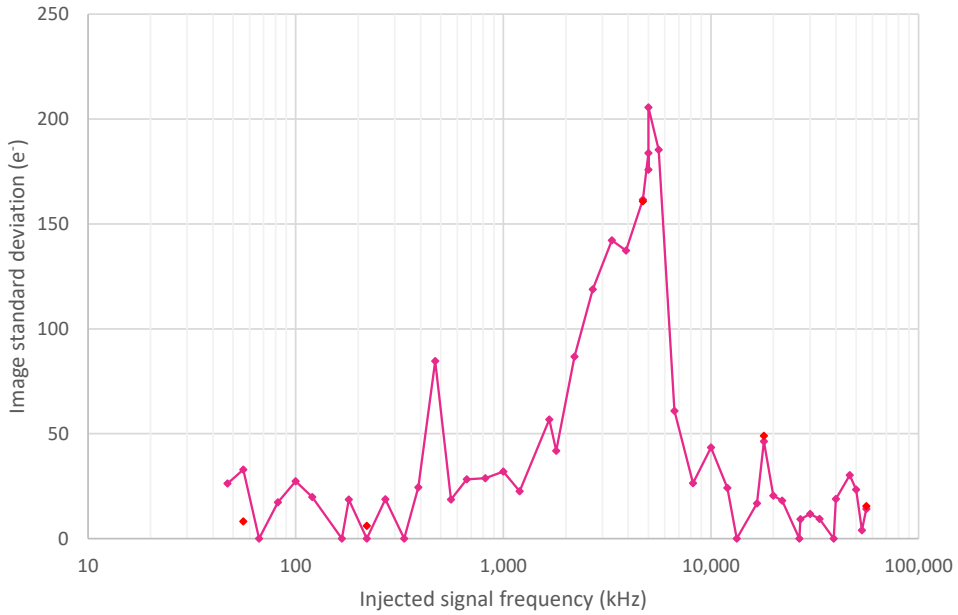

Figure 5.49: Image standard deviation as a function of injected DM interference frequency for the +6 V (VAN1) supply line. The five retested frequencies are plotted in red.

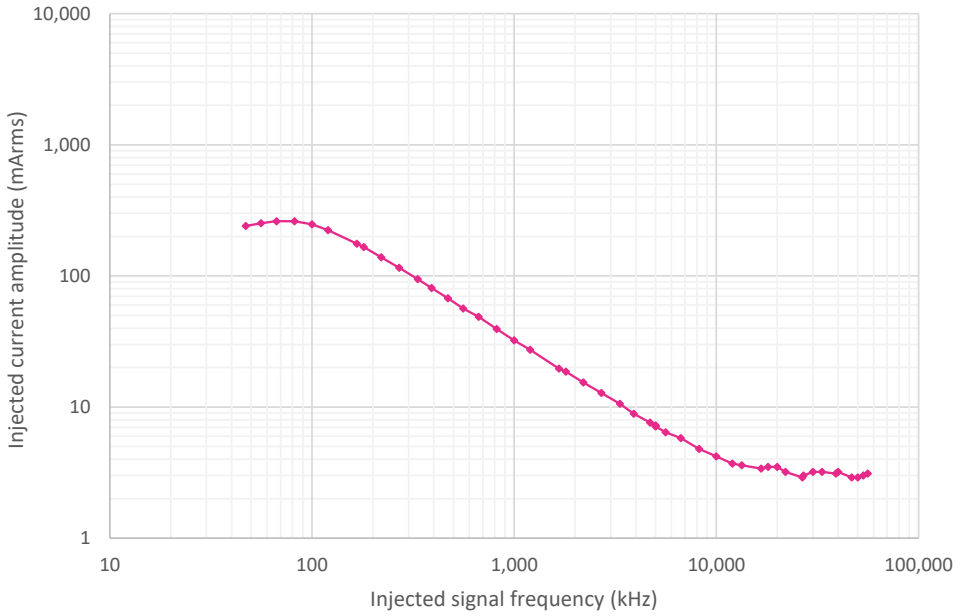

Figure 5.50: Injected DM current amplitude for the +6 V (VAN1) supply line.

The scaled image standard deviation plot, as shown in Figure 5.51, illustrates the +6 V supply line susceptibility to the injected 20 mVpk-pk voltage

amplitude for each tested interference frequency.

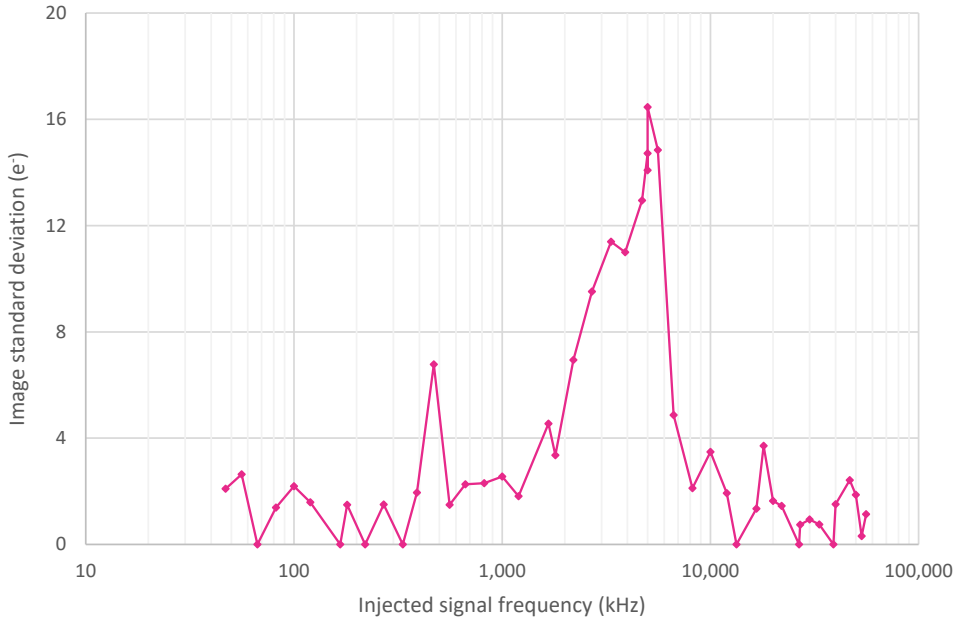

Figure 5.51: Scaled image standard deviation as a function of injected DM interference frequency for the +6 V (VAN1) supply line.

5.4.2.6 Differential Mode Conducted Susceptibility of the +3 V (VDIG_FPGA) Supply Line

The plot in Figure 5.52 shows the impact that injected CM 250 mVpk-pk interference signal has on the output image standard deviation across the tested frequency range (the standard deviations have 57 e^- read noise and the baseline noise subtracted in quadrature). There are three dips on this plot that were predicted by the simulation result: at 6666.$\dot{6}$ kHz, 13 333.$\dot{3}$ kHz and 20 000 kHz.

The curve in Figure 5.53 illustrates the measured injected current amplitude levels at each tested frequency. It peaks at ∼70 kHz and then decays exponentially until it reaches the plateau current of ∼4 mA rms.

The image standard deviation plot from Figure 5.52 scaled to 20 mVpk-pk of injected voltage is shown in Figure 5.54.

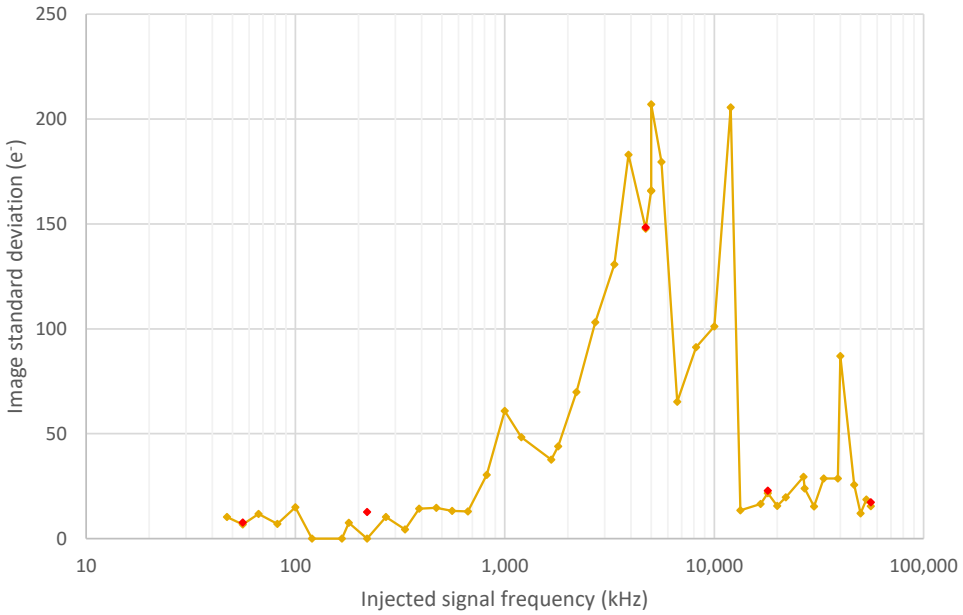

Figure 5.52: Image standard deviation as a function of injected DM interference frequency for the +3 V (VDIG_FPGA) supply line. The five retested frequencies are plotted in red.

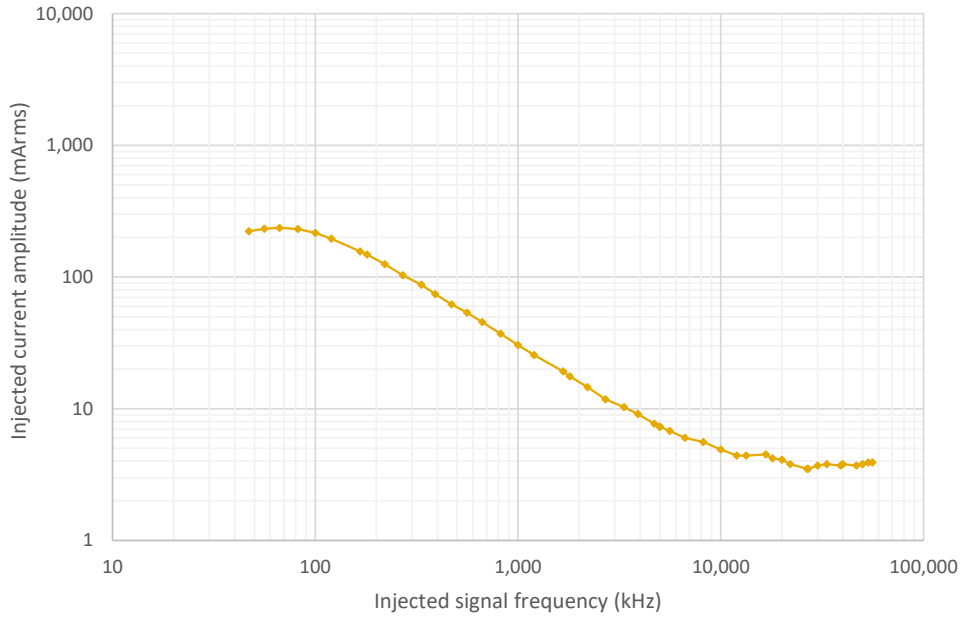

Figure 5.53: Injected DM current amplitude for the +3 V (VDIG_FPGA) supply line.

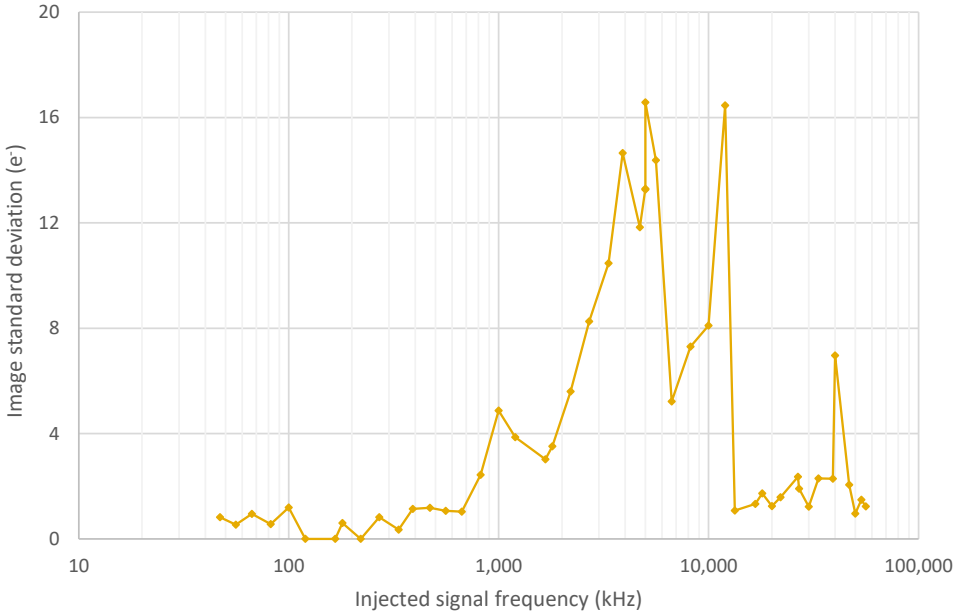

Figure 5.54: Scaled image standard deviation as a function of injected DM interference frequency for the +3 V (VDIG_FPGA) supply line.

5.4.2.7 Differential Mode Conducted Susceptibility of the +3 V (VAN2) Supply Line

The susceptibility of the +3 V power supply line to the 250 mVpk-pk DM sinusoidal interference is shown in Figure 5.55, where the image standard deviation with subtracted in quadrature 57 e^- read noise and baseline noise is plotted as a function of injected signal frequency. A peak at 10 000 kHz and two dips, one at 13 333.$\dot{3}$ kHz and another one at 26 666.$\dot{6}$ kHz, were also present in the simulation output. All five repeated measurements appear very close to the original results.

The amplitude of the injected current is plotted in Figure 5.56 as a function of the injected signal frequency. The curve has a gentle peak at ∼80 kHz, from where it decays exponentially to eventually level out at about 4 mA rms.

Finally, Figure 5.57 shows the standard deviations from Figure 5.55 after scaling to an injected voltage amplitude for each tested frequency of 20 mVpk-pk.

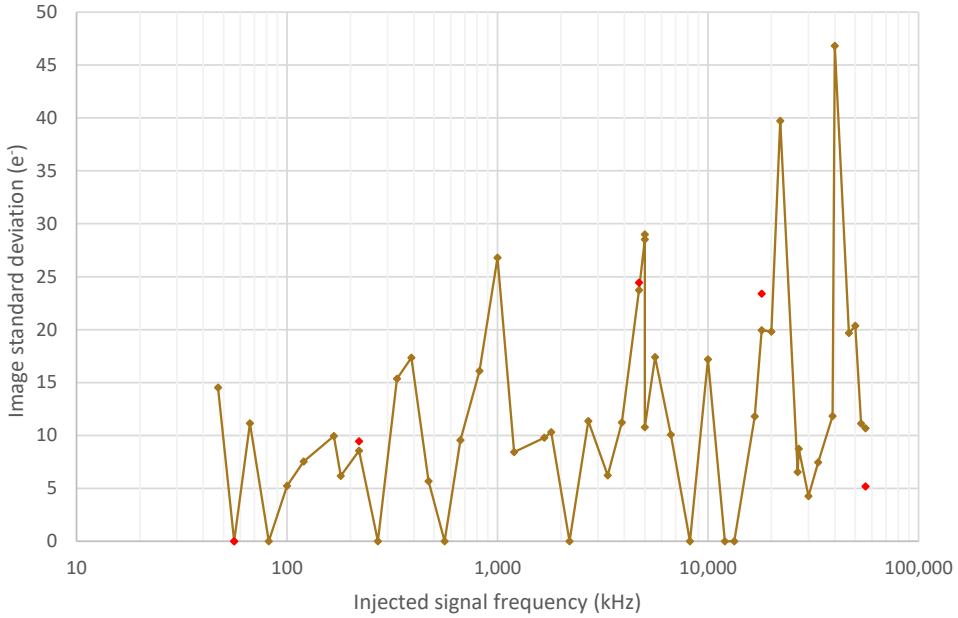

Figure 5.55: Image standard deviation as a function of injected DM interference frequency for the +3 V (VAN2) supply line. The five retested frequencies are plotted in red.

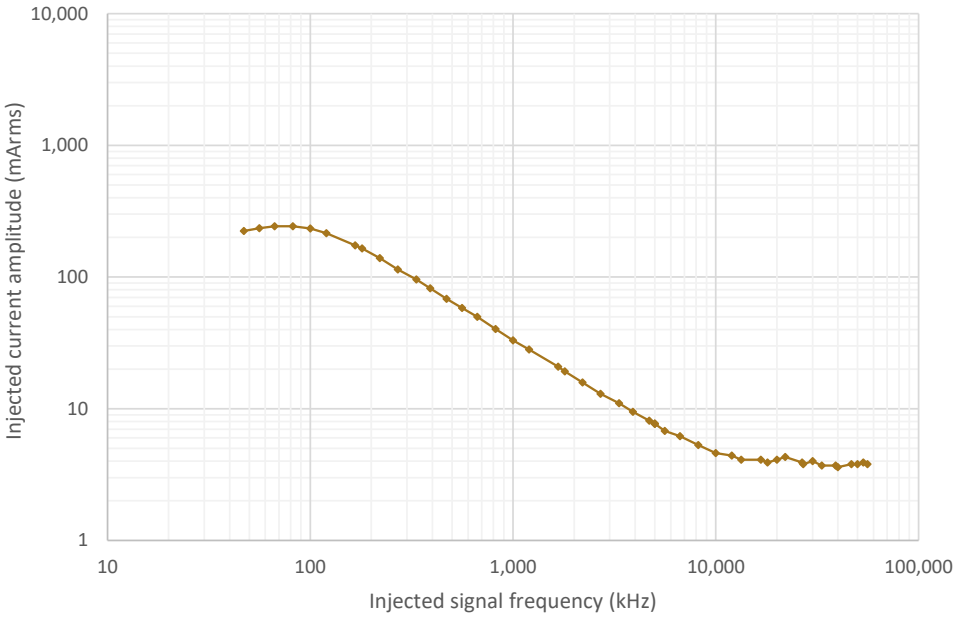

Figure 5.56: Injected DM current amplitude for the +3 V (VAN2) supply line.

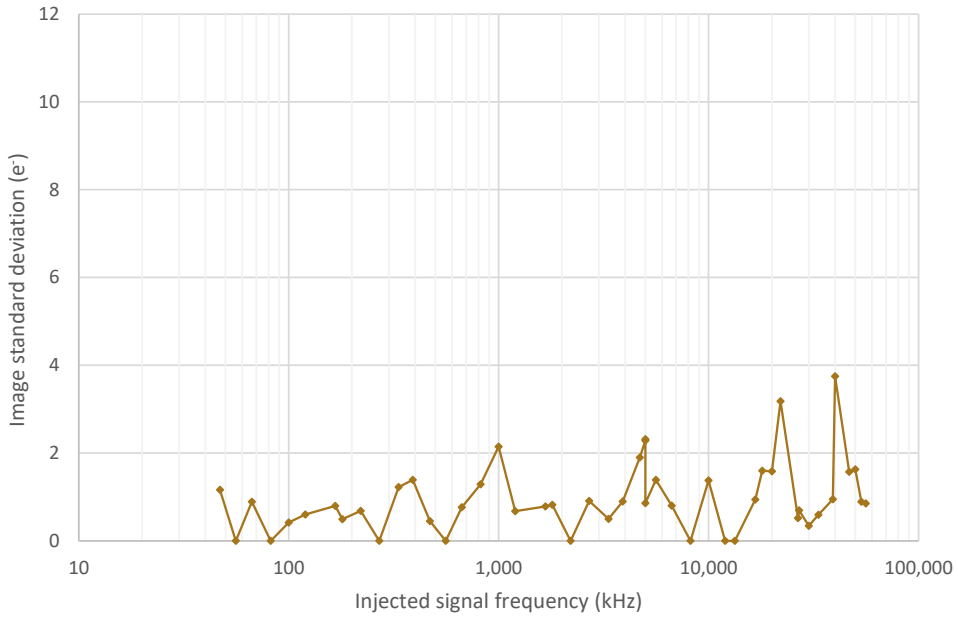

Figure 5.57: Scaled image standard deviation as a function of injected DM interference frequency for the +3 V (VAN2) supply line.

5.4.2.8 Combined Results from the Differential Mode Conducted Susceptibility Measurements

In order to directly compare sensitivities of each of the individual N-FEE power lines to the DM interference, the combined image standard deviation plot is shown in Figure 5.58.

The combined plot of the injected DM current amplitudes is shown in Figure 5.59. All the curves are very similar, especially between 100 and 10 000 kHz.

Table 5.3 provides a list of all the tested frequencies and the corresponding standard deviations for each of the PLATO N-FEE power supply lines. The measured standard deviations were scaled to demonstrate susceptibility of individual power lines that would be measured if the injected interference signal was 20 mVpk-pk.

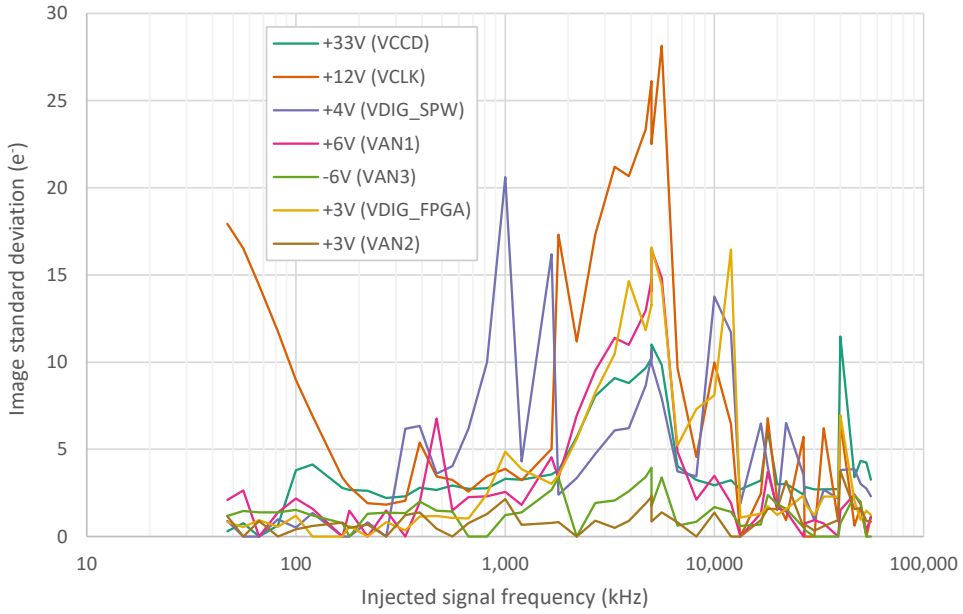

Figure 5.58: Image standard deviation as a function of injected DM interference frequency for all the tested N-FEE power lines. The image standard deviation values were scaled to the levels equivalent to 20 mVpk-pk injection.

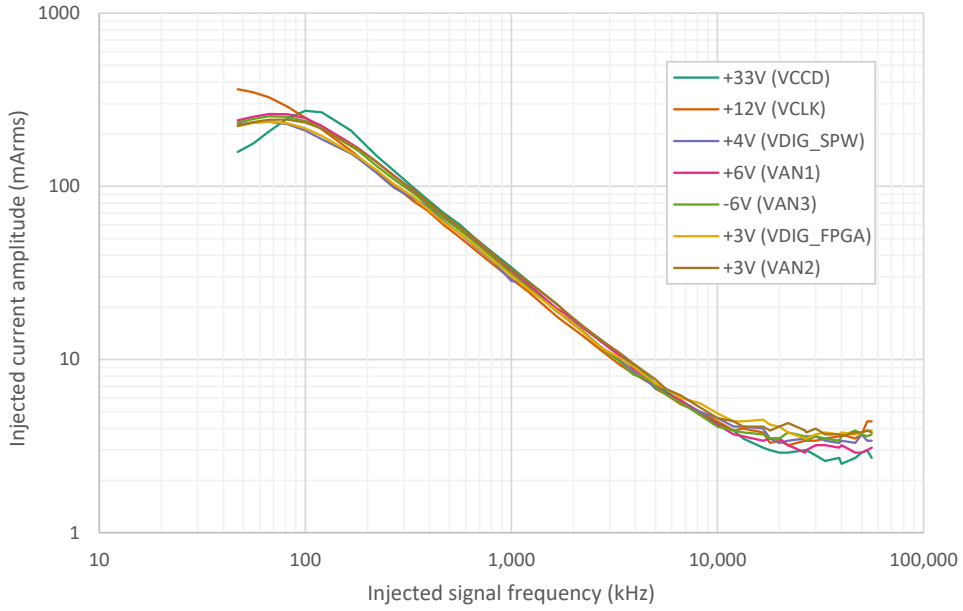

Figure 5.59: Injected DM current amplitudes.

Injected freq. [kHz]	Scaled image standard deviation [e$^-$]						
	+33V VCCD	+12V VCLK	+4V VDIG_ SPW	-6V VAN3	+6V VAN1	+3V VDIG_ FPGA	+3V VAN2
47	5.0	18.8	5.2	5.3	5.7	5.1	5.2
56	5.1	17.4	5.1	5.3	5.9	5.1	5.1
67	5.0	15.5	5.0	5.3	5.2	5.2	5.2
82	5.1	13.0	5.3	5.3	5.4	5.1	5.0
100	6.3	10.6	5.2	5.3	5.7	5.2	5.1
120	6.5	8.9	5.3	5.3	5.5	5.1	5.1
167	5.7	6.5	5.1	5.2	5.1	5.1	5.2
180	5.7	6.3	5.2	5.1	5.5	5.1	5.1
220	5.7	5.9	5.2	5.3	5.1	5.1	5.1
270	5.5	5.9	5.0	5.3	5.5	5.1	5.0
333	5.5	6.0	8.1	5.3	5.1	5.1	5.2
390	5.8	7.8	8.2	5.5	5.6	5.2	5.3
470	5.7	6.6	6.3	5.3	8.6	5.2	5.1
560	5.8	6.5	6.6	5.3	5.5	5.2	5.1
667	5.7	6.2	8.1	5.1	5.7	5.2	5.2
820	5.7	6.6	11.3	5.1	5.7	5.6	5.3
1000	6.0	6.8	21.3	5.3	5.8	7.0	5.5
1200	6.0	6.5	6.7	5.3	5.5	6.4	5.1
1667	6.2	7.5	17.0	5.8	6.9	5.9	5.2
1800	6.3	18.2	5.7	6.1	6.2	6.2	5.2
2200	7.6	12.5	6.2	5.0	8.7	7.6	5.1
2700	9.5	18.2	7.0	5.5	10.9	9.7	5.2
3333	10.4	21.9	8.0	5.5	12.5	11.6	5.1
3900	10.1	21.4	8.1	5.7	12.2	15.5	5.2
4700	10.9	24.0	10.1	6.2	14.0	12.9	5.4
5000	12.0	26.5	11.9	6.3	15.0	14.2	5.6
5600	11.0	28.7	9.5	6.1	15.7	15.2	5.3
6667	6.4	11.2	6.4	5.2	7.2	7.3	5.2
8200	6.0	7.2	6.2	5.2	5.7	8.9	5.1
10 000	5.8	11.4	14.7	5.4	6.3	9.6	5.3
12 000	6.0	8.5	12.8	5.3	5.6	17.2	5.1
13 333	5.7	5.4	5.5	5.2	5.1	5.2	5.1
16 667	6.0	6.1	8.3	5.2	5.4	5.3	5.2
18 000	7.9	8.8	6.5	5.6	6.4	5.4	5.3
20 000	5.9	6.0	5.4	5.4	5.5	5.2	5.3
22 000	5.9	5.7	8.3	5.4	5.4	5.3	6.0
26 667	5.6	8.0	6.3	5.1	5.2	5.6	5.1
27 000	5.8	5.5	5.7	5.1	5.3	5.4	5.1
30 000	5.7	5.3	5.3	5.1	5.3	5.2	5.1
33 333	5.7	8.4	5.8	5.1	5.3	5.6	5.1

39 000	5.7	5.7	5.6	5.1	5.2	5.6	5.2
40 000	12.5	8.6	6.4	5.2	5.5	8.6	6.3
46 667	6.1	5.6	6.5	5.6	5.8	5.5	5.3
50 000	6.6	5.8	6.0	5.5	5.6	5.2	5.4
53 333	6.6	5.5	5.9	5.1	5.3	5.3	5.2
56 000	6.0	5.7	5.7	5.1	5.4	5.2	5.2

Table 5.3: Scaled image standard deviations values obtained from the DM CS measurements for each individual power supply line. For clarity, some frequencies are rounded to the nearest kHz.

The results from this section are discussed in Section 5.5.

5.5 Conclusions and Further Work

The study presented in this chapter was carried out in order to investigate the sensitivity of each of the seven PLATO N-FEE power supply lines to CM and DM sinusoidal interference signals, covering the frequency range from 50 kHz to 50 MHz. The main conclusions of the study are given below:

- After comparing Figures 5.34 and 5.58 it is clear that the N-FEE is much more sensitive to the CM interference than to the DM (image standard deviation values resulting from the CM measurements are an order of magnitude higher than those emerging from the DM test). This is not a surprising result. The undesirable effects caused by the conductively coupled noise can be reduced by using specially designed filters. The ability of such filters to meet the EMC requirements is discussed in Chapter 7.

- Even though the CDS is one of the key components that can affect the frequency response of the N-FEE, the simulation output shown in Figure 5.6 has only a weak correlation with the CM and DM image standard deviation plots (Figures 5.34 and 5.58 respectively). While some individual points of correlation exist and there is a broadly similar envelope shape, detailed correlation is absent. This suggests that noise was also getting through other parts of the circuit and that there were

other effects that played a bigger role. It was beyond to scope of the work to perform a full analysis of the circuit, especially recognizing that noise can penetrate through such elements as capacitive coupling between PCB layers. Nevertheless, a fuller simulation of the next generation of the N-FEE breadboard would be informative (e.g. using a software tool). This is currently under review within the N-FEE design team.

- Figure 5.9 has shown that the noise injected directly into the CDS circuit generated a very similar effect to the one predicted by the simulation, proving that the simulation method was correct.

Regarding the future work, it could be beneficial to extend the range of tested frequencies for the DM measurements, in order to cover the whole required spectrum (starting from 10 Hz up to 50 MHz). Such a work, applied to the next N-FEE breadboard including improved layout and filtering, could be completed using the same technique that was demonstrated in this chapter, but with a different ICP that would cover the lower part of the frequency spectrum. Also, it might be necessary to conduct a similar study again, once the next iteration of the PLATO N-FEE board is available. Finally, the setup could be further improved by tracking and removing the source of the baseline noise that was present in the data.

Overall the general viability of the design has been demonstrated empirically. The next generation of breadboard can be expected to have better noise immunity and less cross-coupling (with, e.g. additional ground planes) and so we can expect better correlation with the simulations. Moreover, the simulations could be improved with additional design details but whether a fully representative simulation is practical remains to be seen.

Chapter 6

Temperature Sensitivity of CCD Output Stage and PLATO Normal-Front-End Electronics

The purpose of the following study was to investigate temperature sensitivities of the CCD output stage and PLATO N-FEE. As there was no access to the intended for PLATO CCD270, an alternative detector was used. CCD47-20, also made by Teledyne e2v, uses a very similar output circuit, which made it an ideal candidate. While the CCD47-20 is a commercial device, temperature sensitivity data of the form described here is not available either from the supplier or in published works.

The test was divided into two main parts. The first one focused entirely on the CCD, while the second one concentrated on the PLATO N-FEE board temperature sensitivity measurements. The digital output from the N-FEE is of the form:

$$y = mx + c, \tag{6.1}$$

where y (in ADU) is the digital output, m (in ADU/e^-) is the system gain, x (in e^-) is the CCD signal and c (in ADU) is a constant ADC offset. In practice, m is composed of a proportion m_{ccd} due to the CCD and a proportion m_{fee} due to the N-FEE; and similarly, c consists of c_{ccd} and c_{fee}. The two m values

and two c values are all generally functions of temperature, approximately linear over a range of temperatures, so that Equation 6.1 becomes:

$$y = m_{ccd}(T_{ccd})x + m_{fee}(T_{fee})x + c_{ccd}(T_{ccd}) + c_{fee}(T_{fee}). \tag{6.2}$$

For PLATO, stability of the measurement of the signal (x in Equation 6.2) is paramount, so it is necessary to know the temperature dependence of the m and c terms. The remainder of this chapter concerns experiments conducted to measure these m (representing the gain) and c (representing the offset) terms for the breadboard N-FEE, to inform the development of subsequent N-FEE models and also algorithms for processing the N-FEE data.

6.1 Temperature Sensitivity of the CCD Output Stage

6.1.1 Experimental Setup

Depending on the purpose of the measurement, two different setup configurations were used. Figure 6.1 shows the basic experimental setup block diagram intended for measuring the CCD output offset temperature sensitivity. The setup consists of the following hardware:

- PLATO N-FEE: BB_V1 (MSSL),
- CCD: CCD47-20 (Teledyne e2v),
- N-FEE DC Power Supplies: QL355TP and PL303QMD-P (TTi),
- Heater Power Supply: PL303QMD-P (TTi),
- Digital Multimeters (DMMs): 34461A (Keysight Technologies),
- Laptop PC: XPS 15 9530 (Dell),
- USB to SpaceWire Interface: SpaceWire Brick Mk2 (STAR-Dundee),

- Heater Element R_1: HS10 Series 150 Ω 10 W (Arcol),
- NTC Thermistor R_{T1}: B57703M Series 10 kΩ (Epcos),
- NTC Thermistor R_{T2}: 44908 10 kΩ (YSI),
- Isolation Box: NB 80 V1 MC (Newbox).

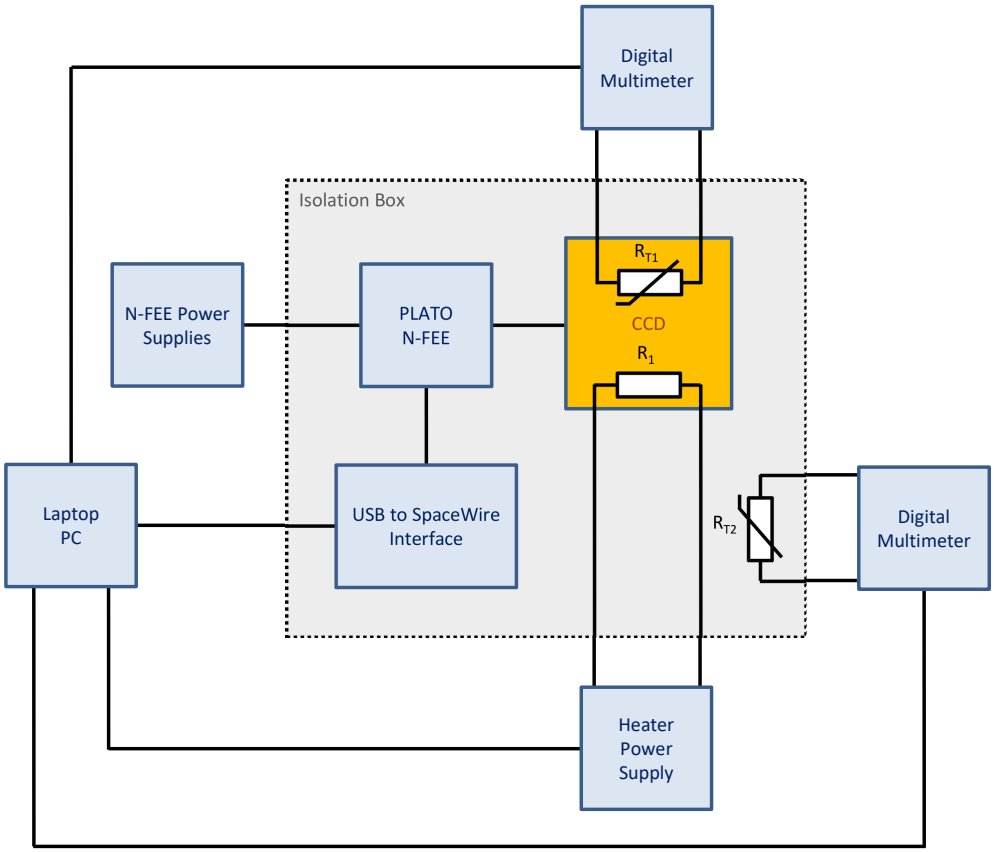

Figure 6.1: Setup block diagram for the CCD output offset temperature sensitivity test.

The CCD was operated in a reverse clocking mode, i.e. with the output registers clocked in a reversed direction. Such a technique allows for isolating the sensor's output stage from the influence of the rest of the detector and, as a result, avoids dark current issues at room temperature so that the offset change with temperature can be measured without signal (the CCD was not cooled). The CCD temperature was varied with the 150 Ω power resistor (R_1) serving

as a heater, and measured with the thermistor (R_{T1}). Both elements were glued to the back of the imaging sensor (see Figure 6.2), with the thermistor positioned 'above' the CCD output stage structure for more accurate readings. The heater was powered from the PC controlled bench PSU, whose varying

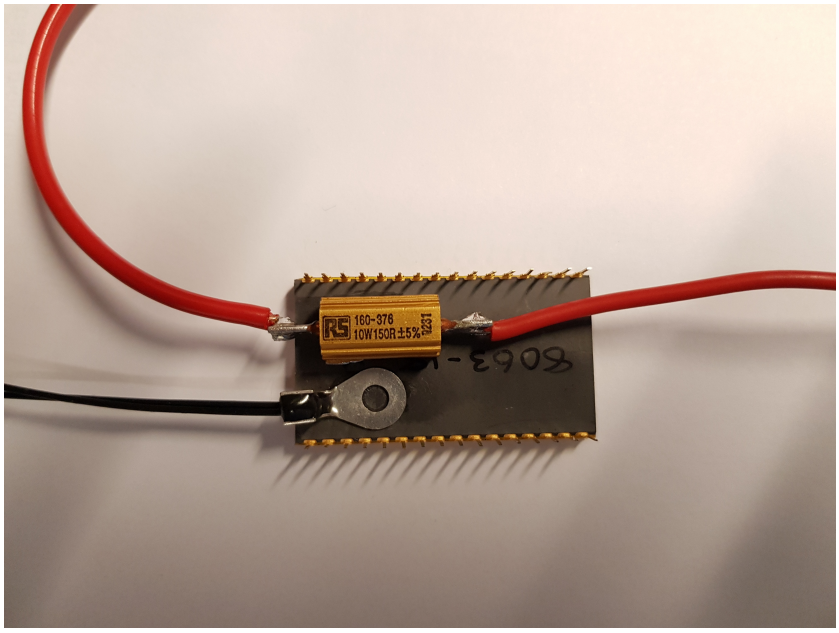

Figure 6.2: Heater element and thermistor on the back of the CCD detector.

voltage, a pre-programmed sine wave, was inducing proportional changes in power dissipated (as heat) by the resistor in accordance with the following equation:

$$P = \frac{V^2}{R} \tag{6.3}$$

where V is the voltage across the resistor (in V) and R is the resistance of the same resistor (in Ω).

As the temperature in the laboratory was controlled by the air-conditioning unit, it was necessary to encapsulate the CCD together with the PLATO N-FEE and, due to the limited interface cable length, also the SpaceWire brick in the electrically dissipative container with a good temperature stability, to protect them from the air blown by the air conditioner. The temperature inside the isolation box was monitored by the thermistor R_{T2}.

A LabVIEW Virtual Instrument (VI), specially created for this experiment (see the schematic in Figure 6.3), was used to regulate the heater power supply's voltage level in a predefined fashion, to periodically trigger synchronous readouts from the multimeters measuring the resistances of the two thermistors, and to save these measurements into an Excel file. The

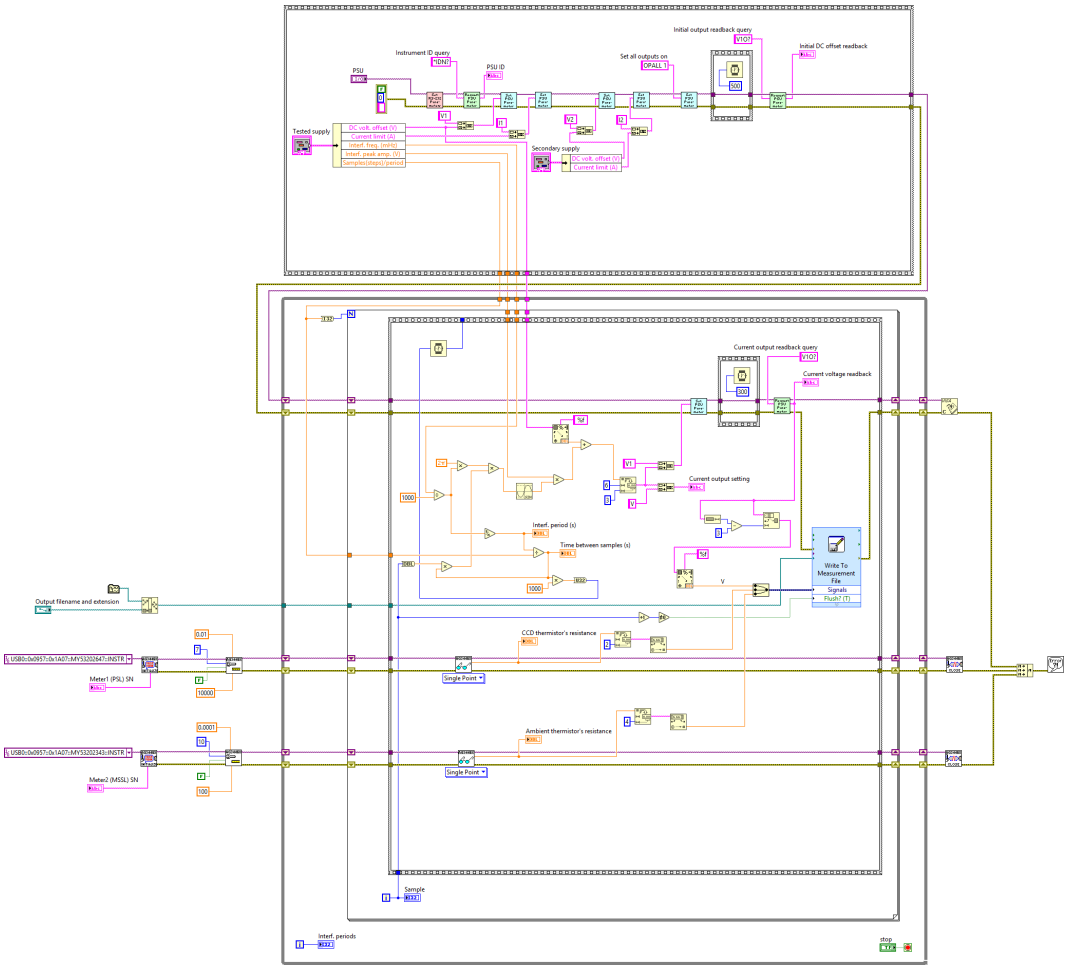

Figure 6.3: LabVIEW Virtual Instrument designed to control and monitor the temperature sensitivity test.

heater's PSU was programmed to output a $0.8\dot{3}$ mHz sine wave, (i.e. with a period of 20 min) with 0 to 10 V voltage swing. The voltage level was regulated in steps, once every 10 s. The 20 min period was chosen as a trade-off; using a significantly shorter period would limit the temperature variation achievable using the power supplies, while using a much longer period would extend the duration of the test unnecessarily.

In parallel with the multimeters' readouts, a single 512 × 512 image frame was automatically acquired and saved to the PC every 10 s, using a modified SpaceWire brick software utility program (the modification was not part of this thesis). The test was terminated after completing two full cycles of the heater's supply voltage (∼40 min). In the next step, the images were processed with the python code from Appendix D, which generates a text file output containing mean ADC values and image standard deviations calculated for each processed image frame. In the case of the standard deviations, it was necessary to divide each image into two separate image-halves (each containing either the odd or even columns' data) before doing the calculations, to overcome a problem caused by the ADCs introducing an undesirable effect of alternating pixel-wide brighter and darker columns as a consequence of the different gain and offset figures from each ADC (see Section 5.3.1 and Figure 5.12 for more details). While the standard deviations were calculated for each image-half separately, the mean ADC values were derived from the whole (complete) image frames. The results were then used for making the relevant plots and to derive the CCD output's offset temperature coefficient.

To measure the gain dependence on temperature, two sets of measurements were conducted. In the first scenario, the detector was set up to output a pseudo-video signal that represented approximately the correct video waveform for a half-full-well signal. In the second scenario, the CCD generated a 'zero-signal' output, containing just the offset values.

Figure 6.4 shows the block diagram of the setup used for measuring the CCD output generating the pseudo-video signal. The CCD was reverse-clocked, hence it was not possible to measure the real signal output from the detector. To overcome this issue, a few connections between the CCD and the N-FEE were modified to allow for generating the pseudo-video signal output. In the normal CCD operation mode, the ϕR (reset pulse for the output node) pin (see Figure 6.5 for the complete CCD47-20 pinout) is connected to the N-FEE, where the correct reset pulse is generated at the beginning of

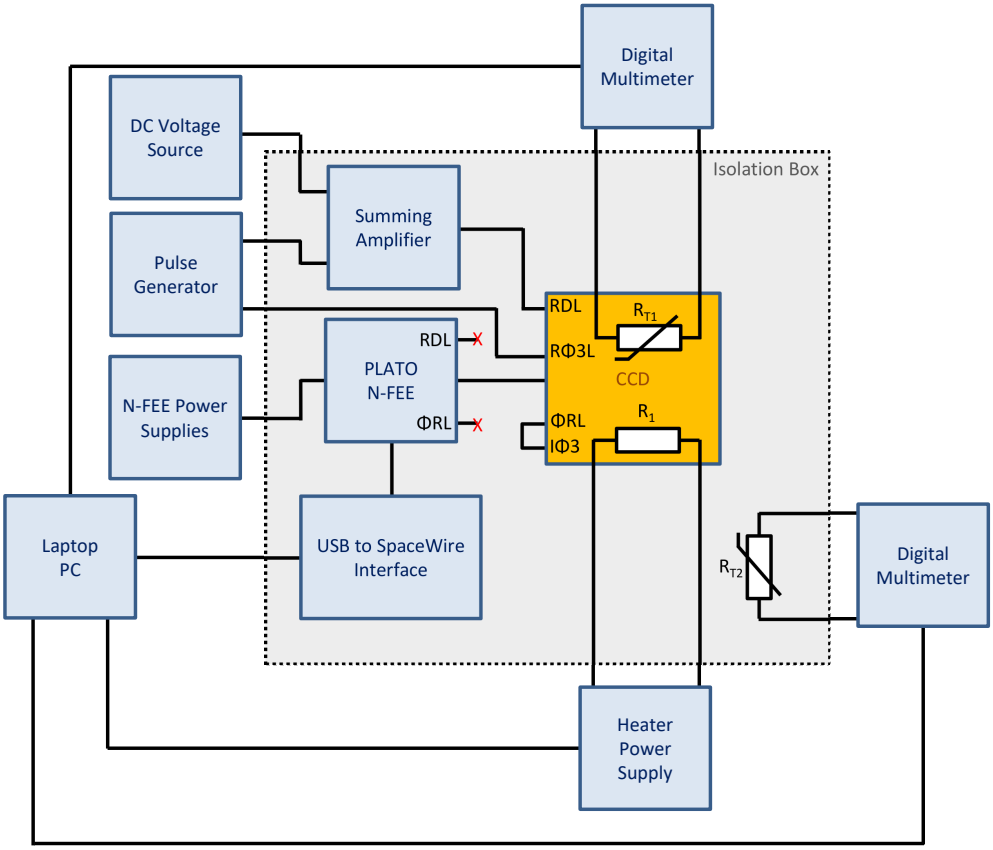

Figure 6.4: Setup block diagram used for measuring the CCD output generating a pseudo-video signal.

each pixel readout period. Such a pulse, when fed into the reset Field-Effect Transistor (FET)'s gate (ϕR), switches this transistor into its active state for the duration of the pulse, which in turn resets the CCD output reset level to a voltage present on the reset transistor drain RD (details of the CCD47-20 output are shown in Figure 6.6). In the described setup, connections between RDL (CCD pin 8) and N-FEE, as well as ϕRL (pin 13) and N-FEE were interrupted, as shown in Figure 6.7. Instead, ϕRL was connected to the image area clock $I\phi 3$ (pin 3), in order to activate the reset FET for the whole line readout period (because the N-FEE CCD270 drivers were mapped to suit the CCD47-20's 3-phase register, the $I\phi 3$ clock of the latter was 'high' during the row readout). This way, it was possible to input the pseudo-video signal through the RDL pin rather than through the output serial register and out-

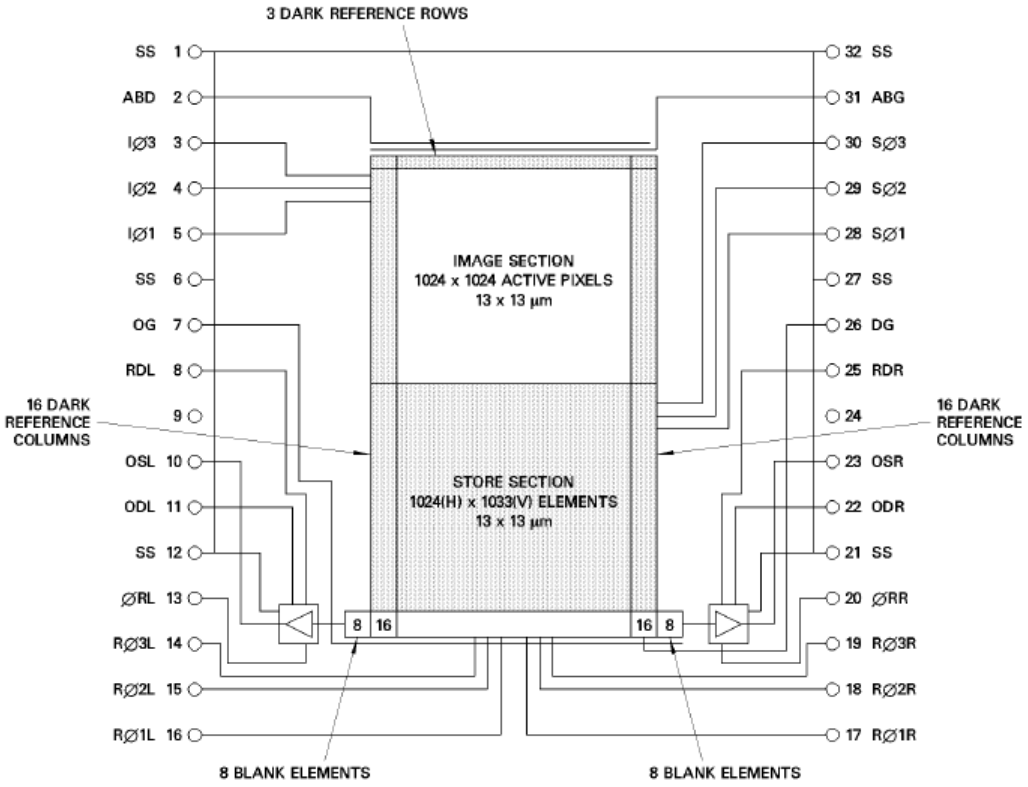

Figure 6.5: CCD47-20 schematic (adopted from E2V Technologies (2011)).

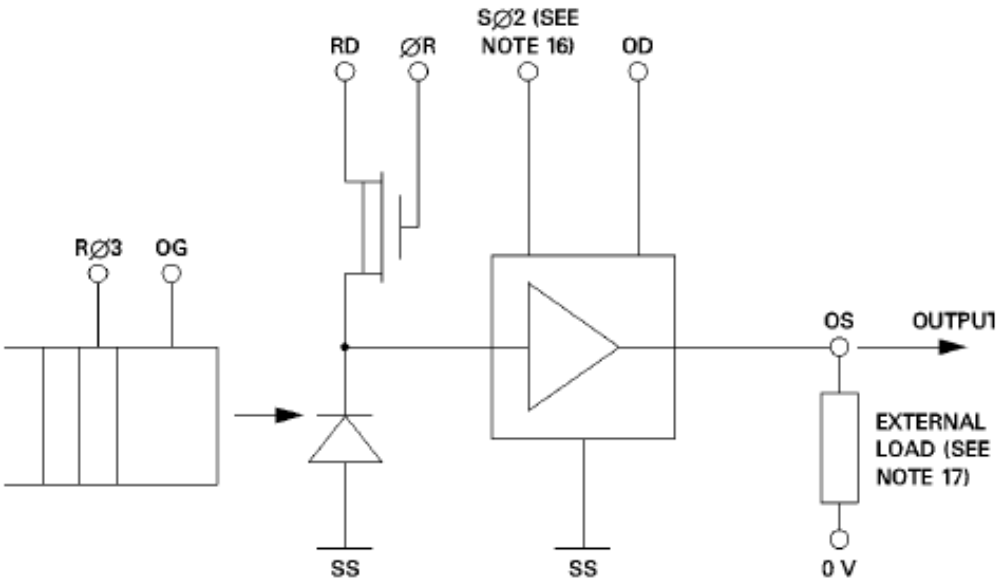

Figure 6.6: CCD47-20 output circuit (from E2V Technologies (2011)).

put gate, as usually happens when operating the CCD in the normal mode (i.e. with the real output signal). The pseudo-video waveform was generated using

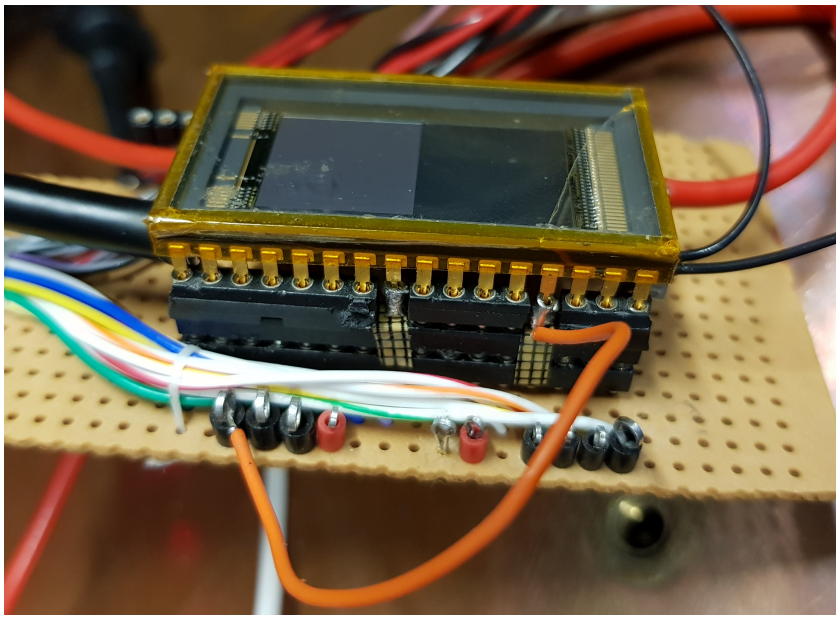

Figure 6.7: Photograph of the modifed socket for the CCD47-20 detector.

a Philips PM 5786B pulse generator, an additional TTi PL303QMD-P bench PSU, a non-inverting summing amplifier (see Figure 6.8 for more details) and the CCD output register clock $R\phi 3L$ (pin 14). The pulse generator was externally triggered from the $R\phi 3$ pin, once per pixel period. Each generated pulse was combined in the summing amplifier with the offset voltage from the DC voltage source, forming the pseudo-video waveform that was an equivalent of a half-full-well signal (typically for the CCD47-20 detector, the RD reset voltage level is about 17 V and the half-full-well signal adds an extra ∼1 V on top of that). The experiment was conducted in the same way as the initial CCD output offset temperature sensitivity measurements. The Labview VI was regulating a voltage of the heater resistor, reading resistances of the two thermistors and saving all the measurements into the Excel file. Simultaneously, 512×512 image frames were acquired using the modified SpaceWire utility program. The test was terminated after completing about 3.5 cycles of the heater's supply voltage (∼70 min).

The same setup as in Figure 6.1 was used for the second part of the CCD output gain temperature sensitivity measurements, however no pseudo-video signal was generated this time and the summing amplifier was outputting

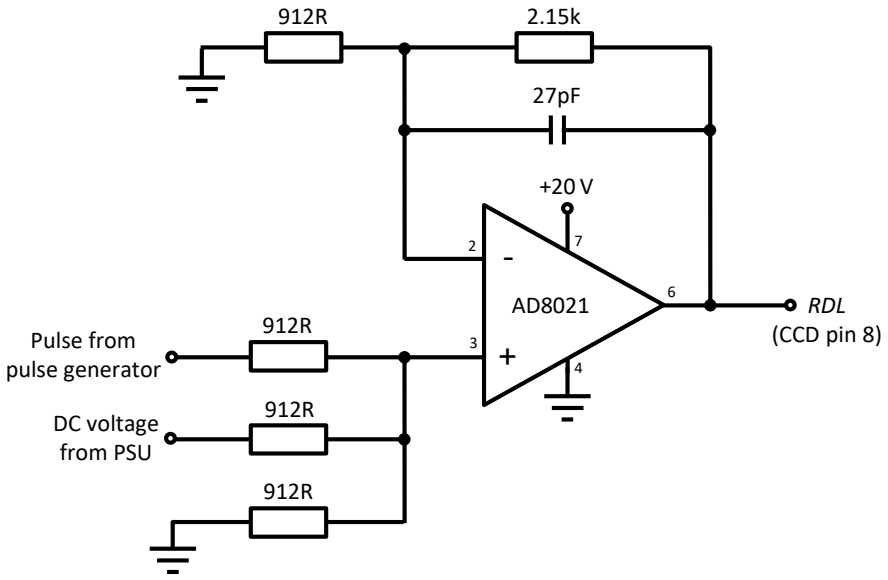

Figure 6.8: Circuit diagram of the non-inverting summing amplifier based on the Analog Devices' AD8021 chip. To improve the schematic readability, it does not show the additional 1 nF capacitor between the supply pins 4 and 7, and the 6.8 pF compensation capacitor that was used between pins 4 and 5 (pin 5 is also not shown).

just an offset voltage. All the previous connections were preserved, the only difference was that the external trigger input of the pulse generator was disabled, so no pulses were generated. The experiment was conducted using the same procedure as described above for the first part of the CCD output gain temperature sensitivity measurements.

6.1.2 Results

6.1.2.1 CCD Output Offset Sensitivity Measurement

Figure 6.9 shows the average ADC value and CCD and ambient (inside the isolation box) temperatures plotted as a function of the sample number (samples were acquired every 10 s). The CCD temperature and average ADC value curves are correlated.

The plot in Figure 6.10 shows the 'zero-signal' CCD output average ADC value (offset) as a function of the CCD temperature. The overwhelming linear dependency with temperature is clear, and in addition the departure from the

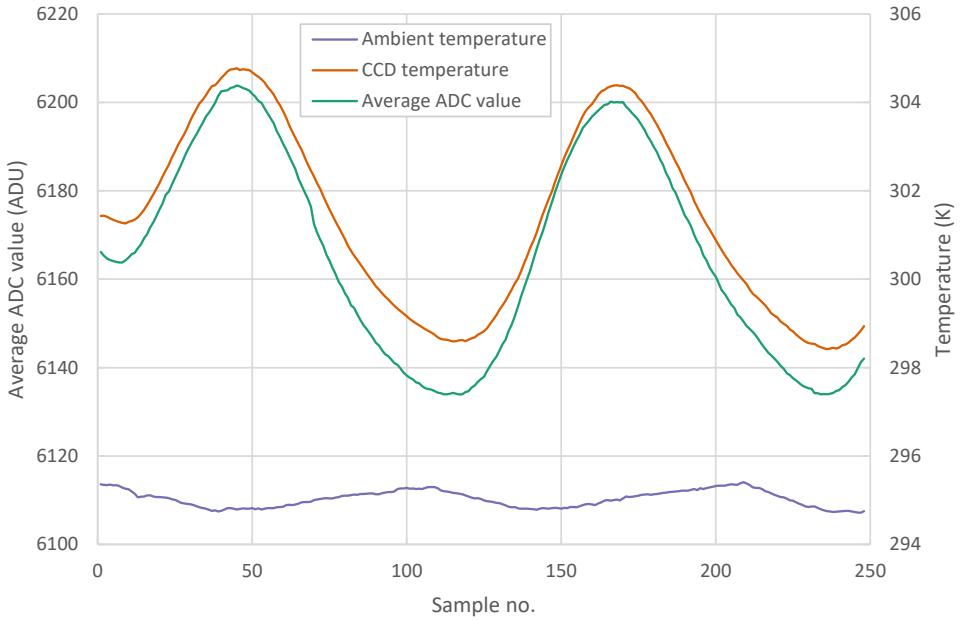

Figure 6.9: Average ADC value, CCD temperature and ambient temperature plotted as a function of sample number for the CCD output offset temperature sensitivity study.

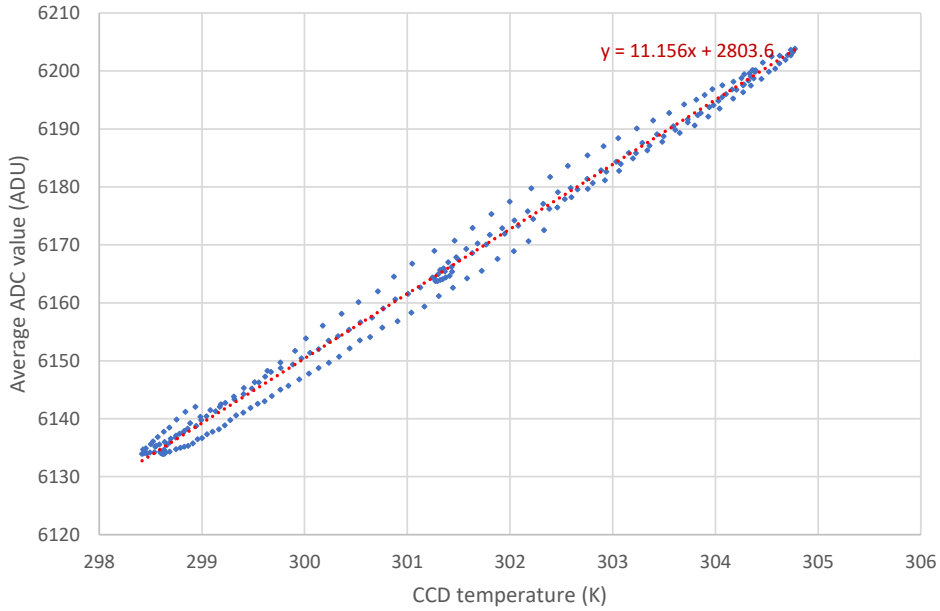

Figure 6.10: CCD output average pixel value as a function of absolute CCD temperature. The best fit line and its equation are shown in red.

straight line fit is a hysteresis effect due to the time delay in the transfer of heat from the heater resistor to the CCD output node and the thermistor.

From the plot, the CCD output offset temperature coefficient is 11.2 ADU/K.

The odd and even image-halves standard deviations are plotted as a function of CCD temperature in Figures 6.11 and 6.12 respectively. There is no

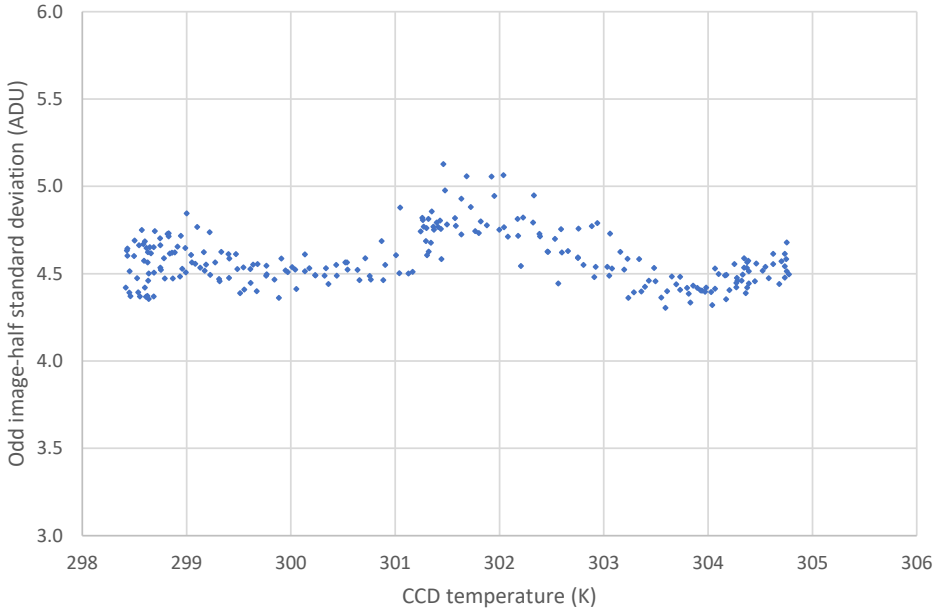

Figure 6.11: Odd image-half standard deviation versus CCD temperature.

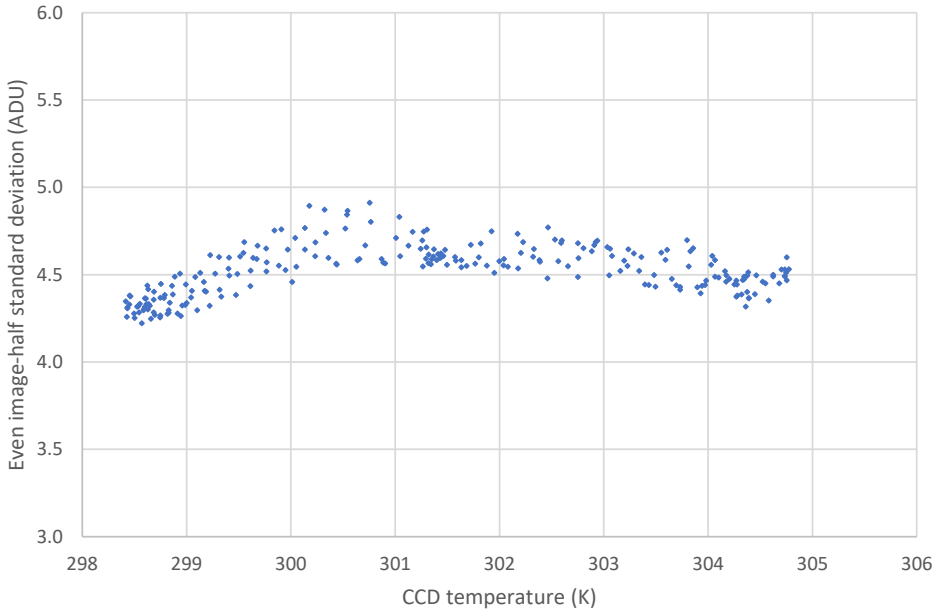

Figure 6.12: Even image-half standard deviation versus CCD temperature.

clear evidence of temperature effect on noise within the tested temperature range.

6.1.2.2 CCD Output Gain Sensitivity Measurement

The plot of the average ADC value along with the CCD and ambient temperatures acquired for the part of the CCD output gain sensitivity measurements where the detector generated the 'zero-signal' output (i.e. offset only) is shown in Figure 6.13. Clearly there is an anticorrelation between the average ADC

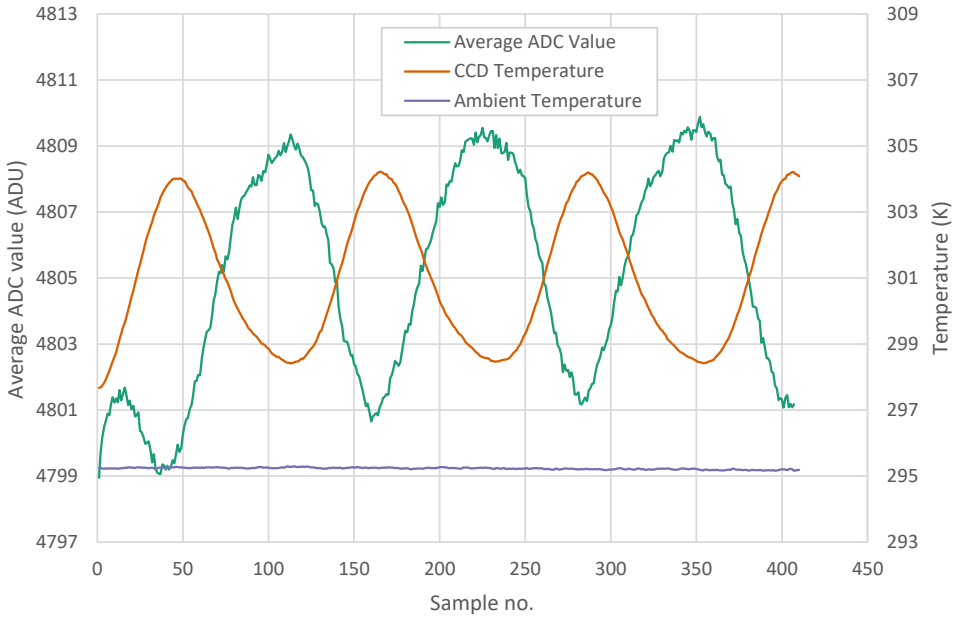

Figure 6.13: Average ADC value and CCD and ambient temperatures obtained for the 'zero-signal' scenario of the CCD output gain temperature sensitivity study.

value and CCD temperature. The ambient temperature (inside the isolation box) was very stable throughout the test.

The average ADC value plotted as a function of absolute CCD temperature is shown in Figure 6.14 (the ADC values contain both the pseudo-video signal, zero in this case, and the offset). Just as in the case of the plot from Figure 6.10, there is a similar hysteresis effect, however the dominating linear dependency with temperature is very clear. The CCD output temperature

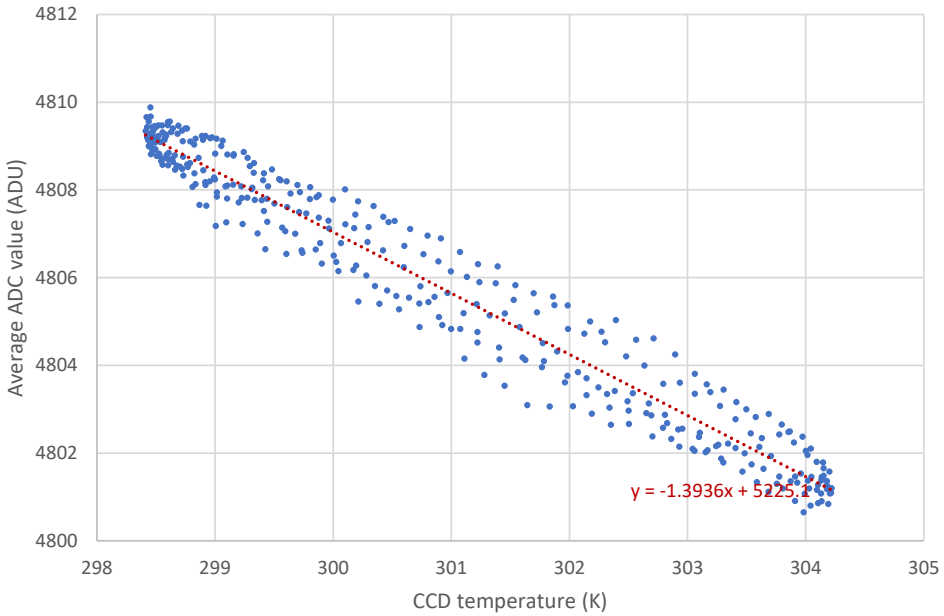

Figure 6.14: Average pixel value as a function of CCD temperature for the 'zero-signal' scenario of the gain sensitivity study. The best fit line and its equation are shown in red.

coefficient of the offset (taken from the best-fit line equation) is -1.4 ADU/K. It was expected to see the same sensitivity ratio as the one derived from Figure 6.10. The discrepancy arises presumably from different aspects of the modified setup used for the gain sensitivity study. Nevertheless, the offset variation with temperature is negligible for the gain measurements, as it accounts for only about 1 % of the signal variation (offset change over temperature range = 8 ADUs while output signal variation was 800 ADUs, see figs 6.14 and 6.16), i.e. the offset variation is a negligible correction to the signal variation in this experiment. Nor does the discrepancy detract from the earlier result (which was taken with a normal CCD measurement set-up) rather than the set-up which while adequate for gain measurement, apparently affected offset measurements. For this reason, it was decided that it was not worthwhile to investigate this issue further.

The plot in Figure 6.15 shows the average ADC value together with CCD and ambient temperatures, acquired for the second part of the CCD output gain sensitivity measurements, where the detector was set up to output the

pseudo-video signal that represented a half-full-well condition. Just as in the case of the first part of the gain sensitivity measurements (shown previously in Figure 6.13), the average ADC value and CCD temperature plots are anti-correlated.

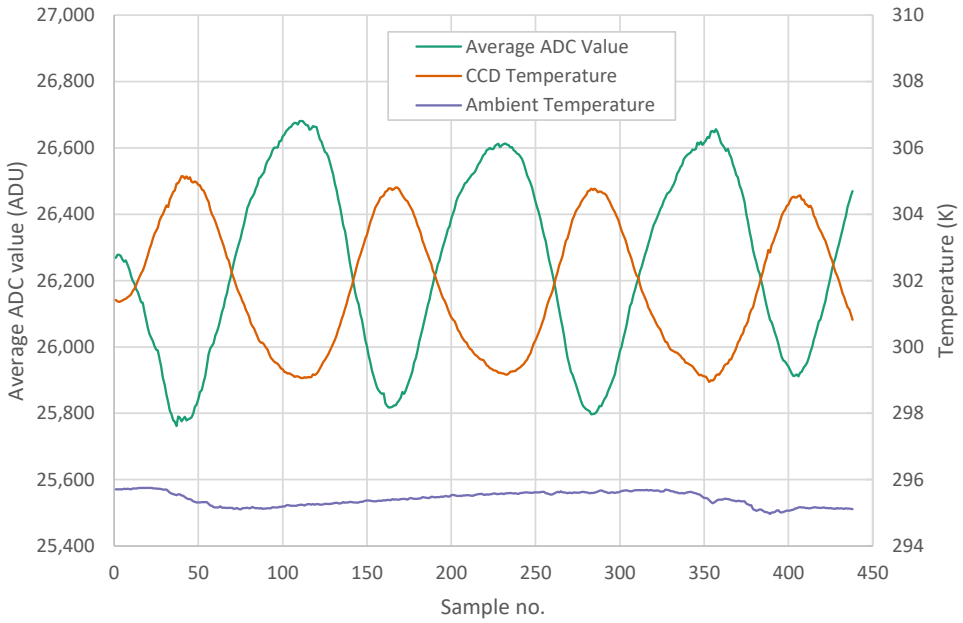

Figure 6.15: Average ADC value and CCD and ambient temperatures obtained for the 'zero-signal' scenario of the CCD output gain temperature sensitivity study.

Figure 6.16 shows the 'signal' average ADC values plotted against CCD temperature (the ADC values have the offset subtracted from them). The CCD output temperature coefficient (read from the plot) is $-142\,\mathrm{ADU/K}$. Similarly to Figures 6.10 and 6.14), the overwhelming dependency with temperature is clear. The CCD output temperature coefficient of the gain is $-0.007/\mathrm{K}$ ($-7000\,\mathrm{ppm/K}$) which was found by dividing the gradient of the best-fit line from Figure 6.16 (-142.45) by the average ADC value at the middle of the tested temperature range ($\sim$21 400 ADU at 302 K).

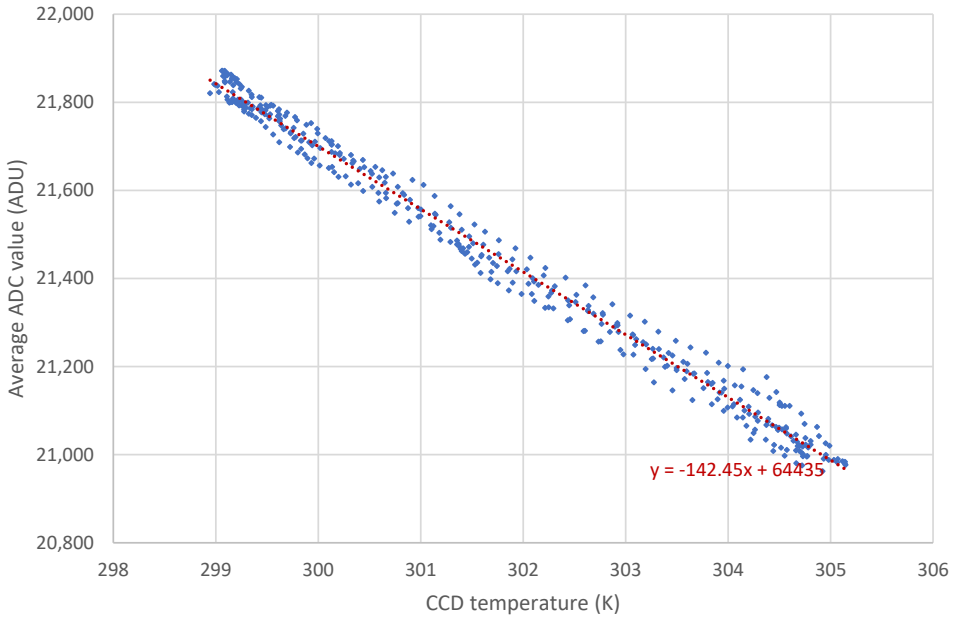

Figure 6.16: Average pixel value as a function of CCD temperature for the scenario with the pseudo-video signal. The best fit line and its equation are shown in red.

6.2 Temperature Sensitivity of the Normal-Front-End-Electronics

6.2.1 Experimental Setup

An alternative method was developed for the PLATO N-FEE temperature sensitivity study. Figure 6.17 shows the setup block diagram used for measuring N-FEE offset and gain temperature coefficients.

The following hardware was used for the setup:

- PLATO N-FEE: BB_V1 (MSSL),
- CCD: CCD47-20 (Teledyne e2v),
- N-FEE DC Power Supplies: QL355TP and PL303QMD-P (TTi),
- DMM: 34461A (Keysight Technologies),
- Laptop PC: XPS 15 9530 (Dell),

- USB to SpaceWire Interface: SpaceWire Brick Mk2 (STAR-Dundee),
- NTC Thermistor R_{T2}: 44908 10 kΩ (YSI),
- Hot Plate: UC150 (Stuart)
- Metal Enclosure: Aluminium Die-cast Case
- Pulse Generator: PM 5786B (Philips),
- DC Voltage Source: PL303QMD-P (TTi),
- Summing Amplifier: AD8021 (Analog Devices),
- Isolation Box: NB 80 V1 MC (Newbox).

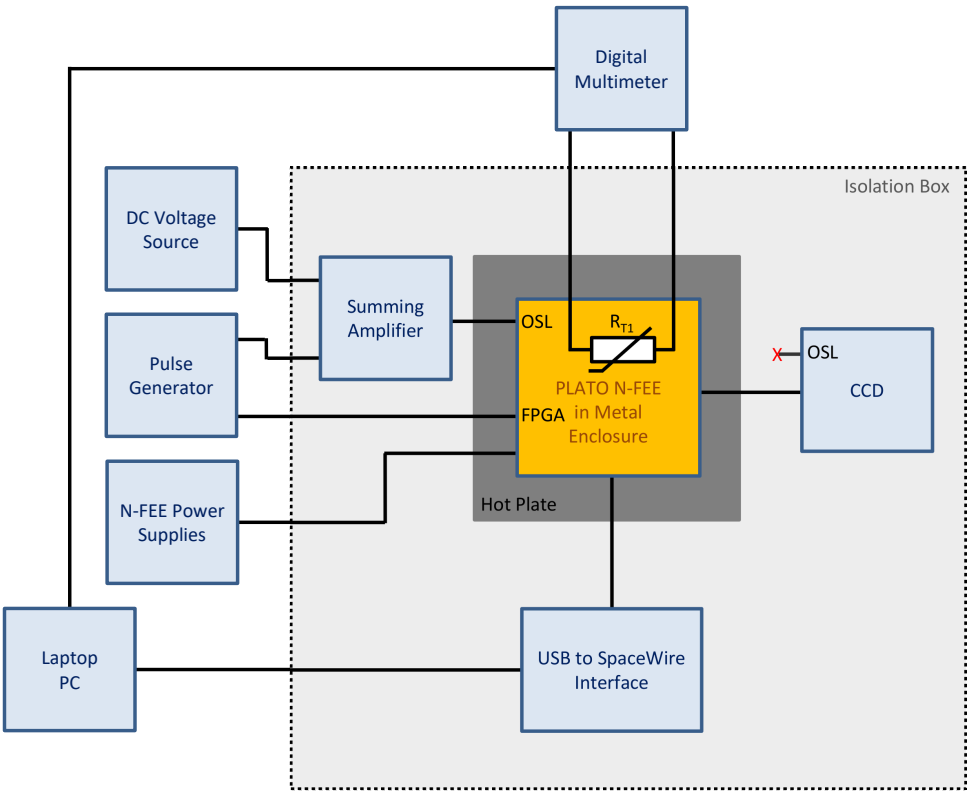

Figure 6.17: Setup block diagram used for the N-FEE temperature sensitivity measurements.

Once again, the CCD was operated in the reverse clocking mode although it was largely irrelevant on this occasion, as the link between the CCD output transistor source OS (pin 10) and N-FEE was interrupted (i.e. the CCD output was disconnected). Instead, one of the FPGA I/O pins was programmed (not part of this thesis) to output a pseudo-video signal for half the pixels of each row to trigger an external pulse generator, which was set up to give a signal with approximately the correct video waveform for a half-full-well signal ($\sim$30 000 ADU). This way, each generated frame had half of the image populated with the 'signal' values (including offset), and the other half filled with just an offset.

The N-FEE was mounted inside the aluminium die-cast enclosure and placed on top of the hot plate. The hot plate temperature was set to $\sim$80 °C and was manually powered off once the N-FEE temperature reached $\sim$45 °C (approximately after 1.5 h). The N-FEE temperature was monitored with the thermistor, whose body was glued to a relatively unpopulated part of the PCB and terminals connected to the DMM. The measurement process was controlled by the same LabVIEW VI that was used for the CCD temperature sensitivity measurements (see Figure 6.3 for the schematic). Due to an unknown issue, the automated recording of the thermistor's resistance did not work and the readings were taken manually approximately every 15 min. Just as in the case of all the previous temperature sensitivity tests, the temperature in the laboratory was controlled by the air-conditioning unit and it was necessary to encapsulate the N-FEE, CCD and SpaceWire brick in the electrically dissipative box, to protect them from the blown air.

The 512 $\times$ 512 image frames were acquired automatically every 10 s, using the modified SpaceWire brick software utility that was used in the previous tests. Data recording was terminated after approximately 2.5 h and the images were processed with the Python code from Appendix D. Finally, all the acquired data was plotted and then used for deriving the N-FEE offset and gain temperature coefficients.

6.2.2 Results

Figures 6.18 and 6.19 show the N-FEE temperature and average ADU values for the offset and pseudo-video signal measurements. Clearly, the offset

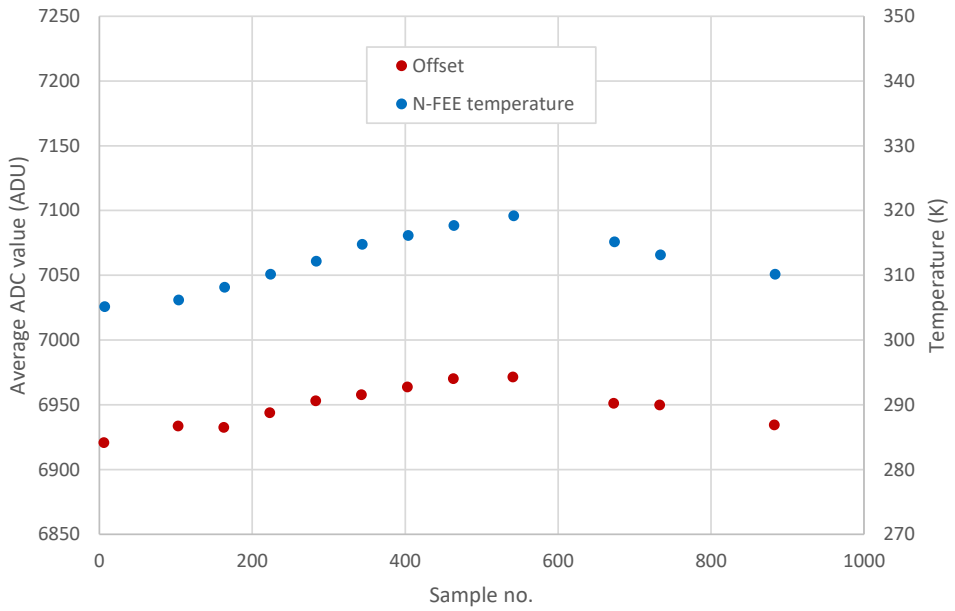

Figure 6.18: N-FEE offset and temperature variation.

data and N-FEE temperature are correlated, while the N-FEE temperature and 'signal' data are anticorrelated. This is also visible in Figures 6.20 and 6.21, where the average ADC values for both scenarios (with and without the 'signal') are plotted as a function of N-FEE temperature. The N-FEE offset temperature coefficient (read from Figure 6.20) is 3.4 ADU/K. The temperature coefficient of the gain is $-0.004\,/\mathrm{K}$ ($-4000\,\mathrm{ppm/K}$) and it was calculated as a quotient of the best-fit line's gradient (-115.24) and the average ADC value at the middle of the tested temperature range ($\sim$28 400 ADU at 312 K).

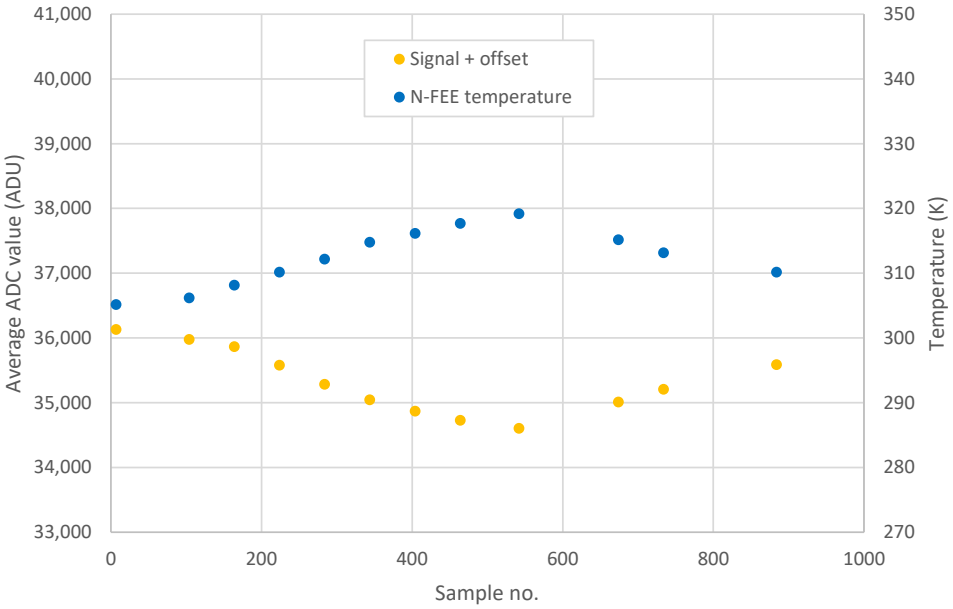

Figure 6.19: N-FEE pseudo-video signal and temperature variation.

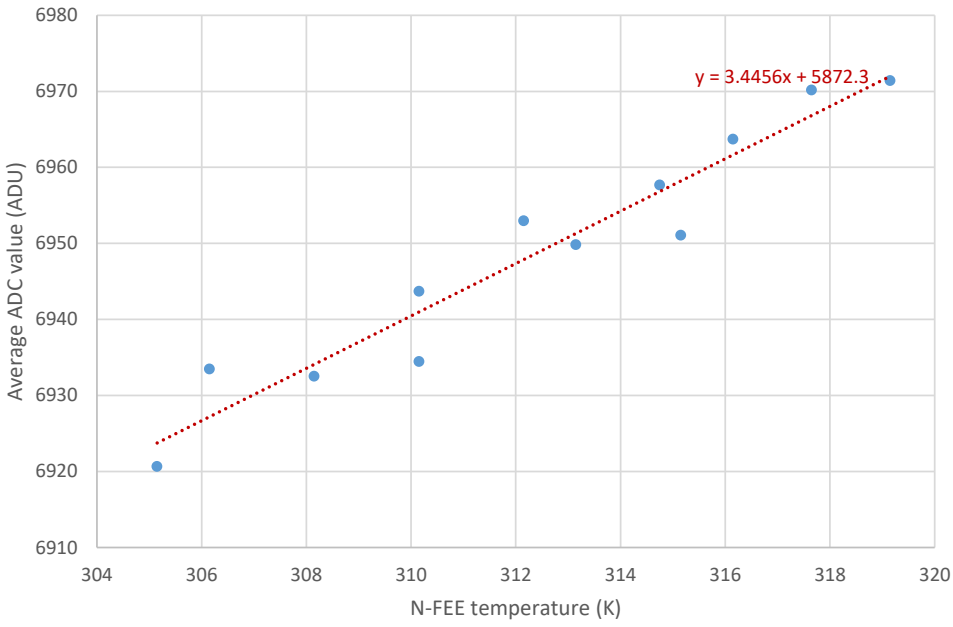

Figure 6.20: Average pixel value (offset) as a function of absolute N-FEE temperature. The best fit line and its equation are shown in red.

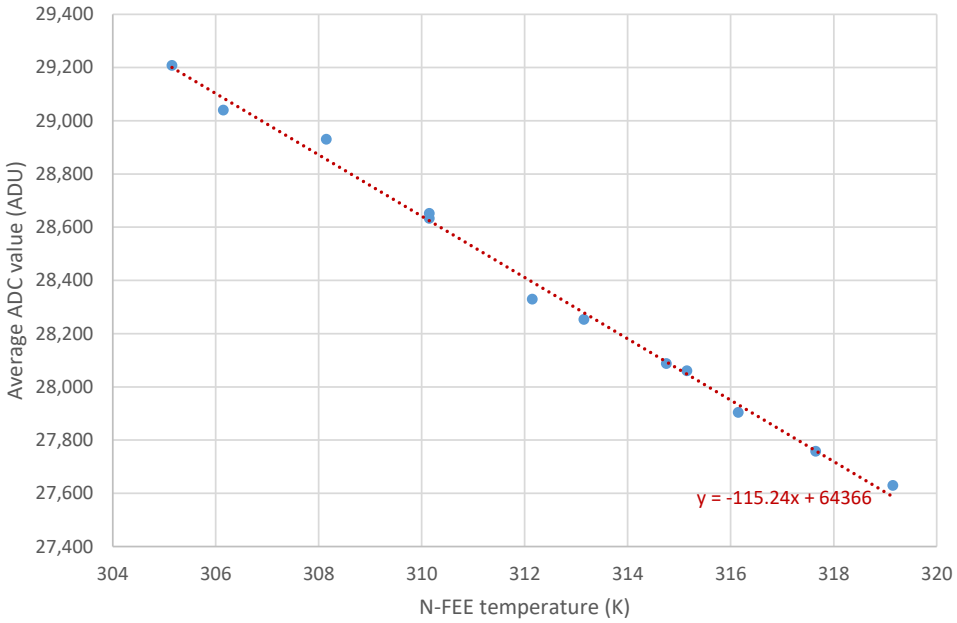

Figure 6.21: Average pixel value (signal with subtracted offset) as a function of absolute N-FEE temperature. The best fit line and its equation are shown in red.

6.3 Conclusions and Future Work

The work presented in this chapter was carried out in order to investigate temperature sensitivities of PLATO N-FEE and the output stage of CCD47-20, being a detector with a very similar output circuit to the one found inside the intended for PLATO CCD270. Two key effects were studied, offset and gain temperature sensitivities. The main conclusions of the study are given below:

- The offset and gain temperature coefficients found from the CCD output stage temperature sensitivity study are 11.2 ADU/K and −7000 ppm/K respectively.
- No temperature effect on noise in the image was observed for the tested temperature range of the CCD.
- There is a correlation between the 'zero-signal' average ADC values (offset) and the CCD/N-FEE board temperature, and an anticorrelation between the 'signal' average ADC values and the CCD/N-FEE temperature.
- The offset and gain temperature coefficients resulting from the N-FEE temperature sensitivity study are 3.4 ADU/K and −4000 ppm/K respectively.

These values are an important input into the next generation of N-FEE design, future CCD characterisation and to the PLATO project performance simulation team who are responsible for estimating the overall performance of the mission, including all aspects (satellite pointing, optics, ...). The presence of the large offset sensitivity is surprising and will need to be accommodated.

As for future work, the CCD temperature sensitivity measurements could be repeated using the same technique for measuring the gain temperature coefficient, as the one developed for the N-FEE temperature sensitivity study, where the offset and 'signal' data were both present within each acquired image frame (half of each row data contained 'signal' ADC values, while the other half just the offset). This would avoid the offset discrepancy seen earlier.

The second level of drift in the measurement that was seen in Figures 6.10, 6.14 and 6.16 could be investigated further, in order to fully understand all the variables that may affect performance of the PLATO normal cameras.

Finally, the experimental methods presented in this chapter could be adopted to carry out a similar study of PLATO CCD270 and the next iteration of the PLATO N-FEE board, which is currently being developed at MSSL.

Chapter 7

Implications for PLATO

This thesis has addressed two areas that are important from the point of view of the preparations for the PLATO mission. One is the susceptibility of the PLATO N-FEE power lines to the conductively coupled CM and DM interference signals. The other is concerned with the temperature sensitivity of the two major camera components: the imaging sensor and the driving electronics (CCD270 and N-FEE in the case of PLATO's twenty-four normal cameras). Both these aspects are important for PLATO, because they affect the stability and noise of the acquired images and hence the minimum detectable transits in the light curves. An interpretation of the findings of each of these two investigations is shown below.

7.1 Requirements for the Filter Board

CS requirements for the PLATO N-FEE power supply lines were presented in Chapter 4. As indicated in Section 4.3.2, the N-FEE shall preserve its specified performance when subjected to 20 mA rms CM sinusoidal interference over the frequency range from 50 kHz to 50 MHz, and when exposed to 20 mVpk-pk DM noise and ripple over the range from 10 Hz to 50 MHz. The specified performance can be preserved provided that the overall noise generated by the N-FEE stays below the predefined allowable limit. Requirement PLT-N-FEE-252 in PLATO-OHB-PL-RS-005 (2017) states that the to-

tal readout noise of the N-FEE shall be less than $50\,e^-$ excluding the CCD contribution (a bandwidth of $5\times$ is assumed, similar to the CCD, as described below). There is an analogous requirement for the CCD270 in Section 5.4 of PLATO-ESTEC-PL-RS-003 (2016), stating that the readout noise shall be lower than or equal to $28\,e^-$rms if a bandwidth of twice the nominal pixel rate is used. In fact, a bandwidth of five times the pixel readout rate was used in all the measurements completed for this thesis, which allows for scaling the readout noise limit to $44\,e^-$ (calculated as $28\,e^- \times \sqrt{5/2}$).

Therefore, the total allowable noise contribution from both the N-FEE and the CCD270 is $67\,e^-$ (calculated as $\sqrt{50^2 + 44^2}$), and this is the limit used in all further analysis.

The highest read noise figure observed during the DM CS study presented in Section 5.4.2 was $58\,e^-$. Subtracting it in quadrature from the allowable budget of $67\,e^-$ leaves a margin of $33\,e^-$ available for other noise sources. However, Figure 5.58 and Table 5.3 have shown that even the highest noise peak present in the data was lower than $30\,e^-$. This leads to the conclusion that there is no need for a dedicated DM filter board, but it should be noted that due to equipment limitations it was not possible to cover the whole frequency range specified for the DM CS measurements in PLATO-OHB-PL-RS-005 (2017) (the lowest injected frequency was 47 kHz).

The following sections provide recommendations for CM filters specified individually for each of the seven PLATO N-FEE power supply lines (the actual filter board design is not part of this thesis).

7.1.1 +33 V (VCCD) Power Line

Figure 5.15 has shown a plot of scaled image standard deviation as a function of injected CM interference frequency for the +33 V (VCCD) power supply line. The plotted values had subtracted in quadrature $36\,e^-$ read noise and the scaling was implemented in order to demonstrate the performance that would be observed if the injected current amplitude was fixed at 20 mA rms.

The same plot with superimposed allowable noise margin is shown in

Figure 7.1. The noise margin line is drawn at 56 e^- level, which was derived by subtracting in quadrature 36 e^- read noise from the total allowable noise budget of 67 e^-.

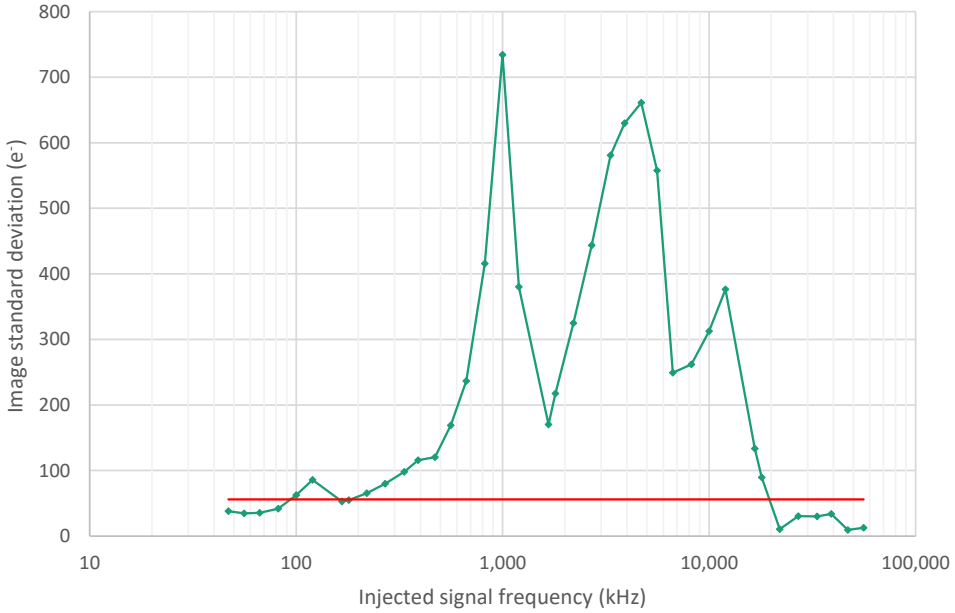

Figure 7.1: Image standard deviation as a function of CM interference frequency for the +33 V (VCCD) power line with superimposed noise allowance limit (red line).

Table 7.1 contains frequency ranges and corresponding recommended attenuation levels for those parts of the plot that are exceeding the 56 e^- noise margin level.

Frequency range	Recommended attenuation
80 kHz to 170 kHz	3.7 dB
170 kHz to 1.7 MHz	22.4 dB
1.7 MHz to 6.7 MHz	21.4 dB
6.7 MHz to 20 MHz	16.6 dB

Table 7.1: Recommended characteristics of the CM filter intended for the +33 V (VCCD) power line.

7.1.2 +12 V (VCLK) Power Line

The image standard deviation plot from Figure 5.18 is reused here in Figure 7.2 with superimposed allowable noise margin of 56 e^- (calculated as 36 e^- read noise subtracted in quadrature from the total budget of 67 e^-).

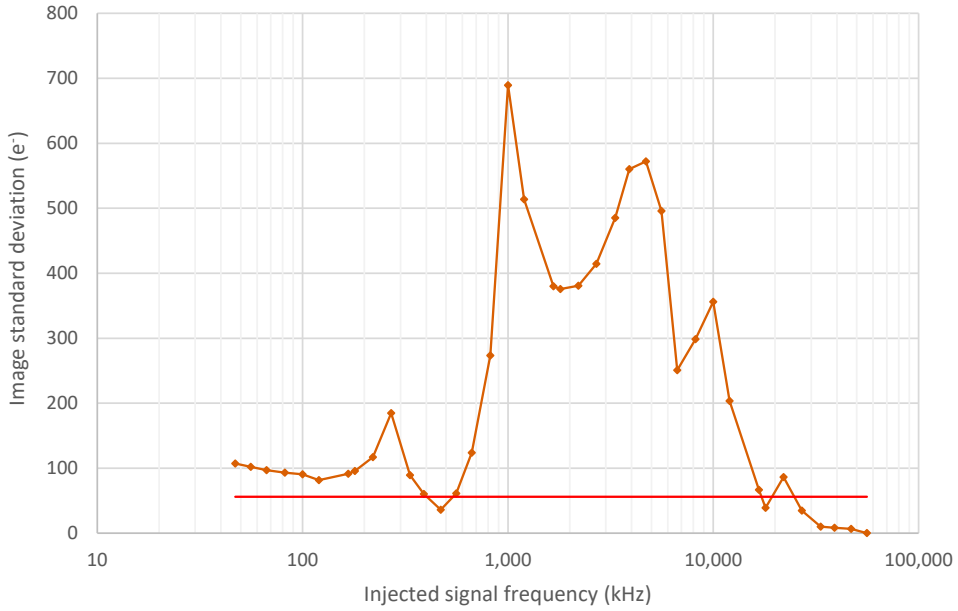

Figure 7.2: Image standard deviation as a function of CM interference frequency for the +12 V (VCLK) power line with superimposed noise allowance limit (red line).

Table 7.2 specifies frequency ranges and the appropriate attenuation levels for parts of the plot that exceed the 56 e^- noise margin and require filtering.

Frequency range	Recommended attenuation
40 kHz to 470 kHz	13.7 dB
470 kHz to 1.8 MHz	21.8 dB
1.8 MHz to 6.7 MHz	20.2 dB
6.7 MHz to 18 MHz	16.1 dB
18 MHz to 27 MHz	3.7 dB

Table 7.2: Recommended characteristics of the CM filter intended for the +12 V (VCLK) power line.

7.1.3 +4 V (VDIG_SPW) Power Line

Figure 5.21 has shown the scaled image standard deviation plotted as a function of injected CM interference frequency for the +4 V (VDIG_SPW) power supply line, with subtracted in quadrature 36 e^- read noise. The same plot with superimposed allowable noise margin of 56 e^- (calculated as $\sqrt{67^2 - 36^2}$) is shown in Figure 7.3.

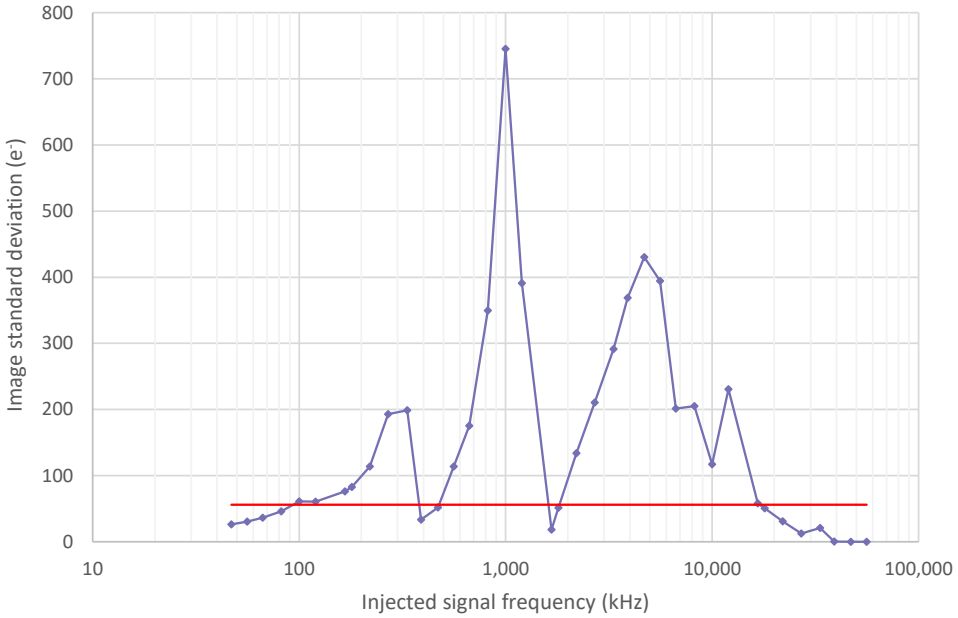

Figure 7.3: Image standard deviation as a function of CM interference frequency for the +4 V (VDIG_SPW) power line with superimposed noise allowance limit (red line).

Table 7.3 contains frequency ranges and corresponding recommended attenuation levels for those parts of the plot that are exceeding the 56 e^- noise margin level.

Frequency range	Recommended attenuation
80 kHz to 390 kHz	11.0 dB
390 kHz to 1.7 MHz	22.5 dB
1.7 MHz to 10 MHz	17.7 dB
10 MHz to 20 MHz	12.3 dB

Table 7.3: Recommended characteristics of the CM filter intended for the +4 V (VDIG_SPW) power line.

7.1.4 +6 V (VAN1) Power Line

The image standard deviation plot from Figure 5.27 with superimposed allowable noise margin of 56 e^- (calculated as 36 e^- read noise subtracted in quadrature from the total budget of 67 e^-) is shown in Figure 7.4.

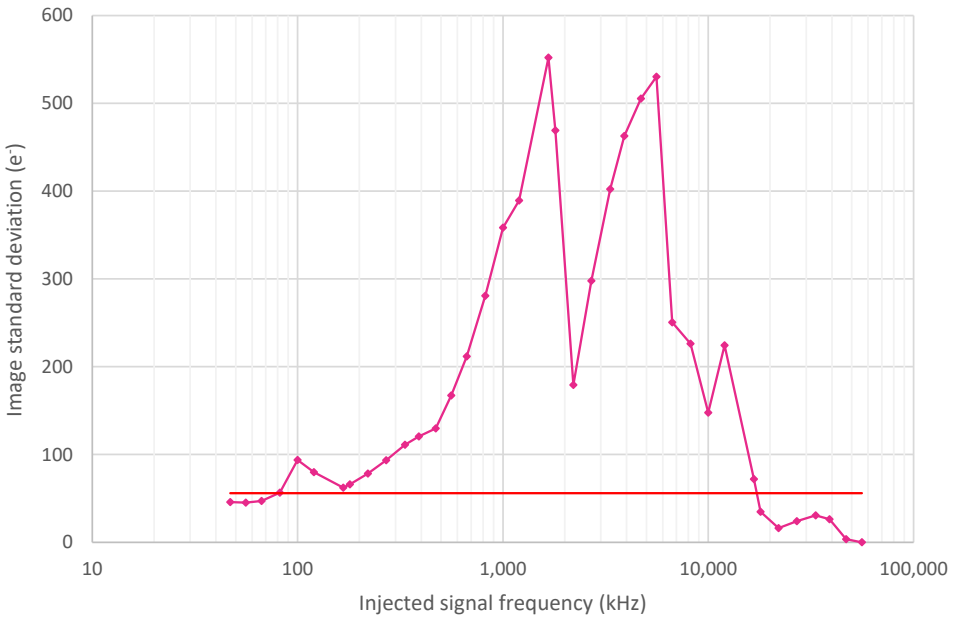

Figure 7.4: Image standard deviation as a function of CM interference frequency for the +6 V (VAN1) power line with superimposed noise allowance limit (red line).

Table 7.4 contains frequency ranges and corresponding recommended attenuation levels for those parts of the plot that are exceeding the 56 e^- noise margin level.

Frequency range	Recommended attenuation
80 kHz to 170 kHz	4.5 dB
170 kHz to 2.2 MHz	19.9 dB
2.2 MHz to 10 MHz	19.5 dB
10 MHz to 18 MHz	12.1 dB

Table 7.4: Recommended characteristics of the CM filter intended for the +6 V (VAN1) power line.

7.1.5 −6 V (VAN3) Power Line

Figure 5.24 has shown the scaled image standard deviation plotted as a function of injected CM interference frequency for the −6 V (VAN3) power supply line, with subtracted in quadrature 36 e^- read noise. The same plot with superimposed allowable noise margin of 56 e^- (derived by subtracting in quadrature 36 e^- read noise from the total allowable noise budget of 67 e^-) is shown in Figure 7.5.

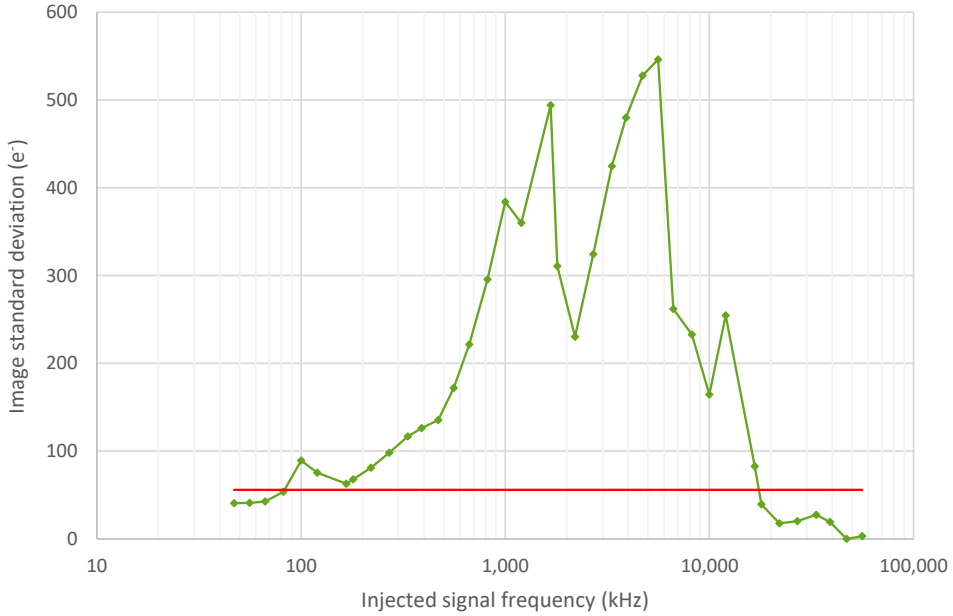

Figure 7.5: Image standard deviation as a function of CM interference frequency for the −6 V (VAN3) power line with superimposed noise allowance limit (red line).

Table 7.5 specifies frequency ranges and the appropriate attenuation lev-

els for parts of the plot that exceed the 56 e^- noise margin and require filtering.

Frequency range	Recommended attenuation
80 kHz to 170 kHz	4.1 dB
170 kHz to 2.2 MHz	18.9 dB
2.2 MHz to 10 MHz	19.8 dB
10 MHz to 18 MHz	13.2 dB

Table 7.5: Recommended characteristics of the CM filter intended for the −6 V (VAN3) power line.

7.1.6 +3 V (VDIG_FPGA) Power Line

The image standard deviation plot from Figure 5.30 is plotted again in Figure 7.6 with superimposed allowable noise margin of 56 e^- (calculated as 36 e^- read noise subtracted in quadrature from the total budget of 67 e^-).

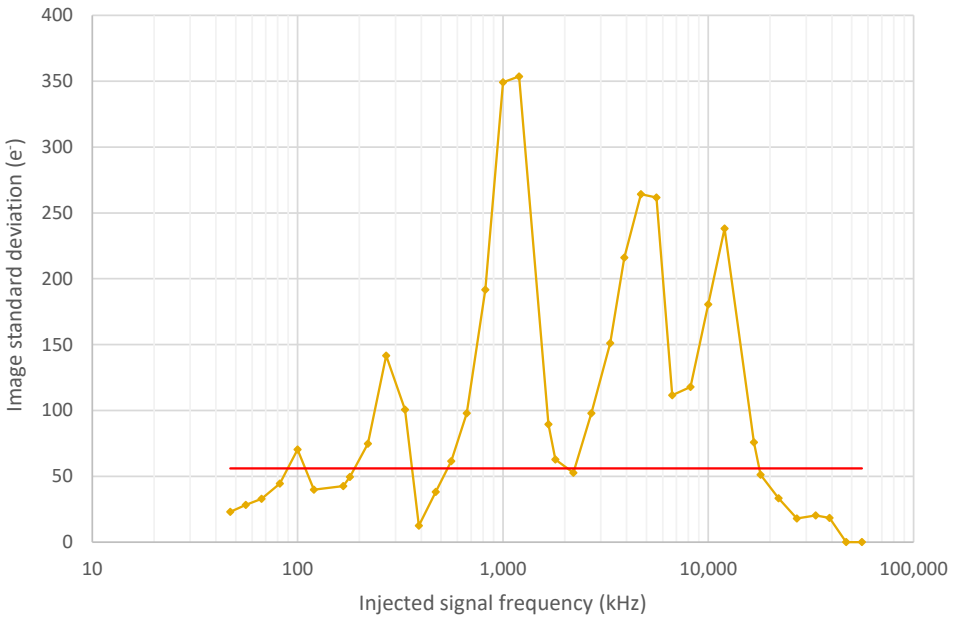

Figure 7.6: Image standard deviation as a function of CM interference frequency for the +3 V (VDIG_FPGA) power line with superimposed noise allowance limit (red line).

Table 7.6 specifies frequency ranges and the appropriate attenuation lev-

els for parts of the plot that exceed the 56 e^- noise margin and require filtering.

Frequency range	Recommended attenuation
80 kHz to 170 kHz	2.1 dB
170 kHz to 390 kHz	8.1 dB
390 kHz to 2.2 MHz	16.0 dB
2.2 MHz to 6.7 MHz	13.5 dB
6.7 MHz to 18 MHz	12.6 dB

Table 7.6: Recommended characteristics of the CM filter intended for the +3 V (VDIG_FPGA) power line.

7.1.7 +3 V (VAN2) Power Line

Figure 5.33 has shown a plot of scaled image standard deviation as a function of injected CM interference frequency for the +3 V (VAN2) power supply line. The plotted values had subtracted in quadrature 36 e^- read noise. The same plot with superimposed allowable noise margin is shown in Figure 7.7. The noise margin line is drawn at the 56 e^- level, which was obtained by subtracting in quadrature 36 e^- read noise from the total allowable noise budget of 67 e^-.

Table 7.7 specifies frequency ranges and the appropriate attenuation levels for parts of the plot that exceed the 56 e^- noise margin.

Frequency range	Recommended attenuation
80 kHz to 170 kHz	3.4 dB
170 kHz to 390 kHz	8.1 dB
390 kHz to 1.7 MHz	16.8 dB
1.7 MHz to 18 MHz	17.9 dB

Table 7.7: Recommended characteristics of the CM filter intended for the +3 V (VAN2) power line.

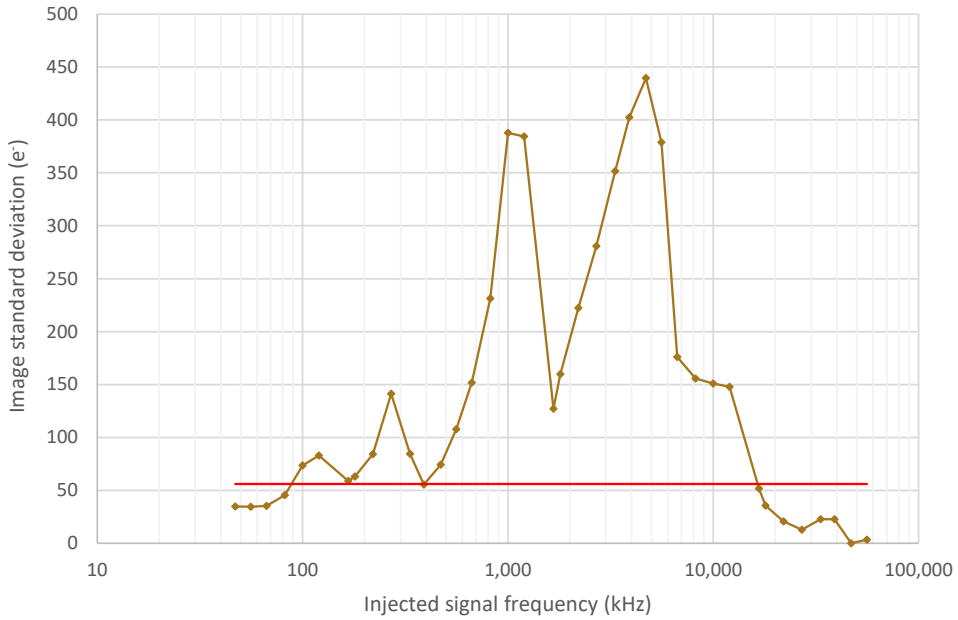

Figure 7.7: Image standard deviation as a function of CM interference frequency for the +3 V (VAN2) power line with superimposed noise allowance limit (red line).

7.1.8 Summary of Filter Requirements and Expected Capabilities

The results in the previous sections show that the frequency range requiring the largest attenuation of conducted EMC is ∼500 kHz to ∼20 MHz. In this range, the results show a required attenuation of ∼15 to ∼20 dB. The present CM filter design for the N-FEE incoming supply lines consists of a series inductor of 500 µH and a capacitor to ground of 10 µF. This combination provides an attenuation factor of 106 dB at 1 MHz and 158 dB at 20 MHz. The results in the previous sections are important for the N-FEE design, as they show that the designed filter is expected to provide the required attenuation with a significant margin.

7.2 Temperature Stability Requirements

7.2.1 N-FEE

Requirements for stability of the video signal chain in N-FEE are defined in PLATO-OHB-PL-RS-005 (2017). According to this document, the temperature coefficient of the offset shall be less than 1 ADU/K, while the temperature coefficient of the gain of the video chain shall be less than 100 ppm/K. If the 67 e^- (∼3.3 ADU) of allowable noise budget described in Section 7.1 was all available to the temperature variation effects, a temperature variation of 3 K would still be within that 67 e^-.

The study presented in Section 6.2 has shown that the actual temperature coefficients of the offset and gain were 3.4 ADU/K and −4000 ppm/K respectively. As the measured temperature coefficient of the gain was 40× higher than the required value, this could have implications for the N-FEE temperature measurement accuracy in order to correct for these temperature variations post facto. The stated discrepancy leaves room for improvement, and the next iteration of the N-FEE design is currently being developed at MSSL, allowing these issues to be addressed. These results will impact this design evolution.

7.2.2 CCD270

According to Section 5.6 in PLATO-ESTEC-PL-RS-003 (2016), the CCD gain sensitivity to temperature changes shall be lower than or equal to −0.2 %/K, i.e. −2000 ppm/K (no figure for the offset temperature sensitivity was given). The actual temperature coefficients of the offset and gain for the CCD output stage were measured as 11.2 ADU/K and −7000 ppm/K respectively (see Section 6.2.2). Even though the tested detector was CCD47-20 rather than CCD270, their temperature sensitivities should be very similar, as the output stages of both detectors are almost identical. The fact that the measured temperature coefficient of the gain was 3.5× higher than the required value, means that the CCD temperature would have to be measured more accurately

in order to correct the temperature variations. However, the CCD thermistor has been upgraded from a PRT100 to a PRT1000 and this is not likely to be an issue. Assuming that there are requirements to be able to detect a 2 ADU variation in the stellar signal, it would be necessary to keep all the instrumental effects to less than this level. This means that the CCD temperature would have to be stabilised to at least 0.2 K (calculated as 2 ADU / 11.2 ADU/K).

7.3 Overall Conclusion

This work has shown the credibility of the PLATO N-FEE design and provided important information for its evolution through the next breadboards and, ultimately, into flight.

The work shows how conducted EMC measurements may be performed for CCD cameras, and, notably, the intricacies associated with such delicate measurements and complexities of the resulting data.

Temperature dependencies were explored and found to be greater than expected. This will have implications for the next generation of N-FEE.

The concept of a laboratory transit simulator was explored in terms of LED stability and advice provided as to how this might proceed. Notable was the observation of discontinuities in LED performance.

Appendices

Appendix A

Python Code for Simulating Correlated Double Sampling Circuit

```
1  import matplotlib.pyplot as plt
2  import numpy as np
3  import pylab as py
4  from pylab import *
5  import scipy.ndimage
6  import glob
7  import time
8  from PIL import Image
9
10 ######################################################################
11
12 def free_memory():
13
14     """Function clears and closes the current figure to free the
       memory"""
15
16     plt.clf() # clear figure
17     plt.cla() # clear axes
18     plt.close() # close figure
19
```

```
20      return
21
22
23  def remap(OldValue, OldMin, OldMax, NewMin, NewMax):
24
25      """Function scales numbers from one range to another"""
26
27      OldRange = OldMax - OldMin
28      if (OldRange == 0):
29          NewValue = NewMin #in case the old min and old max values
        were the same
30      else:
31          NewRange = NewMax - NewMin
32          NewValue = (OldValue - OldMin) * NewRange / OldRange +
      NewMin
33
34      return NewValue
35
36  ##############################################################################
37
38  # Main program
39
40  start_time = time.time()
41
42  data_folder_path = "c:/home/rw/cds_effect_simulation/"
43  t_RowTrans = 250000 - 512 * 300 #row transfer time in ns (300ns
      pixel time)
44  data = np.zeros((512, 512), dtype=np.float64) #define 512x512
      data array
45
46  #get the list of interference frequencies (in GHz) to be tested
47  file = open('c:/home/rw/cds_effect_simulation/freq3.txt', 'r')
48  freq = file.read().splitlines()
49  file.close()
50  f_list =[float(n.strip()) for n in freq]
51
52  #create artificial data arrays containg each interference
```

```
    frequency
for f in f_list:
    for row in range(0, 512):
        t_Row = row * (512 * 300 + t_RowTrans) #row start time
        for col in range(0, 512):
            t_Rst = t_Row + col * 300 + 140
            whole_periods_Rst = int(t_Rst * f)
            t_RstM = t_Rst - (whole_periods_Rst / f)
            t_Sig = t_Row + col * 300 + 290
            whole_periods_Sig = int(t_Sig * f)
            t_SigM = t_Sig - (whole_periods_Sig / f)
            sine_Rst = np.sin(2 * np.pi * f * t_RstM)
            sine_Sig = np.sin(2 * np.pi * f * t_SigM)
            data[row][col] = sine_Sig - sine_Rst

    #ROI coordinates
    startcolumn = 10
    endcolumn = 500
    startrow = 10
    endrow = 500

    #number of columns and rows in ROI
    columns = endcolumn - startcolumn
    rows = endrow - startrow

    roi = data[startrow:endrow,startcolumn:endcolumn]

    #Calculate ROI mean and standard deviations along x-axis, y-
    axis and overall
    xstd = (np.sum((np.array(roi).std(axis=1, ddof=1, dtype=np.
    float64))**2)/rows)**0.5
    ystd = (np.sum((np.array(roi).std(axis=0, ddof=1, dtype=np.
    float64))**2)/columns)**0.5
    ovlstd = np.array(roi).std(ddof=1, dtype=np.float64)
    meanpix = roi.mean()

    mtx = [xstd, ystd, ovlstd, meanpix]
```

```
86
87      #Save mtx into a .txt file
88      f1 = open(data_folder_path + "std.txt","a")
89      for item in mtx:
90          print("%013.9f  " % item, end="", file=f1) # each saved
        number is limited to 13 digits
91      print("", file=f1)
92      f1.close()
93
94      minval = np.amin(roi) #find minimum value in the data array
95      maxval = np.amax(roi) #find maximum value in the data array
96
97      #scale values in the data array to the range 0-255
98      for cell in np.nditer(roi, op_flags=['readwrite']):
99          cell[...] = remap(cell, minval, maxval, 0, 255)
100
101     roi8 = roi.astype(uint8) #cast the 64-bit float data array
        into the unsigned 8-bit data array
102
103     img = Image.fromarray(roi8) #create an image from the data
        array
104     img.save(data_folder_path + str(round(f*1000000000)) + "Hz.
        tiff")
105
106     #free the memory
107     free_memory()
108
109     print("f=", round(f*1000000000), "Hz")
110
111 elapsed_time = time.time() - start_time
112 print(elapsed_time)
```

Appendix B

Python Code for Processing Reference Images

```
1  import matplotlib.pyplot as plt
2  import numpy as np
3  import pylab as py
4  from pylab import *
5  import scipy.ndimage
6  import glob
7  from PIL import Image
8
9  ###################################################################
10
11 #function definitions
12
13 def read_image(path):
14
15     """Function opens a .bin file from a default location and
       creates an array containing all the pixel values."""
16
17     f=open(path,"rb") # open/read the binary file
18     D = np.fromfile(f, dtype='<u2') # each pixel value is 16-bit
       number in big endian ('<')
19     D = D[4:] #get rid of the first 4 words (8 bytes) that don't
       carry the image data
20     D = np.reshape(D,(512, 512)) # reshape 1D array into a 512
```

```
    x512 2D array
21      D = D.astype(float64) #array cast to 64-bit float data type
22      D = np.asarray(D) # convert list of lists into an array
23      D = D[2:,2:]
24      f.close() #close the file
25
26      return D
27
28
29  def remap(OldValue, OldMin, OldMax, NewMin, NewMax):
30
31      """Function scales numbers from one range to another"""
32
33      OldRange = OldMax - OldMin
34      if (OldRange == 0):
35          NewValue = NewMin #in case the old min and old max values
        were the same
36      else:
37          NewRange = NewMax - NewMin
38          NewValue = (OldValue - OldMin) * NewRange / OldRange +
    NewMin
39
40      return NewValue
41
42
43  def free_memory():
44
45      """Function clears and closes the current figure to free the
    memory"""
46
47      plt.clf() # clear figure
48      plt.cla() # clear axes
49      plt.close() # close figure
50
51      return
52
53  ###################################################################
```

```
54
55 # Main program
56
57 data_folder_path = "c:/home/rw/20171209/"
58
59 imgsum = np.zeros(shape=(510,510))
60 imgsum = imgsum.astype(float64)
61
62 #sort and loop through all the .bin files found in the specified
       folder
63 for idx, file in enumerate(sorted(glob.glob(data_folder_path + '
       *.bin'))):
64
65     print(file)
66
67     #load the image file
68     data = read_image(file)
69
70     imgsum = imgsum + data
71
72     #define ROI
73     startcolumn = 10
74     endcolumn = 500
75     startrow = 10
76     endrow = 500
77     roi = data[startrow:endrow,startcolumn:endcolumn]
78
79     #number of rows and columns in ROI
80     rows = endrow - startrow
81     columns = endcolumn - startcolumn
82
83     #calculate mean of each column, creating the so-called
       average row and subtract it from each row
84     roiavrow = roi.mean(axis=0)
85     roicolfix = roi - roiavrow[None,:]
86
87     #calculate mean of each row, creating the so-called average
```

```
        column and subtract it from each row
88      roiavcol = roicolfix.mean(axis=1)
89      roifinal = roicolfix - roiavcol[:,None]
90
91      #Simple statistics
92      stdx = (np.sum((np.array(roifinal).std(axis=1, ddof=1, dtype=
        np.float64))**2)/rows)**0.5
93      stdy = (np.sum((np.array(roifinal).std(axis=0, ddof=1, dtype=
        np.float64))**2)/columns)**0.5
94      stdov = np.array(roifinal).std(ddof=1, dtype=np.float64)
95      meanpxl = roifinal.mean()
96      minval = np.amin(roifinal) #find the minimum value in the
        data array
97      maxval = np.amax(roifinal) #find the maximum value in the
        data array
98
99      #Save calculated stats data into the .txt file
100     fs = open(data_folder_path + "stats0Hz.txt","a")
101     print("{:15.10f}".format(stdx), "{:15.10f}".format(stdy),
102           "{:15.10f}".format(stdov), "{:17.10f}".format(meanpxl),
        file=fs)
103     fs.close()
104
105     #scale values in the data array to the range 0-255
106     for cell in np.nditer(roifinal, op_flags=['readwrite']):
107         cell[...] = remap(cell, minval, maxval, 0, 255)
108
109     roi8 = roifinal.astype(uint8) #cast the 64-bit float data
        array into the unsigned 8-bit data array
110
111     img = Image.fromarray(roi8) #create an image from the data
        array
112     img.save(data_folder_path + file[20:-4] + ".tiff")
113
114     #free the memory
115     free_memory()
116
```

```
117 print("")
118 print("Number of processed images:",idx+1)
119
120 imgav = imgsum / idx+1
121
122 imgav.astype('float64').tofile(data_folder_path + 'avrefimg.dat')
123
124 #save image as .png file
125 fig = plt.imshow(imgav, cmap='gray', norm=None, interpolation='
        none', origin='lower')
126 plt.axis('off') # do not plot axis
127 fig.axes.get_xaxis().set_visible(False)
128 fig.axes.get_yaxis().set_visible(False)
129 fig1 = plt.gcf() # get current figure
130 fig1.set_size_inches(8.5,8.5) # set figure size
131 plt.savefig(data_folder_path + 'avrefimg.png', bbox_inches='tight
        ', pad_inches = 0, dpi = 100)
132
133 #free the memory
134 free_memory()
```

Appendix C

Python Code for Processing Images with Interference

```
1  import matplotlib.pyplot as plt
2  import numpy as np
3  import pylab as py
4  from pylab import *
5  import scipy.ndimage
6  import glob
7  from PIL import Image
8
9  ###################################################################
10
11 #function definitions
12
13 def read_image(path):
14
15     """Function opens a .bin file from a default location and
       creates a 2D array containing all the pixel values."""
16
17     f=open(path,"rb") #open/read the binary file
18     D = np.fromfile(f, dtype='<u2') #each pixel value is big
       endian ('<') 16-bit unsigned integer data type
19     D = D[4:] #get rid of the first 4 words (8 bytes) that don't
       carry the image data
20     D = np.reshape(D,(512, 512)) #reshape 1D array into a 512x512
```

```
        2D array
21      D = D.astype(float64) #array cast to 64-bit float data type
22      D = np.asarray(D) #convert the list into an array
23      D = D[2:,2:]
24      f.close() #close the file
25
26      return D
27
28
29  def remap(OldValue, OldMin, OldMax, NewMin, NewMax):
30
31      """Function scales numbers from one range to another"""
32
33      OldRange = OldMax - OldMin
34      if (OldRange == 0):
35          NewValue = NewMin #in case the old min and old max values
        were the same
36      else:
37          NewRange = NewMax - NewMin
38          NewValue = (OldValue - OldMin) * NewRange / OldRange +
    NewMin
39
40      return NewValue
41
42
43  def free_memory():
44
45      """Function clears and closes the current figure to free the
    memory"""
46
47      plt.clf() # clear figure
48      plt.cla() # clear axes
49      plt.close() # close figure
50
51      return
52
53  ##########################################################################
```

```
54
55 # Main program
56
57 data_folder_path = "c:/home/rw/20171209/"
58
59 for avimg in glob.glob(data_folder_path + '*.dat'):
60     f=open(avimg,"rb") #load the binary file
61     refimg = np.fromfile(f, dtype='float64') #each pixel value is
       64-bit number
62     refimg = np.reshape(refimg,(510, 510)) #reshape 1D list into
      a 510x510 2D list
63     refimg = np.asarray(refimg) #convert the list into an array
64 f.close() #close the file
65
66 print("")
67 print("Processed files:")
68
69 #sort and loop through all the .bin files found in the specified
     folder
70 for idx, file in enumerate(sorted(glob.glob(data_folder_path + '
     *.bin'))):
71
72     #print processed filename on the screen
73     print(file)
74
75     #load the image file
76     data = read_image(file)
77
78     datafix = data - refimg
79
80     #define ROI
81     startcolumn = 10
82     endcolumn = 500
83     startrow = 10
84     endrow = 500
85     roi = datafix[startrow:endrow,startcolumn:endcolumn]
86
```

```
87      #number of rows and columns in ROI
88      rows = endrow - startrow
89      columns = endcolumn - startcolumn
90
91      #Simple statistics
92      stdx = (np.sum((np.array(roi).std(axis=1, ddof=1, dtype=np.
        float64))**2)/rows)**0.5
93      stdy = (np.sum((np.array(roi).std(axis=0, ddof=1, dtype=np.
        float64))**2)/columns)**0.5
94      stdov = np.array(roi).std(ddof=1, dtype=np.float64)
95      meanpxl = roi.mean()
96      minval = np.amin(roi) #find the minimum value in the data
        array
97      maxval = np.amax(roi) #find the maximum value in the data
        array
98
99      #Save calculated stats data into the .txt file
100     fs = open(data_folder_path + "stats.txt","a")
101     print("{:15.10f}".format(stdx), "{:15.10f}".format(stdy),
102           "{:15.10f}".format(stdov), "{:17.10f}".format(meanpxl),
         file=fs)
103     fs.close()
104
105     #scale values in the data array to the range 0-255
106     for cell in np.nditer(roi, op_flags=['readwrite']):
107         cell[...] = remap(cell, minval, maxval, 0, 255)
108
109     roi8 = roi.astype(uint8) #cast the 64-bit float data array
        into the unsigned 8-bit data array
110
111     img = Image.fromarray(roi8) #create an image from the data
        array
112     img.save(data_folder_path + file[20:-4] + ".tiff")
113
114     #free the memory
115     free_memory()
116
```

```
117 #print some info on the screen
118 print("")
119 print("Number of processed images:",idx+1)
120 print("ROI size:",endcolumn-startcolumn,"x",endrow-startrow,"
        pixels.")
```

Appendix D

Python Code for Processing Images from the Temperature Sensitivity Experiment

```
1  import matplotlib.pyplot as plt
2  import numpy as np
3  import pylab as py
4  from pylab import *
5  import scipy.ndimage
6  import glob
7
8  ######################################################################
9
10 # Function definition
11
12 def read_image(path):
13
14     """Function opens a .bin file from a default location and
       creates an array containing all the pixel values."""
15
16     f=open(path,"rb") # open/read the binary file
17     D = np.fromfile(f, dtype='<u2') # each pixel value is 16-bit
       number in big endian ('<')
18     D = D[4:] # get rid of the first 4 words (8 bytes) that don't
```

```
        carry the image data
19      D = np.reshape(D,(512, 512)) # reshape 1D array into a 512
        x512 2D array
20      D = D.astype(float32) # array cast to 32-bit float data type
21      f.close() #close the file
22      D = np.asarray(D) # convert list of lists into an array
23
24      return D
25
26  ######################################################################
27
28  # Main program
29
30  data_folder_path = "c:/home/rw/20180125/"
31  std_file_odd_path = data_folder_path + "std_odd.txt"
32  std_file_even_path = data_folder_path + "std_even.txt"
33  ccd_gain = 20 # constant used for convertion from ADU to e- for
        CCD270
34  no_frames = 0
35
36  print("")
37  print("Processed files:")
38
39  # Sort and loop through all the .bin files found in the specified
        folder
40  for filename in sorted(glob.glob(data_folder_path + '*.bin')):
41
42      # Open and read the image file
43      data = read_image(filename)
44
45      no_frames = no_frames + 1
46
47      # Display processed filename on the screen
48      print("")
49      print(filename)
50
51      # Remove first two rows and columns, as they have untypical
```

```
    data and spoil the contrast-stretching and analysis
52      datafixed = data[2:,2:]
53
54      # Separate the odd and even data columns
55      oddcolumns = datafixed[:,0::2]
56      evencolumns = datafixed[:,1::2]
57
58      # ROI parameters
59      startcolumn = 10
60      endcolumn = 250
61      startrow = 10
62      endrow = 500
63
64      # Number of columns and rows in ROI
65      columns = endcolumn - startcolumn
66      rows = endrow - startrow
67
68      # Define ROIs
69      roi = datafixed[startrow:endrow,startcolumn:endcolumn*2]
70      oddroi = oddcolumns[startrow+90:endrow-90,startcolumn+90:
    endcolumn]
71      evenroi = evencolumns[startrow+90:endrow-90,startcolumn+90:
    endcolumn]
72
73      # Calculate mean pixel value for full frame, as well as for
    odd and even image-halves
74      meanpix = roi.mean()
75      oddmean = oddroi.mean()
76      evenmean = evenroi.mean()
77
78      # Calculate standard deviations along x-axis, y-axis and
    overall for both image-halves
79      xstdodd = (np.sum((np.array(oddroi).std(axis=1, ddof=1, dtype
    =np.float64))**2)/rows)**0.5
80      xstdeven = (np.sum((np.array(evenroi).std(axis=1, ddof=1,
    dtype=np.float64))**2)/rows)**0.5
81      ystdodd = (np.sum((np.array(oddroi).std(axis=0, ddof=1, dtype
```

```
    =np.float64))**2)/columns)**0.5
82      ystdeven = (np.sum((np.array(evenroi).std(axis=0, ddof=1,
    dtype=np.float64))**2)/columns)**0.5
83      stdodd = np.array(oddroi).std(ddof=1, dtype=np.float64)
84      stdeven = np.array(evenroi).std(ddof=1, dtype=np.float64)
85
86      # Save odd columns image-half data into a .txt file
87      mtx_odd = [meanpix, oddmean, xstdodd, ystdodd, stdodd]
88      fo = open(std_file_odd_path,"a")
89      for item in mtx_odd:
90          print("%.11s  " % item, end="", file=fo) # each saved
    number is limited to 11 characters
91      print("", file=fo)
92      fo.close()
93
94      # Save even columns image-half data into a .txt file
95       mtx_even = [meanpix, evenmean, xstdeven, ystdeven,stdeven]
96      fe = open(std_file_even_path,"a")
97      for item in mtx_even:
98          print("%.11s  " % item, end="", file=fe) # each saved
    number is limited to 11 characters
99      print("", file=fe)
100     fe.close()
101
102 # Summary info
103 print("")
104 print("Number of processed images:",no_frames)
105 print("ROI resolution:",columns,"x",rows,"pixels.")
```

References

Aerts, C. (2015). Asteroseismology. *Physics Today*, 68(5):36.

AIAA (2017). Electromagnetic Compatibility Requirements for Space Equipment and Systems, AIAA S-121-2017.

Andor Technology (2012a). CCD Spectral Response (QE). `http://www.andor.com/learning-academy/ccd-spectral-response-(qe)-defining-the-qe-of-a-ccd`.

Andor Technology (2012b). Electron Multiplying CCD Cameras. `http://www.andor.com/learning-academy/electron-multiplying-ccd-cameras-the-technology-behind-emccds`.

Andor Technology (2012c). Sensitivity. `http://www.andor.com/learning-academy/sensitivity-making-sense-of-sensitivity`.

André, P. G. and Wyatt, K. (2014). *EMI Troubleshooting Cookbook for Product Designers*. SciTech Publishing.

Argabright, V. S., VanCleve, J. E., Bachtell, E. E., Hegge, M. J., McArthur, S. P., Dumont, F. C., Rudeen, a. C., Pullen, J. L., Teusch, D. A., Tennant, D. S., and Atcheson, P. D. (2008). The Kepler photometer focal plane array. In *Proceedings of SPIE*, volume 7010, page 70102L.

Avago Technologies (2010). Temperature Compensation Circuit for Constant LED Intensity.

Avago Technologies (2013). HLMP-3750 Datasheet.

Barnes, E. (1998). Integrated Solutions for CCD Signal Processing. *Analog Dialogue*, 32-1.

Bertram, W. J., Mohsen, A. M., Morris, F. J., Sealer, D. A., Sequin, C. H.,

and Tompsett, M. F. (1974). Three-Level Metallization Three-Phase CCD. *IEEE Transactions on Electron Devices*, 21(12):758–767.

Beynon, J. and Lamb, D. (1980). *Charge-Coupled Devices and their Applications*. McGraw-Hill Book Company (UK) Limited, London, England.

Bobeck, A. H. (1972). Magnetic Bubble Devices. *Journal of Vacuum Science and Technology*, 9(4):1145.

Borucki, W. J., Koch, D. G., Dunham, E. W., and Jenkins, J. (1997). The Kepler Mission: A Mission To Determine The Frequency Of Inner Planets Near The Habitable Zone For A Wide Range Of Stars. In *Planets beyond the Solar System and the Next Generation of Space Missions*, page 153.

Boyle, W. S. and Smith, G. E. (1970). Charge Coupled Semiconductor Devices. *The Bell System Technical Journal*, 49(4):587–593.

Brown, T. M. (2003). Expected Detection and False Alarm Rates for Transiting Jovian Planets. *The Astrophysical Journal Letters*, 593:L125–L128.

Brown, T. M., Charbonneau, D., Gilliland, R. L., Noyes, R. W., and Burrows, A. (2001). Hubble Space Telescope Time-Series Photometry of the Transiting Planet of HD 209458. *The Astrophysical Journal*, 552(2):699–709.

Brown, T. M. and Gilliland, R. L. (1994). Asteroseismology. *Annual Review of Astronomy and Astrophysics*, 321(1):37–82.

Burke, B. E., Gregory, J. a., Cooper, M., Loomis, A. H., Young, D. J., Lind, T. a., Doherty, P., Daniels, P., Landers, D. J., Ciampi, J., Johnson, K. F., and Brien, P. W. O. (2007). CCD Imager Development for Astronomy. *Lincoln Laboratory Journal*, 16(2):393–412.

Chaplin, W. J. and Miglio, A. (2013). Asteroseismology of Solar-Type and Red-Giant Stars. *Annual Review of Astronomy and Astrophysics*, 51:353–392.

Charbonneau, D., Brown, T. M., Latham, D. W., and Mayor, M. (2000). Detection of Planetary Transits Across a Sun-like Star. *The Astrophysical Journal Letters*, 529:L45–L48.

Christian, D. J., Pollacco, D. L., Clarkson, W. I., Cameron, A. C., Evans, N., Fitzsimmons, A., Haswell, C. A., Hellier, C., Hodgkin, S. T., Horne, K., Kane, S. R., Keenan, F. P., Lister, T. A., Norton, A. J., Ryans, R., Skillen, I., Street, R. A., West, R. G., and Wheatley, P. J. (2005). Current Status of the SuperWASP Project. In *13th Cambridge Workshop on Cool Stars, Stellar Systems and the Sun*.

Cleve, J. E. V., Howell, S. B., Smith, J. C., Clarke, B. D., Susan, E., Bryson, S. T., Lund, M. N., Handberg, R., and Chaplin, W. J. (2016). That's How We Roll: The NASA K2 Mission Science Products and Their Performance Metrics. *Publications of the Astronomical Society of the Pacific*, 128(965):075002.

Djorgovsky, S. (1984). Proceedings of the Workshop on Improvements to Photometry. In *NASA Conference Publications*, page 2350.

E2V Technologies (2010). PLATO (CCD270) and Radiation Test Vehicle (CCD280), PLATO-E2V-TRE-010. Technical report.

E2V Technologies (2011). CCD47-20 NIMO Back Illuminated High Performance NIMO Back Illuminated CCD Sensor. Technical report.

E2V Technologies (2016a). CCD42-10 Back Illuminated High Performance AIMO CCD Sensor. Technical report.

E2V Technologies (2016b). Full Frame CCD270 Interface Control Document, PLATO-E2V-TRE-118. Technical report.

ECSS-E-ST-20-07C Rev.1 (2012). Space engineering - Electromagnetic compatibility.

Einstein, A. (1905). Uber einen die Erzeugung und Vervandlung des Lichtes betreffenden heuristischen Gesichtspunkt. *Annalen der Physik*, 17(6):132–148.

Endicott, J., Walker, A., Bowring, S., Turner, P., Allen, D., Piersanti, O., Short, A., and Walton, D. (2012). Charge-coupled devices for the ESA PLATO M-class Mission. In *Proceedings of SPIE, High Energy, Optical, and Infrared Detectors for Astronomy V*, number 8453, page 84531J.

ESA (2006a). CoRoT Instruments. http://www.esa.int/Our_Activities/Space_Science/COROT/COROT_instruments.

ESA (2006b). Space in Images: CoRoT. http://www.esa.int/spaceinimages/Missions/COROT/(class)/image?mission=COROT&type=I.

ESA (2016). Impact of 2 MHz operation for the PLATO CCD: preliminary assessment, ESA-SCI-FV-PLO-MO-0001. Technical report.

ESA (2017). PLATO - Definition Study Report, ESA-SCI(2017)1. Technical report.

ESA-PLATO-ESTEC-MIS-SP-002 (2014). PLATO EMC Specification.

Exoplanet.eu (2017). The Extrasolar Planets Encyclopaedia — Catalog Listing. http://exoplanet.eu/catalog/.

Fanson, J., Frerking, M., and Duren, R. (2011). Kepler Mission Development Challenges and Early Results. In *2011 Aerospace Conference*, pages 1–8. IEEE.

Favata, F., Roxburgh, I., and Christensen-Dalsgaard, J. (2000). Eddington Assessment Study Report, ESA - SCI (2000). Technical report, ESA.

Gow, J. P., Walton, D., Smith, A., Hailey, M., Curry, P., and Kennedy, T. (2017). On-ground and in-orbit characterisation plan for the PLATO CCD normal cameras. *Journal of Instrumentation*, 12(11).

Gregory, J., Burke, B., Kosicki, B., and Reich, R. (1999). Developments in X-ray and astronomical CCD imagers. *Nuclear Instruments and Methods in Physics Research Section A: Accelerators, Spectrometers, Detectors and Associated Equipment*, 436(1-2):1–8.

Hamamatsu (2012). CCD Saturation and Blooming. http://learn.hamamatsu.com/articles/ccdsatandblooming.html.

Hamamatsu (2017). Metal Oxide Semiconductor (MOS) Capacitor. http://hamamatsu.magnet.fsu.edu/articles/moscapacitor.html.

Henry, G. W., Marcy, G. W., Butler, R. P., and Vogt, S. S. (2000). A Transit-

ing "51 Peg-like" Planet. *The Astrophysical Journal Letters*, 529:L41–L44.

Holst, G. C. and Lomheim, T. S. (2011). *CMOS/CCD Sensors and Camera Systems*. JCD Publishing & SPIE Press, 2nd edition.

Howell, S. B. (2006). *Handbook of CCD Astronomy*. Cambridge University Press, Cambridge, 2nd edition.

Hu, C. C. (2010). *Modern Semiconductor Devices for Integrated Circuits*. Pearson Education, New Jersey, internatio edition.

Janesick, J. (2001). *Scientific Charge–Coupled Devices*. SPIE Press, Bellingham, WA.

Janesick, J. (2007). *Photon Transfer: DN* $\rightarrow \lambda$. SPIE Press, Bellingham, WA.

Karcher, A., Bebek, C. J., Kolbe, W. F., Maurath, D., Prasad, V., Uslenghi, M., and Wagner, M. (2004). Measurement of Lateral Charge Diffusion in Thick , Fully Depleted , Back-illuminated CCDs. *IEEE Transactions on Nuclear Science*, 51(5).

Lapeyrere, V., Bernardi, P., Buey, J.-T., Auvergne, M., and Tiphène, D. (2006). Calibration of Flight Model CCDs for CoRoT Mission. *Monthly Notices of the Royal Astronomical Society*, 365(4):1171–1179.

Lesser, M. (2014). Silicon sensor quantum efficiency, reflectance, and calibration. In *Proceedings of SPIE*, volume 9154, page 915411.

Lincoln Laboratory (MIT) (2015). High-Sensitivity Imaging. `https://www.ll.mit.edu/mission/electronics/ait/hisensitivityimage.html`.

Mallette, L. A. and Adams, R. (2011). Introduction to EMI/EMC test requirements for space applications. *IEEE Aerospace and Electronic Systems Magazine*, 26(6):24–29.

Marinescu, A., Scornea, A., and Ursea, L. (2006). EMC progress in Romania. In *17th International Zurich Symposium on Electromagnetic Compatibility*, pages 140–143.

Merline, W. J. and Howell, S. B. (1995). A realistic model for point-sources

imaged on array detectors: The model and initial results. *Experimental Astronomy*, 6(1-2):163–210.

MIL-STD-461G (2015). Requirements for the Control of Electromagnetic Interference Characteristics of Subsystems and Equipment.

MIL-STD-462D (1993). Measurement of Electromagnetic Interference Characteristics.

MIL-STD-464C (2010). Electromagnetic Environmental Effects Requirements for Systems.

MIT (2015). TESS (Transiting Exoplanet Survey Satellite). `http://space.mit.edu/space-based-observatories/tess-transiting-exoplanet-survey-satellite`.

Moutou, C., Deleuil, M., Guillot, T., Baglin, A., Bordé, P., Bouchy, F., Cabrera, J., Csizmadia, S., and Deeg, H. J. (2013). CoRoT: Harvest of the Exoplanet Program. *Icarus*, 226(2):1625–1634.

NASA (2015). Kepler and K2 Image Gallery. `https://www.nasa.gov/content/kepler-multimedia`.

NASA (2017a). Characteristics of the TESS Space Telescope. `https://heasarc.gsfc.nasa.gov/docs/tess/the-tess-space-telescope.html`.

NASA (2017b). Kepler and K2: Discoveries. `https://www.nasa.gov/kepler/discoveries`.

Paul, C. (1989). A Comparison of the Contributions of Common-Mode and Differential-Mode Currents in Radiated Emissions. *IEEE Transactions on Electromagnetic Compatibility*, 31(2):189–193.

Paul, C. R. (2006). *Introduction to Electromagnetic Compatibility*. John Wiley & Sons, Hoboken, NJ, second edition.

PLATO-DLR-PL-RP-006 (2016). Instrument Requirements Justification Document.

PLATO-ESTEC-PL-RS-003 (2016). PLATO CCD Requirements.

PLATO-OHB-PL-RS-005 (2017). PLATO N-FEE User Requirements Document.

Pollacco, D. L., Skillen, I., Collier Cameron, A., Christian, D. J., Hellier, C., Irwin, J., Lister, T. A., Street, R. A., West, R. G., Anderson, D., Clarkson, W. I., Deeg, H., Enoch, B., Evans, N., Fitzsimmons, A., Haswell, C. A., Hodgkin, S., Horne, K., Kane, S. R., Keenan, F. P., Maxted, P. F. L., Norton, A. J., Osborne, J., Parley, N. R., Ryans, R. S. I., Smalley, B., Wheatley, P. J., and Wilson, D. (2006). The WASP Project and the SuperWASP Cameras. *Publications of the Astronomical Society of the Pacific*, 118(848):1407–1418.

Ragazzoni, R., Magrin, D., Rauer, H., Pagano, I., Nascimbeni, V., Piotto, G., Piazza, D., Levacher, P., Schweitzer, M., Basso, S., Bandy, T., Benz, W., Bergomi, M., Biondi, F., Boerner, A., Borsa, F., Brandeker, A., Brändli, M., Bruno, G., Cabrera, J., Chinellato, S., De Roche, T., Dima, M., Erikson, A., Farinato, J., Munari, M., Ghigo, M., Greggio, D., Gullieuszik, M., Klebor, M., Marafatto, L., Mogulsky, V., Peter, G., Rieder, M., Sicilia, D., Spiga, D., Viotto, V., Wieser, M., Heras, A. M., Gondoin, P., Bodin, P., and Catala, C. (2016). PLATO: a multiple telescope spacecraft for exo-planets hunting. In *Proceedings of SPIE, Space Telescopes and Instrumentation 2016: Optical, Infrared, and Millimeter Wave*, volume 9904, page 990428.

Rauer, H., Catala, C., Aerts, C., Appourchaux, T., Benz, W., Brandeker, A., Christensen-Dalsgaard, J., Deleuil, M., Gizon, L., Goupil, M. J., Güdel, M., Janot-Pacheco, E., Mas-Hesse, M., Pagano, I., Piotto, G., Pollacco, D., Santos, Smith, A., Suárez, J. C., Szabó, R., Udry, S., Adibekyan, V., Alibert, Y., Almenara, J. M., Amaro-Seoane, P., Eiff, M. A., Asplund, M., Antonello, E., Barnes, S., Baudin, F., Belkacem, K., Bergemann, M., Bihain, G., Birch, A. C., Bonfils, X., Boisse, I., Bonomo, A. S., Borsa, F., Brandão, I. M., Brocato, E., Brun, S., Burleigh, M., Burston, R., Cabrera, J., Cassisi, S., Chaplin, W., Charpinet, S., Chiappini, C., Church, R. P., Csizmadia, S., Cunha, M., Damasso, M., Davies, M. B., Deeg, H. J., Díaz, R. F., Dreizler, S., Dreyer, C., Eggenberger, P., Ehrenreich, D., Eigmüller, P., Erikson, A., Farmer, R., Feltzing, S., de Oliveira Fialho, F., Figueira, P., Forveille, T., Fridlund, M., García,

R. A., Giommi, P., Giuffrida, G., Godolt, M., da Silva, J. G., Granzer, T., Grenfell, J. L., Grotsch-Noels, A., Günther, E., Haswell, C. A., Hatzes, A. P., Hébrard, G., Hekker, S., Helled, R., Heng, K., Jenkins, J. M., Johansen, A., Khodachenko, M. L., Kislyakova, K. G., Kley, W., Kolb, U., Krivova, N., Kupka, F., Lammer, H., Lanza, A. F., Lebreton, Y., Magrin, D., Marcos-Arenal, P., Marrese, P. M., Marques, J. P., Martins, J., Mathis, S., Mathur, S., Messina, S., Miglio, A., Montalban, J., Montalto, M., P. F. G. Monteiro, M. J., Moradi, H., Moravveji, E., Mordasini, C., Morel, T., Mortier, A., Nascimbeni, V., Nelson, R. P., Nielsen, M. B., Noack, L., Norton, A. J., Ofir, A., Oshagh, M., Ouazzani, R. M., Pápics, P., Parro, V. C., Petit, P., Plez, B., Poretti, E., Quirrenbach, A., Ragazzoni, R., Raimondo, G., Rainer, M., Reese, D. R., Redmer, R., Reffert, S., Rojas-Ayala, B., Roxburgh, I. W., Salmon, S., Santerne, A., Schneider, J., Schou, J., Schuh, S., Schunker, H., Silva-Valio, A., Silvotti, R., Skillen, I., Snellen, I., Sohl, F., Sousa, S. G., Sozzetti, A., Stello, D., Strassmeier, K. G., Švanda, M., Szabó, G. M., Tkachenko, A., Valencia, D., Van Grootel, V., Vauclair, S. D., Ventura, P., Wagner, F. W., Walton, N. A., Weingrill, J., Werner, S. C., Wheatley, P. J., and Zwintz, K. (2014). The PLATO 2.0 mission. *Experimental Astronomy*, 38(1-2):249–330.

Ricker, G. R., Winn, J. N., Vanderspek, R., Latham, D. W., Bakos, G. Á., Bean, J. L., Berta-Thompson, Z. K., Brown, T. M., Buchhave, L., Butler, N. R., Butler, R. P., Chaplin, W. J., Charbonneau, D., Christensen-Dalsgaard, J., Clampin, M., Deming, D., Doty, J., De Lee, N., Dressing, C., Dunham, E. W., Endl, M., Fressin, F., Ge, J., Henning, T., Holman, M. J., Howard, A. W., Ida, S., Jenkins, J. M., Jernigan, G., Johnson, J. A., Kaltenegger, L., Kawai, N., Kjeldsen, H., Laughlin, G., Levine, A. M., Lin, D., Lissauer, J. J., MacQueen, P., Marcy, G., McCullough, P. R., Morton, T. D., Narita, N., Paegert, M., Palle, E., Pepe, F., Pepper, J., Quirrenbach, A., Rinehart, S. A., Sasselov, D., Sato, B., Seager, S., Sozzetti, A., Stassun, K. G., Sullivan, P., Szentgyorgyi, A., Torres, G., Udry, S., and Villasenor, J. (2014). Transiting Exoplanet Survey Satellite. *Journal of Astronomical Telescopes, Instruments, and Systems*, 1(1):014003.

Robbins, M. S. and Hadwen, B. J. (2003). The Noise Performance of Electron

Multiplying Charge-Coupled Devices. *IEEE Transactions on Electron Devices*, 50(5):1227–1232.

Saveliev, V. (2010). Silicon Photomultiplier - New Era of Photon Detection. In *Advances in Optical and Photonic Devices*.

SMC-S-008 (2008). Electromagnetic Compatibility Requirements for Space Equipment and Systems.

Smith, A. M. S. and The WASP consortium (2014). The SuperWASP Exoplanet Transit Survey. *Contributions of the Astronomical Observatory Skalnate Pleso*, 43(3):500–512.

Trevisanello, L., Meneghini, M., Mura, G., Sanna, C., Buso, S., and Spiazzi, G. (2007). Thermal stability analysis of High Brightness LED during high temperature and electrical aging. In *Proc. of SPIE, Seventh International Conference on Solid State Lighting*, volume 6669, page 666913.

Trougnou, L. (2012). ECSS Space Systems Electromagnetic Compatibility Handbook. *2012 ESA Workshop on Aerospace EMC*, pages 1–6.

Tsatalas, S. (2018). Electromagnetic Compatibility for Space Applications: Test Specifications, Standards, and Methods. In Nikolopoulos, C. D., editor, *Electromagnetic Compatibility for Space Systems Design*, pages 115–152.

Van Zeghbroeck, B. (2011). Principles of Semiconductor Devices.

Varshni, Y. P. (1967). Temperature Dependence of the Energy Gap in Semiconductors. *Physica*, 34(1):149–154.

Widenhorn, R., Blouke, M. M., Weber, A., Rest, A., and Bodegom, E. (2002). Temperature dependence of dark current in a CCD. In *Proceedings of SPIE, Sensors and Camera Systems for Scientific, Industrial, and Digital Photography Applications III*, volume 4669, pages 193–201.